

1999

## The thermographic nondestructive evaluation of iron aluminide green sheet

Michael L. Watkins  
*College of William & Mary - Arts & Sciences*

Follow this and additional works at: <https://scholarworks.wm.edu/etd>



Part of the [Materials Science and Engineering Commons](#)

---

### Recommended Citation

Watkins, Michael L., "The thermographic nondestructive evaluation of iron aluminide green sheet" (1999). *Dissertations, Theses, and Masters Projects*. Paper 1539623953.  
<https://dx.doi.org/doi:10.21220/s2-j2yd-xf56>

This Dissertation is brought to you for free and open access by the Theses, Dissertations, & Master Projects at W&M ScholarWorks. It has been accepted for inclusion in Dissertations, Theses, and Masters Projects by an authorized administrator of W&M ScholarWorks. For more information, please contact [scholarworks@wm.edu](mailto:scholarworks@wm.edu).

## INFORMATION TO USERS

This manuscript has been reproduced from the microfilm master. UMI films the text directly from the original or copy submitted. Thus, some thesis and dissertation copies are in typewriter face, while others may be from any type of computer printer.

**The quality of this reproduction is dependent upon the quality of the copy submitted.** Broken or indistinct print, colored or poor quality illustrations and photographs, print bleedthrough, substandard margins, and improper alignment can adversely affect reproduction.

In the unlikely event that the author did not send UMI a complete manuscript and there are missing pages, these will be noted. Also, if unauthorized copyright material had to be removed, a note will indicate the deletion.

Oversize materials (e.g., maps, drawings, charts) are reproduced by sectioning the original, beginning at the upper left-hand corner and continuing from left to right in equal sections with small overlaps. Each original is also photographed in one exposure and is included in reduced form at the back of the book.

Photographs included in the original manuscript have been reproduced xerographically in this copy. Higher quality 6" x 9" black and white photographic prints are available for any photographs or illustrations appearing in this copy for an additional charge. Contact UMI directly to order.

**UMI<sup>®</sup>**

Bell & Howell Information and Learning  
300 North Zeeb Road, Ann Arbor, MI 48106-1346 USA  
800-521-0600



# THE THERMOGRAPHIC NONDESTRUCTIVE EVALUATION OF IRON ALUMINIDE GREEN SHEET

---

A Dissertation

Presented to

The Faculty of the Department of Applied Science

The College of William and Mary in Virginia

In Partial Fulfillment

Of the Requirements for the Degree of

Doctor of Philosophy

---

By

**Michael L. Watkins**

1999

**UMI Number: 9942561**

**Copyright 1999 by  
Watkins, Michael Lee**

**All rights reserved.**

---

**UMI Microform 9942561  
Copyright 1999, by UMI Company. All rights reserved.**

**This microform edition is protected against unauthorized  
copying under Title 17, United States Code.**

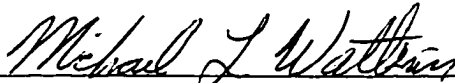
---

**UMI**  
300 North Zeeb Road  
Ann Arbor, MI 48103

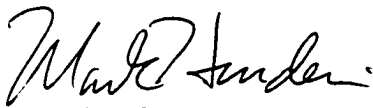
## APPROVAL SHEET


This dissertation is submitted in partial fulfillment of  
the requirements for the degree of

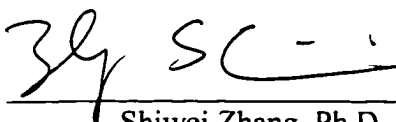
Doctor of Philosophy


  
Michael L. Watkins

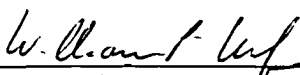
Approved. April 1999

  
Mark K. Hinders, Ph.D.  
Associate Professor of Applied Science

  
Dennis M. Manos, Ph.D.  
CSX Professor of Applied Science and Physics

  
Shiwei Zhang, Ph.D.  
Assistant Professor of Applied Science and Physics

  
Anne C. Reilly, Ph.D.  
Assistant Professor of Physics

  
William P. Winfree, Ph.D.  
NASA Langley Research Center

THE THERMOGRAPHIC NONDESTRUCTIVE  
EVALUATION OF IRON ALUMINIDE GREEN SHEET

Copyright

by

Michael L. Watkins

1999

# Dedication

This work is dedicated to my family

Those far and near, old and young, furry and friendly.

There is a special place in this dedication for my dear wife, Alissa,  
and our wonderful daughters, Alana and Meaghan.

They were with me every moment.

May God bless my family as I have been blessed.



# Contents

Acknowledgments	vi
List of Tables	vii
List of Figures	viii
Abstract	xiii
<b>Chapter 1 Introduction</b>	<b>2</b>
1.1 Background . . . . .	2
1.1.1 Powder metallurgy industry . . . . .	4
1.1.2 Current process overview . . . . .	6
1.2 The need for a new inspection method . . . . .	9
<b>Chapter 2 Thermography</b>	<b>15</b>
2.1 Background . . . . .	15
2.2 Heat conduction in solids . . . . .	18
2.3 Review of thermal nondestructive evaluation. . . . .	24
<b>Chapter 3 Preliminary Investigations</b>	<b>41</b>
3.1 Preliminary characterization of green sheet . . . . .	41
3.2 Preliminary thermography investigations . . . . .	54
3.3 Conclusions of preliminary investigation . . . . .	77
<b>Chapter 4 Development of the Inspection Method</b>	<b>80</b>
4.1 Introduction . . . . .	80
4.1.1 Equipment . . . . .	81
4.2. Reference samples . . . . .	91

4.2.1	Specimen fabrication . . . . .	93
4.2.2	Characterization . . . . .	94
4.2.3	Assessment of heat transfer properties . . . . .	104
4.3	Green sheet heat transfer . . . . .	121
<b>Chapter 5</b>	<b>Results of Process Study</b>	<b>137</b>
5.1	Introduction . . . . .	137
5.2.	Methodology . . . . .	140
5.3	Results . . . . .	144
5.3.1	Yield . . . . .	144
5.3.2	Heterogeneity . . . . .	146
5.3.3	Characterization of production green sheet morphology . .	150
5.3.4	Development of green sheet conformance criteria . . . . .	171
<b>Chapter 6</b>	<b>Conclusions</b>	<b>183</b>

Bibliography

Vita

# Acknowledgements

This effort was made possible with the support and assistance of many people. Foremost, I would like to thank my sponsor, Philip Morris USA, for providing me this opportunity through its financial support and commitment to excellence. I would also like to express my appreciation to Professor Mark Hinders and the other members of my committee for their support and helpful suggestions in preparing the manuscript. I will always look upon my time at The College of William and Mary with a sense of pride, excitement, and enthusiasm. I also owe a great deal of thanks to Bill Winfree and Elliott Cramer of the NASA Langley Research Center for their generosity in providing access to their laboratories and for their numerous helpful technical suggestions.

This work would not have been possible without the interest and active support of those involved in manufacturing. I would like to thank all those at Ametek Specialty Metals Division for supplying samples, data, and for the many fruitful discussions regarding the nuances of powder metallurgy quality. I would also like to thank Vicki Balega and Don Miser of Philip Morris USA for their assistance in producing the micrographs contained within the dissertation.

Finally, I would like to express my deepest thanks to my family and friends. From my dear parents who taught me, by example, to reach higher every day, to the occasional encouraging word of a friend, neighbor, or coworker, all have contributed to the success of this project.

# List of Tables

Table	Page
1.1 Application of NDE in powder metallurgy	10
3.1 Material properties of the green sheet components	43
4.1 Reference blends	94
4.2 Volume fraction of various reference samples	95
4.3 Relative cooling rates of reference samples during the first 168 ms after the end of the heating pulse	111
5-1 Summary of process yield for flaw precursor study	145

# List of Figures

Figure		Page
1.1	Green sheet compaction process.	7
2.1	Geometry for through-heating.	25
2.2	Heating curves for through-heating with pulsed excitation.	27
2-3	Geometry for front-side heating.	29
2-4	Cooling curves for front-side impulse excitation.	31
2-5	Heating curves for front-side step heating.	32
3-1	Typical water atomization process for the production of alloyed powder.	45
3-2	Optical micrograph depicting the irregular shape of FeAl particles.	46
3-3	Polarized light micrograph showing the distribution of binder on the surface of green sheet.	47
3-4	Secondary (SEI) and backscatter (BEI) SEM images showing alloy powder distribution..	48
3-5	Diffusion bonding associated with particle sintering.	50
3-6	Formation of a grain boundary between two diffusion bonded particles.	51
3-7	Change in microstructure associated with de-binder operation.	52
3-8	Changes in microstructure associated with de-binder operation.	53
3-9	Detection of defects using step heating with quartz lamps.	56
3-10	Detection of cellophane tape layers.	58

3-11	Optical image, thermal slope image, and micrometer readings for tapered sample.	60
3-12	Comparison of a digital x-ray image and a thermal image.	61
3-13	Details of thermal slope image obtained early in the step heating.	62
3-14	Line scan of thermal slope image obtained early in the step heating.	65
3-15	Sequential images showing thermal response through progressively thicker regions of the tapered sample.	66
3-16	Normalized temperature evolution for through heating of green sheet using an impulse excitation.	67
3-17	Optical image of green sheet specimen as tested.	69
3-18	Thermal image data obtained 32 ms after flash.	70
3-19	Thermal images for opposite sides of the same green sheet specimen.	72
3-20	Thermal images showing regions A through G which were removed from the specimen for characterization.	73
3-21	Thermal image intensity versus bulk density.	75
3-22	Backscatter images illustrating the difference in FeAl volume fraction for regions A and G.	76
3-23	Comparison of data collected for a tapered green sheet sample using several techniques.	78
4-1	Geometry of prototype inspection system.	82
4-2	Wide angle view of inspection prototype.	83
4-3	View of major prototype components.	84
4-4	Inspection platform showing specimen orientation, reference plate, and scale.	85
4-5	Close-up view of inspection platform.	86
4-6	Variation of pixel distribution from a single green sheet sample.	89
4-7	Data acquisition flow chart.	90

4-8	Variation of bulk density as it depends on compaction force and loading binder.	97
4-9	Compact strength as a function of binder loading.	98
4-10	Alloy volume fraction as a function of percent FeAl powder.	99
4-11	Alloy volume fraction as a function of compaction force.	100
4-12	Thermal image of green compact reference panel.	102
4-13	Variation of thermal decay curve as a function of extremes in weight percent binder.	103
4-14	Thermal test panel with variations in binder concentration.	105
4-15	Thermal decay curves for various values of binder concentration.	106
4-16	Thermal test panel with variations in compaction level.	107
4-17	Thermal decay curves for various compaction forces.	108
4-18	Relative cooling rate of reference samples during the first 168 ms after the flash.	112
4-19	Relative cooling rate of reference samples during the first 168 ms after the flash.	113
4-20.	Variation in thickness as a function of binder loading.	114
4-21	Variation in thickness as a function of binder loading.	115
4-22	Normalized temperature rise for through-thickness heating as a function of binder loading.	116
4-23	Normalized temperature rise for through-thickness heating as a function of compaction level.	117
4-24	Variation in thermal diffusivity as a function of binder loading.	119
4-25	Variation of thermal diffusivity as a function of compaction level.	120
4-26	Variation in bulk diffusivity with alloy volume fraction and process history.	125
4-27	Particle shape function.	128

4-28	Particle composite model for three values of aspect ratio.	130
4-29	Optical micrograph depicting the irregular shape of FeAl particles as dark on a white background.	131
4-30	Thermal decay curve comparing model with data from reference specimen.	132
4-31	Thermal decay curve comparing model with data from reference specimen.	133
4-32	Relative variations of thermal response with thickness.	134
4-33	Variation of thermal response for various volume fractions of alloy.	135
5-1	Reference coordinates for FeAl sheet.	138
5-2	Camber results from excessive loading of FeAl on one side of the sheet.	139
5-3	Reference frame for the location of green sheet flaw precursors.	143
5-4	Green sheet heterogeneity as a predictor of crack formation during densification.	148
5.5	Multiple fine cracks in FeAl sheet result from heterogeneity in green sheet.	149
5.6	Thermal images illustrating the extension of morphological features through the thickness of the green sheet.	152
5-7	Thermal images illustrating the extension of morphological features through the thickness of the green sheet.	154
5-8	Normal edge symmetry.	155
5-9	Asymmetry of green sheet edge due to roller misalignment.	156
5-10	Transverse variation in FeAl volume fraction.	157
5-11	Disruption of blend flow from feed hopper.	159
5-12	Morphology resulting from unstable blend flow.	160
5-13	Crack in sintered green sheet resulting from low volume fraction of FeAl during compaction.	161
5-14	Characteristic longitudinal variation of FeAl volume fraction.	163
5-15	Longitudinal line scan illustrating the longitudinal modulation of FeAl volume fraction.	164



5-16	Digital x-ray image of sample 23B.	165
5-17	Transverse digital x-ray and thermal signals both indicate the relative alloy volume fraction.	166
5-18	Location of low FeAl volume fraction in the green sheet predicts the location of cracks resulting from rolling down to 0.25 mm (0.010").	168
5-19	Longitudinal band of low alloy volume fraction in this green sheet resulted in severe cracking during rolling down to 0.25 mm (0.010").	169
5-20	Severe cracking in the 0.010" sheet associated with low alloy volume in the green state.	170
5-21	At early times variations in the thermal map is indicative of the relative effusivity across the green sheet.	173
5-22	Transverse relative effusivity profiles associated with Sheet #1.	174
5-23	Transverse relative effusivity representing the population of green sheet which survived densification to provide acceptable alloy sheet. This profile is the basis for the conformance criteria.	175
5-24	Transverse relative effusivity representing the population of green sheet which failed during the attempt process the green sheet.	176
5-25	A comparison of the relative effusivity profiles for sheet #1 and the conformance standard predicted that the material would fail during post compaction processing.	178
5-26	The zero crossing of the spatial derivative of the relative effusivity profile locates the green sheet flaw.	179
5-27	Relative effusivity profile showing that green sheet defect precursors fall outside the conformance band.	180
5-28	Relative effusivity profile for "good" green sheet.	181
6-1	Arrangement depicting the integration of a front-flash thermal inspection technique into a roll compaction process.	189

# Abstract

The recent development of manufacturing techniques for the fabrication of thin iron aluminide sheet requires advanced quantitative methods for on-line inspection. An understanding of the mechanisms responsible for flaws and the development of appropriate flaw detection methods are key elements in an effective quality management system. The first step in the fabrication of thin FeAl alloy sheet is the formation of a green sheet by cold rolling FeAl powder mixed with organic binding agents. The green sheet composite has a bulk density, which is typically less than about 3.6 g/cc. The finished sheet, with a density of about 6.1 g/cc, is obtained using a series of process steps involving binder elimination, densification, sintering, and annealing. Non-uniformities within the green sheet are the major contributor to material failure in subsequent sheet processing and the production of non-conforming finished sheet. The production environment and physical characteristics of the composite provide for unique challenges in developing a rapid nondestructive inspection capability. The method must be non-contact due to the fragile nature of the composite. Limited access to the material also demands a one-sided inspection technique. An active thermographic method providing for 100% on-line inspection within an industrial process has been developed. This approach is cost competitive with alternative technologies, such as x-ray imaging systems, and provides the required sensitivity to the variations in material composition. The mechanism of flaw formation and the transformation of green sheet flaws into defects that appear in intermediate and finished sheet products are described. A mathematical model which describes the green sheet

heat transfer propagation, in the context of the inspection technique and the compact heterogeneity, is also presented. The potential for feedback within the production process is also discussed.

**THE THERMOGRAPHIC NONDESTRUCTIVE  
EVALUATION OF  
IRON ALUMINIDE GREEN SHEET**

# Chapter 1

## Introduction

### 1.1 Background

The inspection and evaluation of products fabricated from powder metal (P/M) technology is significant to the automotive, aerospace, medical, and electronic industries all of which use components derived from powder metallurgy. In many instances, this manufacturing approach can provide parts and stock materials of higher quality and reliability than those obtained using other manufacturing techniques [1]. The enhanced reliability of incoming materials and components contributes directly to the reliability of the products in which they are used. As the market for P/M parts grows, suppliers are seeking new means to monitor, control and optimize the powder metallurgy process. The focus of this work is the nondestructive evaluation of thin rolled iron aluminide alloy using thermal techniques designed for quality control during manufacturing. Iron aluminides are a group of intermetallic alloys containing primarily iron and aluminum which have a resistance to high temperature oxidation. Unlike many high temperature alloys, they provide good strength

without the addition of chromium.

While the formation of products from powder metallurgy can be quite complex, the typical process can be divided into four stages. In the first stage, powder metal constituents (the synthesis of these powders is often a multistage process in itself) are mixed with a binder and/or solvent. In the second stage pressure is used to compress the constituents into a single part. These are commonly referred to as green parts. The third stage is the removal of the binder and sintering of the metal particles into a solid structure. The density of the final material may vary greatly depending on the design requirements of the part. A fourth stage involving machining or forming process is often required. Each of these stages usually has several intermediate steps and each step exhibits characteristic defect morphologies and underlying formation mechanisms. The guiding principle in minimizing the impact of these flaws, with the goal of zero defects in the final product, is to identify the most significant flaws as early in the process as possible. Early detection provides the opportunity to correct the defect downstream in the process. If the flaw cannot be repaired, the defective part can at least be systematically removed from the process without disrupting product flow or investing further process resources in a bad part. It is in this context that the development of technologies that detect and quantify the quality of intermediate and final products will have a significant impact on future developments and applications of powder metallurgy technology.

The goal of this research is to develop a non-contact, real-time method of inspecting 100% of the green sheet produced by an existing industrial process. The relatively slow production rate (about 300 cm<sup>2</sup>/min.) allows time for adequate signal processing to provide

process feedback. It is anticipated that the technique could be adapted to much faster production rates and may be extended to applications for non-planar part geometries. This research provides a method and instrumentation specifications to quantitatively evaluate the formation of green sheet using time-resolved infrared thermography (often referred to as transient thermography). The technique involves heating the sheet using a programmed thermal excitation. The time evolution of the radiated energy contains information on variations in mass distribution, species, homogeneity, and thickness of the sheet. These variations give rise to anisotropic and heterogeneous heat transfer in the sheet. Both a theoretical basis for the interpretation and analysis of the data as well as a method for reducing the data to a form appropriate for process monitoring are developed. The results of this research will be used to specify instrumentation for product inspection.

### **1.1.1 Powder metallurgy industry**

The Metal Powder Industries Federation (MPIF) reported [2] in a 1996 industry review that North American companies had sales of about \$2 billion. Powder metal (P/M) components are used in wide variety of products (automotive, appliance, aerospace, electronic, business machine, chemical, construction, lawn & garden, medical, petroleum). For example, the typical passenger car contains approximately 30 pounds of parts derived from powder metallurgy processes. In recent years there has been an increased demand for P/M parts and all indications are that demand will continue to grow. P/M manufactures have realized that in order to compete globally they will have to transition their manufacturing practices from the traditional "powder metallurgy art form" to a total quality approach. A key element is the development of quality inspection tools and methodologies. Since the

industry is in the early stages of implementing this business strategy and P/M products are highly diverse. many opportunities exist to apply quantitative nondestructive evaluation.

Increasing dependence on P/M technology is driven by the need to reduce cost and increase the reliability of metal parts. There are several aspects of this technology which are attractive to P/M customers. P/M production methods can be used to fabricate near-net-shape components. Manufacturing techniques which provide near-net-shape parts reduce production costs by eliminating intermediate machining steps. Complex shapes can often be obtained without the need for cold working, which can result in crack formation. This advantage allows the cost of machining components to final tolerances to be reduced or in some cases eliminated. In addition, P/M part fabrication avoids the powder melting step in obtaining the part geometry. This is advantageous because the diffusion processes associated with solidification of a melted casting have a significant impact on the distribution of grain sizes and residual stresses within the final part. These material characteristics can have a significant impact on components reliability [3].

While the above advantages have been appreciated for many years, a significant incentive for using powder metallurgy is the ability to synthesize parts out of high performance super alloys. The fabrication of beta phase iron aluminide, FeAl, into a thin sheet by rolling a large starting volume of FeAl is not practical. For example, attempts to form sheet in this manner results in significant work-hardening which results in cracking. Attempting to process the material at elevated temperatures, near the melting point, is not feasible because the aluminum oxidizes and the alloy tends to dissolve hydrogen. Oxidation inhibits formation of the desired phase while excess hydrogen creates voids which increase



porosity. Both compromise the mechanical properties of the material. Processes involving extended periods at high temperatures promote grain growth. Increased grain size reduces low temperature ductility which can be important in part forming. A preferred process for FeAl synthesis minimizes these effects. The major process steps are described below.

### 1.1.2 Current process overview

The initial step, for the production of metal sheet from powder, is the formation of a green sheet composite which is approximately 700  $\mu\text{m}$  thick. This is achieved by roll compacting a mixture of powder alloy, binding agent and solvent (see figure 1-1). The production rate is about 300  $\text{cm}^2/\text{min}$ . The green sheet then undergoes a series of process steps (binder elimination, densification, sintering, annealing) to form the final FeAl sheet product. This final sheet product will be referred to simply as "sheet" to distinguish it from green sheet and intermediate products. The intermediate products have a thickness from 300  $\mu\text{m}$  to 200  $\mu\text{m}$  thick and densities as low as 60% of the theoretical density, about 6.12/ cc for the fully dense material. A process flow chart is shown in figure 1-2.

Mass distribution and thickness are critical attributes throughout the sheet forming process. The relatively high viscosity of the green sheet composite and the characteristically low malleability of the iron aluminide particles inhibit modification of the mass distribution once the green sheet is formed. Process variables such as mixture feed rate, roller speed, pressure and alignment are candidates for statistical process control (SPC) using feedback from the inspection system. The impact of non-uniform mass distribution can vary from the formation of final sheet material that contains flaws to an intermediate sheet product which fails during processing. Current yields are below production targets.

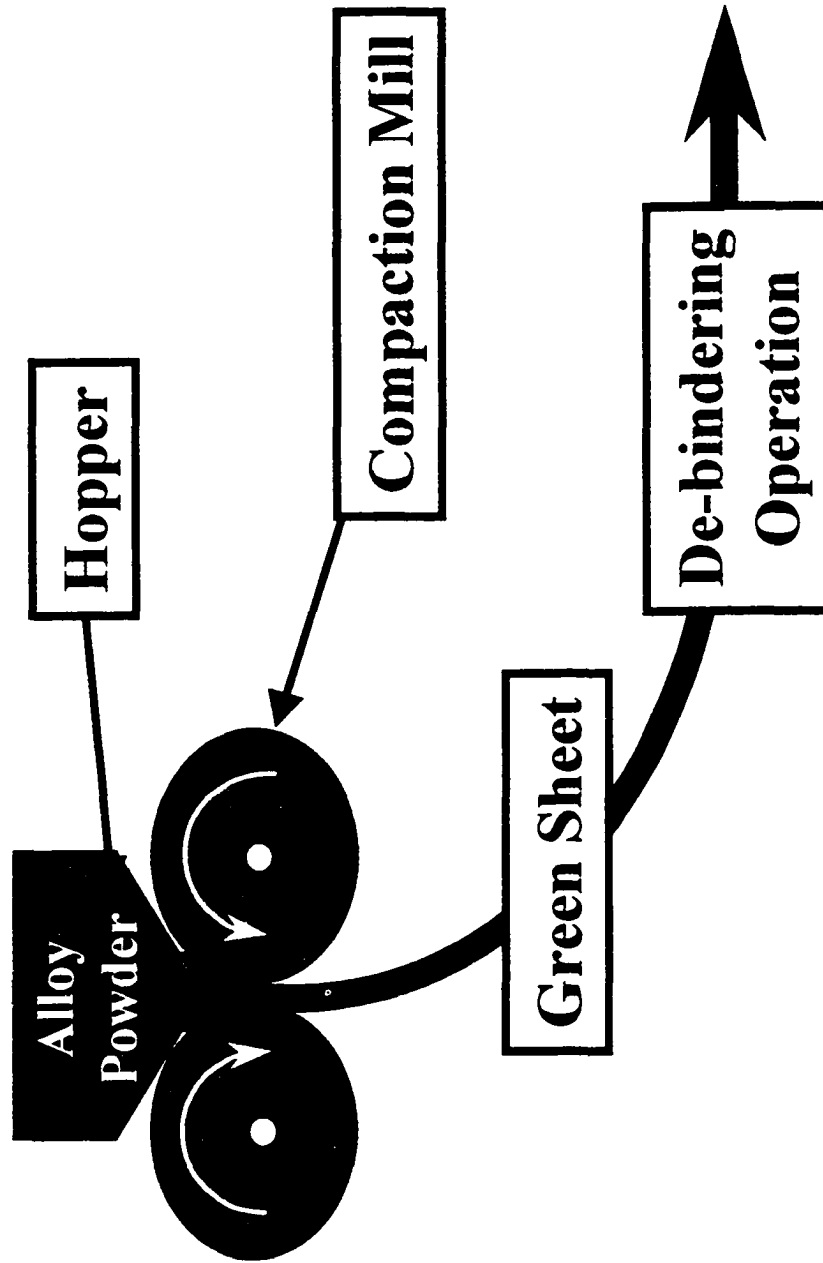


Figure 1-1: Green sheet compaction process.

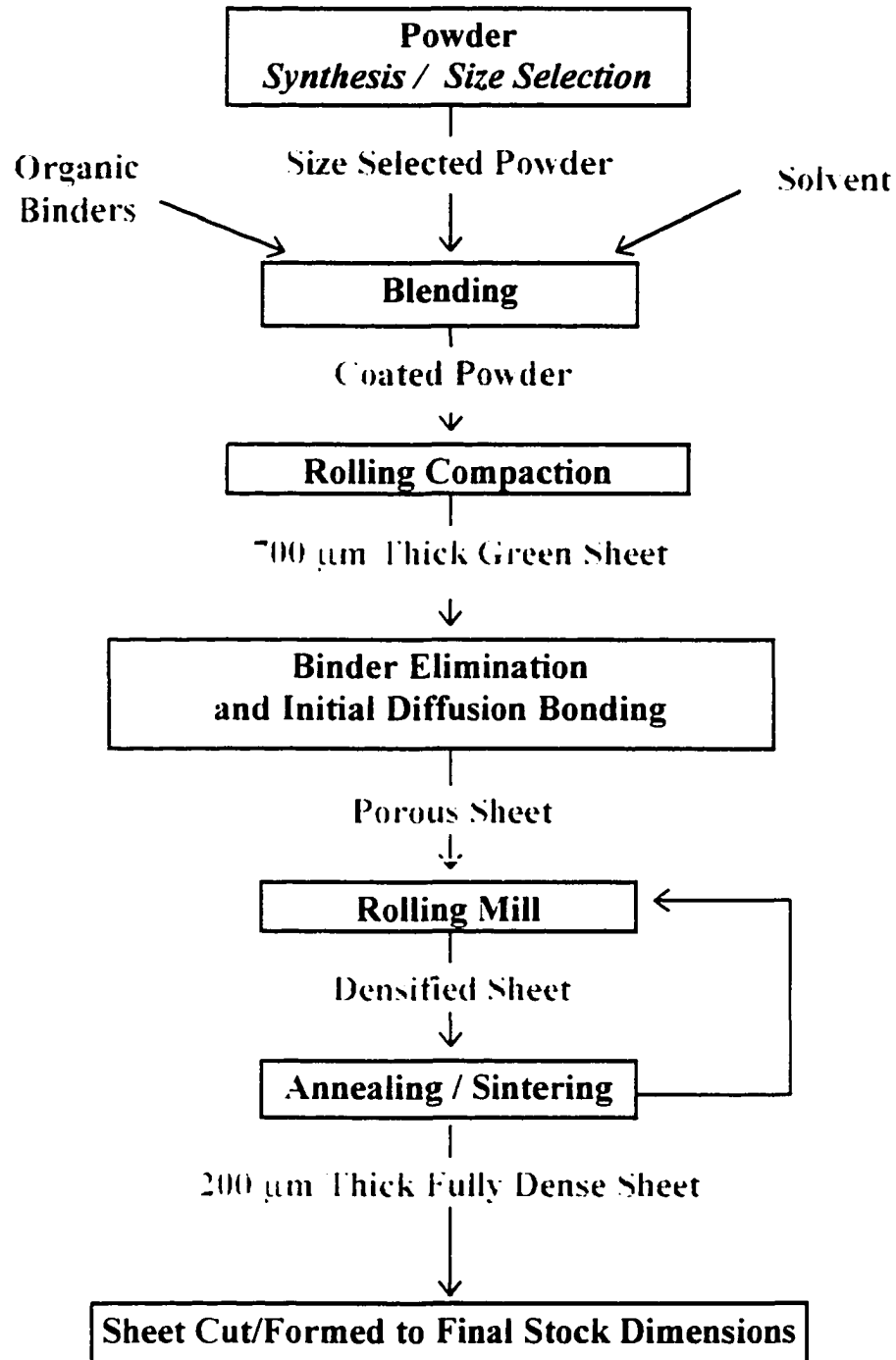


Figure 1-2: Flow chart of iron aluminide fabrication via roll compaction.

The dominant failure mode is the development of through thickness cracks in the sheet. Green sheet heterogeneity was hypothesized to be associated with this low yield yet there were no quantitative data to support this idea. Some fraction of the shipped finished material contains flaws, arising from the green sheet defects, which are not detected via the current inspection techniques. Attempts to form or machine materials with these defects results in part failure. A fraction of the defective material will survive fabrication into the final application structure. The compromised mechanical/electrical integrity of these structures will result in premature failures and reduced reliability. Thus, having an effective means of evaluating green sheet quality is critical.

## 1.2 The need for a new inspection method

Research into the application of modern quantitative NDE techniques to enhance the quality of P/M parts is relatively recent, with the first symposium dedicated to the application of NDE in powdered metallurgy held in the Summer of 1998 [4]. The most recently applied and newly emerging techniques and methods for the evaluation of P/M parts were presented and discussed at that meeting, but thermal techniques were not considered. A recent publication [5] on test methods by The Metal Powder Industries Federation (MPIF) reviewed the current NDE techniques being investigated for application in the industry. Table 1-1 illustrates an applications summary chart. Most noteworthy is the conclusion of the authors that thermal techniques have, "no application for green P/M parts". MPIF's 1998 edition of "Standard Test Methods for Metal Powders and Powder Metallurgy Products" [6] includes only off-line and destructive test methods. A comprehensive literature search

### Summary Matrix

Method	Description	Advantages	Limitations	Applicability
Eddy Current Testing	An alternating magnetic field induces eddy currents in the test part which produces a secondary field. If there is a defect in the test part, the electrical conductivity is altered and the signal response will change.	Sensitive to surface cracks; can be automated; inspection can be performed at high rates; flaws are indicated immediately; extensive software and computer packages are available.	Defects near the corner of an edge or in the subsurface are difficult to detect; detection interpretation can be complicated by more than one variable.	Has been used in the detection of sintered parts. Most promising for detecting flaws in green state parts.
Electrical Resistivity Inspection	A four point probe is moved across a part, the two outer probes generate the current, the two inner probes measure the voltage drop. The voltage drop is influenced by structural irregularities.	The testing equipment can be designed to read various ranges of resistivities; the probes can be adapted for the shape of test parts; testing equipment is inexpensive, easy to handle and portable.	The sharp probes may be damaging to the surface; the location of the defect must be known.	Some uses found for sintered parts. For green parts, the method may be applicable.
Ultrasonic Testing	Sound waves travel through the material are attenuated and are reflected at interfaces. The reflected beam is displayed and analyzed to determine the presence and location of flaws.	Ability to penetrate to substantial depths in many materials; high sensitivity to detect small flaws; rapid, and automated inspection	Requires experienced technician; requires couplant; difficult to detect flaws in rough, irregular and thin parts; flaws that are very near the surface may not be detectable.	Can be used in sintered P/M parts. For green P/M parts, it is not applicable ( high attenuation).
Thermal Imaging	Thermal Wave inspection involves the measurement or mapping of surface temperatures when heat flows in a test piece. The flaws in the test piece alter the heat flow patterns.	Applicable to test pieces having complex shapes and having wide area of coverage; can be used on one side of the test object; sensitive to defects close to the surface.	The condition of the surface has to be handled carefully; the equipment needed are complicated and high priced.	No application for green P/M parts.
X-ray Inspection	The part is rotated through a penetrating x-ray beam that may detect a defect and magnify its image on a screen.	Can be used to detect internal defects and detect significant variations in composition.	It is a high cost and cumbersome process; certain types of flaws are difficult to detect; safety measures are required.	Not applicable for green parts. Special analysis work for sintered parts.
Liquid Penetrant Inspection	Allowing a part to absorb a liquid penetrant, and then with special lighting equipment, view the part and look for the flaw areas.	No limit in the configuration of the workpiece and flaw orientation; the process is simple to utilize and control.	The major limitation is that it can detect only imperfection that are open to the surface; the surface roughness and porosity also limit the use.	Work has been done for sintered P/M parts. Not suited for green P/M parts, too much penetration.
Resonant Frequency Testing	Vibration of an exciter plate adjacent to a part causes a frequency with an increased amplitude through the part, the difference is measured.	Easy set up and fast inspection; reliable repeatability.	Can acknowledge a defect but does not locate it; can not be used in low density materials.	Works well on some sintered parts. Not applicable to green parts.

Table 1-1: Application of NDE in powder metallurgy [5].

revealed that few NDE techniques are currently employed within the industry. Those which are in use are highly specific to the part being inspected [4] and no commercially available solution exists for the problem at hand.

The preliminary technique for green sheet inspection was an off-line x-ray transmission. This involved interrupting the fabrication process and taking a sample to an on-site test laboratory. It took about 15 minutes to generate results and modify the settings on the roller feeder equipment. The method was labor intensive, had questionable capability, and a poor spatial resolution ( $> 30 \text{ mm}^2$ ). That the method is capable of detecting variation underscored the need for an improved inspection method. The near term solution was to upgrade the x-ray unit with an automated source and detector pair which would scan the material. This instrument samples the attenuation of the material at some predetermined number of areas. The aperture is an oval geometry approximately 1" x 1/4" resulting in a sampling area size of about 160 mm<sup>2</sup>, over which a particular reading is averaged. Due to the low x-ray attenuation by the green sheet the inspection rate is limited by the integration time. The maximum on-line sampling rate was approximately 50% of the manufactured material.

The physical characteristics of the green sheet require special consideration in developing an appropriate NDE technique. A non-contact technique is necessary since the material has minimal mechanical integrity. Conventional electromagnetic techniques (eddy current, magnetic flux leakage, etc.) have been used for green parts which have densities significantly higher than the iron aluminide green sheet. The green sheet has a very high impedance and is non-magnetic, these techniques are not suitable. While

optical/visual inspection techniques may prove useful, they cannot provide the through-thickness information desired. Also, modern on-line x-ray systems require special shielding, do not provide the required high speed three dimensional specimen information and come with some regulatory constraints.

With the development of high speed focal plane array infrared detectors and increased computing power, inspection using time resolved infrared thermography now has the potential to inspect large volumes quickly and with high spatial resolution. In addition, this approach provides for on-line inspection and the implementation of an SPC program.

In the proposed inspection technique, the time-radiance history for all points on the surface of the specimen is obtained. The time dimension carries information about the nature of the material beneath the surface (i.e. it provides three-dimensional data). In contrast, x-ray transmission yields a signal proportional to the integral of the absorption through the line of flight<sup>1</sup>. With transient thermography, material properties related to the rate of temperature change, i.e. thermal diffusivity, are significant rather than the absolute temperature. Thus, the impact of factors such as emissivity and array detector sensitivity variation, which introduce error in absolute temperature determinations, are reduced.

Several challenges were presented by this work. Thermal techniques have traditionally been used for material thickness several times greater than those of interest here. The composite material had not been characterized in terms of particle/binder distributions and constituent thermal properties. At the small thicknesses and fast thermal transient times through the thickness of the sheet, high speed detectors and data acquisition systems are

---

<sup>1</sup>While there are techniques/instrumentation for x-ray tomography and laminography, these are currently expensive and time consuming.

necessary. Recent developments in detector technology and high speed computers have resulted in instrumentation which provides the required speed. A major aim of the work has been to develop the appropriate spatial and temporal excitation protocol and data analysis techniques. This involves identifying key green sheet morphological features which result in final product defects and the development of a theoretical model to describe heat transfer in the green sheet.

At the start of this work, very little information was available on the thermal properties, defects properties, or defect geometries associated with the composite. In many cases the green sheet material that had undergone visual inspection with no noticeable defects would fail during processing. Thus the research strategy was to divide the effort into two phases. The first phase consisted of an exploratory effort to gain an understanding of the range of thermal properties and defects exhibited by commercially produced green sheet. Artificial defects and part geometries were used to explore the sensitivity of several techniques. These initial results were used to narrow the focus for the second phase. In this phase a prototype inspection system was assembled to accommodate the required rate of inspection and the geometry of the part presentation in the manufacturing environment. Reference composites were fabricated by controlling the compact composition and fabrication pressure. Data from these samples provided a fundamental understanding of the dependence of composite thermal properties on key process variables and allowed for model calibration. The normal range of green sheet process variations and flaw morphologies were investigated by conducting a process study in which a large volume of material from a production run was characterized. This data was then used to develop an inspection protocol



which provides for the prediction of defect occurrence in densified FeAl sheet, based on flaw precursors in the green sheet.

## Chapter 2

# Thermography

### 2.1 Background

The primary advantages of thermography are that it does not require direct contact with the object of interest and provides full field information. Thermographic techniques are typically divided into two categories: passive and active. Passive thermography is more qualitative while active thermography is more quantitative and can be tailored to optimize the inspection. Passive techniques rely on the detection of thermal gradients from surfaces in their normal operating state. Examples are heat leakage from buildings, heat generated from friction or other mechanical processes, reaction processes, and ohmic heating. In contrast, active thermography is based on the generation and monitoring of thermal gradients in structures by inducing heating and/or cooling. This approach produces larger gradients and better differentiation of flaws than is typically possible using passive techniques. Common heat sources are heating lamps, lasers, microwaves, and electromagnetic induction. Examples of techniques to induce gradients in an already heated object are convective air

cooling, quenching with liquid nitrogen, and parasitic conduction. Excitation may be temporally and/or spatially modulated and is driven by the flaw morphology and excitation mechanism. For example microwaves can be used to heat water trapped inside an electrical insulating material. Care must be taken not to exceed stresses and/or temperature thresholds which may damage the material.

Modern thermography has its roots in the early work of William Herschel [7]. His 1800 observation that "light rays" outside of the visible spectrum could transfer energy to glass thermometers revealed the infrared region of the electromagnetic spectrum. It was not until much later that the theoretical work of James Maxwell and Max Planck provided the theoretical basis for interpreting the relationship between emitted energy and the electromagnetic spectrum. The availability of modern infrared detector systems has, of course, been key in allowing for the development of effective thermal inspection techniques. Two factors have impeded the development of useful detectors. The first is the lack of photons emitted by bodies near room temperature. The second is atmospheric scattering. Thus most sensors have been designed to operate in the 2-5  $\mu\text{m}$  and the 8-12  $\mu\text{m}$  transmission bands. Infrared detectors can be divided into two broad categories. The first is a thermal detector. Thermal detectors operate on the basis that the material properties of the sensor vary with temperature. For a given detector system (i.e. known optics, sensor absorption characteristics, and thermal time constant) the monitored changes in material properties can be used to infer the temperature of the source. Development efforts associated with these devices dominated the first century after Herschel's discovery. Seebeck's discovery of the thermoelectric effect gave rise to the thermopile and Langley [8] invented the bolometer

which relies on knowing the variation of resistivity with temperature. Both of these devices are broad band infrared detectors. The inherent lag in thermal response and the minute changes in electrical signals provide for rather slow and noisy devices. Even at this early stage of development Langley was able to detect a cow at a distance of 1/4 mile in 1901.

The second type of detector, photon or quantum detectors, relies on the interaction of the electromagnetic radiation with the electronic band structure of the material. By 1917 Theodore Case[8] had developed the thallos sulfide detector. This material had a much faster response time than earlier bolometers. By WWII lead sulfide had been developed and was the detector of choice for military surveillance applications. The post war era saw commercial applications and by the 60's and 70's commercial cameras became available. InSb and HgCdTe were popular due to their high conversion efficiencies (device quantum efficiency) from photon energy to detector output current. These detectors require cryogenic cooling to reduce background signals associated with system packaging.

There are two equally important issues which must be addressed to develop a thermal inspection technique. First, can one access and monitor thermal information of the structure of interest? Secondly, can relevant details of flaw morphology and formation mechanisms be inferred from this information? Over the last 20 years the development of focal plane array detectors and read-out architecture has increased infrared imaging speeds. Many of these technological advances have been driven by the defense industry. In addition, the advances in computing speed and reduced circuit size have combined to provide the power necessary to perform the near real time data processing necessary for quantitative materials/structures evaluation. The second question leads us to a discussion

of the heat transfer within solids which is the topic of the next section. This is followed by a review of the literature describing applications of thermal NDE.

## 2.2 Heat conduction in solids

The essence of quantitative thermography is to understand the interaction between temperature fields and discontinuities within the structure of interest. The mathematical formalism for heat conduction provides the theoretical basis for understanding these interactions. Carslaw and Jaeger [9] extended the work of earlier mathematicians and scientists to provide a practical theory of the conduction of heat in solids [10] [11] [12]. Equation 2.1 is the equation of continuity for heat conduction in a stationary solid.

$$\rho(\mathbf{r})C_p(\mathbf{r})\frac{\partial T(\mathbf{r}, t)}{\partial t} = \{\nabla \cdot [\boldsymbol{\kappa}(\mathbf{r}, T) \cdot \nabla T(\mathbf{r}, t)]\} + g(\mathbf{r}, t) \quad (2.1)$$

$T(\mathbf{r}, t)$  is the time dependent temperature field and  $\boldsymbol{\kappa}(\mathbf{r}, T)$  is the second rank thermal conductivity tensor. The terms  $\kappa_{ij}$  (with  $i$  and  $j = 1, 2, 3$ ) describe the anisotropy of the conductivity. The rate of heat generation per unit volume is represented by  $g(\mathbf{r}, t)$ . Most active thermography applications involve temperature excursions which are typically less than 200 °C. Under these conditions bulk material properties (density,  $\rho(\mathbf{r})$ , and specific heat,  $C_p(\mathbf{r})$  and  $\boldsymbol{\kappa}(\mathbf{r}, T)$ ) are approximately independent of temperature. Equation 2.1 is a manifestation of the conservation of energy. Consider an arbitrary volume  $V$ . The right hand term in curly brackets represents the heat flow across the boundary,  $S$ , surrounding  $V$ . The term  $g(\mathbf{r}, t)$  represents sources of internal heat generation (e.g. chemical exothermic reactions). The term on the left hand side represents the rate of energy storage per unit volume of the material occupying  $V$ .

The Fourier or diffusion equation 2.2 is obtained under the conditions for an isotropic homogeneous solid with no heat generation and small temperature excursions.

$$\frac{\partial T(\mathbf{r}, t)}{\partial t} = \alpha \nabla^2 T(\mathbf{r}, t) \quad (2.2)$$

With the thermal diffusivity,  $\alpha$ , defined as

$$\alpha = \frac{\kappa}{\rho C_v} \quad (2.3)$$

In the steady state case 2.4 reduces to Laplace's equation.

$$\nabla^2 T(\mathbf{r}) = 0 \quad (2.4)$$

The analytical solution to the boundary-value problem, presented by equation 2.1, is obtained from the general solution in combination with the initial field values and the boundary conditions. The form of the general solution depends on the coordinate system which is generally chosen to suite the symmetry of the problem. The associated constants are evaluated using the initial field  $T_0(\mathbf{r}, t)$  and the boundary conditions. We require the solution to approach  $T_0(\mathbf{r}, t)$  in the limit of  $t = 0$ . Thermal boundary conditions consist of three categories. A prescribed surface temperature  $T(\mathbf{r}, t)$  is the simplest case. Another condition is to have the heat flux components,  $F_i$ , defined across a prescribed surface where  $\eta$  the outward surface normal. Equation 2.5 illustrates this condition in differential form. When  $F_i = 0$  we have the special case of an insulated boundary with no heat flow.

$$\kappa_i \frac{\partial T(\mathbf{r}, t)}{\partial \eta} = F_i(\mathbf{r}, t) \quad (2.5)$$

The third situation provides for linear heat transfer at the surface. This is sometimes referred to as the radiation boundary condition. For small temperature differences between a

surface and its surroundings a linear approximation of the  $T(\mathbf{r}, t)$ <sup>4</sup> Stefan-Boltzman radiative heat transfer is often used. The linear heat transfer associated with convective losses is more commonly employed in NDE applications. For either mechanism the flux across the surface can be approximated as linear with a proportionality constant  $H$ . This relationship is shown in equations 2.6

$$\kappa \frac{\partial T(\mathbf{r}, t)}{\partial \eta} + H \cdot [T(\mathbf{r}, t) - T_m(\mathbf{r}, t)] = 0 \quad (2.6)$$

Where  $T_m(\mathbf{r}, t)$  is the temperature of the surrounding medium. An alternative form is to define a thermal resistance as  $R = \frac{1}{H}$ . Equation 2.6 can then be cast into a form (equation 2.7) analogous to Ohm's law in which the product of the current density and average electrical resistivity between two points is equal to the associated voltage difference. The alternative form of Equation 2.6 is

$$-\kappa \frac{\partial T(\mathbf{r}, t)}{\partial \eta} \cdot R = T(\mathbf{r}, t) - T_m(\mathbf{r}, t) \quad (2.7)$$

The process of inspecting via active thermography involves imposing certain initial and boundary conditions on the part to be characterized. The resulting time dependent thermal field reflects the relevant flaw information. The easiest conditions to generate experimentally and treat analytically are pulsed, step, and periodic surface heating. A few general comments are in order before discussing these techniques in detail. The choice of excitation mode requires a balance of several factors. For on-line inspection the primary constraint is the time available for inspection. In the laboratory the time available for the inspection may be arbitrarily long. However, in a production environment the inspection time will be limited by product flow rates. Pulsed heating minimizes the excitation time.

Signal to noise level is also important. A periodic excitation allows for background noise to be significantly reduced by using lock-in signal processing. In this approach the thermal signal is sampled so that only the forced time varying thermal response is measured. The DC background is eliminated. As will be shown, the frequency of the excitation can be chosen to emphasize various depths in the structure of interest. Step function excitation is typically used to induce large surface signals which induce significant heating into the volume of the sample. This may be required when the features of interest are deep in the sample or the material is particularly slow. Both periodic and step function heating typically require inspection times of several seconds to several minutes. Inspection of large structures, such as buildings and bridges take advantage of solar cycles. In these cases the time between sampling observations can be many hours.

The analysis of thermal excitation modes fall into two categories. Both the pulse and step excitation involve a time domain signal analysis of the heating and/or cooling curve. For periodic excitation a frequency domain treatment of the heat equation reveals the wave nature of the conduction. The latter is often associated with the concept of "thermal waves". A direct result of the Fourier transform theorem is that both the time domain and frequency domain treatments of the heat conduction problem equation are mathematically valid. Thus with the appropriate assignment of physical entities the heat diffusion process can be described as critically damped dispersive thermal waves. Both of these constructs are equally valid.

Consider one dimensional heat conduction, in an isotropic, homogeneous material half-space with properties  $\rho$ ,  $C_p$ , and  $\kappa$ . For convenience the convention will be a rectangular



coordinate system with heat flow in the  $x$  direction. Any surface excitation at  $x = 0$  can be described as a linear combination of harmonic functions of the form

$$T(0, t) = T_0 \cos \omega t = T_0 \operatorname{Re} e^{i\omega t} \quad (2.8)$$

Recalling Fourier's equation

$$\frac{\partial T(x, t)}{\partial t} = \alpha \nabla^2 T(x, t) \quad (2.9)$$

With the thermal diffusivity,  $\alpha = \frac{k}{\rho c_p}$ . We assume a general solution of the form  $T(x, t) = T(x) e^{i\omega t}$  and upon the application of equation 2.9 the Helmholtz wave equation is obtained.

$$\left[ \nabla^2 - \frac{i\omega}{\alpha} \right] \cdot T(x) = 0 \quad (2.10)$$

The general solution is

$$T(x) = A \cdot \exp\left[-\sqrt{\frac{\omega}{2\alpha}}(1+i)x\right] + B \cdot \exp\left[\sqrt{\frac{\omega}{2\alpha}}(1+i)x\right] \quad (2.11)$$

The requirement that the field be finite far from the excitation surface requires that  $B = 0$ .

After rearrangement the field solution can be written down as

$$T(x, t) = T_0 e^{-x\sqrt{\frac{\omega}{2\alpha}}} \cdot \cos\left(\omega t - x\sqrt{\frac{\omega}{2\alpha}}\right) \quad (2.12)$$

This represents a thermal wave with wavenumber  $k = \sqrt{\frac{\omega}{2\alpha}}$ , frequency  $f = \frac{\omega}{2\pi}$ , and wavelength  $\lambda = \sqrt{\frac{4\pi\alpha}{f}}$ . Several features of equation 2.12 provide insight into the thermal behavior of an arbitrary excitation waveform with various frequency components. First, the spatial decay depends strongly on the ratio of the excitation frequency to the thermal diffusivity. The penetration depth,  $d = \sqrt{\frac{2\alpha}{\omega}}$ , is the distance at which the field has fallen to  $e^{-1}$  of its peak value. This is often referred to as the thermal diffusion length. As examples, the

penetration depth for aluminum ( $\alpha \approx 0.5 \frac{\text{cm}^2}{\text{sec}}$ ) when  $\omega = 1$  Hz. is about 1 cm. For brick,  $\alpha \approx 0.004 \frac{\text{cm}^2}{\text{sec}}$ , the penetration depth is only 0.1 cm. In order to achieve the same penetration depth in brick the frequency would have to be decreased by a factor of a hundred. We can re-write the time dependant term of equation 2.12 as

$$\cos \omega(t - \frac{x}{\sqrt{2\alpha\omega}}) \quad (2.13)$$

The term  $\sqrt{2\alpha\omega}$  is clearly a frequency dependent (i.e. dispersive) propagation velocity. High frequencies propagate faster and are more attenuated than low frequencies. As the frequency approach infinity so does its speed of propagation. The mathematical treatment of the diffusion equation by transforming the problem into the frequency domain shows that the dual distortion (dispersion and attenuation) of an arbitrary thermal wave is physically equivalent to diffusion.

It is important to take the above results into account when developing an on-line inspection method. Consider a same side excitation thermal imaging arrangement. The observed field perturbation (at the  $x = 0$  surface) result from the propagation and scattering of the thermal waves from the internal discontinuities of the flaw boundaries. The dominant excitation frequency modes should be low enough to penetrate and return from the flaw boundary. However, the frequencies need to be high enough to propagate during the allotted inspection time. Another important consideration, not explicitly addressed by the one dimensional treatment, is that three dimensional diffusion distorts the flaw signal. Approaches to handling this issue will be discussed in the following section.

## 2.3 Review of thermal nondestructive evaluation

This section reviews the techniques and applications of thermal NDE. There are many terms that have been coined in reference to active thermal nondestructive evaluation techniques. Examples are active thermography, transient thermography, time-resolved infrared thermography, thermal wave imaging, pulsed photothermal inspection, thermal NDT or TNDT, lock-in thermography, pulsed-echo thermal wave imaging, thermal inertia imaging, and others. The recent proliferation of descriptive labels is indicative of the growth and activity in this field [13]. While there are variations in excitation, data acquisition, and filtering among the various methods, the underlying mechanism is heat transfer within structures. The first part of this section describes the analytical solutions relevant to the current application. The second part provides an overview of the pertinent literature.

One of the earliest and most cited applications of heat transfer theory to thermal NDE is the work of Parker [14]. This technique involves the application of a pulsed heat flux uniformly incident upon one side of a slab while the temperature rise of the opposite side is monitored (see figure 2-1). Parker used this approach to determine the one-dimensional thermal diffusivity,  $\alpha$ , via thermocouple measurements. It is assumed that the pulse heating (at  $x = 0$ ) of a material slab ( $\rho, \kappa, C_p$ ) of thickness  $L$  is adiabatic.  $F$  is the radiant energy per unit area,  $\varepsilon$  is the emissivity. Thus the total heat input per unit area is  $F\varepsilon$  and the pulse time is small compared to the times of interest. For times much greater than the duration of the pulse the temperature of the back side of the slab,  $T(L, t)$ , is asymptotic to a peak

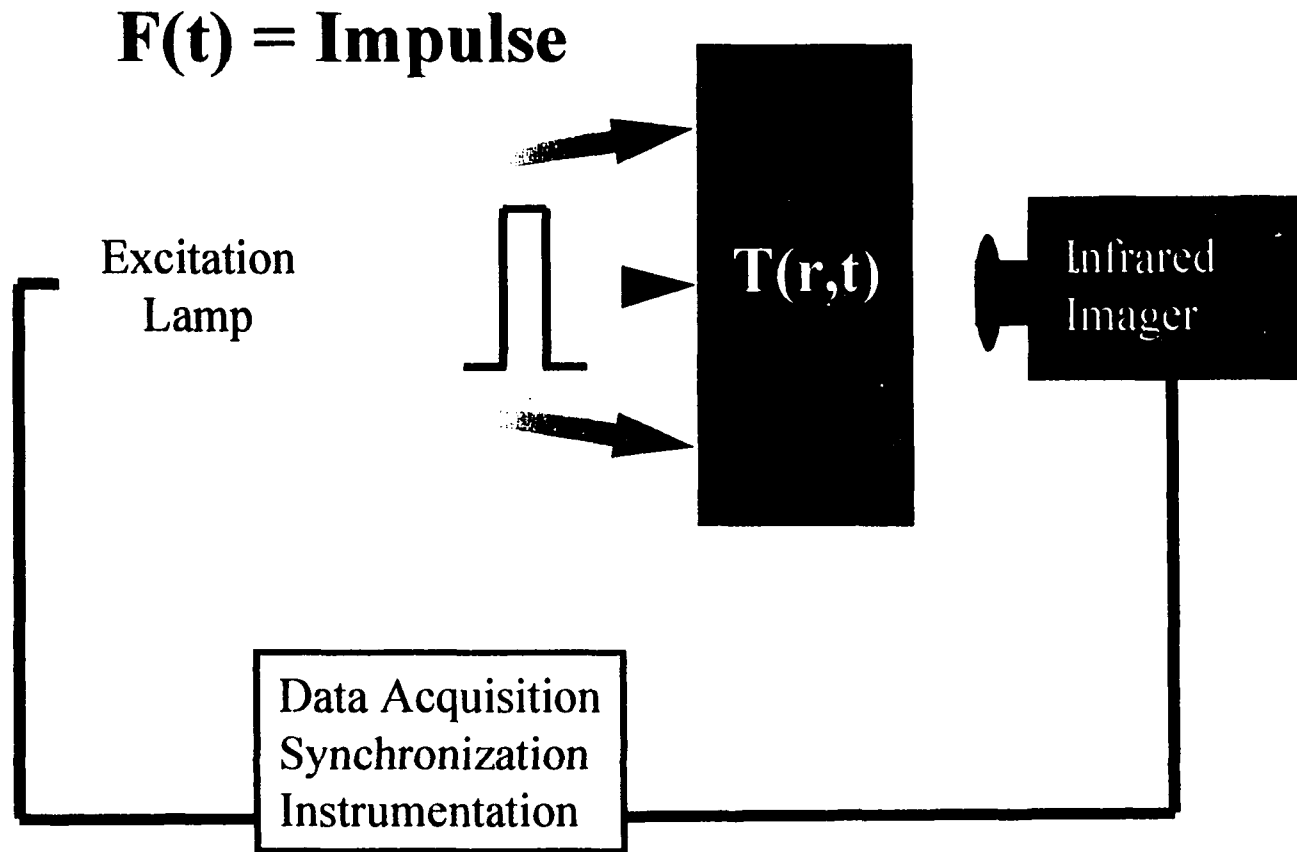


Figure 2-1: Geometry for through-heating.

value given by equation 2.14

$$T(L, t) = \frac{F\epsilon}{\rho C_v L} \left[ 1 + \sum_{n=1}^{\infty} (-1)^n \exp\left(\frac{-n\pi^2}{L^2} \alpha t\right) \right] \quad (2.14)$$

The maximum temperature slope is reached at  $T(L, t) \approx 0.6$  and  $t \equiv t_{1,2}$ . This yields the following relationship for the diffusivity.

$$\alpha = 1.38 \cdot \frac{L^2}{\pi^2 t_{1,2}} \quad (2.15)$$

Note that the determination of diffusivity depends only on having knowledge of the temperature history. Thus all that is required is that  $F$  is large enough to provide a significant temperature increase on the back surface of the sample. This treatment assumes no change in material properties over the induced temperature excursion. For a given value of  $t_{1,2}$ , the calculated value of  $\alpha$  varies as the square of the slab thickness. This dependence is expected considering the change in diffusion length with  $\alpha$ . Off-the-shelf analytical instruments, based on this technique, are available. They typically incorporate laser excitation sources. These methods are invasive since they impose restrictions on specimen geometry. Samples are typically prepared as a small, 1 to 2 cm<sup>3</sup>, cylinders. Figure 2-2 illustrates the dependence of the back side thermal response of a homogeneous slab for three different combinations of  $\frac{L^2}{\alpha}$ . Using the value of  $t_{1,2}$  from the plot, the ratio of  $\frac{L^2}{\alpha}$  can be determined. Knowing either  $\alpha$  or  $L$  allows for the determination of the remaining unknown. As indicated in figure 2-2, **A** has the smallest value of  $\frac{L^2}{\alpha}$  and **C** has the largest.

Of particular interest in the present work is the situation in which only one side of a planar specimen is accessible. During production iron aluminide green sheet is supported by a conveyor belt. For convenience we will replace  $T(0, t)$  with  $T(t)$  where it is under

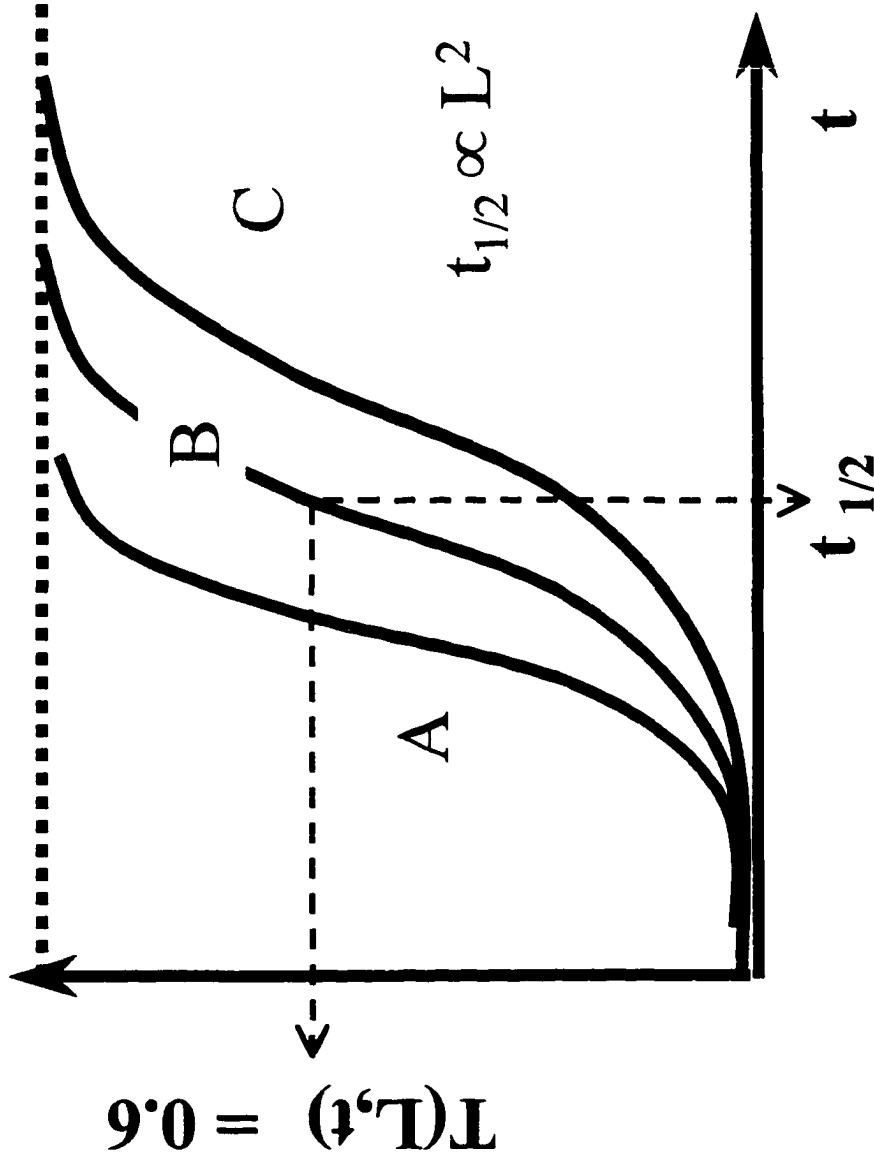


Figure 2-2: Heating curves for through-heating with pulsed excitation.

stood that the front surface is  $x = 0$ . The analytical solution for periodic front surface heating has been described. Two other cases, single pulse and step function heating, will now be considered.

The solution for the cooling curve resulting from the uniform square pulsed excitation of a slab of thickness  $L$ , with insulated boundary conditions on the side opposite the excitation, is given by equation 2.16 [15]. Figure 2-3 illustrates the excitation geometry.

$$T(t) = \frac{2F\epsilon}{(\sqrt{\rho\kappa C_p}\sqrt{\pi})} \left\{ (\sqrt{t} - \sqrt{t-\tau}) - 2\sqrt{t} \sum_{n=1}^{\infty} (1)^n F(t) - 2\sqrt{t-\tau} \sum_{n=1}^{\infty} (1)^n F(t-\tau) \right\} \quad (2.16)$$

Where  $F(t)$  is defined by:

$$F(t) = \exp\left(\frac{-n^2 L^2}{\alpha t}\right) - \sqrt{\frac{n^2 L^2}{\pi \alpha t}} \operatorname{Erfc}\left(\frac{n^2 L^2}{\alpha t}\right) \quad (2.17)$$

Where  $F\epsilon = Q$  is the radiant energy per unit area absorbed by the surface and  $\tau$  is the pulse duration. For  $t \gg \tau$  a square pulse can be approximated as an instantaneous pulse in which the total energy is deposited in the outer most region of the slab. In this case the cooling curve is governed by equation 2.18 [15].

$$T(t) = \frac{F\epsilon\tau}{(\sqrt{\rho\kappa C_p}\sqrt{\pi t})} \left[ 1 + 2 \sum_{n=1}^{\infty} (1)^n \exp\left(\frac{-n^2 L^2}{\alpha t}\right) \right] \quad (2.18)$$

For the case in which  $\frac{L^2}{\alpha t} \gg 1$  the temperature response of the specimen approximates the response of a half-space with the same material properties and is described by

$$T(t) = \frac{F\epsilon\tau}{(\sqrt{\rho\kappa C_p}\sqrt{\pi t})} \quad (2.19)$$

Thus during this period the temperature of the specimen decreases with the inverse of the square root of time. With a slope indicative of the bulk material parameter

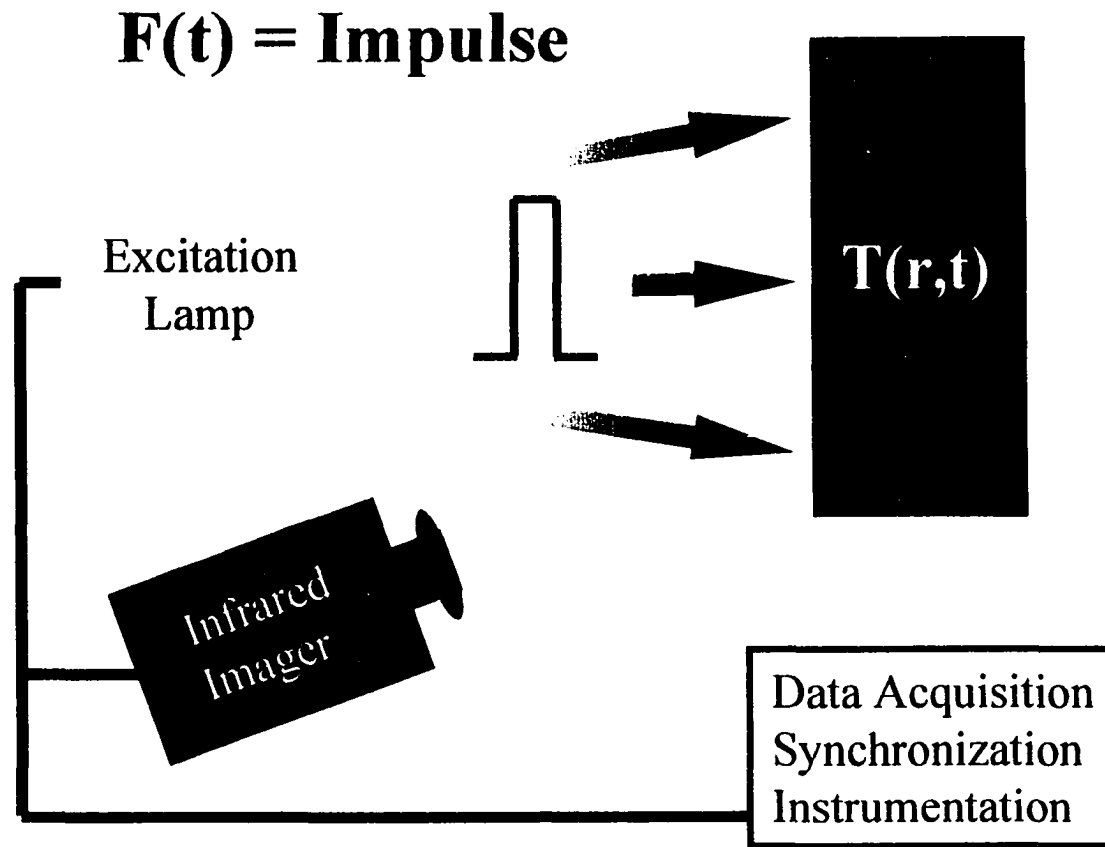


Figure 2-3: Geometry for front-side heating.



defined as the thermal effusivity,  $e = \sqrt{\rho\kappa C_p}$ . Thermal effusivity corresponds to the ratio  $\frac{\text{Flux}}{\text{Temperature}}$  which is the inverse of the thermal impedance. Thus for a large effusivity the thermal impedance is low and the temperature rapidly decays with time. Alternatively a material with a small effusivity cools much slower. The deviation of a cooling curve from the thermally thick response (i.e. the point at which the series term becomes significant) is indicative of a discontinuity in the material. Figure 2-4 provides a qualitative comparison of three cases. For one dimensional heat flow in an isotropic homogeneous slab line, **A** represents the decay curve of the reference half space. Line **B** shows the upward deflection associated with a discontinuity of lower effusivity (e.g. heterogeneity or air interface). Line **C** shows the downward deflection associated with the discontinuity from a lower effusivity to a higher effusivity (e.g. heterogeneity).

In the limit that  $t \ll \tau$  the excitation approaches a step function. The thermally thick response is described by

$$T(t) = \frac{2F_0\sqrt{t}}{(\sqrt{\rho\kappa C_p}\sqrt{\pi})} \quad (2.20)$$

Thus during this time interval the surface of the sample heats proportional to the square root of time. Again the slope is indicative of the effusivity. Figure 2-5 provides a qualitative comparison of three cases for one dimensional heat flow in an isotropic homogeneous slab. Line **A** represents the heating curve of the reference half space. Line **B** shows the upward deflection associated with a discontinuity of lower effusivity (e.g. heterogeneity or air interface). Line **C** shows the downward deflection associated with a discontinuity of higher effusivity (e.g. heterogeneity).

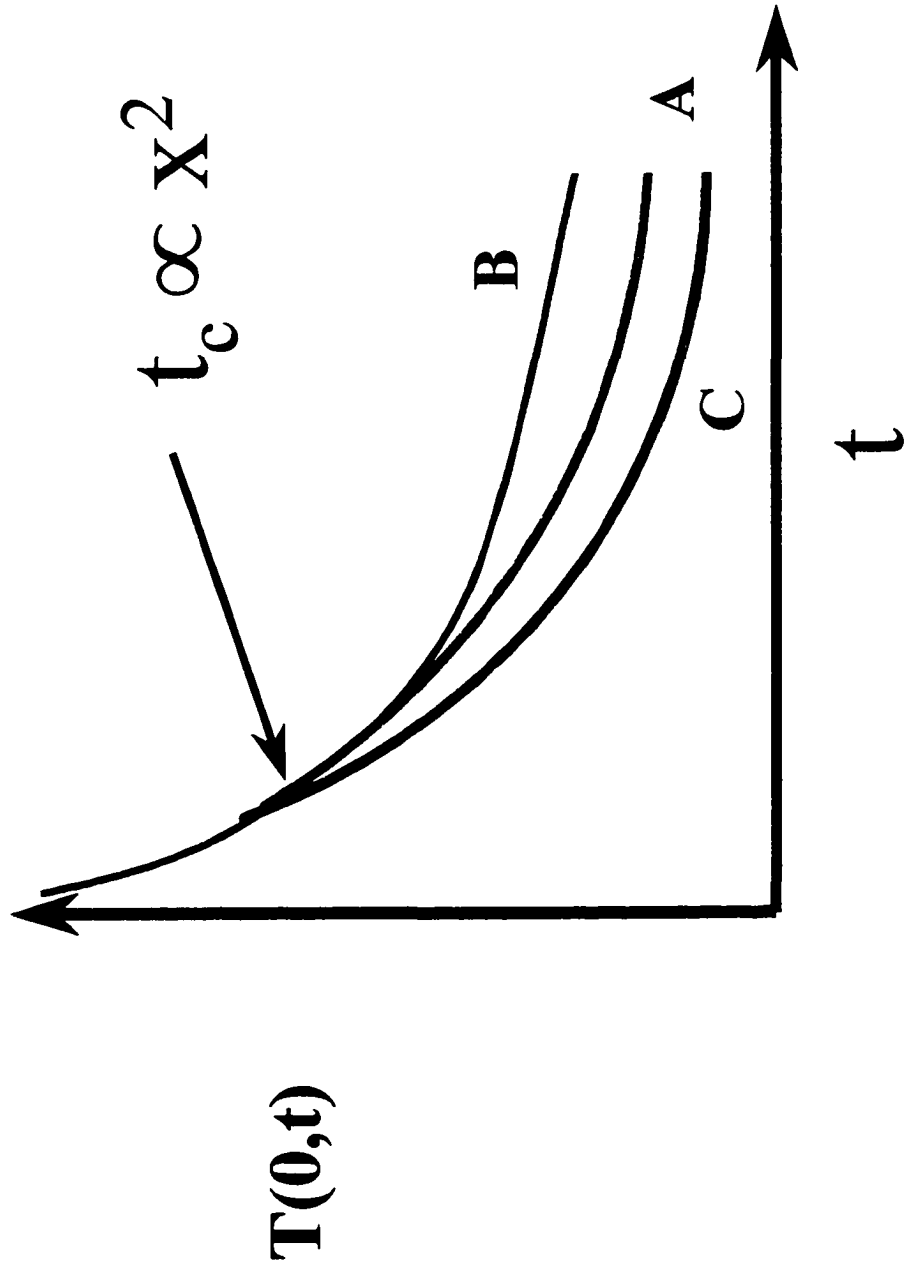


Figure 2-4: Cooling curves for front-side impulse excitation.

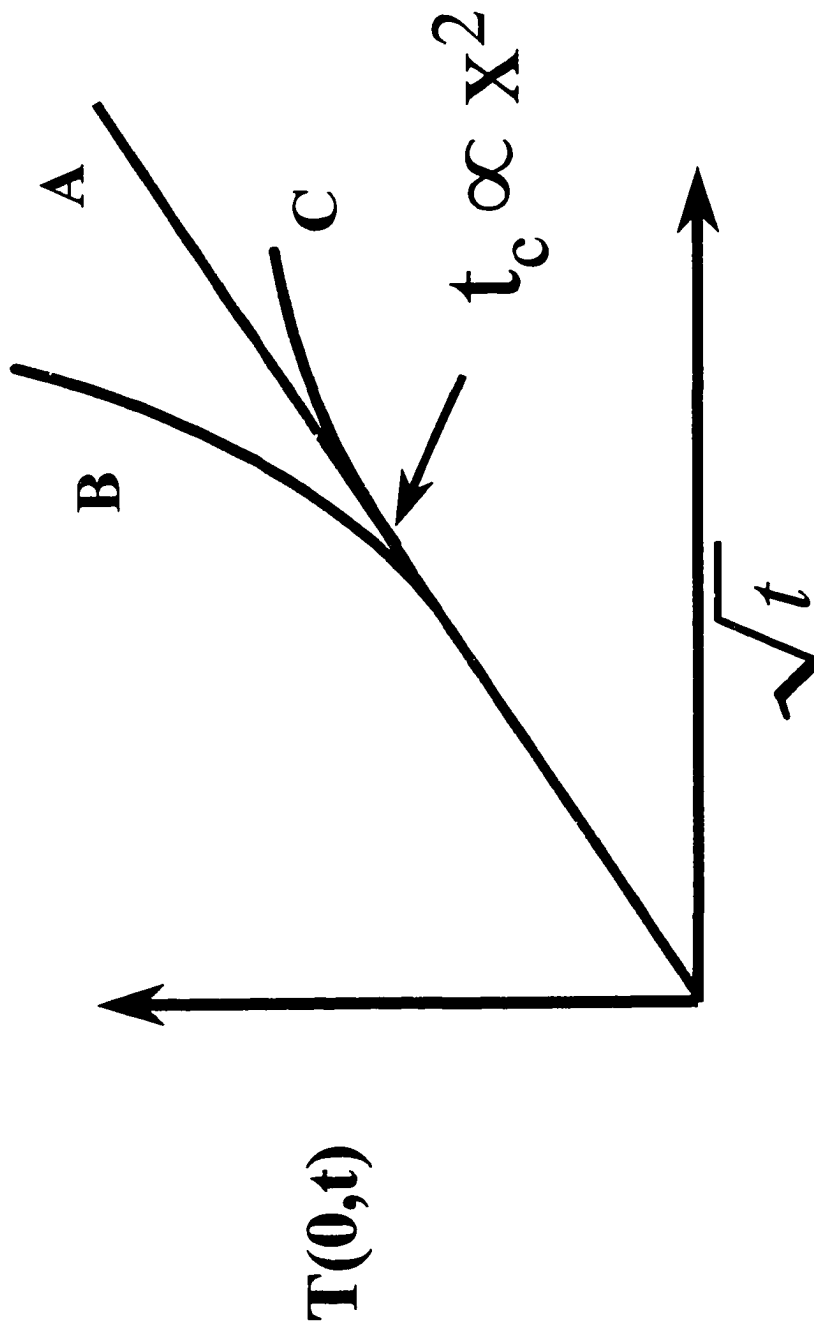


Figure 2-5: Heating curves for front-side step heating.

Recent research efforts have focused on the application of front or same sided heating techniques. The primary reason for this focus has been the demand for field deployment of thermal NDE systems. Many applications, such as the present inspection problem, must be achieved in an environment where access to the material/structure is limited. Another driving factor for the modality of deployment is the volume of the material to be inspected. The development of high speed high volume inspection capabilities was mandated by the Aviation Safety Research Act of 1988 (Public Law 100-591). This law charges the Federal Aviation Administration to research and develop methods for improving aircraft reliability. A major component of this effort is to enhance the ability to detect the onset of cracking delamination, and corrosion of aircraft structures. These activities are particularly relevant for the aging commercial and military aircraft fleet. Another motivation is the application of new composite materials for high speed and stealth aircraft. These materials are typically formed from complex processes and result in composites with unique physical properties and failure modes. The associated inspection challenges are not easily addressed by the standard testing methods. Hobbs [16] provides a thorough review of the advantages of thermographic inspection techniques for aerospace materials. These interests, in conjunction with the federal government's efforts to transfer developing technologies into the private sector, have resulted in more recent applications within industrial processes. While the materials of interest vary widely, applications typically involve at least one of the following flaw types: corrosion, cracking, porosity, thickness of monolithic or coated structures, composite anisotropy and disbonding/delamination, and fundamental measurements. The following provides a review of the work in these areas.

Connolly [17] used a through-thickness laser heating method to assess the porosity within fiber-reinforced polymeric matrix composites. Porosities were low, in the 0.5 % to 8% range. A linear correlation was found between the thermal technique and the porosity determined using an acid digestion method. Cramer et al.[18] used through flash heating to produce full thermal diffusivity maps for SiC fiber-reinforced silicon nitride ceramic matrix composites. These composites are used in high temperature environments which result in carbon depletion via oxidation. This material loss was correlated to the effective reduction in bulk diffusivity. More recently others [19] have refined this technique in conjunction with a scanning thermal imaging to determine the variation in diffusivity through the volume of planar samples. Nonlinear least square routines were employed to provide thermal diffusivity images for ceramic matrix and delaminated composites. Algorithms were developed to fit the data of each pixel to the analytical solution for the time dependence. Emeric et al. [20] developed a mathematical model based on the scattering of a harmonic time varying thermal excitation from an embedded fiber with different properties from the composite matrix. Favro et al.[21] have measured the principal components of the thermal diffusivity of unidirectional fiber reinforced polymer composites using through heating with a circular source.

Several workers have investigated both metallic and composite structures using thin-plate approximations. In this approach the heating and data acquisition regimes are chosen so that the through thickness thermal gradients are small and the heat flow is predominantly in the plane. There are several advantages of this technique. The time scale of thermal diffusion events, in the plane (the larger dimension), are longer than those

through the thin regions of the material. This means that, for isotropic materials, the bulk diffusivity can be measured using relatively slow data acquisition rates. In the case of anisotropic materials, the in-plane components of the diffusivity tensor can be measured and related to the principal components. Welch et al. [22] [23] [24] [25] [26] achieved this for several metals and graphite epoxy composites using a laser generated line of heat. Hartikainen et al. [27] used a fast line scanning infrared system to characterize plasma-sprayed coatings. More recently Cramer et al. [28] have developed a scanning system which employs an infrared camera and thermal line source to quantify the thickness of metallic plates. The camera and line source scan the surface at a fixed separation and velocity resulting in a known time delay between the heating and the data acquisition, to assure through thickness thermal saturation. The relative temperature increase is indicative of the local thickness. Data reconstruction provides for an image representing variations in local thickness. This technique has the potential to effectively detect corrosion over large areas of an aircraft fuselage.

Crack detection in structures is of particular importance in the aerospace industry. Upon ascent above about 10,000 ft. most aircraft fuselages are pressurized to about 5 psi. During descent for landing the aircraft is equilibrated to atmosphere. Over many take-off and landing cycles cracking can occur in regions of high stress, such as rivets. At typical commercial fuselage skin consists of about 0.040" Al. Cramer et al. [29] [30] developed a technique to detect the presence of cracks in thin Al plates using planar heat flow. In this application a line source is oriented parallel to the simulated (EDM) crack direction. Cracks were not through the thickness and were detected from the blind side of the panel. After

thermal equilibrium was achieved, through the thickness of the sheet, the heat diffused within the plane. The presence of a crack creates a discontinuity in thermal gradient, which is perpendicular to the common long axis of the line source and crack. It was shown that the raw thermal data could be filtered using a Laplacian operator to detect the location of this discontinuity and thus the distance of the crack from the line source. The peak in this signal was shown to depend on the heating time, the distance from the heating source and the principal components of the thermal diffusivity. Optimization of this detection technique depends on anticipating the crack mode, i.e. typical location and orientation, and the material diffusivity tensor.

Shiratori et al. [31] investigated various excitation schemes to detect cracks in metal sheets. These included laser heating, plastic-induced heating, induction heating, resistive heating, connective heating, and spot cooling with a refrigerant. White et al. [32] [33] developed a thermal microscope capable of detecting crack propagation during thermo-mechanical fatigue cycling. Crack tips were detected by scanning the surface with a small, 50  $\mu\text{m}$  spot, laser excitation. The combination of increased emissivity associated with the crack width and the in-plane thermal impedance across the crack boundary allowed for crack detection. Watkins [34] used an improved version of the infrared thermal microscopy to investigate flaws in thin sheets of iron aluminide. Through cracks with widths as small as 2  $\mu\text{m}$  were easily detectable. In addition, surface flaws from pitting and heterogeneities associated with aluminum oxidation were imaged.

The advantages of rapid, same-sided, full field thermal NDE techniques have been discussed. The theoretical foundations of these techniques can be found in the work of

Fourier, Carslaw, and Jaeger [9]. The roots of the experimental applications are found in the early works of Angstrom and the more recent development of scanning photoacoustic microscopy (SPAM) [35]. Scanning photoacoustic microscopy relies on the detection and analysis of the acoustic signal generated by the thermo-elastic strains induced by heating a specimen with a narrow laser spot, typically on the order of  $50\ \mu\text{m}$  in diameter. The beam is rastered across the surface of the sample. Obviously the thermal wave propagation, described in the section on heat conduction in solids, is a part of the coupled thermo-elastic wave propagation problem associated with the SPAM technique. This approach, often referred to as "lock-in thermography", required the thermal excitation to be synchronized with the acquisition of thermal data. The availability of high speed snapshot focal plane array cameras has had a dramatic impact on the development of photo-thermal inspection techniques. The combination of minimum detectable temperature differences as low as 25 mK, frame rates in around of 6 M pixels/sec, and enhanced computer power has made it feasible to inspect materials by monitoring the thermal field at the front surface. This is typically achieved by using a broad uniform spatial excitation in place of the rastered laser beam. Over the past ten years the application of these techniques for aerospace and nonaerospace materials and structures has grown dramatically.

Watkins et al. [36] have used front flash and step heating to investigate defects and thermal properties in powder metal material. These techniques are capable of detecting thickness variations, heterogeneities, and cracks in iron aluminide green sheet. The thermal diffusivity of the material was measured for both the green state and the fully dense material. The diffusivity increased by an order of magnitude upon densification. Favro et al. [37]



[38] provided an outline of experimental developments in the pulsed thermal inspection of aircraft components. This work was sponsored by the FAA-Center for Aviation Systems Reliability. Disbonds and corroded regions were detected at rivet sites for Al alloy materials. Disbonds of layered structures such as fiberglass skin and foam cores were also shown to be detectable. Impact damage to composite fiber reinforced laminated structures were also identified. Del Grande [39] et al. performed similar tests on Al aircraft skin.

Significant effort has gone into quantifying the sensitivity of front flash techniques using samples with known defects. This is typically achieved by fabricating artificial “defects” of known geometries. Han et al. [40] considered the thermal response of flat bottom holes of various diameters and depths. They found that the depth of the hole could not be uniquely determined from the time of peak contrast in the image. The peak contrast depends on both through-plane and in-plane diffusion. However, the peak rate of contrast was found to be linearly dependent on the depth and independent of diameter. It should be noted that this region of linearity is a function of the geometry and the thermal properties of the material. For longer times the finite diameter of the hole, or edge effects, become important. Daniels [41] used flash thermography to study the layers of Al alloy plates and air gaps to simulate corrosion. He found that the depth of the voids (8 mm in diameter) simulating 30% mass loss could be readily detected and that the depth of the voids could be determined within 10%. Stiglich [42] et al. used a similar technique to inspect the formation of channels in gas turbines. Due to the complex surface of the turbine, this application required the development of a non-planar heat source to achieve uniform heat flux.

The disbonds and voids associated with corrosion are special cases of the more

general situation of a layered specimen [43] [44]. These structures are of particular importance in protecting substrates in harsh environments. Oksanen et al. [45] investigated the sensitivity of flash thermography for  $ZrO_2$  coatings plasma sprayed onto ferritic steel substrates. This ceramic coating provides a protective barrier which inhibits oxidation. While the technique was able to detect the presents of known defects, the thickness could not be quantified due to camera limitations. With diffusivities of  $0.002 \text{ cm}^2/\text{sec}$  and thickness of about 0.2 mm the fastest camera frame rates could not capture the early time data associated with through thickness heating. McKnight et al. [46] used step heating to characterize blister defects in thin (10 - 100  $\mu\text{m}$ ) organic coatings (e.g. polyamide) on steel substrates. The insulating effect of the boundary layer between the substrate and the coating allowed for the location of the blister to be determined.

The current work is aimed at extending the application of active thermography to quantify critical defects in powder metal green sheet. Three full field excitation techniques were explored. These were through heating with a flash lamp as well as same side heating with both step and flash techniques. The thermal parameters, diffusivity and effusivity, were measured at various steps in the processing of the green sheet. Thermal nondestructive techniques have been used in the inspection of monolithic structures for porosity, corrosion, wall thickness, and disbonds. They have also been used to inspect multi-phase composites such as fiber reinforced polymers. In all of these cases the inspection data is used to asses the quality of a finished product or a product in service. Typically the product or part is either in conformance and fit for use or it is not acceptable. The advantage of these inspections is that a defective structure will either be taken out of service or not put into

service in the first place. The application of quantitative thermography to powder green sheet is new [4]. The current investigation takes a broader approach. The objective is not only to detect flaws but to improve the manufacturing process by identifying key flaw precursors and their cause. The impact is two-fold. At the simplest level green sheet can be removed from the product stream prior to adding more value to bad material. A more important aspect of the work is that it contributes to the understanding of the process by identifying the mechanisms responsible for the defects. This allows fundamental and systematic improvement to the process.

## Chapter 3

# Preliminary Investigations

### 3.1 Preliminary characterization of green sheet

An important step in the strategy to develop any characterization technique is to make an initial assessment of the relevant material properties. This provides an indication of the potential for a particular technique to successfully determine quality. In the present case the relevant compact constituents properties are the density, specific heat and thermal conductivity. The relevant thermal conduction parameters are thermal effusivity, for same sided excitation, and the thermal diffusivity, for through heating (see section 2.3). These properties, in combination with the distribution of constituents and voids, gives rise to the effective bulk properties measured during inspection.

The primary constituents of the green sheet are water atomized FeAl powder and Methocel<sup>®</sup>. Methocel<sup>®</sup>, produced by the Dow Chemical Company, is a powder form of the widely used industrial gum methylcellulose. Methylcellulose and its derivatives have a broad range of applications [47], including adhesives, cosmetics, food, paper, and textiles.

The 1993 production levels were more than 168 million pounds. The primary advantages of using Methocel in the production of FeAl green sheet are rheology during compaction, its effectiveness as a binding agent, and the relatively low carbon residue upon decomposition. High carbon levels can have an adverse effect on the strength of grain boundaries. FeAl properties were readily available as part of the manufacturer's product specification. Data for the density of methylcellulose was available, yet the other properties were not. The primary market for Methocel<sup>®</sup> is for use in solution (typically 1 to 10% in water). The properties of such dilute solutions, provided by Dow Chemical are dominated by water and are not particularly useful in the present context. An estimate of the binder's specific heat and thermal conductivity were made from those of other cellulose material. The ratios of thermal effusivity and the thermal diffusivity for the relevant materials were calculated. Table 3.1 illustrates the data. Two results were particularly significant. First, the thermal diffusivity and thermal effusivity are an order of magnitude and two orders of magnitude, respectively, higher for the metal than for the binder powder. Secondly, the binder was anticipated to behave, thermally, like void volume. Thus regions of green sheet with different ratios of binder to alloy would be expected to have significant differences in thermal response. This preliminary assessment provided a quantitative indication that thermographic inspection would be promising as a method to detect the heterogeneity associated with FeAl powder distribution in green sheet.

The detailed conduction of heat through the bulk of the green sheet is a function of both the constituent properties and their spatial distribution. To this point, a brief description of the production process through the de-binding is provided. A process flow

Bulk Property	FeAl	Methocel Powder	Air	Ratio FeAl/Meth	Ratio Meth/Air
Density (g/cc)	6.1000	0.3500	0.001290	17.4	271.3
Specific Heat (J/g-C)	0.6300	0.3000 *	0.240000	2.1	1.3
Thermal Conductivity (W/cm-C)	0.1100	0.0001 *	0.000058	1100.0	1.7
Effusivity (J/(cm <sup>2</sup> -C-sec <sup>1/2</sup> ))	0.6502	0.0032	0.003240	200.6	1.0
Diffusivity (cm <sup>2</sup> /sec)	0.0286	0.0010	0.000952	30.1	1.0
* estimated					

Table 3.1: Material properties of the green sheet components. The relatively large ratio of the thermal properties of the alloy to binder and the alloy are important considerations in the application of thermographic techniques.

diagram is illustrated in figure 1-2. The FeAl powder is produced via a water atomization process in which a liquid phase mixture of primarily Fe (75 % by wt.) and Al (24 % by wt.) is atomized and quenched in a spray to form alloy particles. Figure 3-1 [1] shows a typical industrial water atomization system. The result is a broad distribution of irregularly shaped particles. The small grains, resulting from the high cooling rates, are conserved during processing of the final FeAl sheet and are essential to provide strength for applications at elevated temperatures. The irregular shape of the particles is believed to enhance the strength of the green sheet by increasing the inter-particle friction. The powder size distribution is selected by sieving to a mean particle diameter of approximately 60  $\mu\text{m}$ . Figure 3-2 illustrates the irregular shape of the particles. The specified ratio of binder and FeAl powder is blended and placed in the feed hopper for green compaction (see figure 1-1). The compacted sheet is heated to decompose the organic binder and subsequently densified and annealed to form the finished iron aluminide sheet.

Although the fully dense FeAl product had been well characterized during process development, little effort had been made to characterize the microstructure of the green compact. The first indication of the green sheet's morphology came from its bulk density, determined to be 3.6  $\text{g}/\text{cm}^3$ . Considering the relatively low density and loading of the binder (1.1  $\text{g}/\text{cm}^3$  at about 2.8 % wt.) and a bulk alloy density of 6.1  $\text{g}/\text{cm}^3$ , the green sheet was estimated to have a total void volume of about 40 %. Polarized light microscopy, figure 3-3, of the green sheet surface provided the first insight into the binder distribution. The agglomerates of binder are distinguished as light regions in the micrograph. Figure 3-4 illustrates two SEM images of a broken cross section of green sheet. The secondary emission

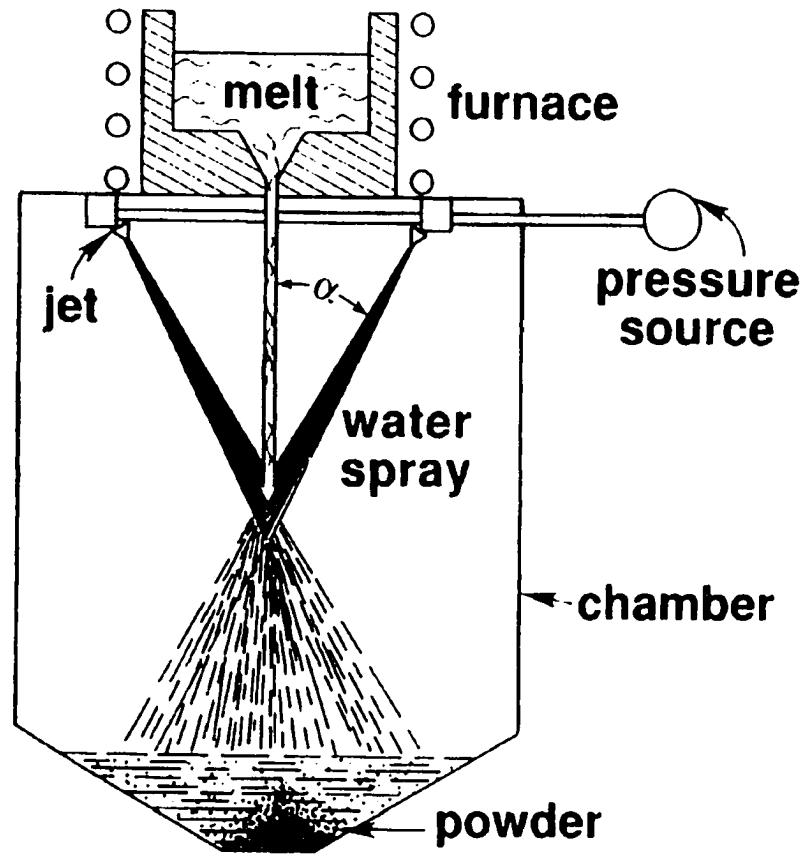


Figure 3-1: Typical water atomization process for the production of alloyed powder [1].





— 200  $\mu\text{m}$

Figure 3-2: Optical micrograph depicting the irregular shape of FeAl particles.

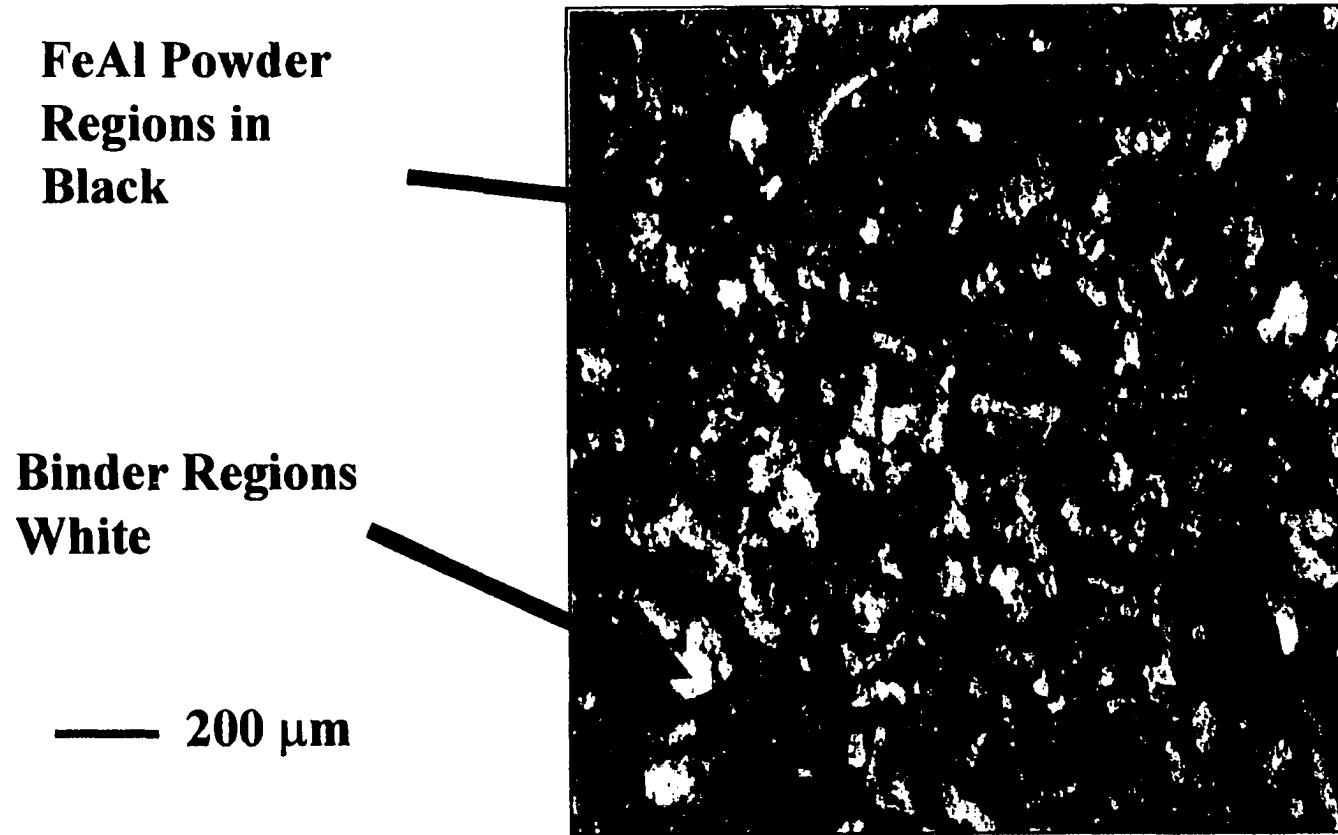


Figure 3-3: Polarized light micrograph showing the distribution of binder on the surface of green sheet.

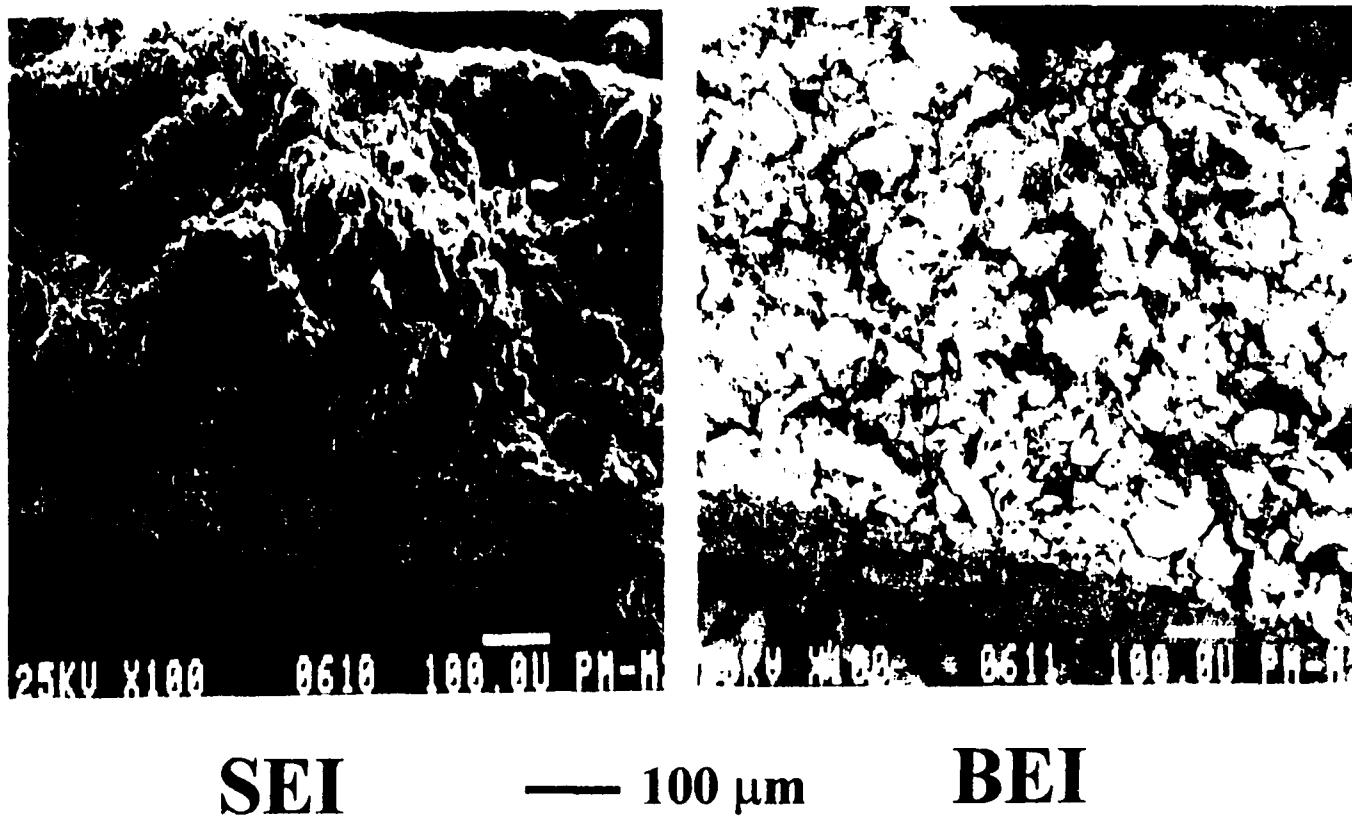


Figure 3-4: Secondary (SEI) and backscatter (BEI) SEM images showing alloy powder distribution. Light regions in the BEI image indicate alloy while dark regions indicate binder and/or voids.

(SEI) image, on the left, provides a large dynamic range to illustrate the morphology of the break. FeAl particles which are pulled out of one surface of the break leave recesses in the mating surface. The backscatter (BEI) image provides a high contrast which distinguishes alloy surfaces from binder and void surfaces. Regions of alloy are indicated by light grey to white areas while regions of binder and voids are indicated by dark areas.

Figure 3-5 is a micrograph illustrating the neck formed during diffusion bonding, or sintering, of two metallic spherical particles. Figure 3-6 illustrates the growth of a grain boundary between two particles. The degree of densification is a function of the time and temperature allowed for diffusion. By controlling these parameters, metals and ceramics formed in this manner can be produced with various porosities. In the case of FeAl, the de-binder step minimizes the temperature and time to reduce to maintain small grain sizes. Figure 3-7 provides a view of this transformation. The micrograph on the left is a region of green sheet as it appears after compaction. The image on the right is a region of compacted sheet that has been de-bindered. Figure 3-8 offers a similar set of SEM images at higher resolution. Note the reduction in the faceted nature of the FeAl particles, the elimination of the machine marks from the rolling operation, and the creation of voids in the place of binder volume. At the end of the de-binder step the green sheet has been transformed from a weak, flexible, friable material into a porous metal with only a few percent bulk volume reduction.

The investigation of the green sheet constituent properties and their distribution in the compacted form yielded several important results. First, the microstructure of the green sheet cannot be described by a simple geometry. For purposes of modeling it is

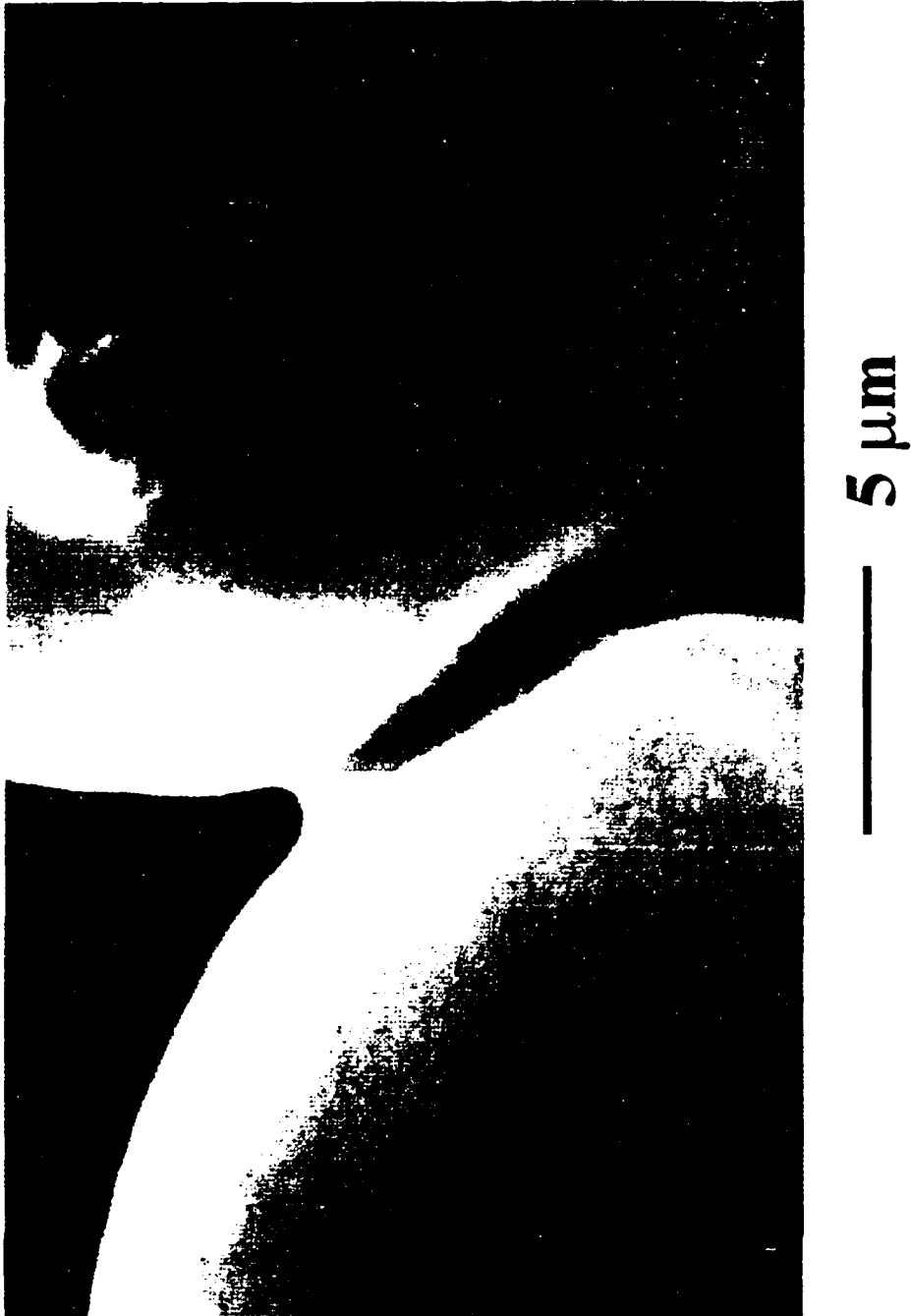


Figure 3-5: Diffusion bonding associated with particle sintering [1].

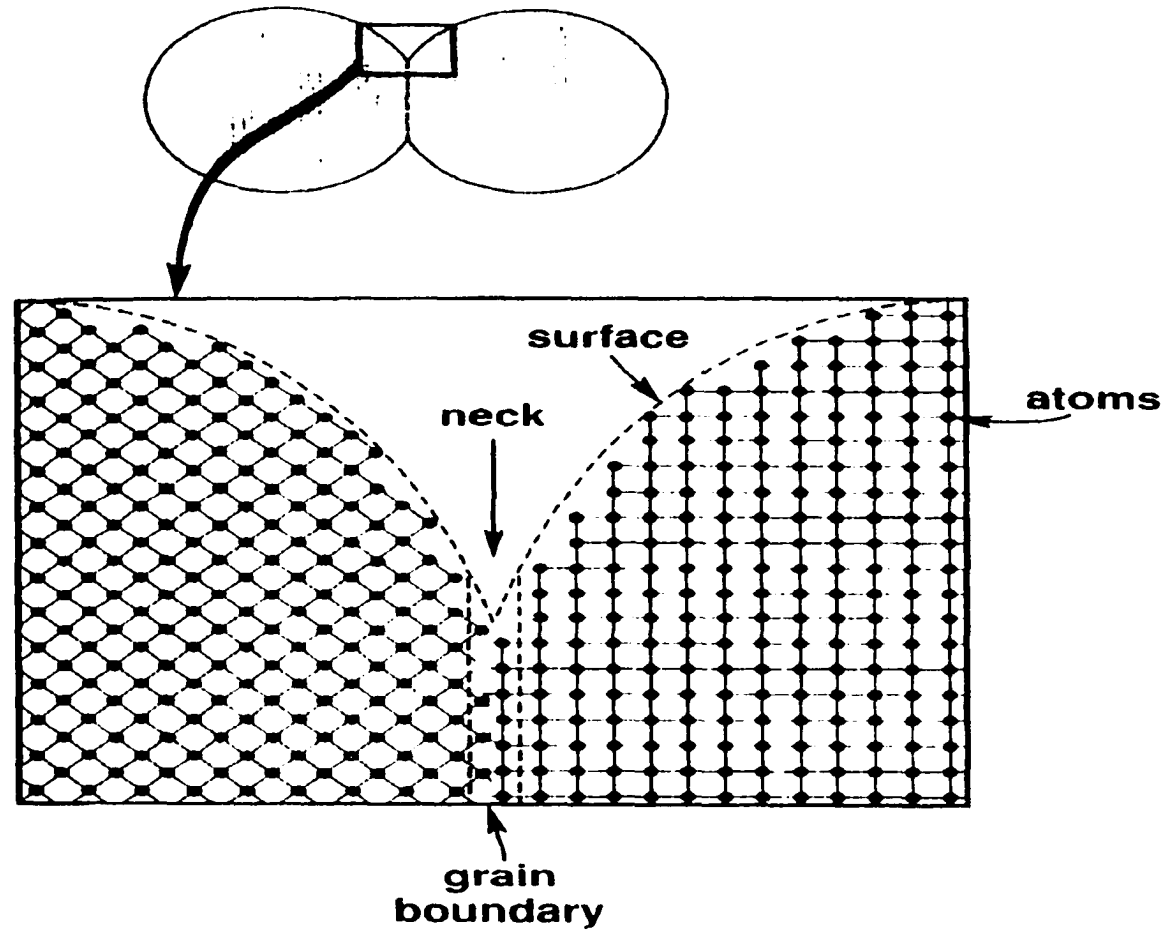


Figure 3-6: Formation of a grain boundary between two diffusion bonded particles [1].

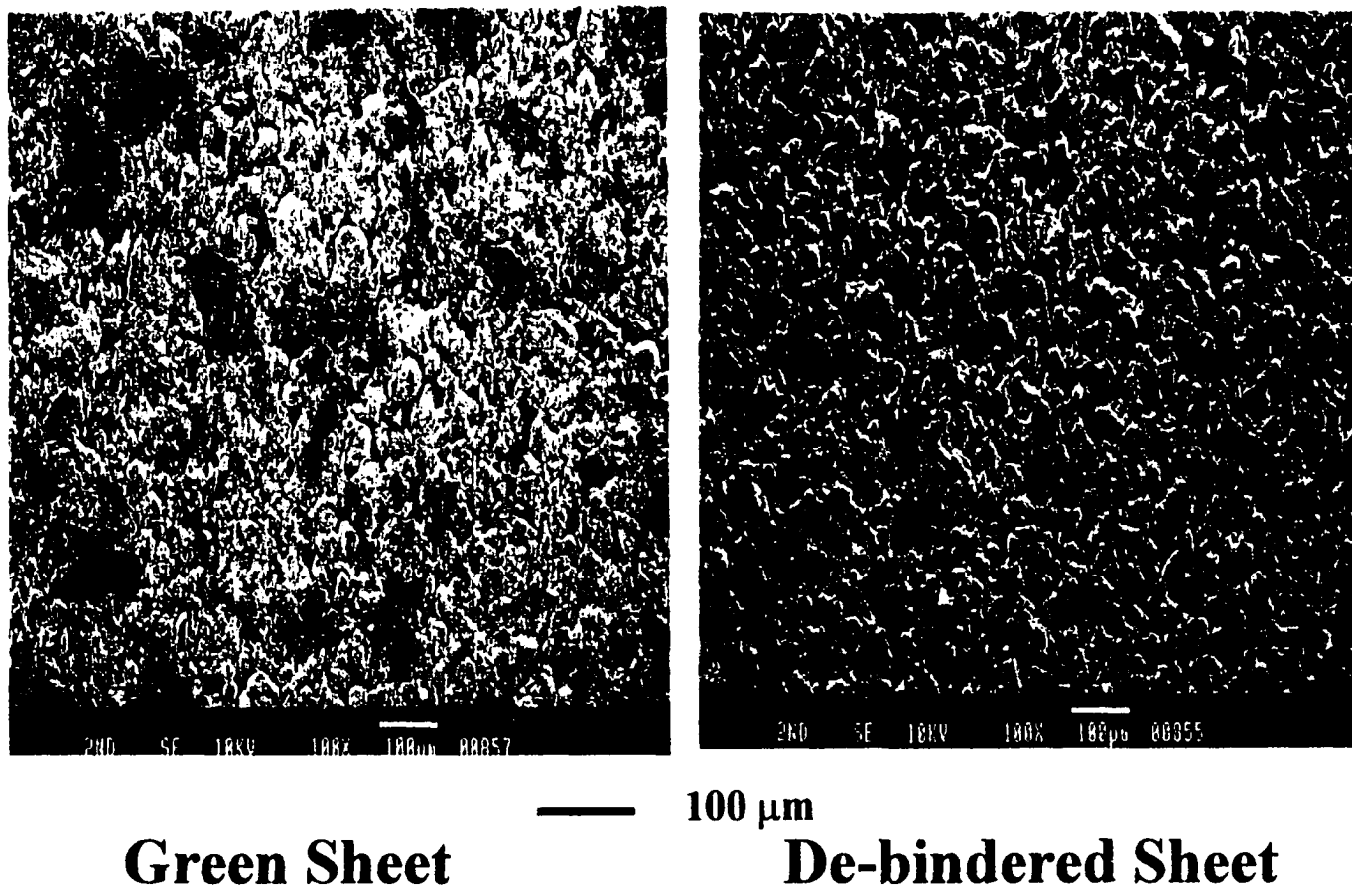


Figure 3-7: Change in microstructure associated with de-binding operation.

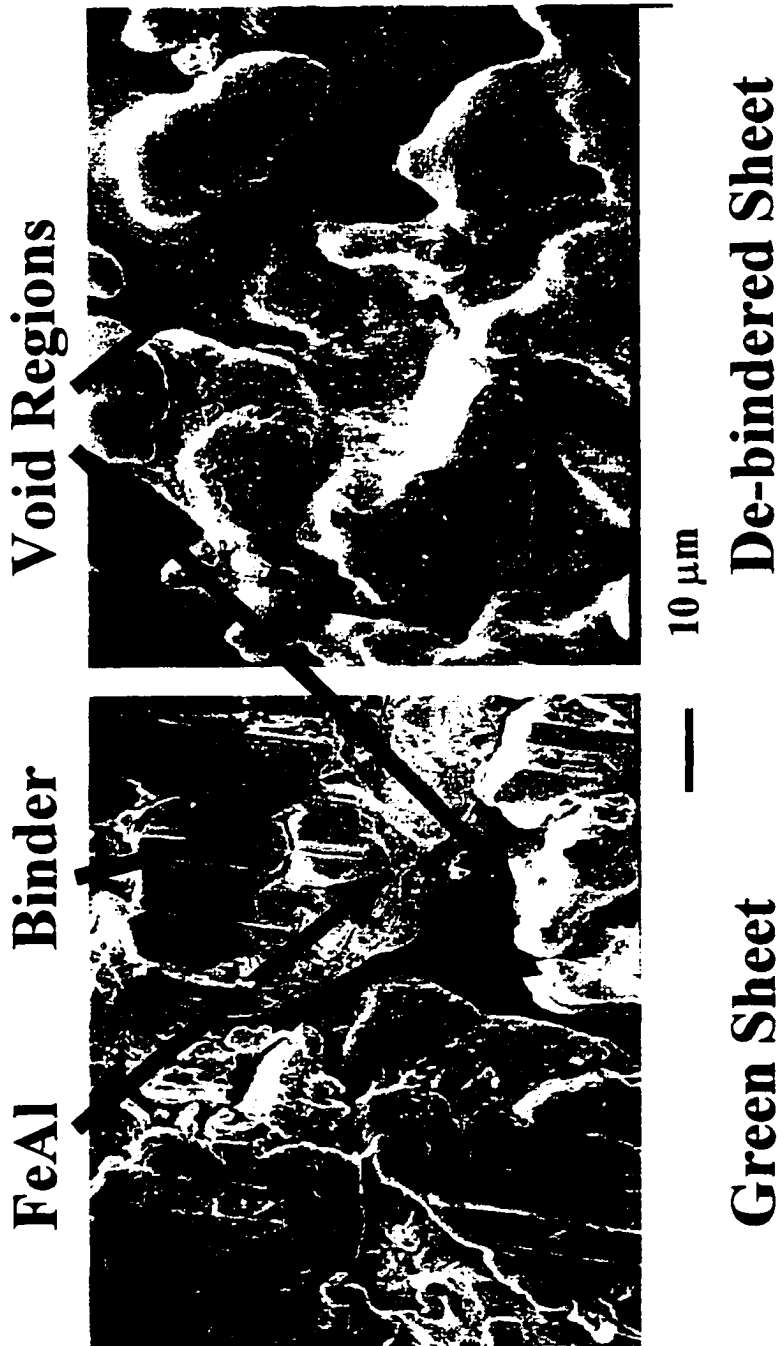


Figure 3-8: Changes in microstructure associated with de-binding operation.



advantageous to identify composite features such as planes of symmetry, preferred particle orientation, geometrical packing relationships for particles of known shapes and size distributions, etc. The green sheet is best described as a composite material with three constituents: alloy particles, binder, and voids. Based on the constituent densities, weight fractions, and bulk green sheet density the compact mass is estimated at about 97% alloy occupying only 50 to 60 percent of the bulk volume. The green sheet is a loose assembly of irregularly shaped thermally conductive particles which are partly coated by a much less conductive binder which also agglomerates to form regions of low conductivity. In addition, significant voids are present throughout the structure. It is tempting to describe the composite as a matrix-filler system. However, this description is usually reserved for composites in which the minor and major volume constituents are readily distinguishable (e.g. 10% volume conducting filler particles in a polymer matrix). The designations "filler" and "matrix" are somewhat arbitrary in the present case.

### **3.2 Preliminary thermography investigations**

Preliminary experimental work focused on investigating the sensitivity of thermography to obvious defects such as thickness variation, cracks, and artificial flaws. The delicate nature of the green sheet made it relatively simple to induce surface mass loss by lightly rubbing the a sample with a soft implement. Cracks could be induced by slightly bending the pliable sheet. Production samples with various non-conforming anomalies were also provided.

Initial experiments were conducted using flash through-heating, same side step

heating, and same side flash heating (see section 2.3). Insulated boundary conditions were approximated by suspending the samples in air during heating. Data were collected using three different sets of instrumentation. Images from the front surface step heating were obtained using an Amber Radiance I infrared camera, with a maximum frame rate of 60 Hz, in conjunction with two 500 W quartz lamps. This system provided a temperature slope image at a specified time after initiation of a step flux. The gray levels in these images correspond to the variation of the rate of temperature change on the surface. The front surface flash heating experiments were conducted using an Amber Radiance HS camera in conjunction with two Balcar<sup>®</sup> 6.4 kJ xenon flash lamps. The duration of the pulse was approximately 10  $\mu$ s. This system is capable of providing thermal images at frame rates in excess of 1 kHz. The through-heating technique was implemented using an Inframetrics 760<sup>®</sup> infrared camera in conjunction with a single Balcar<sup>®</sup> 6.4 kJ xenon flash lamp. This camera had a maximum frame rate of 30 Hz. A rate of 60 Hz can be obtained by separating the interlaced images. This Images were collected and stored for post processing using a Perceptics<sup>®</sup> computer and image capture software. Post processing and analysis of all images was conducted using Visilog<sup>®</sup> image analysis software.

Figure 3-9 illustrates the ability to detect defects using step heating from the same side as the observation. This specimen was provided as a part which was discarded due to a crack which formed along its lower edge. The defects are distinguishable from the surrounding material due to their difference in heating rates. The intensity values in the image represent the instantaneous slope of temperature with time at 6 seconds after the initiation of heating with the quartz lamps. The absolute temperature remained

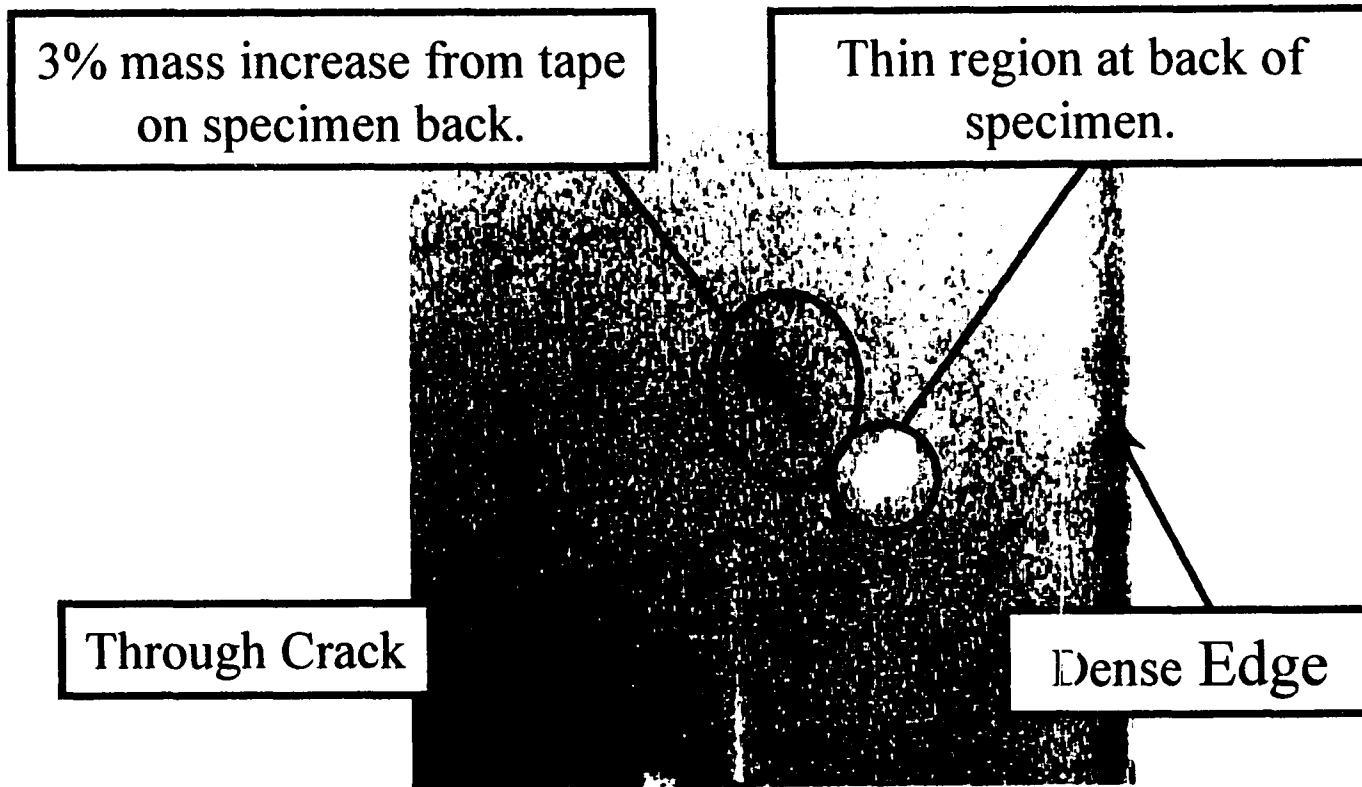


Figure 3-9: Detection of defects using step heating with quartz lamps.

below 40<sup>0</sup> C. At this point in time the finite thickness of the sample is reflected in the image contrast. The through crack and dense edge were pre-existing sheet defects. This densified edges are created due to the deflection of the compaction rollers. Prior to this data the only quantitative indication of this feature was a horizontal x-ray line scan. None of these two dimensional subtleties had been observed. The thin region on the back side of the specimen was created by lightly abrading the surface. It is estimated that less than 10% of the material was removed. The low mass region is distinguished from the surrounding material by a relatively large rate of temperature increase. The triangular shaped piece of masking tape was placed on the back side of the sample to locate the abraded region. The effective mass contribution of the tape, normalized to area, was estimated to be 3%. This added thermal load is reflected in temperature time derivative slope smaller than that of the surrounding material. The relative intensity of the crack has two contributing factors. First the crack consisted of a "V" shaped groove. Thus the material closest to the crack was actually thinner than the surrounding material. Secondly, cracks tend to exhibit locally higher emissivity due to a cavity effect [34].

Standard thermographic investigations usually involve the testing of a series of flat bottom holes, of various diameters and depths, which are milled into the back side of a test panel [48]. Since this was not a feasible using the green material, a test was performed by adding increments of mass using cellophane tape. Different thermal loads were achieved by adding successive layers of tape. A single layer of tape was estimated to provide less than 1% added mass. Figure 3-10 illustrates the resulting thermal slope image from step heating. One layer was not easily discernible from the background. Layers two through five

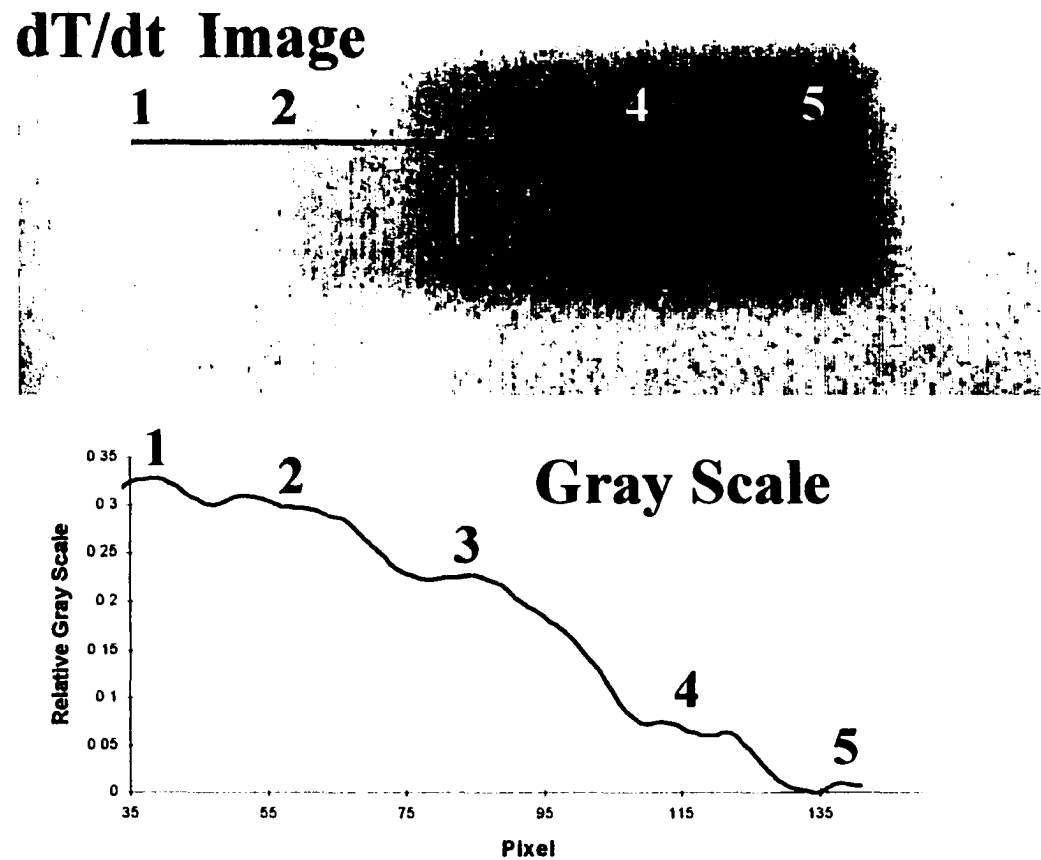


Figure 3-10: Detection of cellophane tape layers. Air gaps are believed to cause non-uniform gray scale steps.

were easily detectable. Although this image does not show the distinction of layers four and five, they were differentiated using the full dynamic range of the data as illustrated in the accompanying line plot. Air gaps between tape layers are believed to have caused variations in the step heights seen in figure 3-10.

A sample with well behaved mass and thickness variation was obtained from routinely discarded production material. Sheet obtained during the depletion of the hopper charge is deformed. As the blend trickles out a thin tapered edge is formed. The material has a nominal thickness at one end with the thin end taking on a "V" shape. Micrometer readings were taken by placing the green sheet on a granite slab. The specimen had a thickness of 700  $\mu\text{m}$  at the thick end and a thickness of 350  $\mu\text{m}$  at its thin end. Figure 3-11 illustrates three different images of the tapered sample. The optical image shows the grid upon which the micrometer readings were taken. The thickness of these white cross-hair lines are scaled to the actual thickness of the green sheet. This provides a relative thickness to width reference. The middle image represents the rate of temperature change,  $\partial T/\partial t$ . As in the case of figures 3-9 and 3-10 the thin regions are clearly indicated by their relatively large thermal slopes. Figure 3-12 compares an x-ray image, taken using a Digiray<sup>®</sup> digital x-ray instrument, with the heating rate image. Both depict the thin tapered edge toward the bottom of the figure. Even though the x-ray image was generated using a relatively long integration time (about 10 minutes), the thermal image contains many more detailed features.

Figure 3-13 provides a more detailed illustration of other thermal features. The best contrast was achieved by sampling the thermal slope just after the quartz lamps had

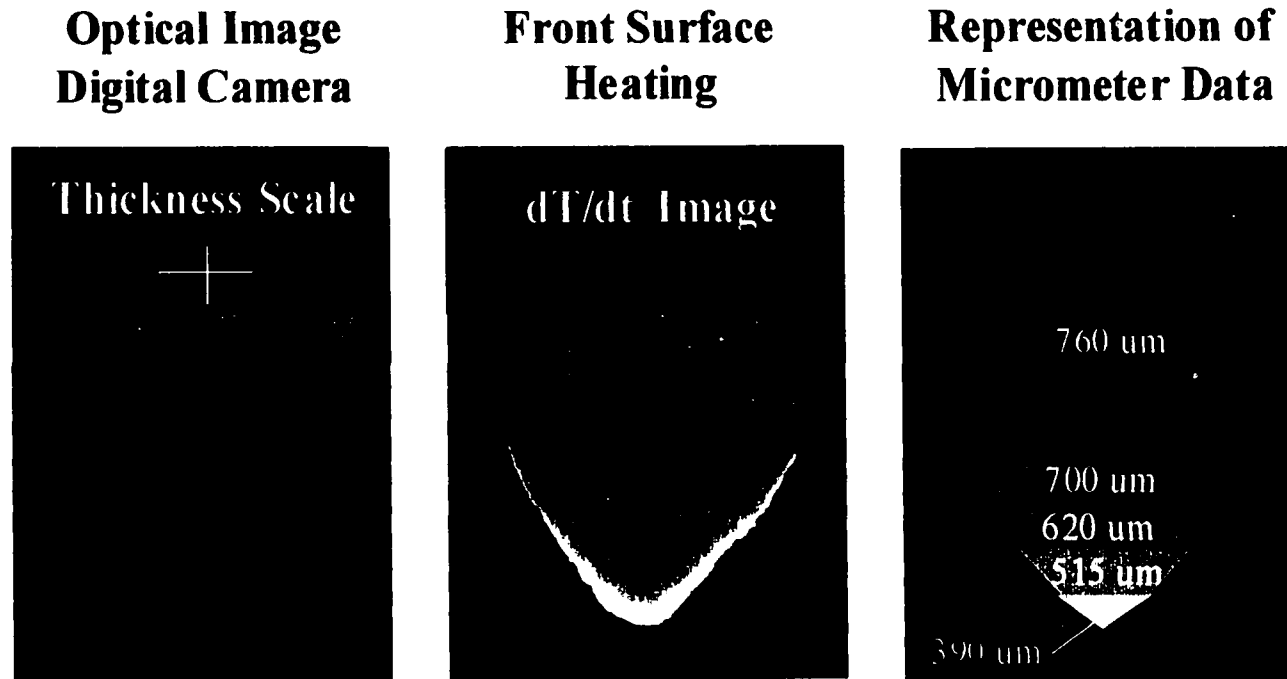


Figure 3-11: Optical image, thermal slope image, and micrometer readings for tapered sample [36].

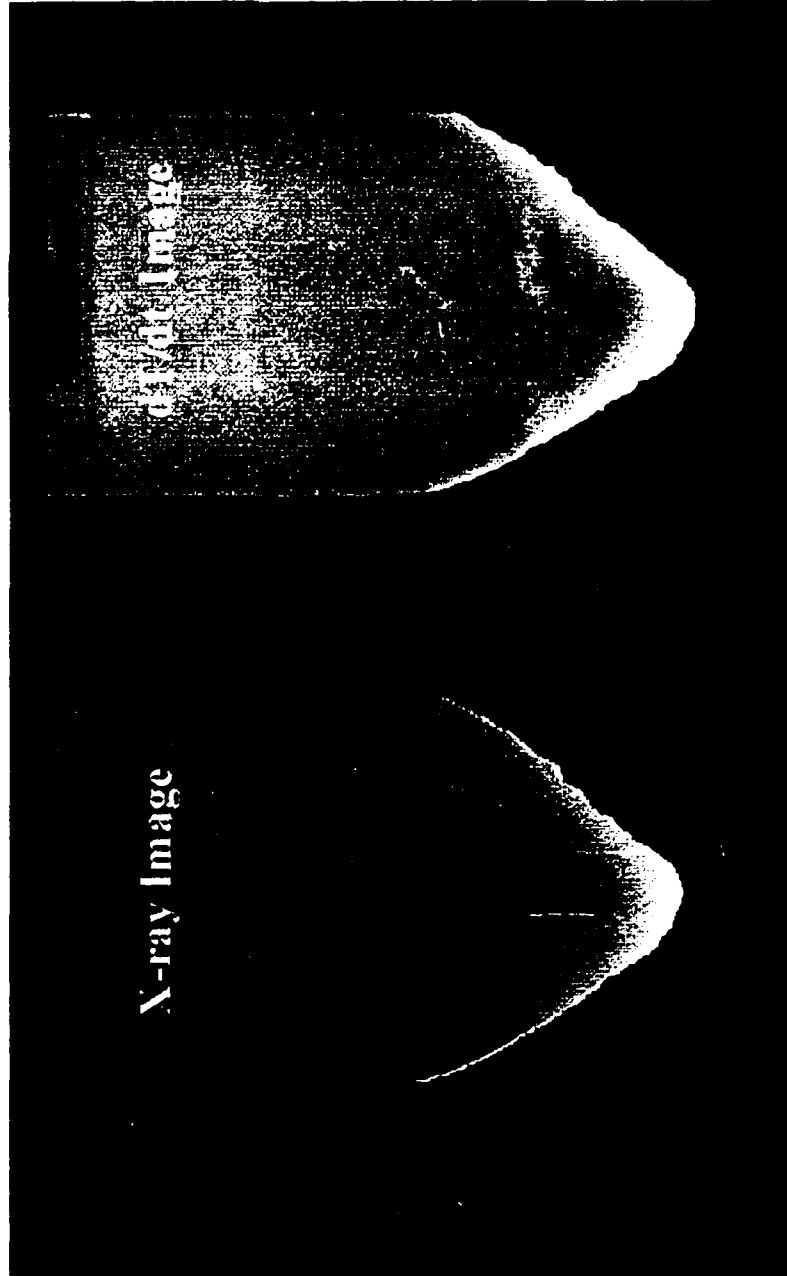


Figure 3-12: Comparison of a digital x-ray image and a thermal slope image.



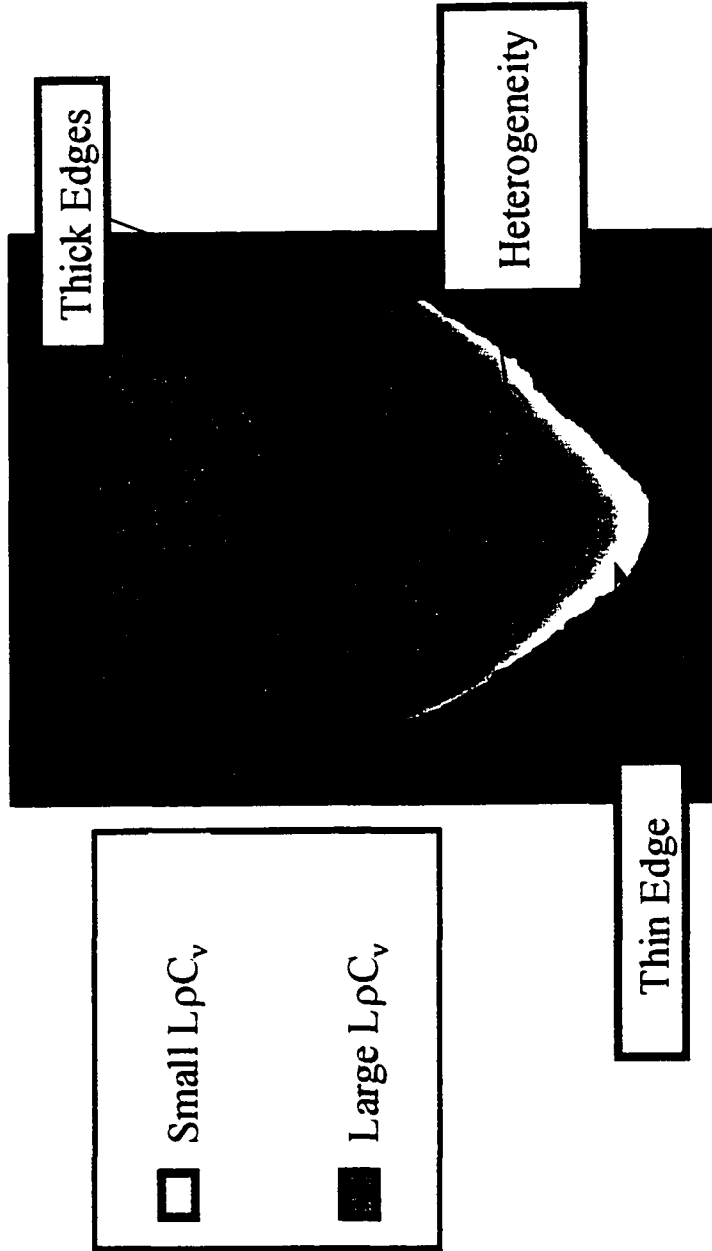


Figure3-13: Details of thermal slope image obtained early in the step heating.

been turned on (i.e. during the ramp portion of the step heating). After allowing the sample to reach equilibrium, on the order of 10 seconds, the contrast in the raw thermal image minimal. This indicated that the variation in emissivity across the surface of the sample was negligible. When the thermal gradient through of the thickness material is small the gray levels in figure 3-13 are indicative of the magnitude of  $\frac{\partial T(t)}{\partial t}$  (equation 3.1).

$$\frac{\partial T(t)}{\partial t} = \frac{Q}{L\rho C_p} \quad (3.1)$$

Thus for a uniform radiant energy per unit area,  $Q$ , absorbed by the surface the light gray levels are indicative of a combination of thin sheet and/or low thermal mass. As is shown in figure 3-11 the lower edge of the specimen was measured as having a thickness almost half that of the nominal thickness. However, the translation to geometrical thickness can only be made if variations in bulk thermal properties are known. At the time the lack of compositional information made it impossible to de-couple these factors. The effort to conclusively separate these effects became a focal point of later investigations and will be discussed later in the context of samples with controlled composition. However, it is instructive to point out the process features which influenced these results and the conclusions which can be drawn from this sample. It is clear from the micrometer readings that a thermally thin response would be expected at the tapered end of the sample. However, without independent confirmation of local sheet composition an effect from a gradient in blend composition could not be eliminated. It was observed that as the vibrating hopper emptied the metal and binder powder segregated. The lighter binder rises to the top of the blended charge. As described in the section on blend components, the binder has a value of  $\frac{\rho C_p}{\kappa}$  orders of magnitude smaller than that for the FeAl powder. Therefore a higher

of  $\frac{\rho C_p}{\kappa}$  orders of magnitude smaller than that for the FeAl powder. Therefore a higher concentration of binder along the tapered edge could have contributed to an enhanced heating rate. Note that the circled region in figure 3-13, denoted as a heterogeneity, exhibited a pronounced localized heating rate. This region displayed no obvious thickness anomalies yet, to the eye, it was lighter in a color consistent with the binder. As will be shown, such regions were later confirmed to be areas rich in binder. Figure 3-14 depicts the variation in heating rate (gray level) along the length (dotted line) of the specimen.

The same specimen illustrated in figure 3-14 was investigated using the through-heating technique. This approach, typically referred to as the Parker method [14], relies on the temperature increase at the surface opposite that of the excitation source, i.e. the specimen is between the camera and the flash lamp. Figure 3-15 illustrates the diffusion of the heat through progressively thicker regions of the sample. The lack of detail exhibited in the front surface step heating (see figure 3-14) resulted from several factors. The Infracor 760<sup>®</sup> camera had less spatial resolution and a frame rate half that of the Radiance I. In addition, the signal at the back surface of the sample arrives late enough to allow for lateral diffusion. Thus features highlighted by boundaries in the plane would be less discernible.

Figure 3-16 illustrates the quantitative data obtained from this technique. The graphs represent the time-evolved temperature at each of three different positions. Note that the characteristic time to reach half the maximum temperature increases with increasing thickness. The region of nominal thickness reached its maximum temperature in less than about 0.50 sec. The estimate of thermal diffusivity from this data is about 0.0023 cm<sup>2</sup>/sec.

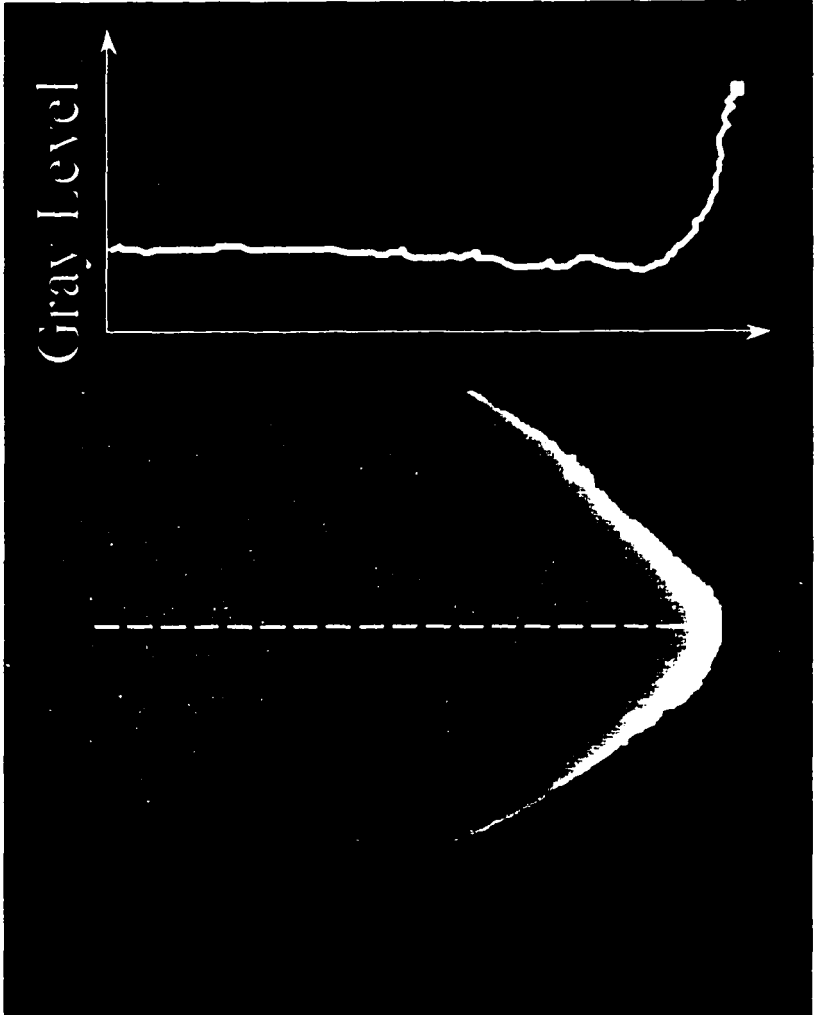


Figure 3-14: Line scan of thermal slope image obtained early in the step heating [36].

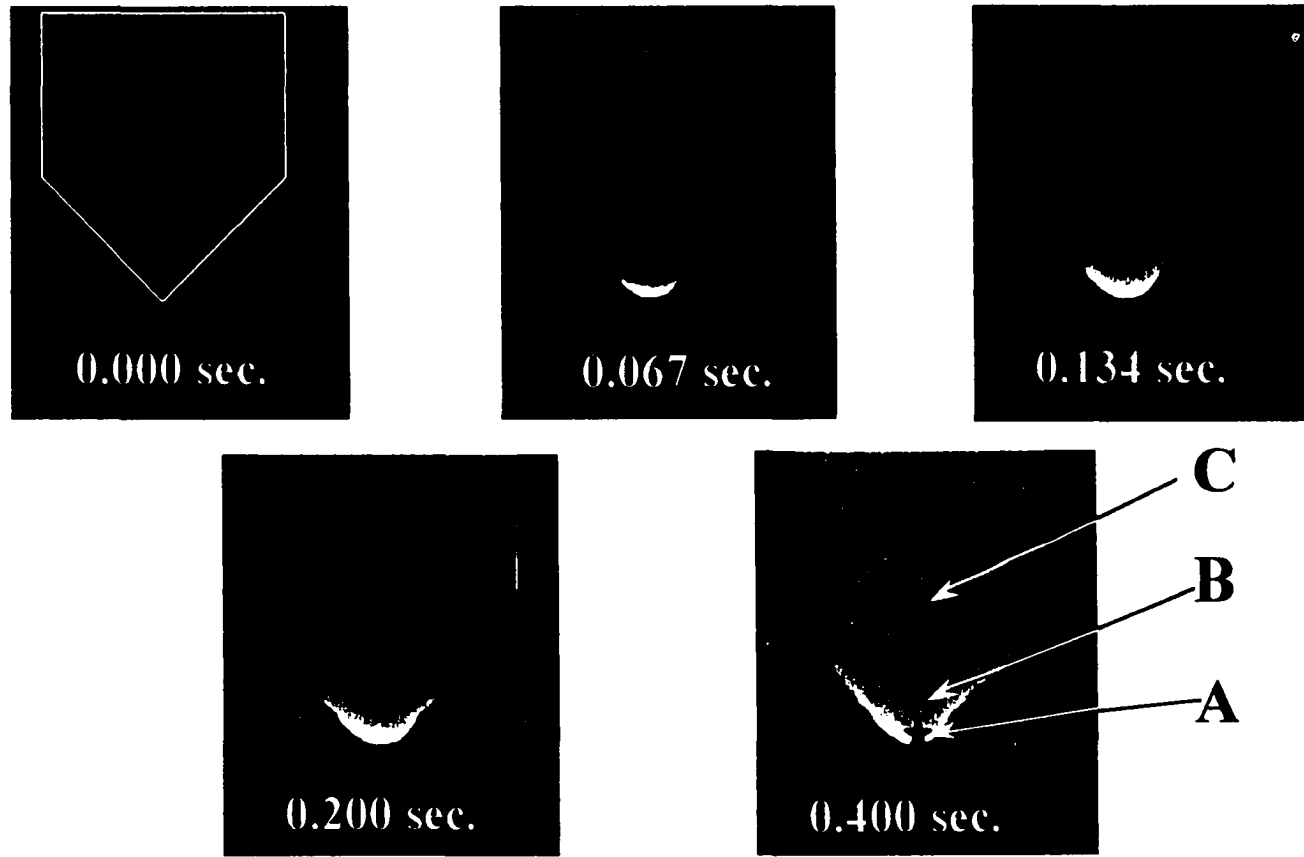


Figure 3-15: Sequential images showing thermal response through progressively thicker regions of the tapered sample. "A" is the thinnest region and "C" is the thickest region [36].

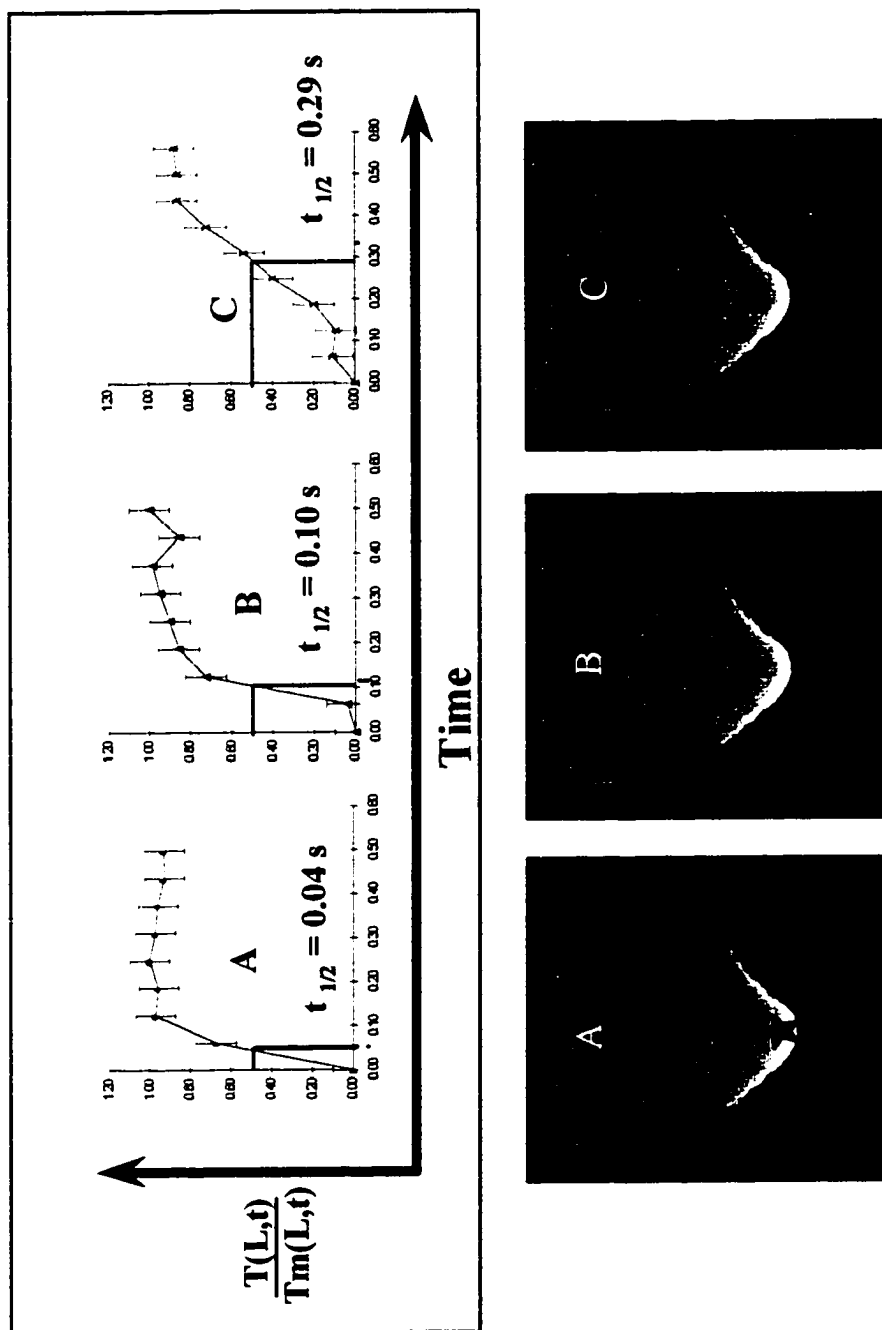
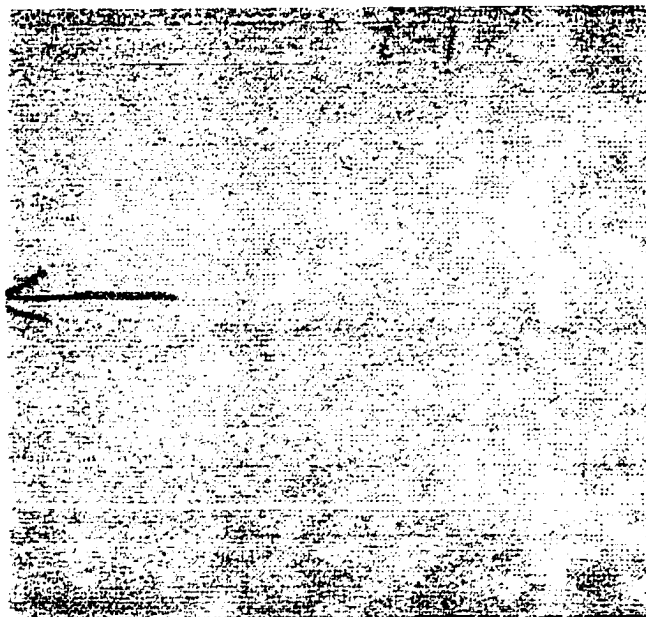


Figure 3-16: Normalized temperature evolution for through heating of green sheet using an impulse excitation [36].

As would be expected, from the material properties of the binder, this is much lower than that obtained for the final sheet material, about  $0.030 \text{ cm}^2/\text{sec}$ .

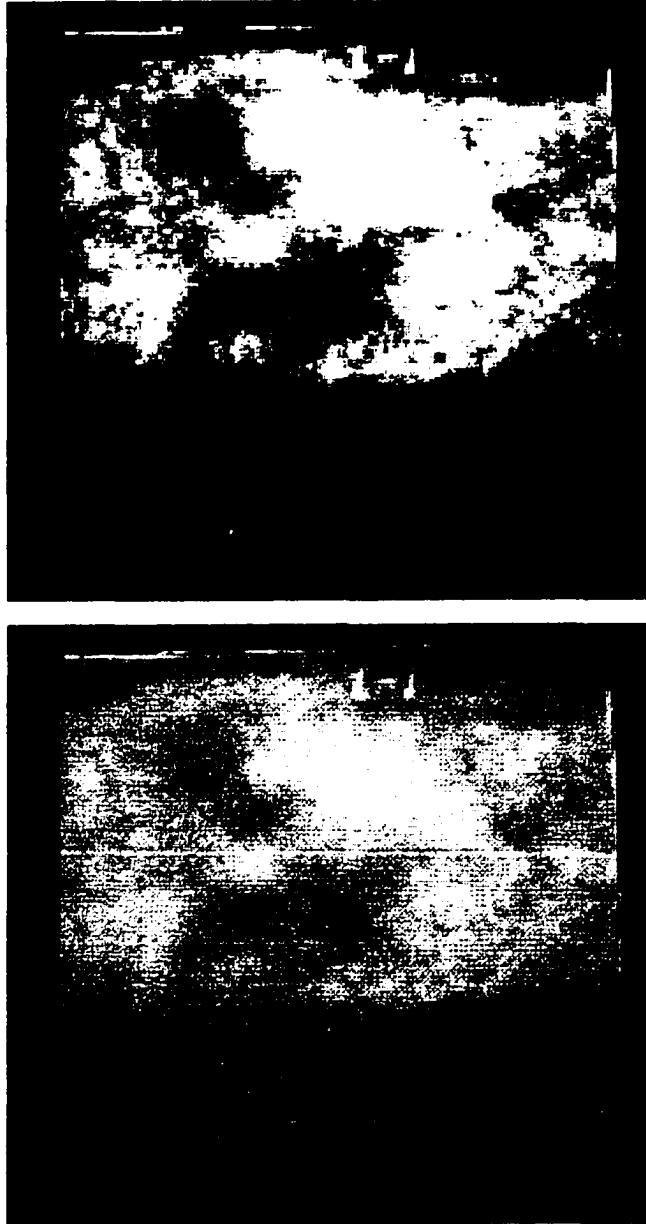
Data from the previously described experiments indicated that active thermography could provide significant qualitative information and had the potential to provide important quantitative information as well. The next step was to investigate the ability to extract this information while considering the manner in which the green sheet would be presented for inspection in the production environment. The material would need to be inspected as it was translated, supported by a substrate, across the field of view at about  $0.5 \text{ cm}/\text{sec}$ . The early tests, through-heating and same-side step-heating, indicated that a same-side flash technique could provide the speed and sensitivity necessary to detect the features of interest. For example: At early times, less than about 200 ms, the substrate has a negligible effect on the thermal field within the sheet, i.e. sheet is thermally thick over this time regime and approximates a half space (see figure 3-16). In addition the sheet would travel less than about 1 mm during this time resulting in reasonable spatial resolution in the plane. These effects will be discussed in greater detail in the model development.

Figure 3-17 is an optical image of a specimen. The arrow indicates the material machine direction. Note that the surface is fairly uniform with only small regions of minor discoloration. A Radiance IIS camera was used to acquire thermal images at 500 Hz. Interesting features were obtained very early in the image sequence. Figure 3-18 I is a thermal image obtained 32 ms after the flash. Figure 3-18 II provides a view of the same data with the gray scale adjusted to enhance the contrast. According to early time data, from the through heating experiments, it is obvious that the thermal diffusion distance



**Figure 3-17: Optical image of green sheet specimen as tested. Visual inspection provides little useful indication of green sheet defects.**





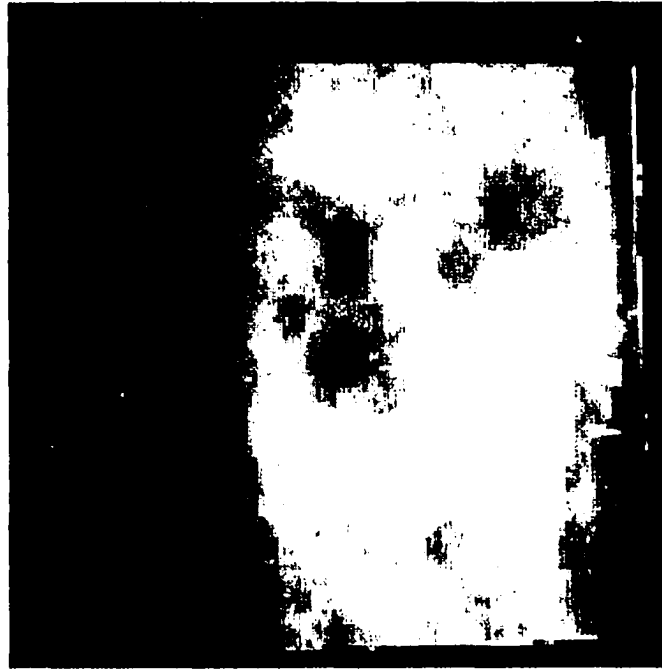
**I - Low Contrast      II - High Contrast**

Figure 3-18: Thermal image obtained 32 ms after flash.

at 32 ms is a small fraction of the thickness of the material thickness (see figure 3-16). The features persisted through the temporal sequence of thermal images. In order to verify that these features extended through the volume of the sheet an image sequence was captured for the opposite side of the sample. Figure 3-19 clearly shows that, as far as the dominant features are concerned, the images are transposes of each. Tests with other samples were consistent with this result. Thus the inference is that the thermal properties of the sheet are essentially two dimensional. This is not surprising if one considers the extent of these features relative to the thickness of the material (see cross-hair lines in figure 3-11).

The next step was to identify the physical differences contributing to the difference in thermal behavior. The sample was sacrificed to determine the weight and thickness of five regions. Since the features were not visible to the eye, a template was devised using a high contrast thermal image printed to scale on transparency medium. The regions to be sampled were then cut out of the template using a cork bore tool. The template was taped over the specimen and the green sheet sample plugs removed using the same cork bore. Figure 3-20 identifies sampled regions per the thermal image.

The mass of each core was measured. An area normalization factor was determined for each core by converting the optical image of the core sample into a binary image. The pixel count for each hole was proportional to the core area. This was then calibrated using known reference dimensions from the specimen. The mass per unit area in combination with the various core thicknesses could be used to calculate local bulk densities. Several failed attempts were made to determine the thickness of the cores by mounting, cross-sectioning, and inspecting them under SEM. Unfortunately the material was too fragile for



**Front Side**



**Back Side**

**Figure 3-19: Thermal images for opposite sides of the same green sheet specimen. The transposition of the dominant features shows that they are present through the thickness.**

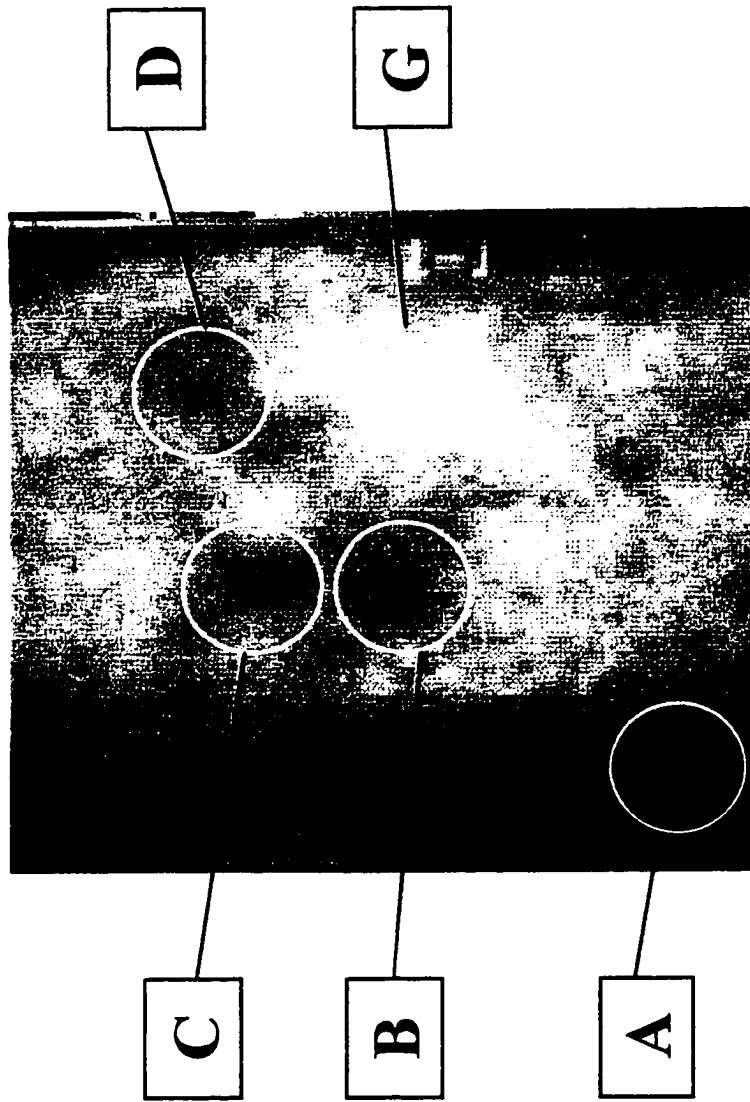


Figure 3-20: Thermal image showing regions A through G which were removed from the specimen for characterization.

this to be accomplished and most samples disintegrated during the mounting for microscopy. The few measurements made indicated that thickness variations were less than a few percent. Recall from the analytical heat conduction solution for an isotropic homogeneous solid that for early times it is expected that the thermal signal should be linear with the inverse of the thermal effusivity,  $t = \sqrt{\rho\kappa C_p}$ . The detailed dependence of effusivity and the associated material properties are discussed later using reference samples of known composition. At this point in the study the only the bulk density was determined. Figure 3-21 shows a plot of the signal, normalized with respect to the range of the regions sampled, versus the inverse of the square root of the bulk density, normalized with respect to the range of regions sampled. The fact that the plot is a reasonable linear fit indicates that the product of  $\kappa C_p$  would be expected to vary approximately linearly with the volume fraction of alloy. This issue will be addressed quantitatively in the composite model described in chapter 4. The error bars for the intensity values are based on the range of intensity over the sample region and would have been smaller if it had been feasible to sample smaller regions. The data are in good agreement with the analytical solution. Figure 3-22 is an SEM backscatter micrograph of the cross section of the regions (A and G in Figure 3-20) with the highest contrast in the thermal image. The image has been converted to binary form to estimate the relative volume fraction of FeAl. The dark regions in figure 3-22 represent the metal species and the light regions indicate binder and, or, void regions. The pixel statistics indicates that region A contained 51% FeAl by volume while region G contained only 15% FeAl. This result was confirmed by calculating the ratios of the bulk densities of samples A and G, using the mass data and taking into account the difference in thickness. The details of this

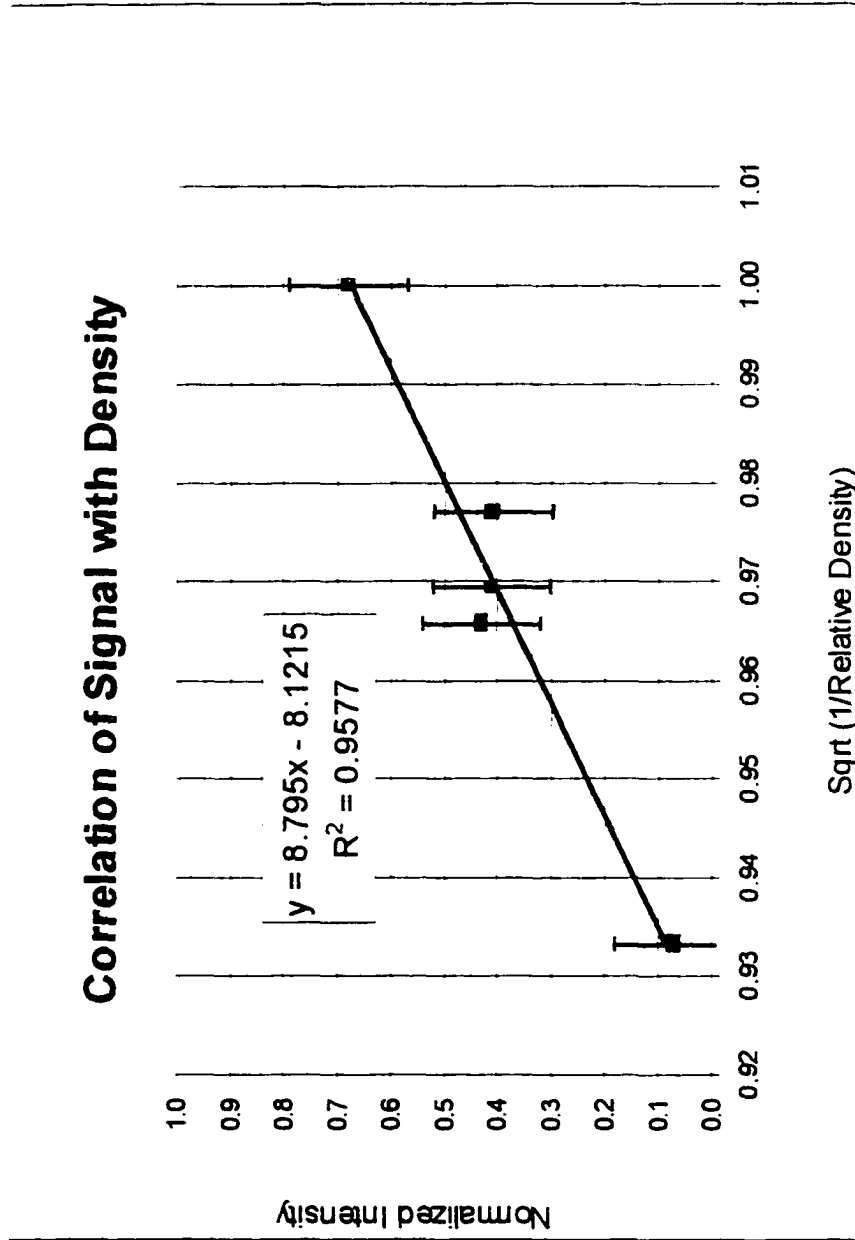


Figure 3-21: Thermal image intensity versus bulk density.

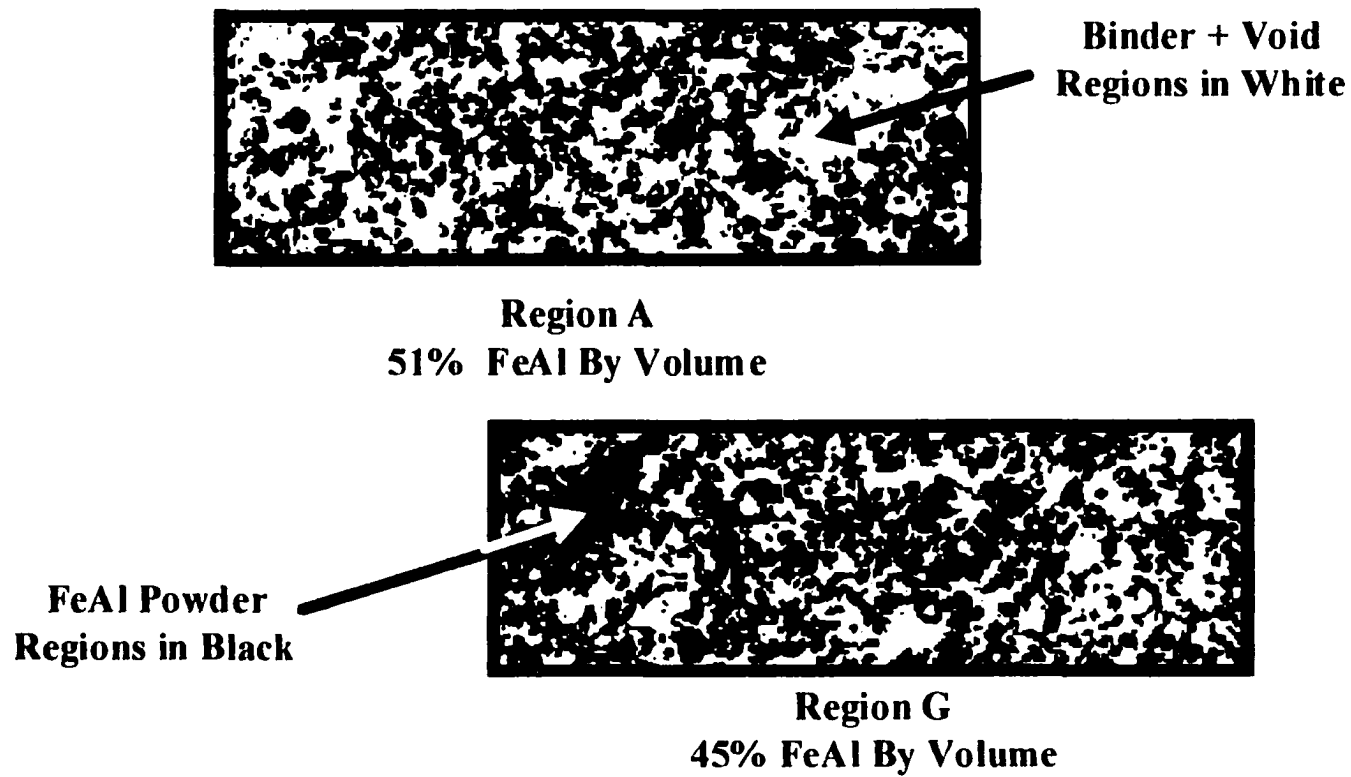


Figure 3-22: Backscatter images illustrating the difference in FeAl volume fraction for regions A and G.

relationships and the impact on quality will be discussed later in the context of process influences, large scale production sampling, and standard reference material.

### 3.3 Conclusions of preliminary investigation

These investigations were important in establishing the viability of the thermographic inspection of green sheet and defining the inspection parameters. Minor artificial defects and, more importantly, naturally occurring variations in production green sheet could be detected and located. Figure 3-23 provides a comparison of the different techniques applied in the preliminary investigations. The front flash technique provides the speed required for production and has resolution comparable if not superior to the through heating techniques. In the production environment the material is presented lying on a conveyor belt with production rates of about  $300 \text{ cm}^2/\text{min}$ . In the present study image areas approximately  $250 \text{ cm}^2$  were acquired and displayed within several seconds. The spatial resolution was as high as  $0.5 \text{ mm}$ . Thus it was concluded that 100% inspection at good spatial resolution was feasible. It was also important to understand the conditions under which the supporting substrate should be taken into account. The through heating experiments showed that after about  $500 \text{ ms}$  significant interaction with the substrate would perturb the thermal field within nominal green sheet. In other words, beyond this period the finite thickness and non-insulated boundary of the specimen must be considered. Several questions were left unanswered. The correlation between local bulk mass and the thermal data was promising yet further work was necessary to provide conclusive results



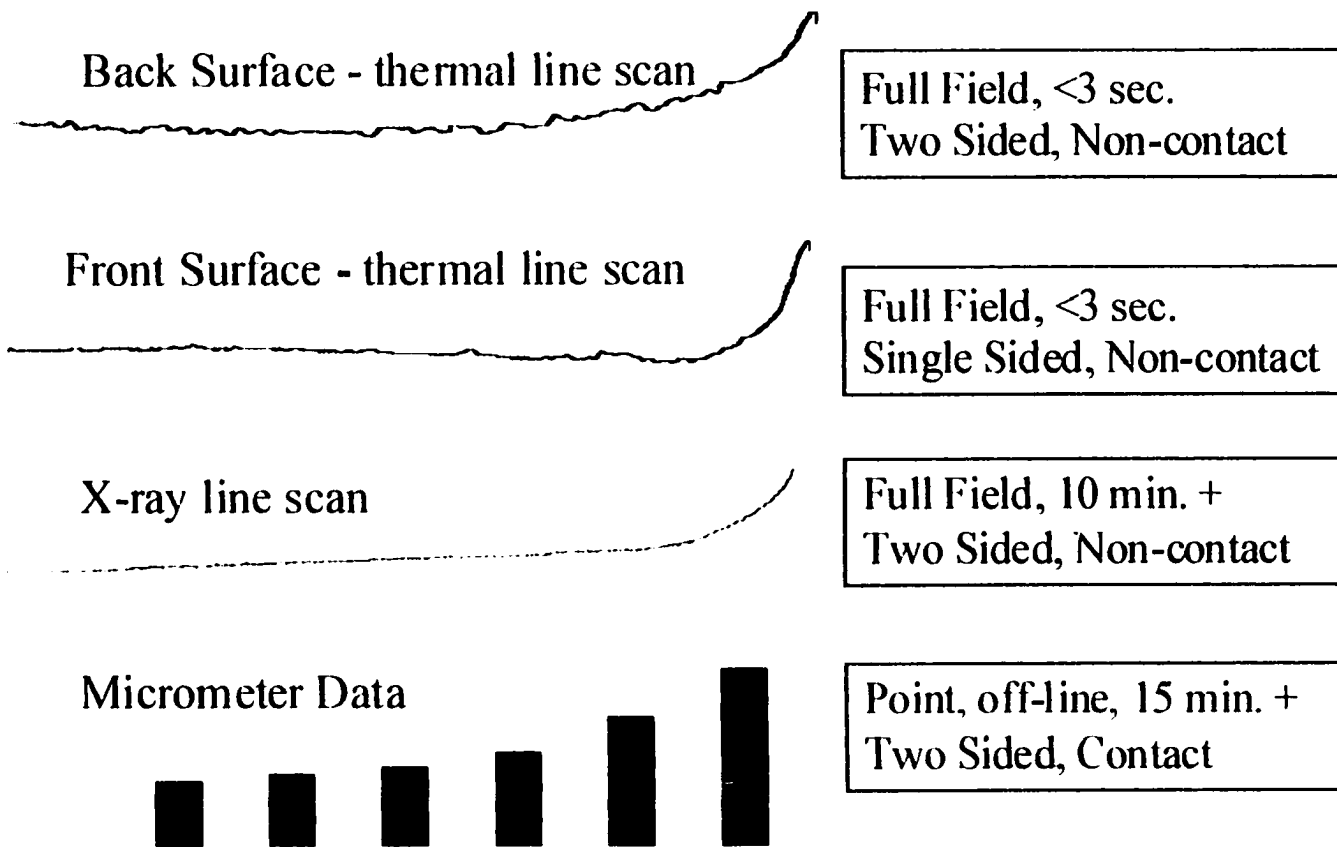


Figure 3-23: Comparison of data collected for a tapered green sheet sample using several techniques.

as to the variation in composition. Furthermore, the relevance of these variations to the quality of the final product was not established.

## Chapter 4

# Material Inspection Method

### 4.1 Introduction

At the onset of the research neither the nature of the green sheet defects nor the morphology of its microstructure were well characterized. Most of the materials development effort had gone into characterizing the fully dense FeAl product. Within the defined process parameters, green sheet deemed acceptable would often fail during processing. The first phase of this experimental work focused understanding the sheet morphology, on the level of the FeAl particles, and establishing the viability of detecting gross flaws with thermography. This involved preliminary investigations using several different techniques and equipment available at the Nondestructive Science Branch of the NASA Langley Research Center. This work provided the basis for a preferred inspection mode and indicated that a more detailed investigation of the bulk thermal properties, as manifested by the relative concentration of FeAl powder, was in order. In this second phase of the research a dedicated laboratory inspection system was assembled and a systematic study of the heat transfer

within green sheet was conducted. The understanding of the thermal transport properties as a function of FeAl volume fraction provided for the development of a calibrated mathematical model. The goal of identifying the mechanisms associated with flaw formation, in FeAl sheet, from green sheet precursors, was achieved by conducting a process tracking study. In this investigation thermal data were collected for a large quantity of production green sheet. The sheet was then processed in the normal fashion. After each step in the process the resulting material was inspected using the standard production practices and procedures. These data allowed for the spatial correlation between the heterogeneity associated with FeAl volume fraction and critical defects which emerged down stream in the process. The result was an inspection protocol which provides for the prediction of defect occurrence, in densified FeAl sheet, based flaw precursors in the green sheet.

#### **4.1.1 Equipment**

Several experimental arrangements were used over the course of this research. During the preliminary or exploratory phase, both the same side and opposite side techniques were used with step function and flash heating modes (see Chapter 2). The bulk of the production and reference materials, used to identify material flaw morphologies and provide for model calibration, were investigated using a front flash system assembled specifically for the inspection of green sheet. A description of this system follows.

Figure 4-1 illustrates the inspection geometry. Figure 4-2 is a wide angle view of the laboratory inspection system and figure 4-3 identifies the major hardware components. These are the Raytheon Radiance HS infrared camera, the Balcar flash lamps, the specimen platform, and the data acquisition computer. Figures 4-4 and 4-5 are views of the

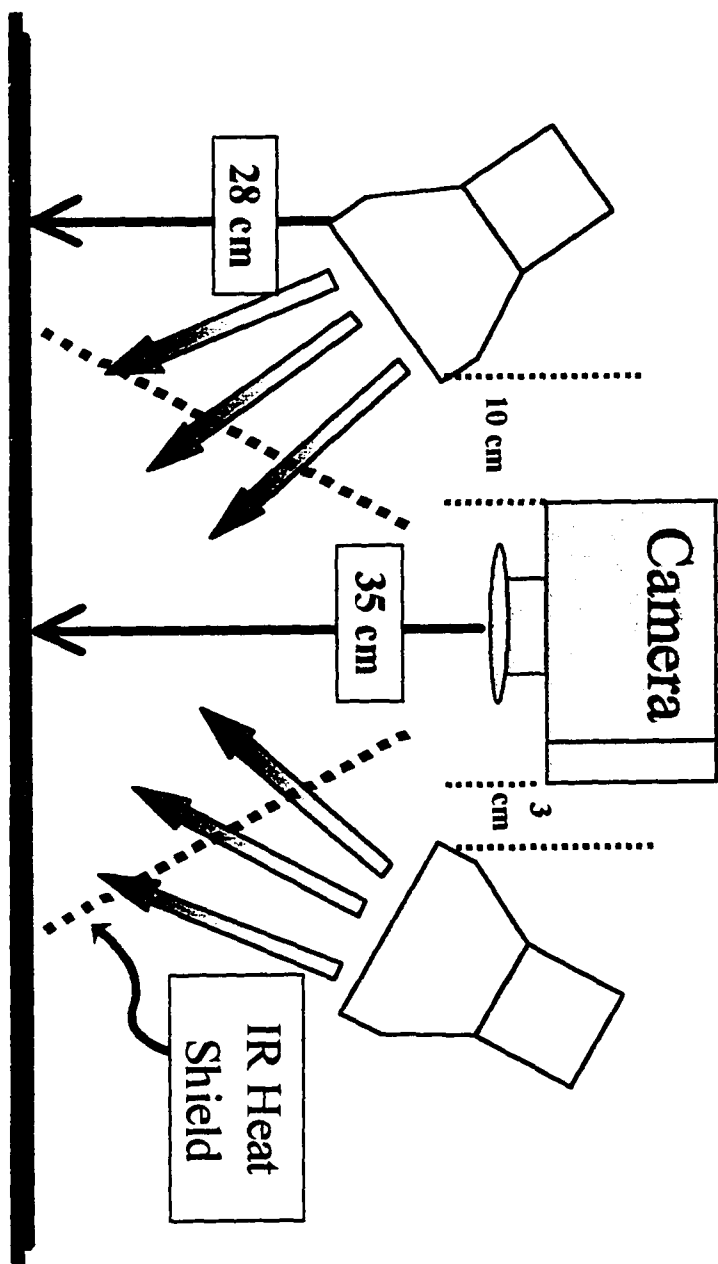


Figure 4-1: Geometry of prototype inspection system.

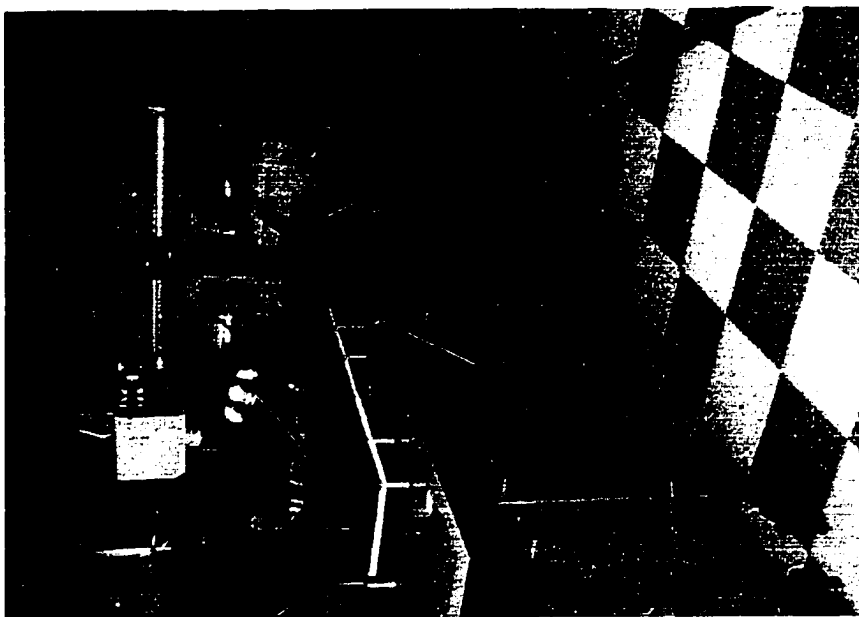


Figure 4-2: Wide angle view of inspection prototype.

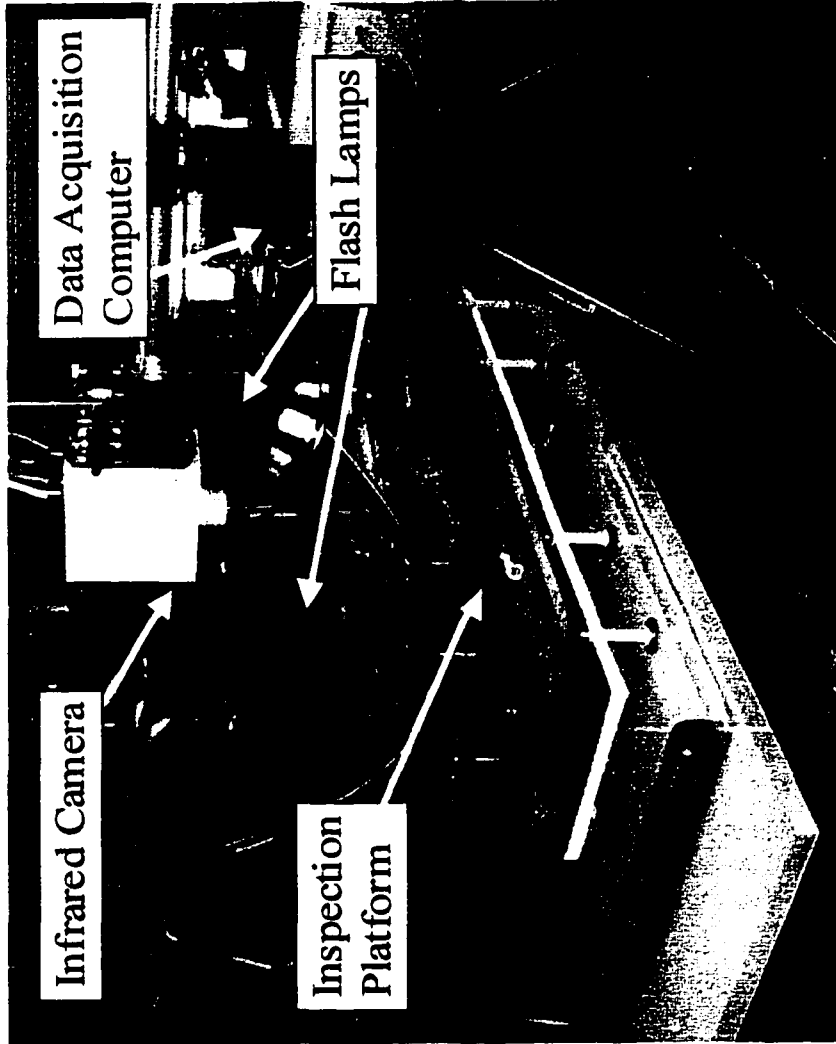


Figure 4-3: View of major prototype components.

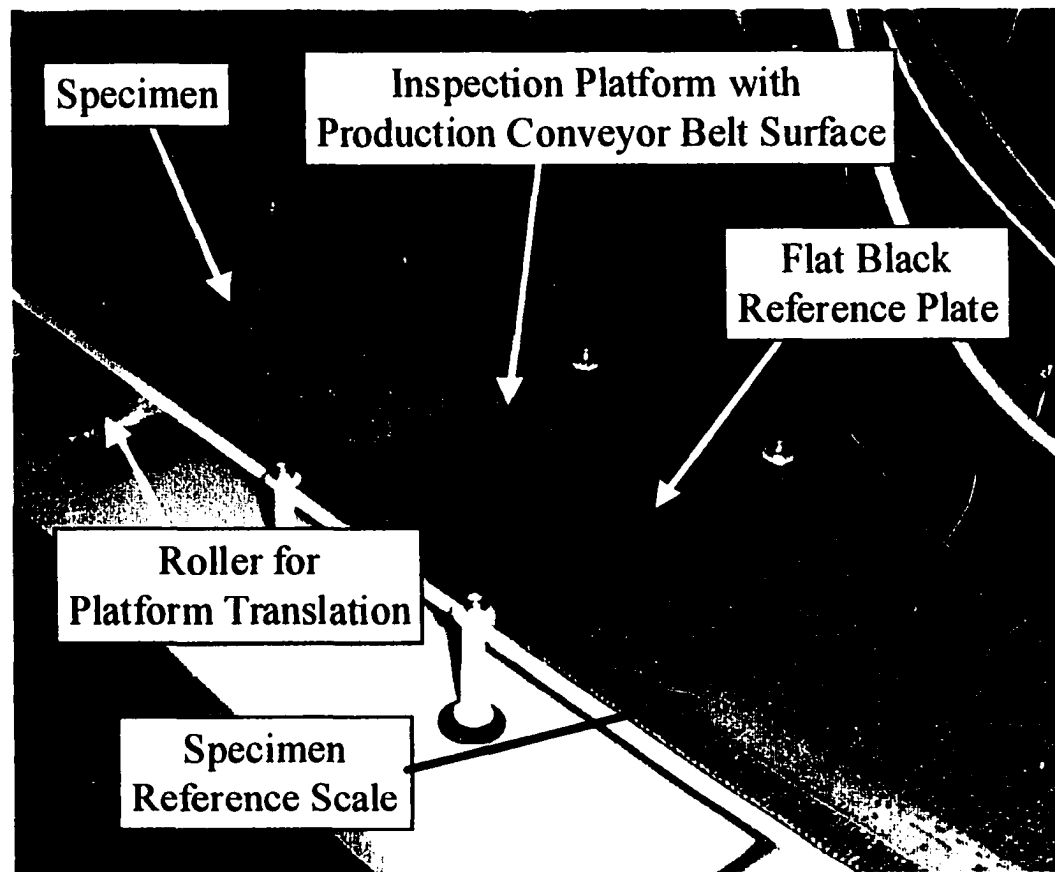


Figure 4-4: Inspection platform showing specimen orientation, reference plate, and scale.



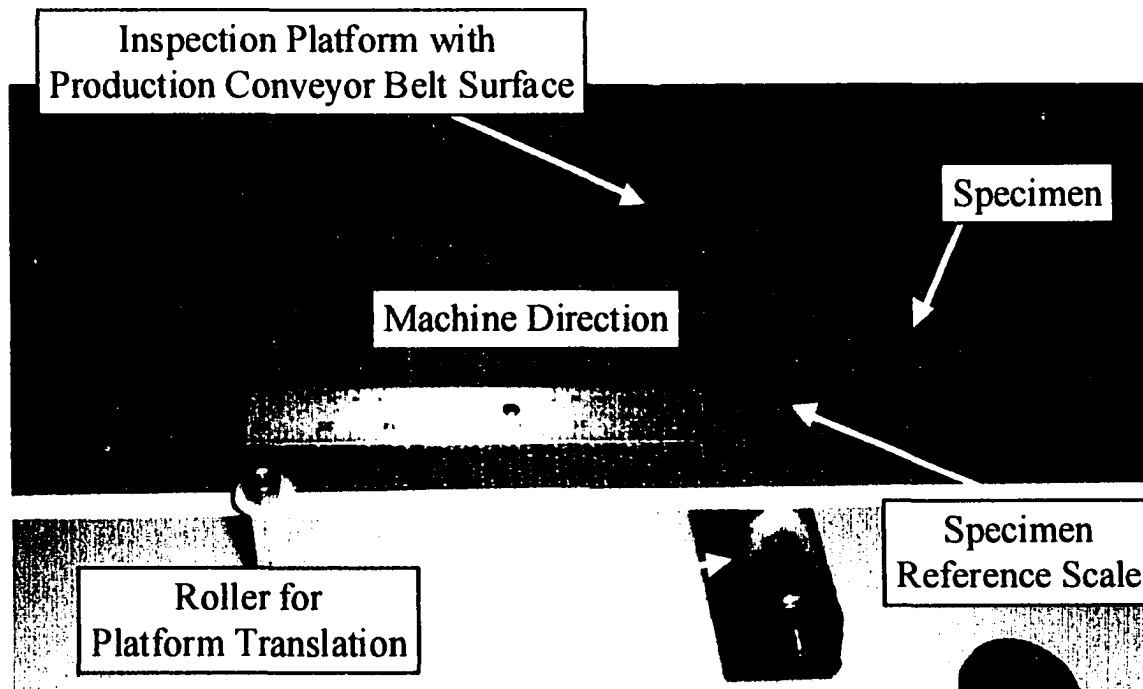


Figure 4-5: Close-up view of inspection platform.

inspection platform. The working surface of the platform was covered with the same belt material used for the compaction take-off conveyor in the factory. An aluminum reference scale with engraved black markings was attached to the top of the platform. This served two purposes. First it provided a straight edge and origin to locate the sheet samples. Secondly it provided an absolute reference from the end of the sheet which was imaged during the acquisition of thermal data. The high emissivity of the markings on the aluminum background provided sufficient contrast to read the scale in the thermal image. This scale was critical in developing a spatial correlation between the thermal features of the green sheet and the flaws which evolved during processing. The platform was mounted on a set of rollers which allowed for translation of the sheet in the field of view. A flat black reference plate was provided to check the response of the camera-lamp system.

The camera, Raytheon's Radiance IIS infrared camera, contains a 256 x 256 InSb focal plane array. A 25 mm lens was used in combination with a camera to sample distance which provided a field of view approximately 4" x 4". This arrangement was chosen to allow for the full width of the specimen to be imaged at one time. InSb detector technology was chosen for two several reasons. First, it has a high quantum efficiency (>85%). In comparison the more popular and less expensive PtSi focal plane array cameras have a quantum efficiency of less than 10%. In addition the readout electronics of the InSb camera provides "snap shot" data acquisition. This capability allows all 65,536 CCD detectors to be integrated over the same time period. The combination of high efficiency, parallel detector integration, and 12-bit digital output provides for high spatial resolution of fast thermal events. An integration time of  $5 \mu s$  and a frame rate of 60 Hz was used for the

inspections. The system exhibited variation due to flash timing and detector drift. The flash was synchronized to the camera clock and occurred on the next clock cycle after the trigger. The uncertainty was found to be less than one frame (e.g.  $< 17$  ms). The combined effect is illustrated in figure 4-6. The plot shows the distribution of the detector signals for 5 flash inspections over a period of 6 hours. The specimen remained the same and the instrument settings were held constant over the six hour period. This data demonstrated the need to frequently calibrate the camera. Detector variation can be accounted for by having a reference sample in the field of view during inspection.

Figure 4-7 provides a flow chart of the inspection procedure. Prior to inspection the alignment of the system (lamps, platform, and camera) would be verified. The symmetry of the heat flux was characterized using the flat black reference plate shown in figure 4-4. The camera was calibrated using two internal references set at room temperatures and  $50^{\circ}$  C. The resulting two point calibration look-up table spanned the heating range of the samples. Polycarbonate shields were used to minimize heating after the initial flash. A sequence of post-flash thermal images were obtained for each position or frame along the sheet. With a typical sheet length of 86.1 cm eight full frames and a ninth partial frame were required to image the complete part. An overlap of about 1.5 cm on each end of every frame was used to assure coverage of the whole sheet. This also provided for redundant data for regions of the sheet at both the left and right edge of the flux field. Artifacts due to asymmetry in the excitation could be detected by comparing the data obtained at the two edges.

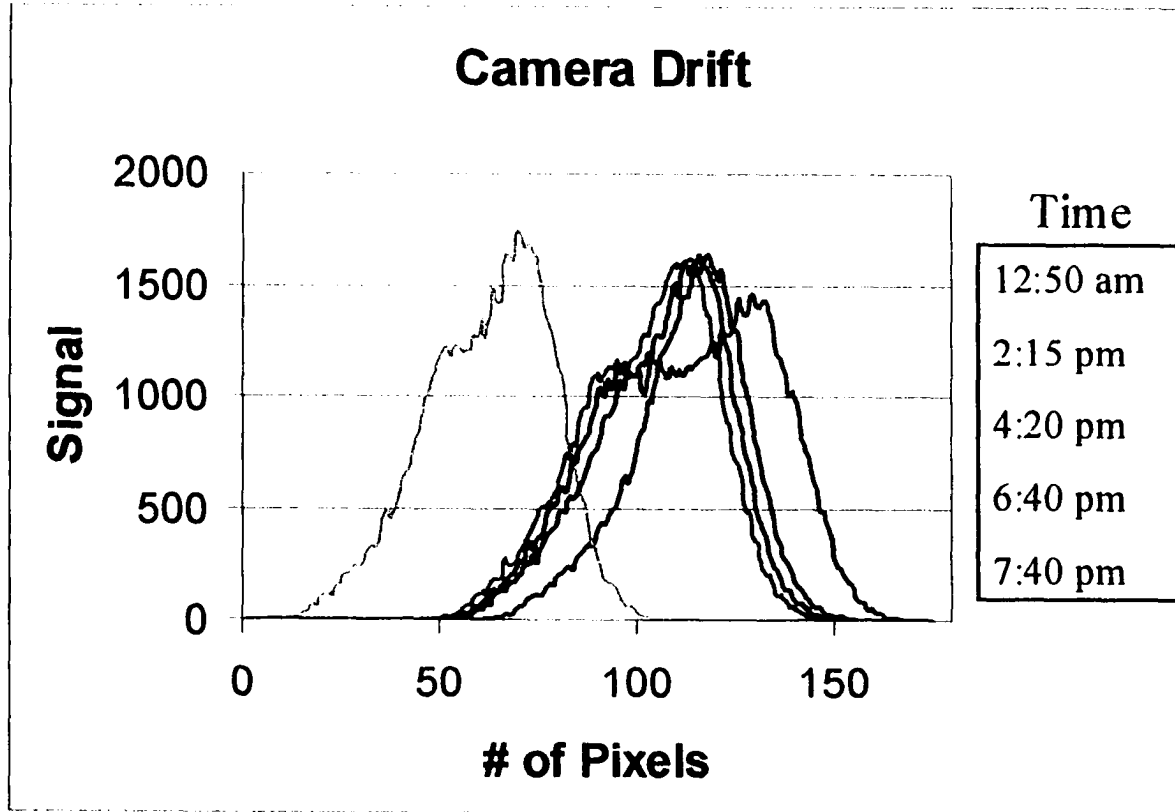


Figure 4-6: Variation of pixel distribution from a single green sheet sample. Variation is due to camera drift and flash timing. Data was obtained at five different times over a period of six hours.

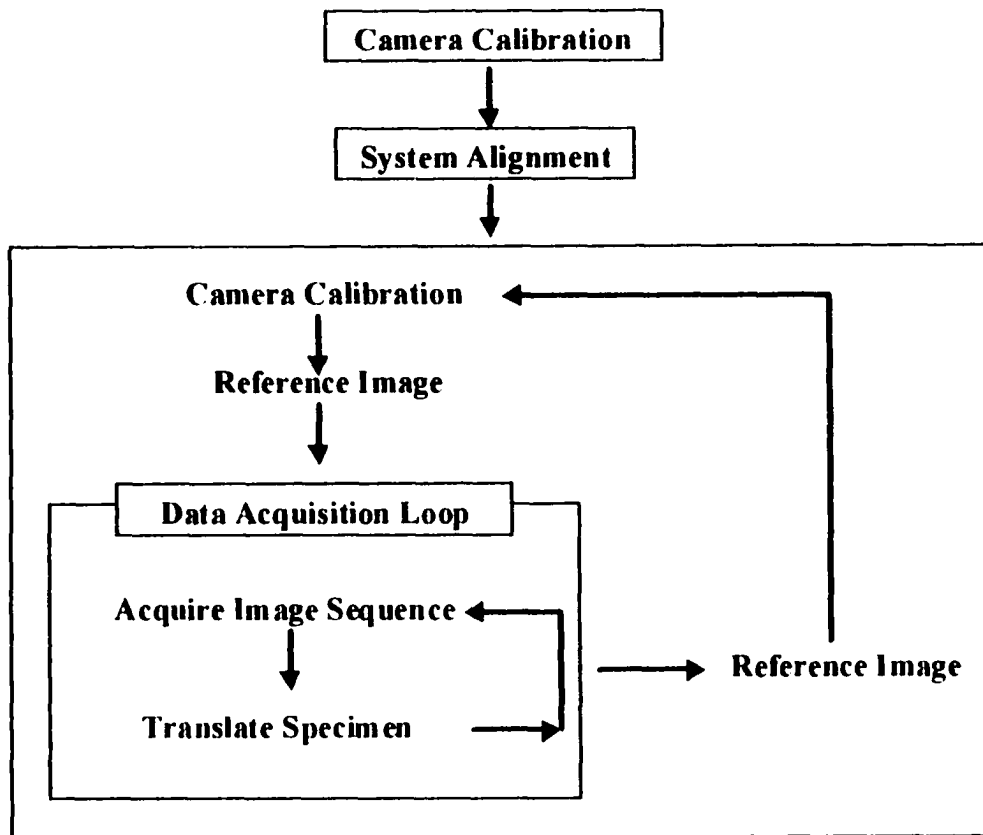


Figure 4-7: Data acquisition flow chart.

## 4.2 Reference samples

Prior to the current investigation, little information on the properties of the green sheet was available. Reference composites were fabricated by controlling for compact composition and fabrication pressure. This provided for a fundamental understanding of the dependence of composite thermal properties on key process variables and allowed for model calibration. Qualitatively, it was known that high binder levels resulted in low green density and subsequently porosity in the final FeAl sheet. In extreme cases, preliminary sintering, during binder elimination, could not be achieved and the compact disintegrated in the furnace. At the low binder content extreme, the green material lacked the strength to be handled, making further processing impossible. For the most part, the green sheet “database” on which the process had been developed consisted of the collective experiences and intuition of a few production experts. Thus, quantitative relationships between green sheet properties and the mechanisms of flaw development in final sheet had not been established. The systematic development of appropriate reference standards was required to provide for this fundamental understanding.

The characterization and understanding of this filler-binder distribution is an important step in the design of any powder metallurgy manufacturing technique [1] [49]. In the present case the primary design objective was to optimize green sheet strength while minimizing binder content since excessive binder contributes carbon which can have an adverse effect on the final microstructure of the fully dense FeAl. As will be demonstrated, the relationship between binder concentration and filler particle separation is dominated by two effects. At low binder concentrations the addition of binder lubricates the composite

by reducing the friction between the filler particles. Thus, for a given compaction pressure, the alloy particle separation decreases with binder addition and the volume fraction of FeAl increases. As the binder level increases the effect of dilution dominates and the FeAl volume fraction decreases. This effect is manifested in the bulk density, strength, and thermal transport properties of the compact. The data provided herein represent the first systematic characterization of the FeAl-binder system. Prior to this work the optimum binder loading, 2.8 wt.%, had been determined by trial and error using large batch production runs. The current approach compacting small batches of test blends, is much less expensive and provides convenient performance relationships.

The reference samples provided significant insight into the properties of the compaction material. Several aspects of the samples and their characterization are presented. The sample population was based on a matrix of blends and compaction pressures designed around standard production parameters. Details of composition will be described followed by a description of the bulk mechanical properties: density, strength, and volume fraction of FeAl. A preliminary investigation into the thermal properties involved the "nominal production reference" and two extremes in formulation, 100% binder powder and 100% FeAl powder. The details of the thermal behavior were explored using a range of compaction conditions and formulations. Through and same side flash excitation modes were used to determine the thermal diffusivity and effusivity of the specimens. These data were then used to calibrate the green sheet heat transfer model. A description of the model, which accounts for composition and green sheet thickness, follows.

### 4.2.1 Specimen fabrication

A primary objective of fabricating FeAl green references was to produce specimens that spanned the variations observed in the roll compaction process. The thermal and mechanical properties of these samples were then characterized as the parameters of the fabrication process were systematically varied. Ideally standards would be fabricated using the production process. For example, batches of known combinations of binder and alloy powder would be mixed and formed into green sheet. Preliminary attempts at this approach confirmed that the production process lacked the capability necessary to provide such samples. The fabrication technique used is based on the Metal Powder Industry Federation (MPIF) standard method for the assessment of green compact strength [49]. The MPIF test proscribes a weight of metal powder to be loaded into a die and compacted, using a uni-axial press. No binders or lubricants are added to the metal powder in this standard method. The result is a compacted green bar, measuring 3.20 cm by 1.25 cm by  $T$  cm. The thickness ( $T$ ) varies with the powder properties. The strength of the bar is measured using a three-point break test. This test provides for alloy powder quality screening since the strength is indicative of the particle size distribution, particle shape, and hardness. In the preliminary investigations two types of samples were made with blends of FeAl and binder powders. The first were "thin" samples with thicknesses on the order of the production sheet specification (0.069 cm). The second were "thick" specimens, which were on the order of ten times that of the production sheet (0.640 cm). The later provided a green fracture strength and served as an effective thermal half-space, relative to the production thickness.



Reference Blend	Master Blend (g)	FeAl (g)	Binder (g)	% Binder	% FeAl
S1	0.00	200.00	0.00	0.00	100.00
S2	200.00	475.00	0.00	0.84	99.16
S3	200.00	204.00	0.00	1.40	98.60
S4	200.00	69.00	0.00	2.10	97.90
S5	200.00	0.00	0.00	2.82	97.17
S6	200.00	0.00	5.30	5.33	94.66
S7	200.00	0.00	16.75	10.33	89.66
S8	200.00	0.00	44.00	20.34	79.65

Table 4.1: Reference blends

#### 4.2.2 Characterization

The study involved two sets of references provided by the production facility. Blends were produced by taking 200 g portions of the standard production blend of binder and alloy and diluting them with either binder or alloy powder. The reference blend codes and percentage weights are listed above in table 4.1. These mixtures were used to determine the compaction force at which the master blend yielded the roll compaction specification of thickness and density ( $686 \mu\text{m} \times 3.47 \text{ g/cc}$ ). From this it was determined that a 925 mg blend loading would be needed for the die. These samples were based on the blends described in table 4.1. The effect of compaction pressure was explored using the production blend (S5). This blend was widely available from the production stock whereas the non-standard blends were available only in limited quantities. The resulting matrix consisted of the 13 samples described in table 4.2. The volume fraction of alloy was calculated from the ratio of the bulk density of the specimen, the density of FeAl, and the ratio of alloy to binder in the blend.

## FeAl Volume Fraction (%)

Reference Blend	Binder (% wt.)	Press Setting Tons				
		9.7	11.9	13.9*	18.9	23.9
<b>S1</b>	0			53.8		
<b>S2</b>	0.8			54.6		
<b>S3</b>	1.4			55.1		
<b>S4</b>	2.1			55.7		
<b>S5*</b>	<b>2.8*</b>	49.7	53.2	<b>55.3*</b>	59.1	63.6
<b>S6</b>	5.3			53.7		
<b>S7</b>	10.3			48.7		
<b>S8</b>	20.3			38.1		

\* Standard production conditions

Table 1.2: Volume fraction of various reference samples

Figure 4-8 shows the dependence of bulk density on compaction force and binder content. The lubrication effect dominates at low binder levels and the density actually increases. Since the binder density is about 1 g/cc and the FeAl density is about 6.1 g/cc, the density begins to decrease at binder levels above about 2.0 % by weight. An increase in compaction pressure shifts the curve to higher densities. The details of this behavior will be different for each binder-alloy compact system, but the general shape of the curves and trends are common for production materials[1]. It was determined that 13.9 tons of compaction force yielded the target density at the nominal binder to alloy ratio. Figure 4-9 shows the dependence of the green compact strength as a function of binder content for this compact. The error bars indicate the range of three tested samples. This curve is consistent with the same phenomena illustrated in the density curves. As the pure alloy compact is lubricated with minor additions of binder the strength is reduced. The internal friction in the bar supports a lower and lower stresses before yielding. The minimum strength occurs around a few weight percent binder. The strength of the compact approaches that of the binder for large binder volume fractions.

The same mechanisms, lubrication and dilution, responsible for the bulk density and strength behavior are reflected in the change in volume fraction with compaction force and FeAl loading. Figure 4-10 illustrates the peak in the volume fraction which occurs at 97.2 wt. % FeAl loading. For the nominal production ratio of alloy to binder the volume fraction of FeAl increases monotonically as the compaction force is increased (see figure 4-11). The increase in FeAl volume fraction results from the elimination of compact voids with higher pressure application. The FeAl volume fraction approaches a maximum

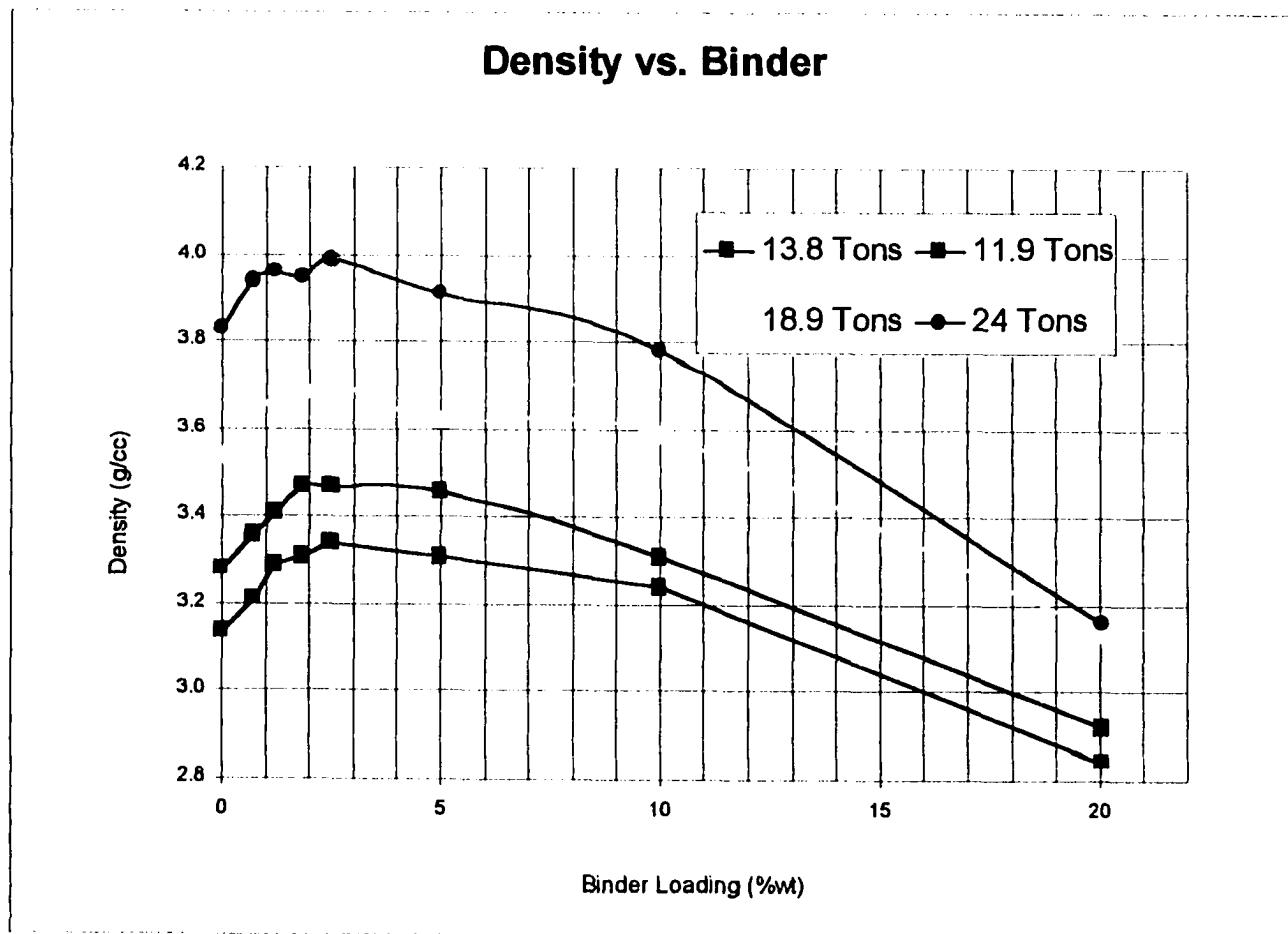


Figure 4-8: Variation of bulk density as it depends on compaction force and binder loading.

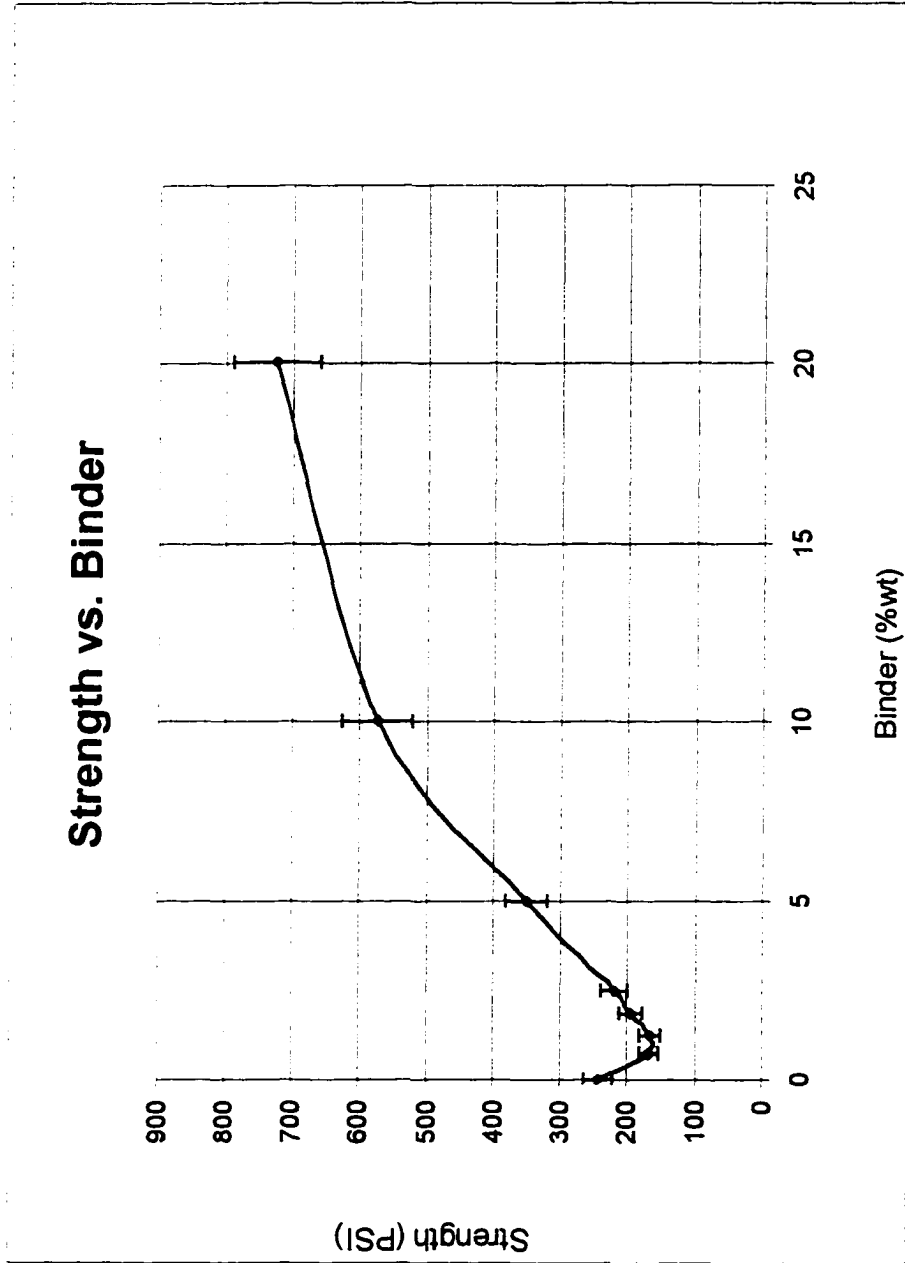


Figure 4-9: Compact strength as a function of binder loading.

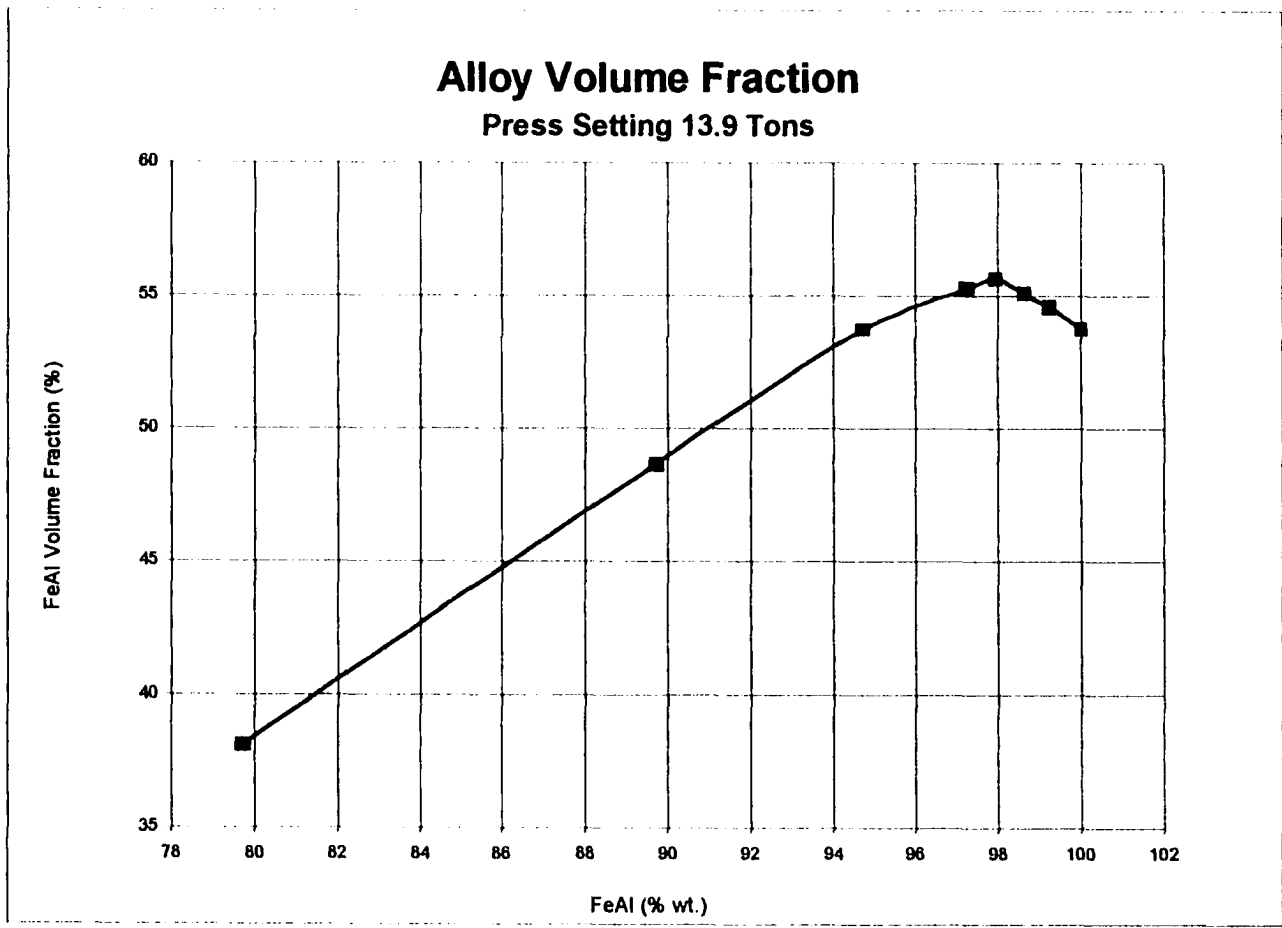


Figure 4-10: Alloy volume fraction as a function of percent FeAl powder. Data are for a nominal compaction force of 13.9 tons.

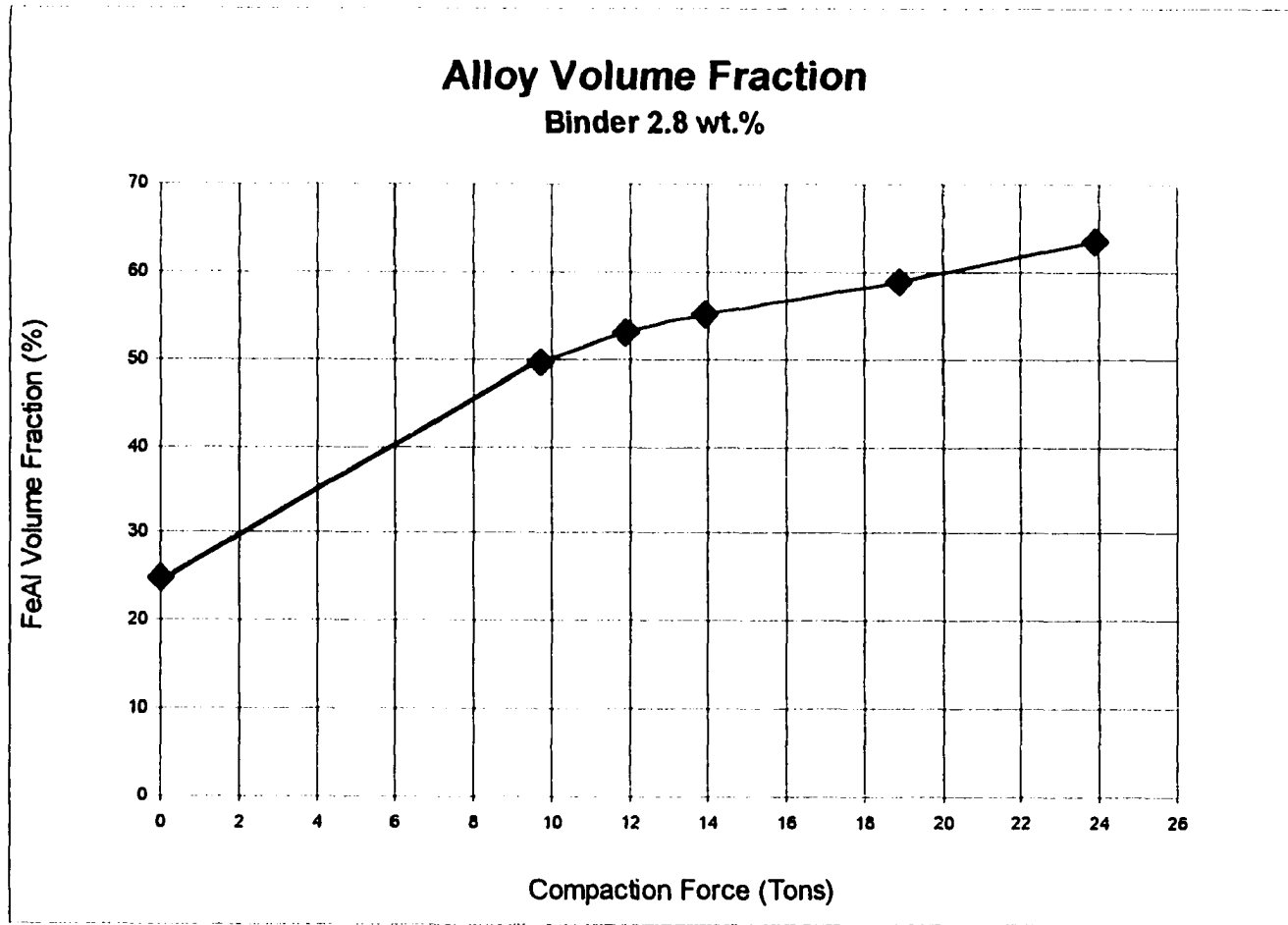


Figure 4-11: Alloy volume fraction as a function of compaction force. Data are for a nominal FeAl powder loading of 97.2 % by weight.

associated with the approach of zero void volume. The compaction force associated with this asymptote was not explored since it was found to be over twice that of the normal processing levels.

Thermal data were collected for reference panels constructed by arranging groups of specimens. Figure 4-12 is a thermal image illustrating a typical panel layout. A thermal time sequence was captured for various reference samples and the signal analyzed. At each point in time a spatial average for every part was determined. The mean signal was obtained within a rectangle covering approximately 75% of the 4 cm<sup>2</sup> specimen area. The initial thermal investigation was based on three compositions: 100 % wt. binder, 97.2 wt.% FeAl (the production level) and 100 wt.% FeAl. Figure 4-13 shows duplicate curves of flash responses for these samples. The thermal data were normalized by dividing subsequent image data with a reference image obtained just after the pulse. Recalling that the analytical solution for the normalized temperature transient can be obtained from normalizing equation 2.16, which is

$$T(t) = \frac{2F\epsilon}{(\sqrt{\rho\kappa C_p}\sqrt{\pi})} \left[ (\sqrt{t} - \sqrt{t-\tau}) - 2\sqrt{t} \sum_{n=1}^{\infty} (1)^n F(t) - 2\sqrt{t-\tau} \sum_{n=1}^{\infty} (1)^n F(t-\tau) \right] \quad (4.1)$$

With  $F(t)$  defined by:

$$F(t) = \exp\left(\frac{-n^2 L^2}{\alpha t}\right) - \sqrt{\frac{n^2 L^2}{\alpha t}} \operatorname{Erfc}\left(\frac{n^2 L^2}{\alpha t}\right) \quad (4.2)$$

Where  $F\epsilon = Q$  is the radiant energy per unit area absorbed by the surface and  $\tau$  is the pulse duration. Thus  $T_N(t)$  is defined by

$$T_N(t) = \frac{T(t)}{T(\Gamma)} \quad (4.3)$$



**Area of interest (AOI)  
used to obtain  
spatial average**

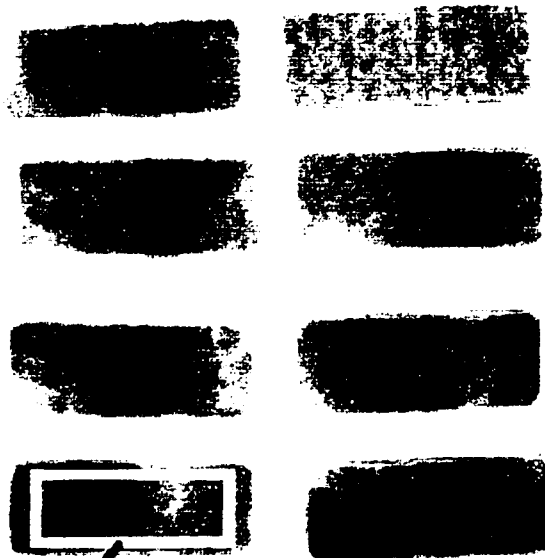


**Figure 4-12: Thermal image of green compact reference panel.**

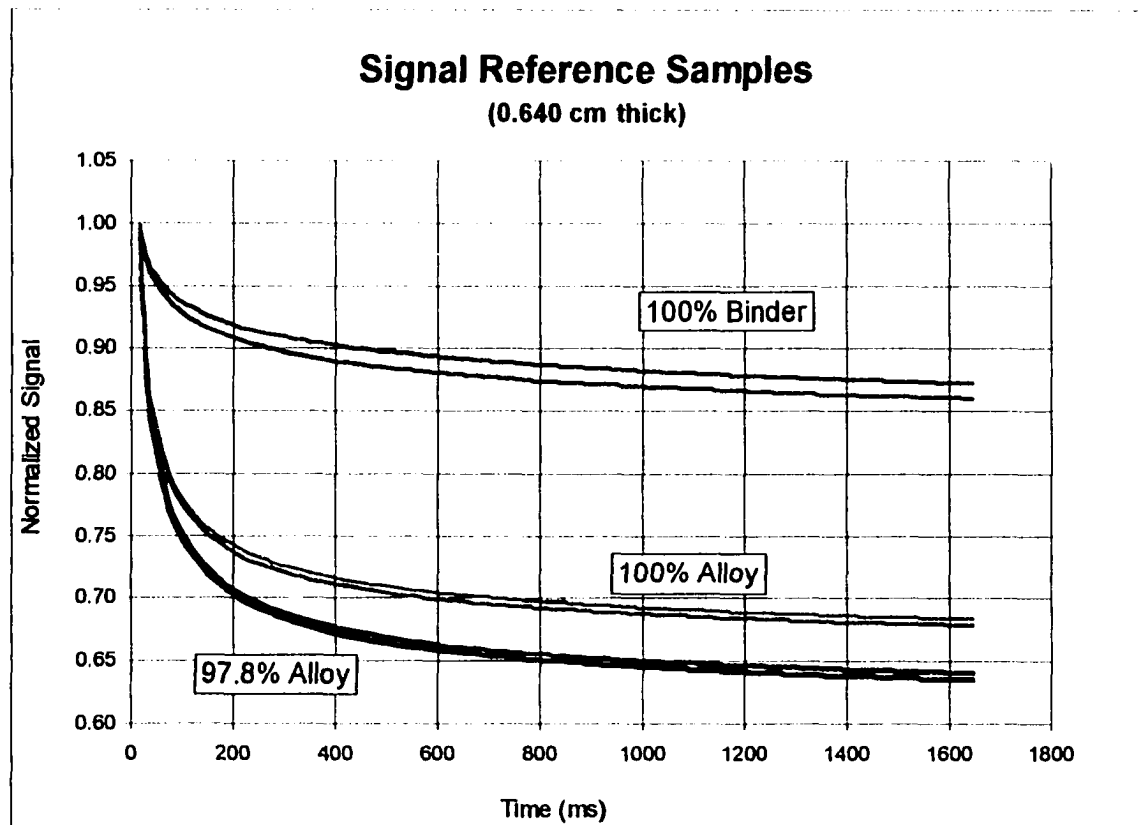


Figure 4-13: Variation of thermal decay curve as a function of extremes in weight percent binder.

Where  $\Gamma$  is the time at which the reference thermal data is obtained. Thus the normalized cooling curve is clearly independent of the effusivity and differences in cooling rate are indicative of the relative value of  $\frac{L^2}{\alpha t}$ . Since the samples were nominally the same thickness 0.640 cm., the differences in the relative cooling curves are indicative of the relative diffusivity of the compacts. As expected the 100% binder sample exhibited the slowest decay rate associated with a relatively low diffusivity. The 100% alloy powder has the next lowest diffusivity. However, a slight addition of binder to the alloy compact increased the diffusivity. This reflects the effect of binder on the reduction of FeAl volume fraction and thus the mean alloy particle distance while enhancing the particle connectivity.

### 4.2.3 Assessment of heat transfer properties

Reference panels were assembled by arranging groups of reference samples on a substrate. Figure 4-11 shows a thermal image for the series of references fabricated with nominal compaction pressure and variations in binder addition. This image was obtained at 50ms after a front flash excitation. Figure 4-15 illustrates the normalized cooling curves for the series of thin samples representing variations in binder level. The cooling curves shift to lower values as the binder level is decreased from the highest level of 20.3 % by weight. This is consistent with the results for thick specimens. The dependence of diffusivity on binder level is non-trivial due to the lubrication and dilution effects on alloy particle percolation paths. Below the 2.8% binder level the signal differences are in the noise level. Figure 4-16 shows a thermal image, 50ms after the excitation, for the series of references with the nominal binder addition and variations in compaction pressure. Figure 4-17 illustrates the effect of pressure on the thermal decay. For the nominal binder concentrations, increasing

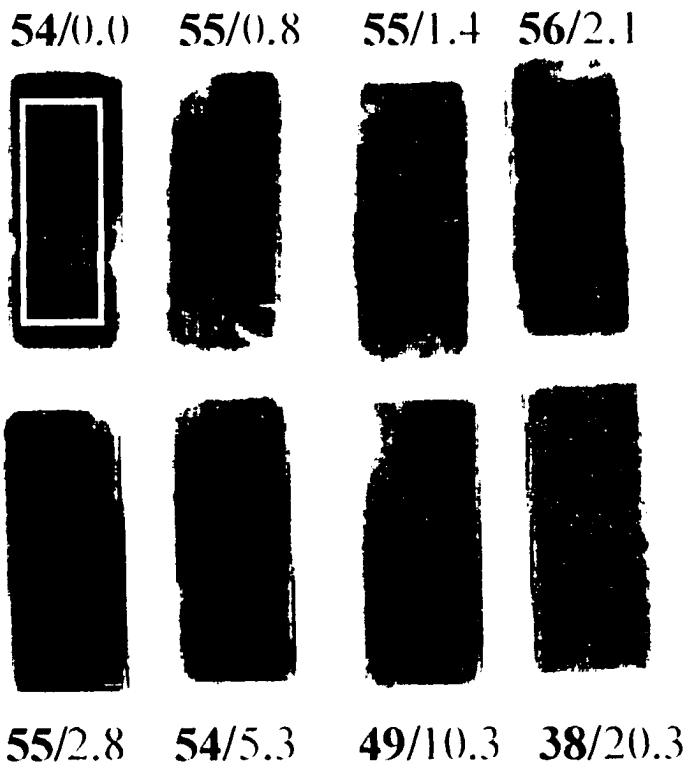


Figure 4-14: Thermal test panel with variations in binder concentration. Composition is indicated as percent volume fraction alloy, top number, and percent weight binder, bottom number. The thermal image was obtained 50 ms after the heating pulse.

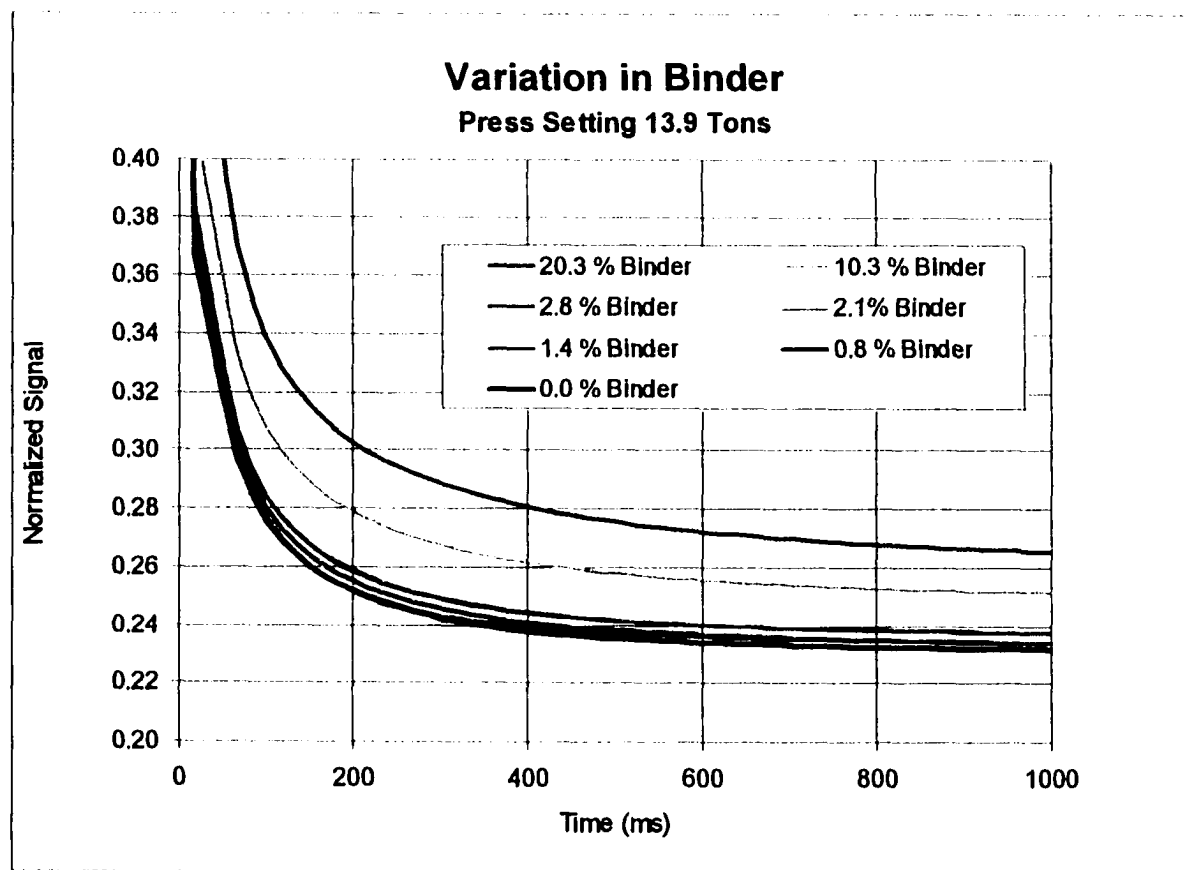


Figure 4-15: Thermal decay curves for various values of binder concentration. In general, the higher levels of binder result in increased bulk diffusivity and a decrease in the decay time.



Figure 4-16: Thermal test panel with variations in compaction level. Compaction force is indicated in tons. The thermal image was obtained 50 ms after the heating pulse.

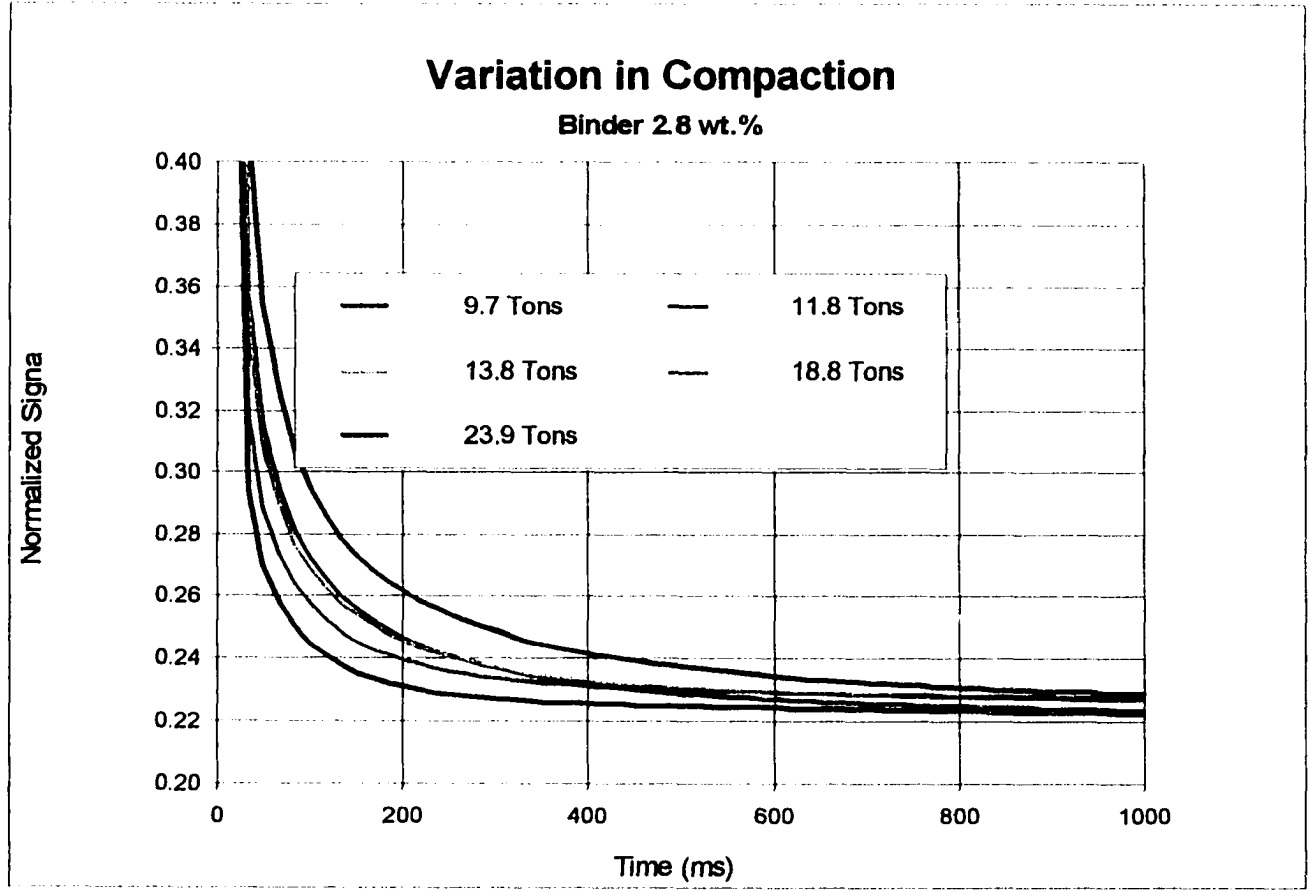


Figure 4-17: Thermal decay curves for various compaction forces. The higher pressures result in an increased bulk diffusivity and a decrease in the decay time.

the pressure increases the alloy volume fraction and increases the thermal diffusivity.

The quantitative comparison of the thermal behavior of reference samples takes advantage of fundamental heat transfer relationships described in Chapter 2. For convenience the relevant definitions are restated here. The thermal diffusivity,  $\alpha$ , and thermal effusivity,  $e$ , are defined in terms of the bulk material properties of density,  $\rho$ , specific heat,  $C_p$ , and thermal conductivity,  $\kappa$ , as follows.

$$\alpha = \frac{\kappa}{\rho C_p} \quad (4.4)$$

$$e = \sqrt{\rho C_p \kappa} \quad (4.5)$$

The thermal diffusion length,  $\delta$ , describes the distance to which the thermal field has diffused into the bulk material at a time,  $t$ , after the excitation.

$$\delta = \sqrt{\alpha t} \quad (4.6)$$

It was determined in the preliminary investigations that these times were on the order of a few hundred milli-seconds. For times shorter than this the thermal diffusion length is small relative to the geometrical thickness,  $L$ . This condition is described by

$$\frac{\alpha t}{L^2} \ll 1 \quad (4.7)$$

In the case of through heating the thermal diffusivity can be determined from the normalized heating profile at the back surface of the sample [14], where  $t_{1/2}$  is the time to half the normalized peak temperature.

$$t_{1/2} = \frac{(1.38)L^2}{\pi^2 \alpha} \quad (4.8)$$



A relevant thermal parameter for same side flash thermography is the thermal effusivity,  $e$ . For large values of  $\frac{L^2}{\alpha t}$ , after the end of the excitation pulse, the effusivity can be described by the decay in temperature governed by

$$e = \frac{F\epsilon\tau}{T(t)\sqrt{\pi t}} \quad (4.9)$$

Where  $F\epsilon\tau$  is the energy absorbed per unit area by the surface during the pulse,  $t$  is the time referenced from the end of the pulse. Effusivity is given by the slope of  $T(t)$  vs.  $\frac{1}{\sqrt{t}}$  is the absolute change in the temperature as measured from the peak temperature.

The difficulty in measuring absolute effusivity and diffusivity lies in the precision with which the reference time can be established. It is obvious from equation 4.9 that the error in effusivity is strongly dependent on the accuracy with which one can determine the reference time from the end of the flash. This is of particular concern at small times (i.e. when the error in knowing  $t = 0$  is a significant fraction of the absolute time). For the conditions under which the current data was obtained the reference time was known within one frame ( $\approx 60$  Hz) or about 17 ms. With signal decay rates of 70% during the first 50 ms, an uncertainty in the reference time of 17 ms yields a 23% error in the signal level. For this reason the normalized temperature  $T_N(t)$  was obtained by dividing subsequent signals by the peak signal obtained just after the end of the pulse. The thermal diffusivity determination was conducted using the through-flash technique. The accuracy of measuring the thickness of the samples is known and the relative error in the time measurement was small. As will be shown in the next section, the results obtained for the diffusivity are consistent with the observed front surface temperature decay.

Reference Blend	Binder (% wt.)	Press Setting Tons				
		9.7	11.9	13.9*	18.9	23.9
<b>S1</b>	0			0.95		
<b>S2</b>	0.8			0.90		
<b>S3</b>	1.4			0.89		
<b>S4</b>	2.1			0.89		
<b>S5*</b>	<b>2.8*</b>	1.00	0.96	<b>0.92</b>	0.92	0.86
<b>S6</b>	5.3			0.83		
<b>S7</b>	10.3			0.83		
<b>S8</b>	20.3			0.76		
<b>* Standard production conditions</b>						

Table 4.3: Relative cooling rates of reference samples during the first 168 ms after the end of the heating pulse.

The relative cooling rates were explored as an indicator of binder loading and compaction force. The use of a few selected frames, from the decay sequence, as a measure of quality can significantly reduce the time required for computations during the inspection. An average cooling rate was determined from the thermal data obtained at 168 ms after the end of the flash (i.e. the relative temperature, at 168 ms, obtained from the curves depicted in figures 4-15 and 4-17). This time was used since the relative temporal error, 17 ms, was small yet the signal-to-noise was still good. Figures 4-18 and 4-19 illustrate the dependence of cooling on the sample composition and compaction level. Table 4.3 provides the same data. Specimen thickness data is illustrated in figures 4-20 and 4-21. The change in thickness is directly related to the change in bulk density previously described.

Figures 4-22 and 4-23 depict the normalized heating curves associated with the temperature rise on the back side of the specimens used in the through heating experiments.

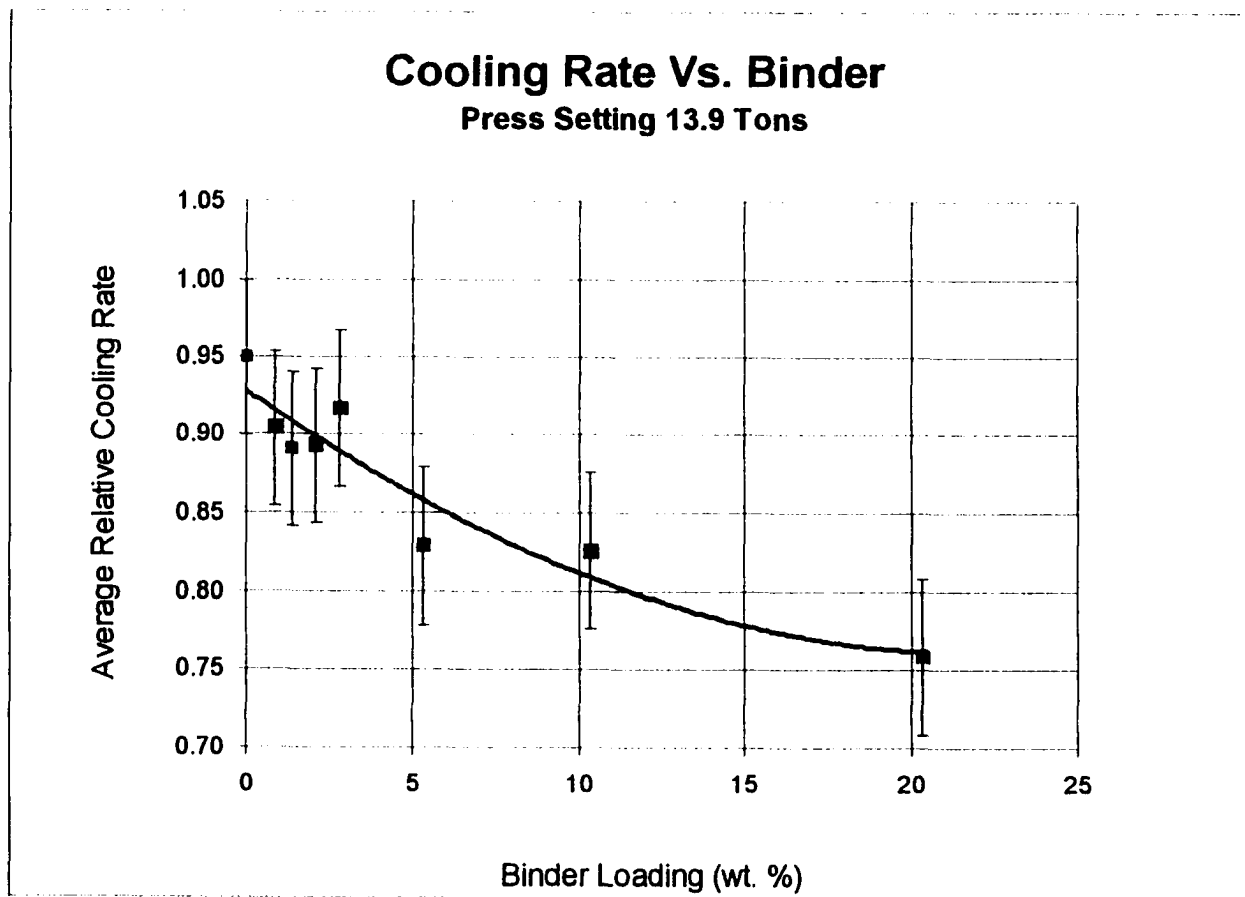


Figure 4-18: Relative cooling rate of reference samples during the first 168 ms after the flash. The higher binder concentrations result in a decreased front surface cooling.

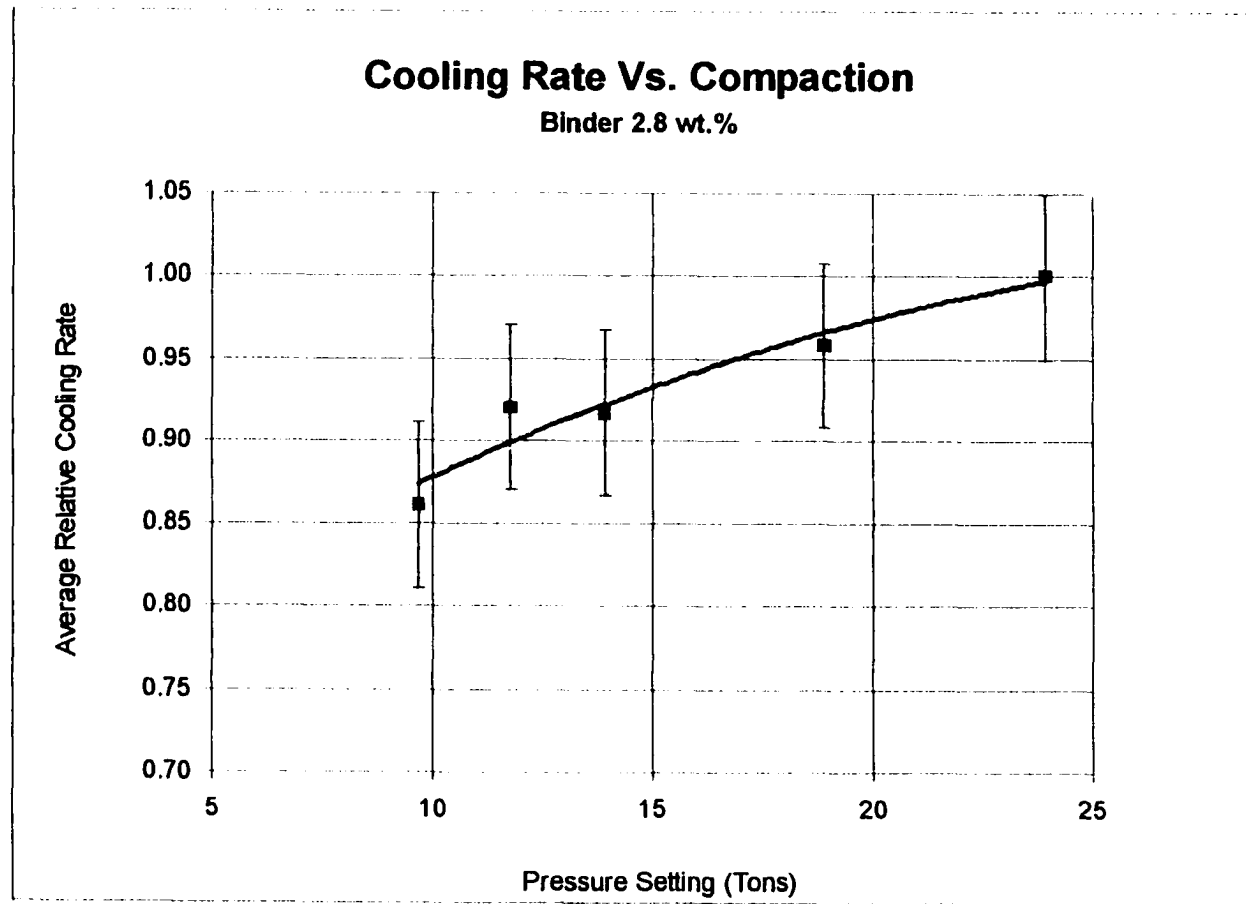


Figure 4-19: Relative cooling rate of reference samples during the first 168 ms after the flash. The higher compaction levels result in an increase in front surface cooling.

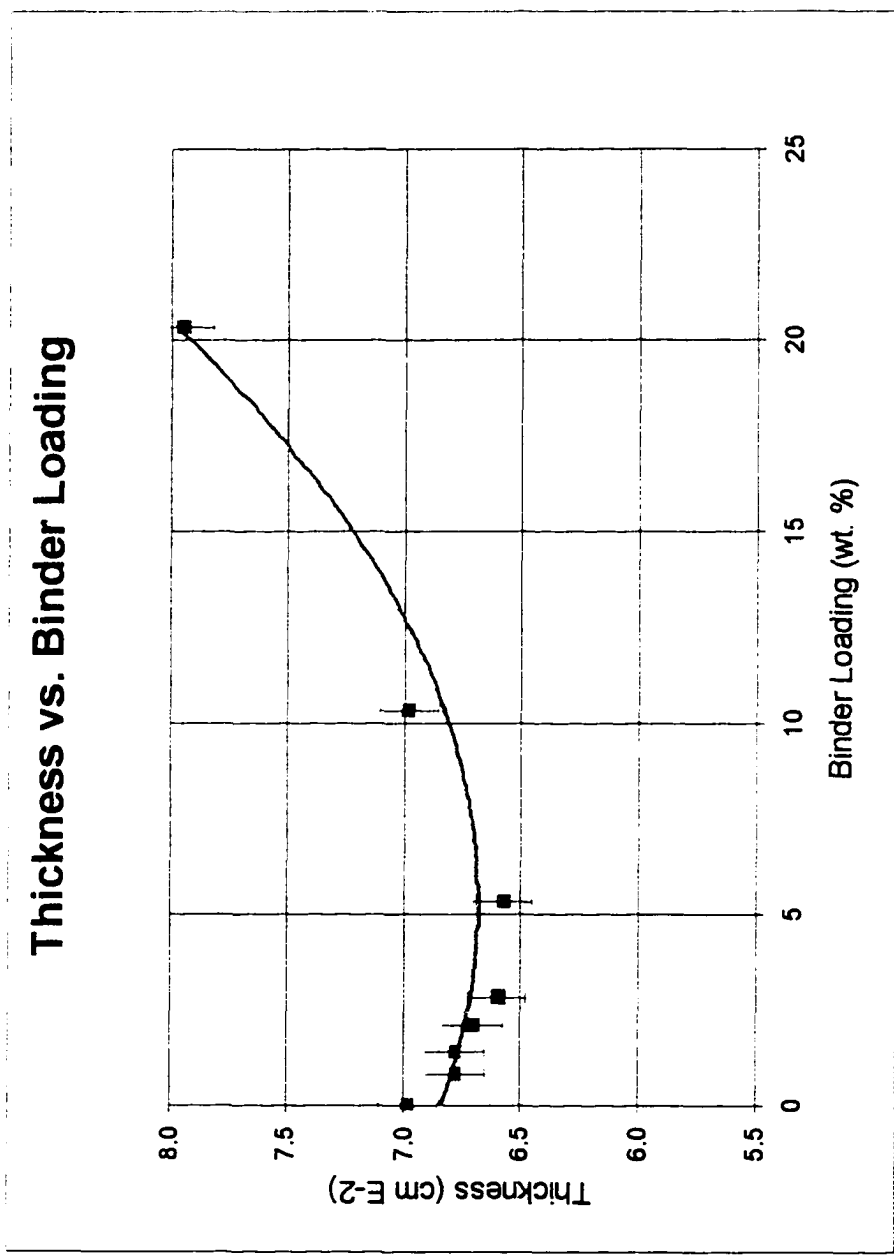


Figure 4-20: Variation in thickness as a function of binder loading.

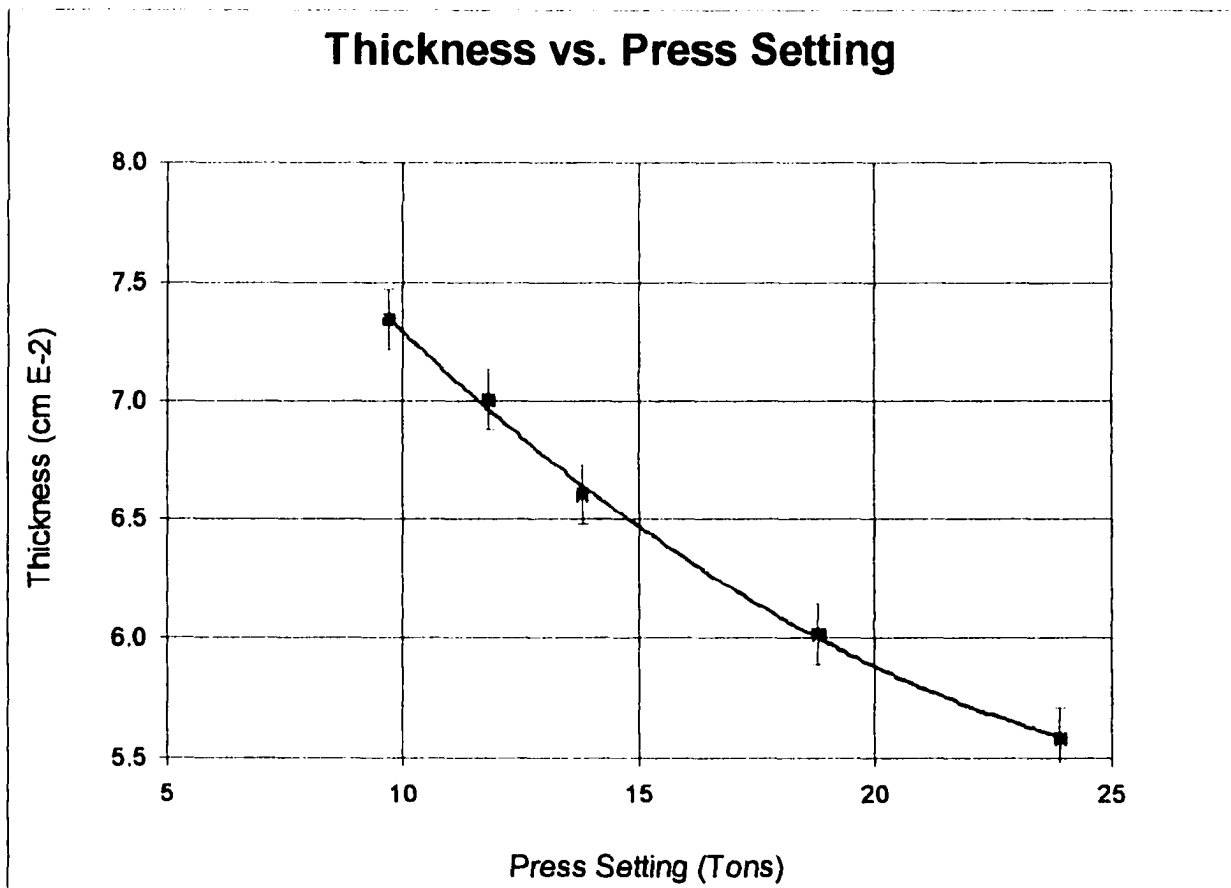


Figure 4-21: Variation in thickness as a function of binder loading.

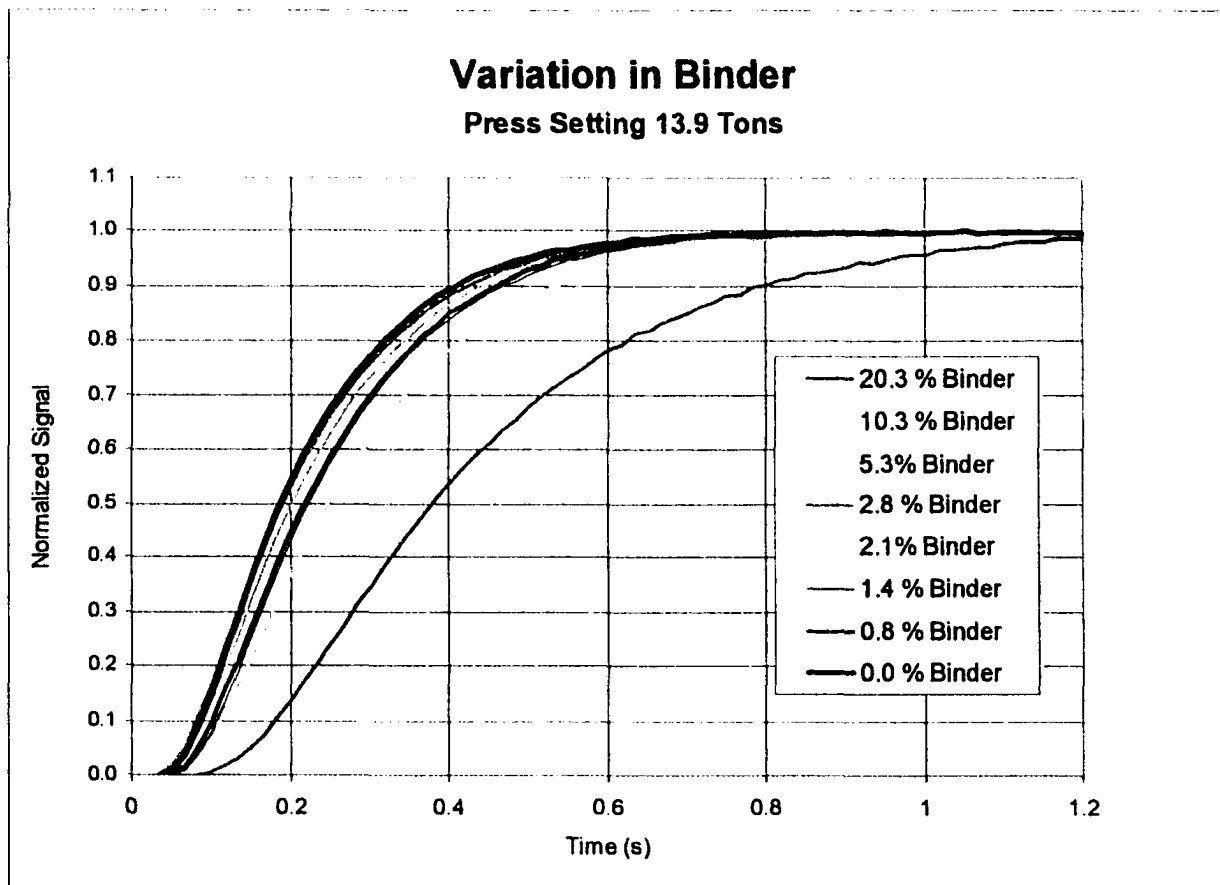


Figure 4-22: Normalized temperature rise for through-thickness heating as a function of binder loading.

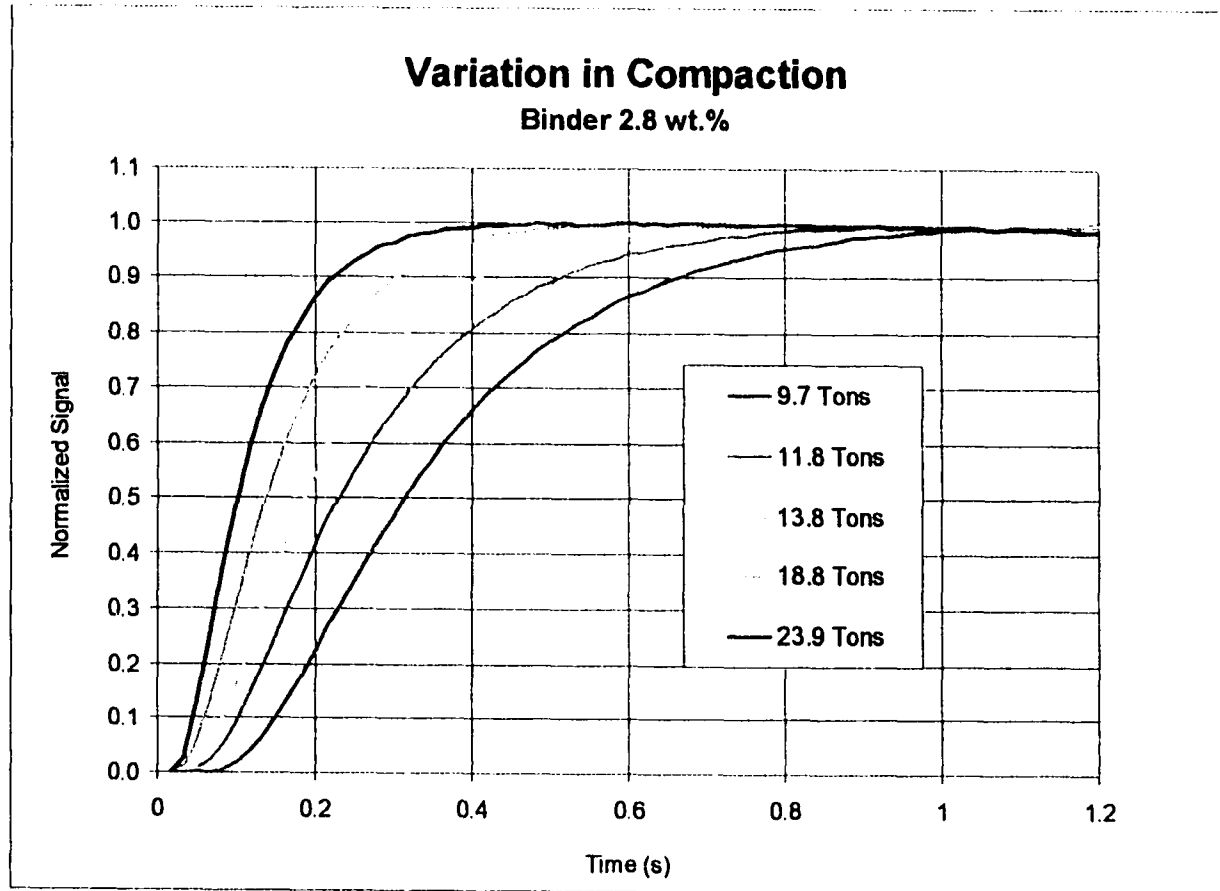


Figure 4-23: Normalized temperature rise for through-thickness heating as a function of compaction level.



At early times no significant temperature rise is detected. This is the "thermally thick" regime. Later in time the temperature increases in accordance with the bulk thermal diffusivity. The larger the diffusivity the higher the rate of temperature rise. At long times, within the validity of the adiabatic assumption, the peak temperature is reached. These thermal transients are consistent with those obtained for the same side flash inspection (see figures 4-15 and 4-17). Figure 4-22 illustrates the increase in back side heating as the level of binder is modified. The 20.3 wt. % binder sample exhibits the slowest response and below a few percent binder the curves are not significantly different. The effect of compaction, figure 4-22, is much more pronounced as it was for the same side excitation (see figure 4-17). Equation 4.8 was used to determine the diffusivity of each sample. The thickness measurements were found to have an uncertainty of  $\pm 0.0013$  cm. This contributed an uncertainty of 3.5% to the calculation of  $\alpha$ . The uncertainty in  $t_{1/2}$  was  $\pm 16.7$  ms resulting in an average uncertainty of 5.1%. Thus the uncertainty in the value derived from 4.8 was typically  $\pm 9\%$ . Figures 4-24 and 4-25 are plots of the variation of thermal diffusivity as a function of binder loading and compaction respectively.

To summarize, the heat transfer behavior of the compacted blends are consistent with the physical changes resulting from variations in compaction pressure and composition. Although the behavior is complicated by lubrication at small levels of binder, this regime is associated with high volume fractions of FeAl. It was anticipated, and eventually verified, that the alloy poor regions would be associated with porosity and its associated defects. In the next section a model will be developed which explains the observed heat transfer

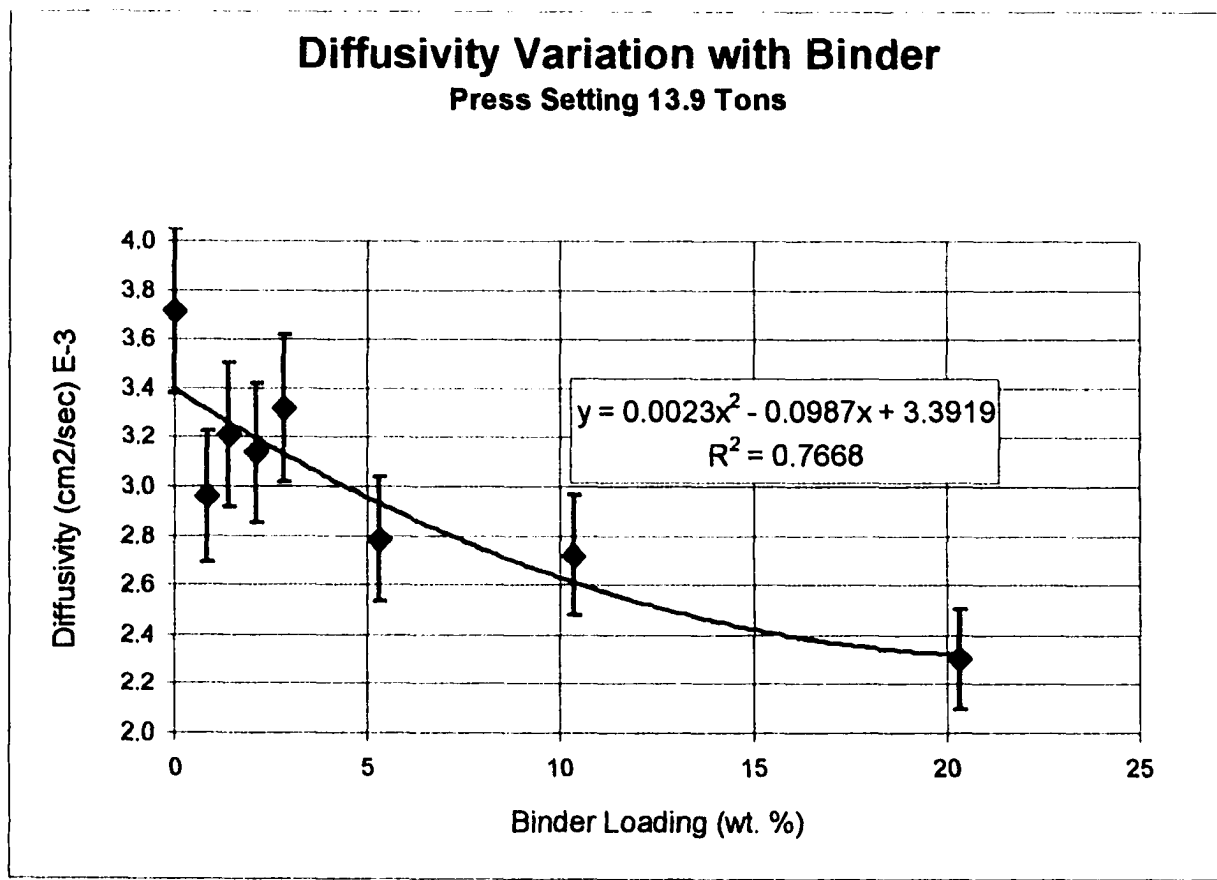


Figure 4-24: Variation in thermal diffusivity as a function of binder loading.

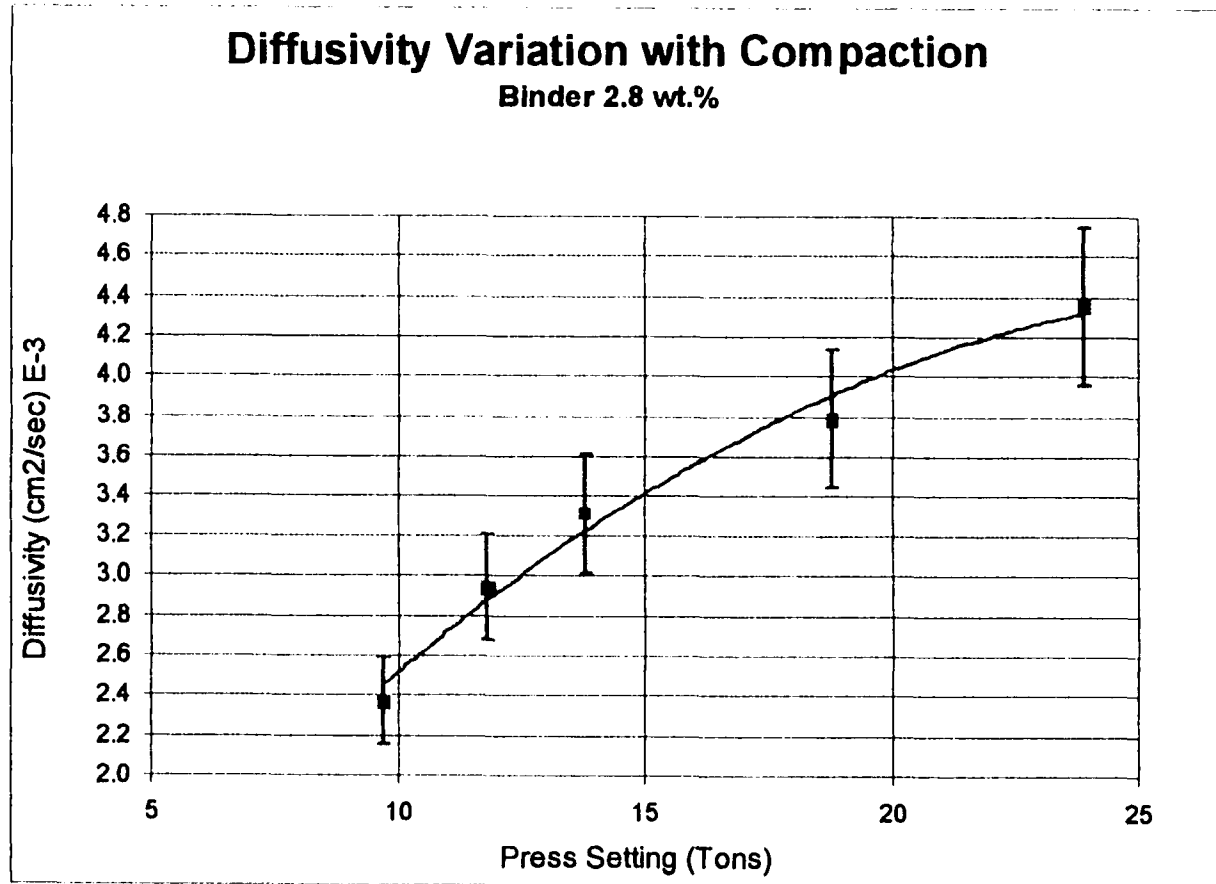


Figure 4-25: Variation of thermal diffusivity as a function of compaction level.

in terms of the properties of the blend constituents, the volume fraction of FeAl, and the structure of the compact.

### **4.3 Green sheet heat transfer model**

The development of a valid heat transfer model is important for several reasons. It provides a basis for exploring the sensitivity of the inspection technique to material designs outside the current manufacturing regime. Having this capability is particularly important in an environment where the inspection technology is being developed concurrently with the manufacturing process. For example if the production specification for the ratio of binder to alloy were to change during process development it would be necessary to validate the effectiveness of the current inspection method for the new composite. The amount of experimental work can be significantly reduced using results provided by the model. In the extreme case a completely different process may be used. Tape casting is being explored as a replacement for compaction. In the tape casting process the alloy powder is mixed with binding agents and significant quantities of solvent. The result is a slurry which is cast directly onto a conveyor belt. The slurry is dried into a green sheet yielding alloy volume fractions in the same range as those of the compaction process. A valid heat transfer model provides a basis for assessing the limits of a particular inspection method.

The model is designed to take advantage of the green sheet morphology and the geometry of the flaw precursors. The planar geometry of the green sheet and the demonstrated two dimensional nature of the flaw morphology makes the use of a rectangular coordinate system appropriate. The time dependent thermal response of the green sheet is described

by the solution for heat conduction in a slab with a pulsed excitation and insulating boundary conditions. This solution assumes bulk properties assigned to the slab. As has been described in the section on heat conduction in solids, the important thermal parameters are the effective diffusivity,  $\alpha_{eff} = (\kappa/\rho C_v)_{eff}$  and effusivity,  $e_{eff} = (\sqrt{\rho\kappa C_v})_{eff}$ . Thus, a key feature of the model is determining how to handle the bulk properties.

The microstructure of the green sheet cannot be described by a simple geometry. For purposes of modeling it would be advantageous to identify composite features such as planes of symmetry, preferred particle orientation, geometrical packing relationships for particles of known shapes and size distributions, etc. Examples are models developed to describe the thermal behavior of composites consisting of parallel layers. The green sheet is best described as a composite material with three constituents: alloy particles, binder, and voids. Based on the constituent densities, weight fractions, and bulk green sheet density the compact mass is estimated at about 97% alloy occupying only 40 to 60 percent of the bulk volume. The green sheet is a loose assembly of thermally conductive particles which are partly coated by a much less conductive binder. While significant voids are present throughout the structure, a region of binder has very low effusivity and diffusivity and can be approximated as a void.

Several approaches have been taken to describe the effective transport properties of various composites. These include electrical conductivity, thermal conductivity, electrical permittivity, and magnetic permeability. The generic situation address at least one "transport species" embedded within a medium with reduced transport capability. For the purpose of discussion the term conductivity will be used to describe the generic phys-

ical transport. Diffusive models assume some uniform distribution of a conductive species throughout the matrix, while percolation models focus on the preferred paths of transport within the composite. Both types of models provide for shape factors to describe the conductive species (e.g. particles, fibers, flakes, etc.) embedded in a less conductive matrix. An important feature of the percolation models is a volume fraction dependent transport property. This feature provides for the sharp transition in bulk composite properties typically observed above some threshold concentration. This phenomena is associated with the development of transport paths created between conductive elements.

Various theoretical models [50] [51] [52] [53] have been developed to describe the *anisotropic electrical conductivity for matrix composites involving different fiber constituents*. These models include the component properties, orientation, shape, and concentration. Louis et al. [54] simulated the electrical conductivity in a polymer matrix filled with carbon spheres. This model provided for the percolation threshold by accounting for the transition which occurs as the volume fraction approaches the maximum spherical packing density. Jagota et al. [55] has proposed a thermal transport model that assumes some nominal contact area between closely packed spheres in a non-conducting medium. Maiti [56] investigated the thermal characteristics of a polypropylene matrix filled with silver powder. As anticipated, the thermal conductivity of the composite increased with silver concentration. However, this enhancement was non-linear. A semi-empirical relationship was used to model the data.

Scattering theory has also been used to describe fields within composites [20]. The independent scattering approximation for spherical scatterers is valid for low loadings,

typically below about a 30% volume fraction. Beyond this concentration the independent scattering assumption is no longer valid and multiple scattering effects must be included. It is clear from studying the microstructure and the 40 to 60 percent volume loading with non-spherical alloy particles, that this physical model is not valid for the green sheet. McCullough [57] has developed a general diffusion model which reduces to both the Rayleigh and Maxwell mixture formulas for the dependence of electrical properties on the volume fraction of non-contacting spherical particles in a filler matrix. The Rayleigh formula describes the dielectric constants derived for a cubical array of spheres and the Maxwell relationship describes the specific conductivity of a suspension of spheres in an insulating medium.

The first step in modeling the thermal behavior of the green sheet was to determine where, in the spectrum of volume fraction behavior, the typical compact resided. The reference compaction samples and samples of the iron aluminide product at different stages of production allowed the percolation behavior to be characterized. Figure 4-26 illustrates the dependence of thermal diffusivity on the microstructure of the iron aluminide product. The curve represents a best fit to the data. In the green state, for both pressure and binder content variations, the diffusivity is relatively low (on the order of  $0.003 \frac{m^2}{sec}$ ). After sintering and densification of the sheet to a 0.012" thickness a significant rise in diffusivity takes place. Further densification is asymptotic to that of the fully dense alloy,  $0.029 \frac{m^2}{sec}$ . Typical percolation curves describe the spectrum of behavior for a particular morphology (e.g. particles in a matrix) and exhibit a symmetrical transition through the percolation threshold. The skewed form of the curve in figure 4-26 is related to the transition from individual particles to a sintered network.

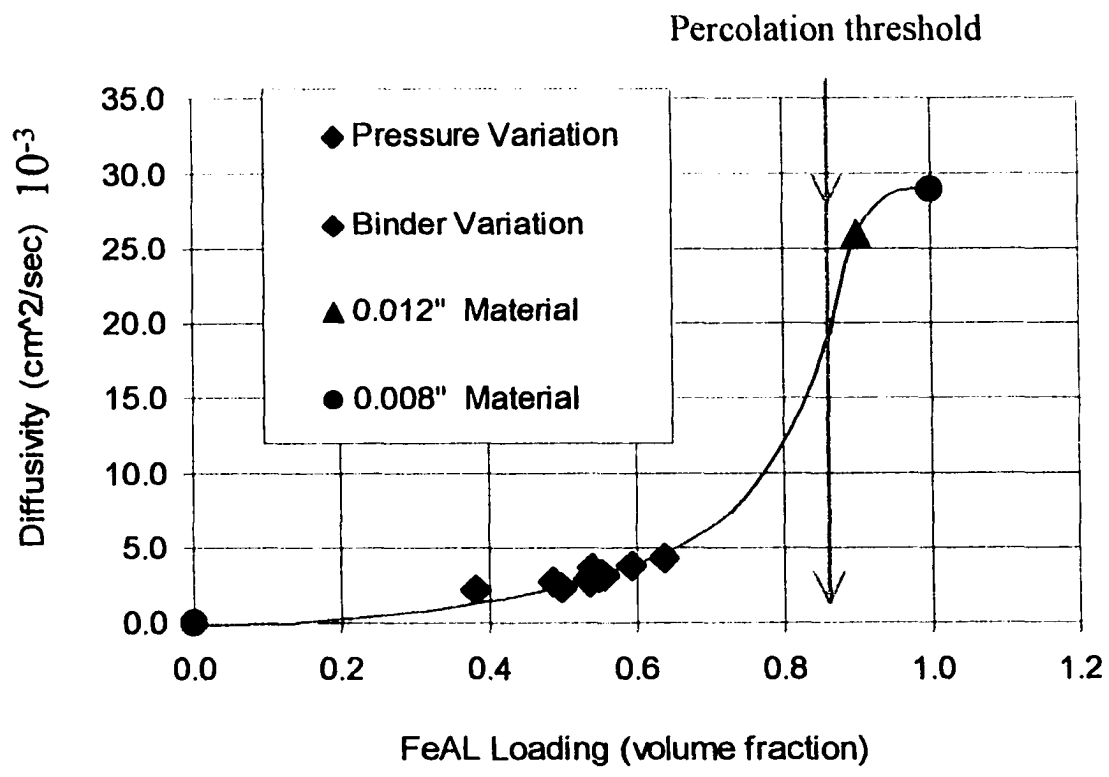


Figure 4-26: Variation in bulk diffusivity with alloy volume fraction and process history.



The green sheet will be modeled using a combination of the general diffusion model presented by McCullough [57] and the heat conduction model for the front flash excitation. The assumptions are that the particles are randomly oriented and that the volume fraction is below the percolation threshold. This is clearly the case as illustrated by the green sheet data illustrated in figure 4-26. The effective bulk diffusivity can be expressed as

$$\alpha_{eff} = (\kappa / \rho C_v)_{eff} \quad (4.10)$$

Where  $\kappa$  is the effective thermal conductivity,  $\rho$  is the bulk density, and  $C_v$  is the bulk specific heat. From McCullough [57] we can express the effective diffusivity as

$$\alpha_{eff} = \alpha_m \left[ \frac{V^2 \kappa (1 - h(a))}{V \kappa (1 - h(a)) + h(a)(1 - V)} \right] \quad (4.11)$$

Where  $V$  is the volume fraction of metal,  $h(a)$  is a function which describes the shape of the particles, and  $\alpha_m = 0.029 \text{ cm}^2/\text{sec}$  is the bulk diffusivity of the alloy. Likewise we can describe an effective bulk effusivity as

$$\tau_{eff} = (\sqrt{\alpha} \rho C_v)_{eff} \quad (4.12)$$

It is assumed that  $(\rho C_v)_{eff}$  can be taken as a weighted average of the relative volumes of the binder and the alloy. Thus we have

$$\tau_{eff} = \sqrt{\alpha_{eff}} [b(1 - V) + mV] \quad (4.13)$$

Where  $m = (\rho C_v)_{metal}$  and  $b = (\rho C_v)_{binder}$ , and  $V$  is the volume fraction of metal. Recall (see chapter 2) that the solution for the front surface cooling curve of the sheet can be expressed as

$$T(t) = \frac{2Q}{(\alpha_{eff}\sqrt{\pi})} \left[ (\sqrt{t} - \sqrt{t-\tau}) - 2\sqrt{t} \sum_{n=1}^{\infty} (1)^n F(t) - 2\sqrt{t-\tau} \sum_{n=1}^{\infty} (1)^n F(t-\tau) \right] \quad (4.14)$$

With sheet thickness  $L$ , radiant energy per unit area absorbed by the surface  $Q$ , pulse duration  $\tau$ , and  $F(t)$  defined by:

$$F(t) = \exp\left(\frac{-n^2 L^2}{\alpha_{eff} t}\right) - \sqrt{\frac{n^2 L^2}{\alpha_{eff} t}} \operatorname{Erfc}\left(\frac{n^2 L^2}{\alpha_{eff} t}\right) \quad (4.15)$$

The combination of equations 4.11, 4.13, and 4.14 yields the green sheet cooling curve as an explicit function of the energy absorbed by the sheet, constituent properties, the volume fraction of alloy, the sheet thickness, and the particle aspect ratio:

$$T = T(t, Q, (\rho C_v)_{metal}, (\rho C_v)_{binder}, V, L, l, d) \quad (4.16)$$

The particle shape is modeled as an ellipsoid of major and minor axes  $l$  and  $d$  with an aspect ratio given by  $a = \frac{l}{d}$ . For ellipsoidal particles  $h(a)$  is described by

$$\begin{aligned} h(a) &= \frac{a^2}{1+a^2} \left[ \left( \sqrt{\frac{a^2}{1+a^2} + \frac{1}{\sqrt{1-a^2}}} \right) * \arctan\left(\frac{1}{\sqrt{\frac{a^2}{1+a^2}}}\right) - 1 \right] & \text{for } 0 < a < 1 \\ h(a) &= \frac{2}{3} & \text{for } a = 1 \\ h(a) &= \frac{a^2}{a^2-1} \left[ 1 - \frac{1}{2} \left( \sqrt{\frac{a^2}{a^2-1} - \frac{1}{\sqrt{a^2-1}}} \right) \ln \left[ \frac{\sqrt{\frac{a^2}{a^2-1} + 1}}{\sqrt{\frac{a^2}{a^2-1} - 1}} \right] \right] & \text{for } 1 < a < \infty \end{aligned}$$

Figure 4-27 illustrates  $h(a)$  over a range of aspect ratios. For  $a < 1$  the particles are platelets. For  $a \gg 1$ , the particles become fibers and the shape factor approaches

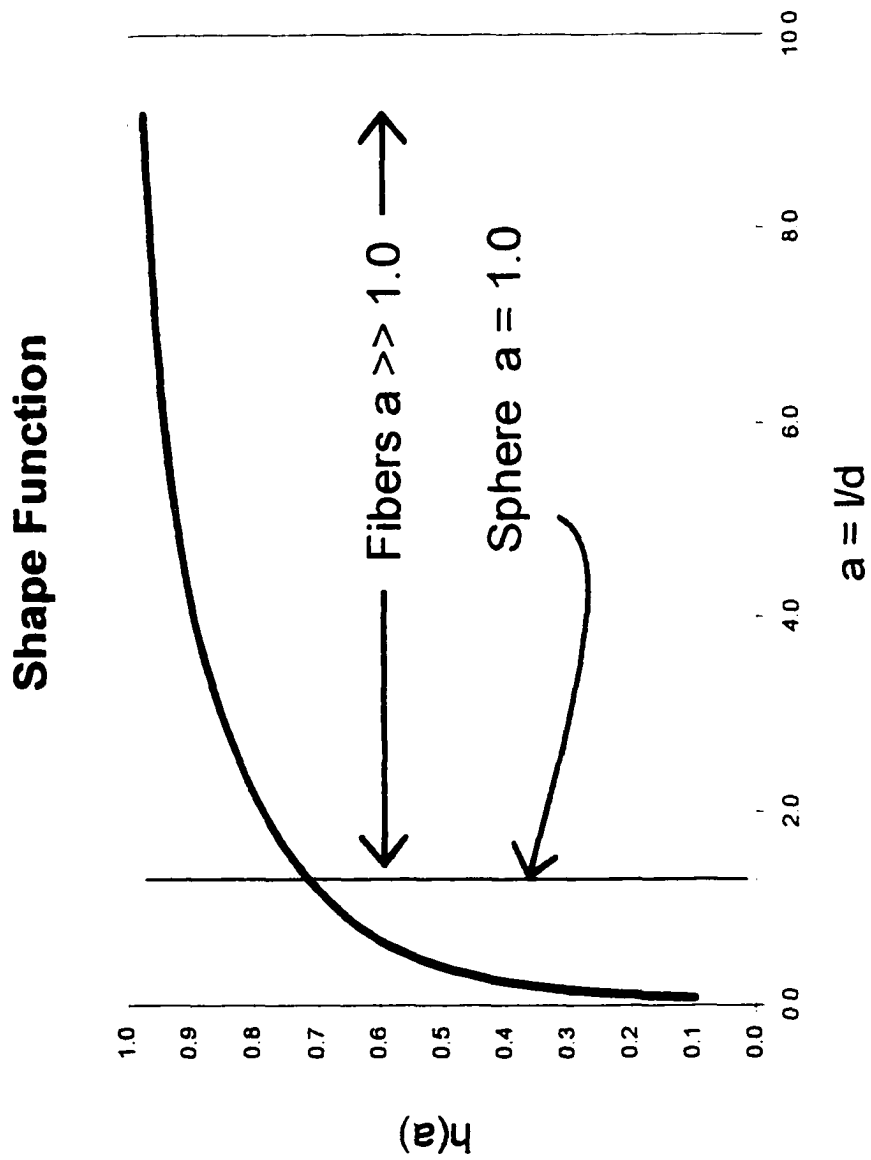


Figure 4-27: Particle shape function [57]

unity. Figure 4-28 illustrates the results from equation 4.11 using particle aspect ratios of 1, 2, and 3, with  $\alpha_m = 0.029 \frac{\text{cm}^2}{\text{sec}}$ . An aspect ratio of  $l/d = 2$  provides the best fit to the diffusivity data. This mean aspect ratio is reasonable considering the microscopic particle morphology (see figure 4-29).

Using an aspect ratio of 2, the explicit form of 4.16 provides a basis for exploring the sensitivity of the model to the parameters of interest. Figure 4-30 compares the model prediction with the cooling curve data (see section on reference samples) for the nominal compaction reference sample (2.8 wt. % binder at 13.8 tons compaction, measured  $\alpha = 0.0033 \frac{\text{cm}^2}{\text{sec}}$ ). Figure 4-31 provides the same illustration for the nominal green sheet material compacted at a much lower level (9.7 tons,  $\alpha = 0.0024 \frac{\text{cm}^2}{\text{sec}}$ ). The model shows very good agreement with the data.

Figure 4-32 illustrates the thermal decay as a function of green sheet thickness with a nominal material composition. The nominal thickness is 0.066 cm. This curve provides an excellent description of the time and thickness regimes over which the compact is "thermally thick" and "thermally thin". Note that for very small thicknesses the decay curve deviates from the decay for thick samples at a very early time. For the nominal green sheet composition the material response is that of a half-space up to about 300 ms (i.e. thermally thick). Figure 4-33 combines the variation in diffusivity with the established dependence on composition and compaction force. The result is a family of cooling curves. As has been described, the inspection of a green sheet specimen yields different rates depending on the local volume fraction of alloy. It is these local differences that provide contrast in the thermal images. The results of the model allows for the quantitative investigation of the

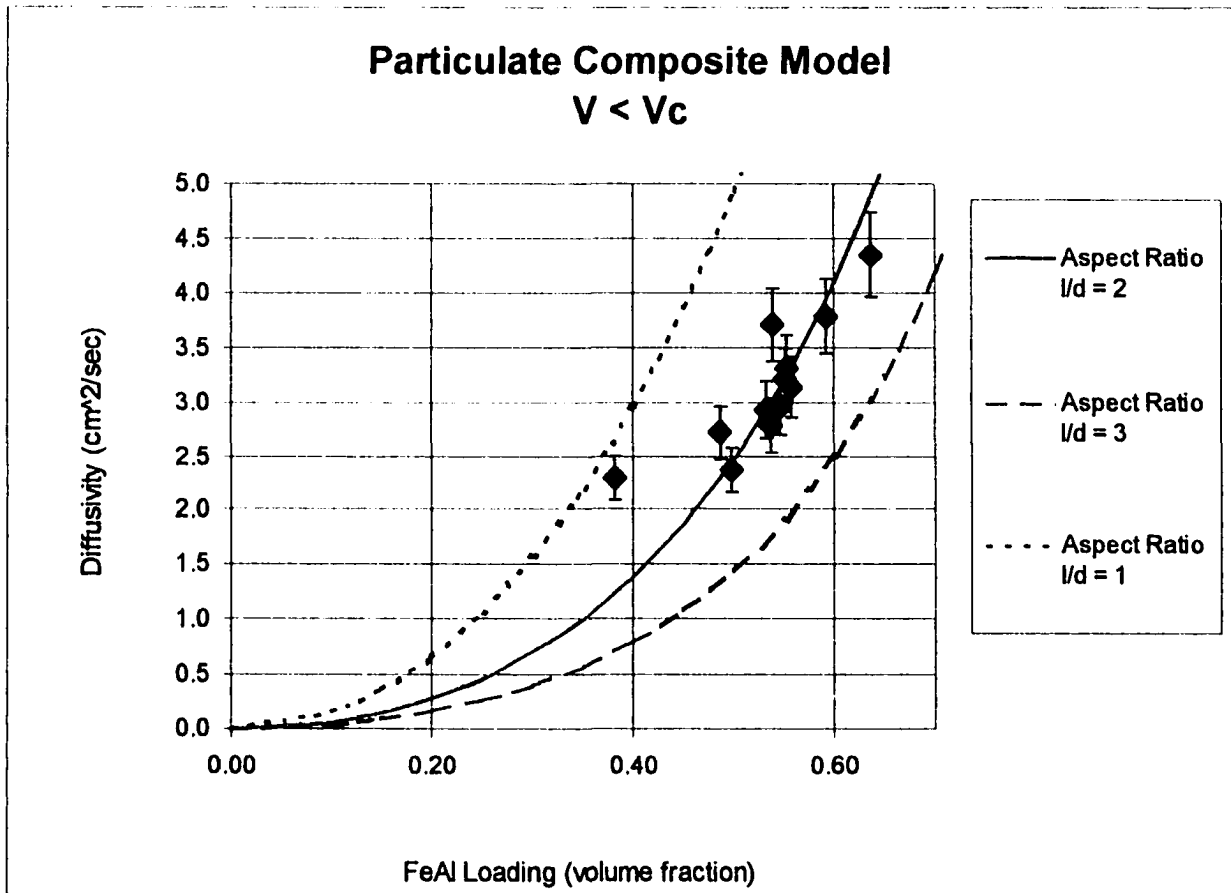


Figure 4-28: Particle composite model for three values of aspect ratio. For the volume fraction of alloy below the percolation threshold,  $V < V_c$ , the experimental data is consistent with an aspect ratio of 2.

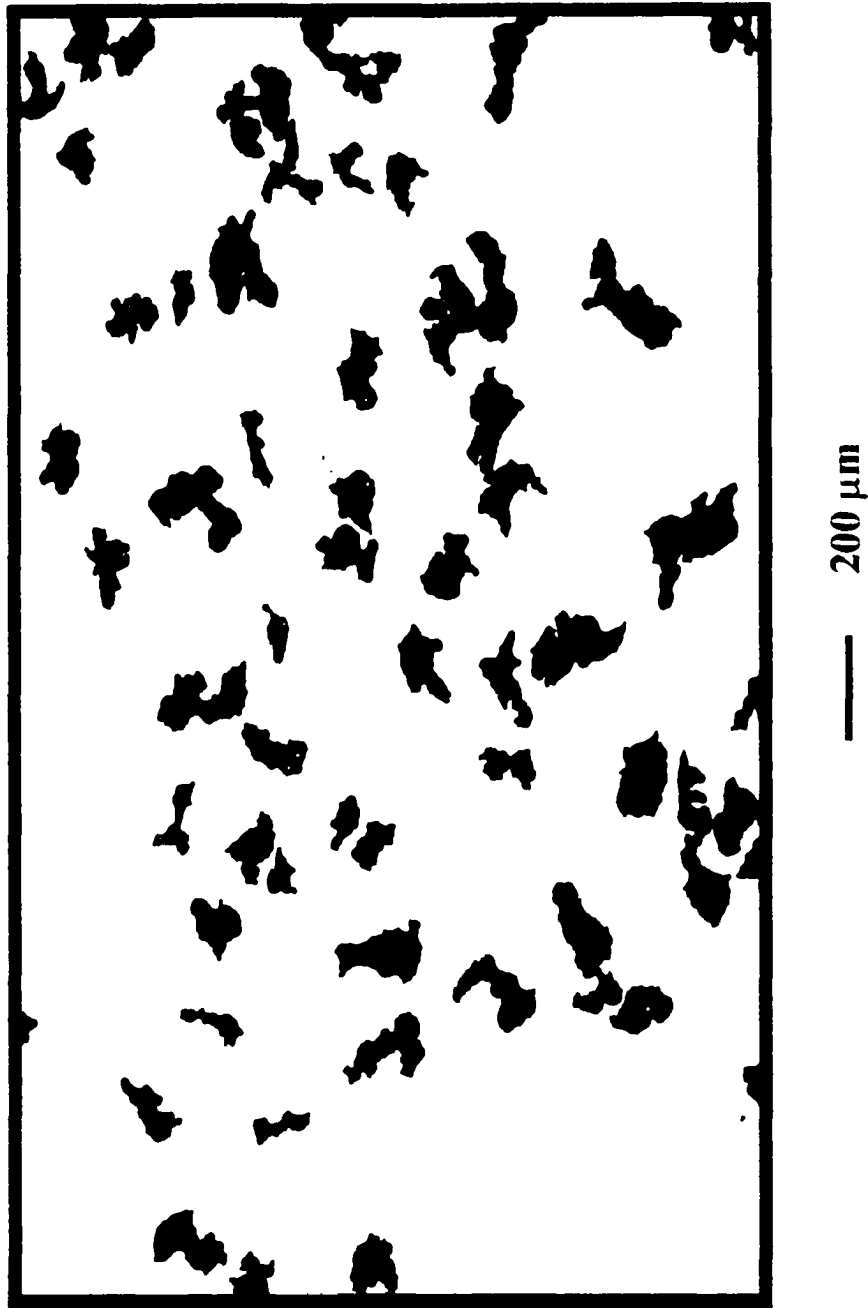


Figure 4-29: Optical micrograph depicting the irregular shape of FeAl particles as dark on a white background.

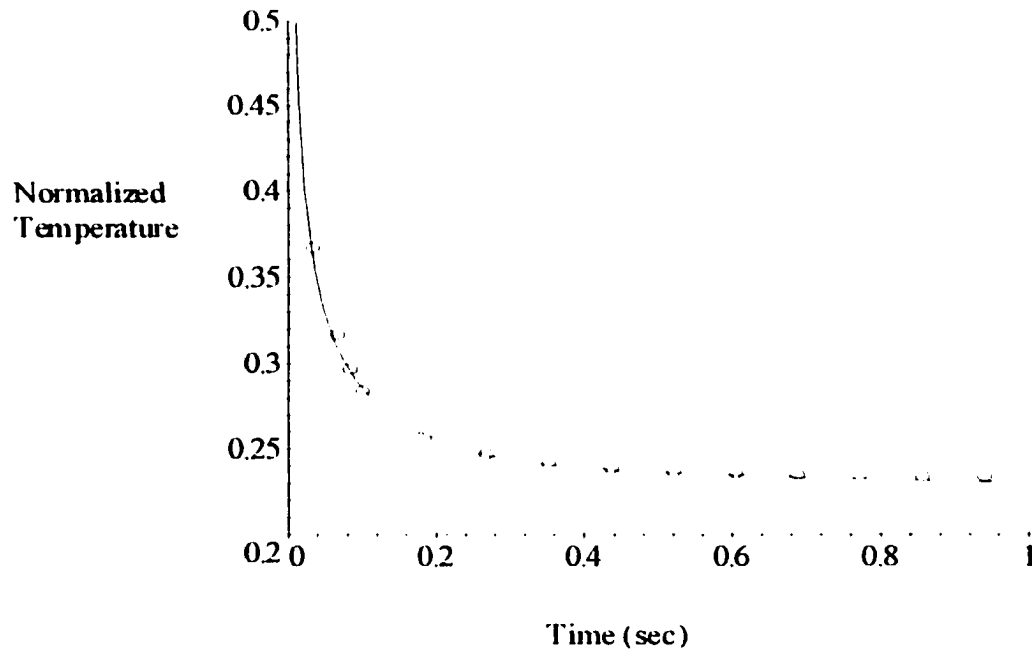


Figure 4-30: Thermal decay curve comparing model with data from reference specimen. The specimen fabricated with a binder loading of 2.8 % by weight and a compaction of 13.8 tons. The effective bulk diffusivity was 0.0033 cm<sup>2</sup>/sec.

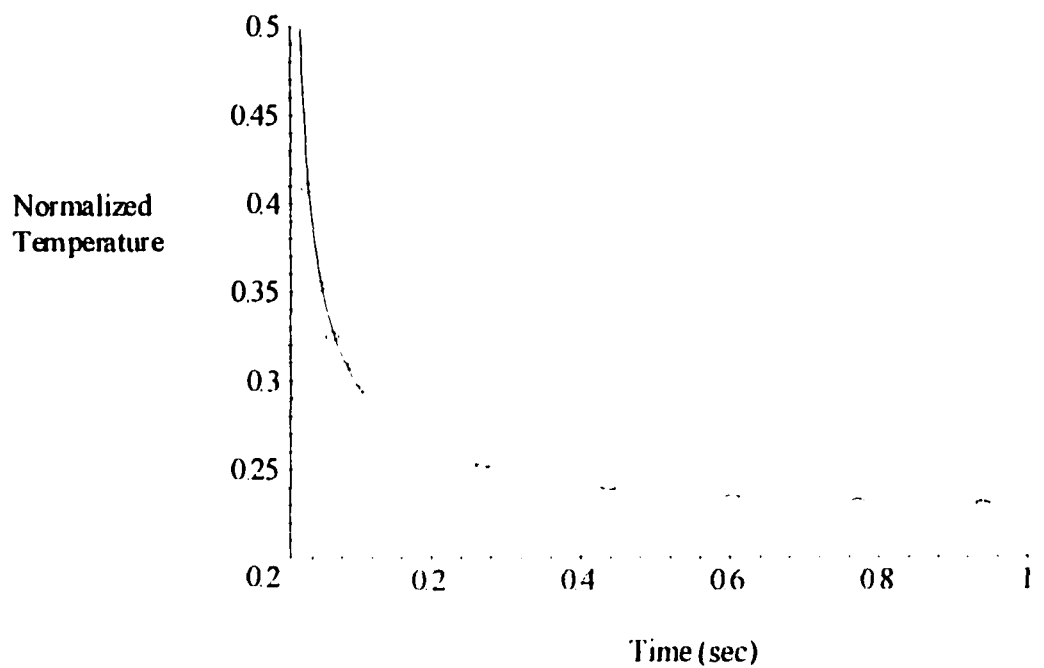


Figure 4-31: Thermal decay curve comparing model with data from reference specimen. The specimen was fabricated with a binder loading of 2.8 % by weight and a compaction of 0.7 tons. The effective bulk diffusivity was 0.0024 cm<sup>2</sup>/sec.



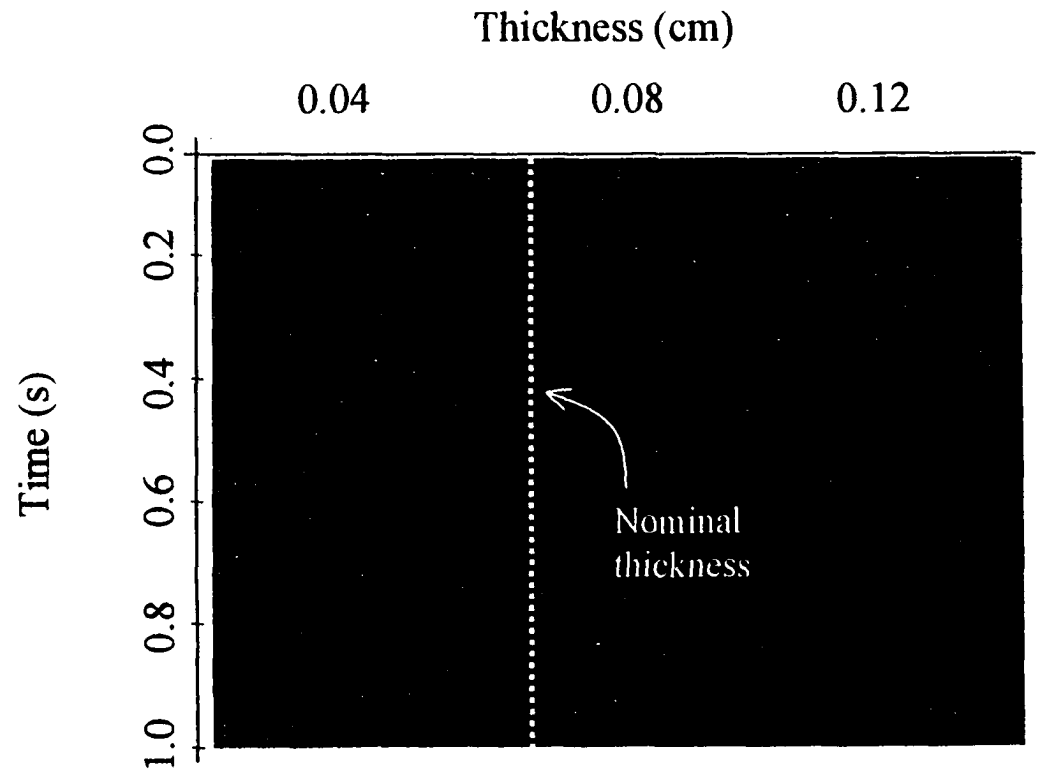


Figure 4-32: Relative variations of thermal response with thickness. The nominal alloy volume fraction has been assumed in this case. Red indicates high temperatures and the blue indicates lower temperatures. The black lines are isotherms this space. The broken white line is the nominal thickness.

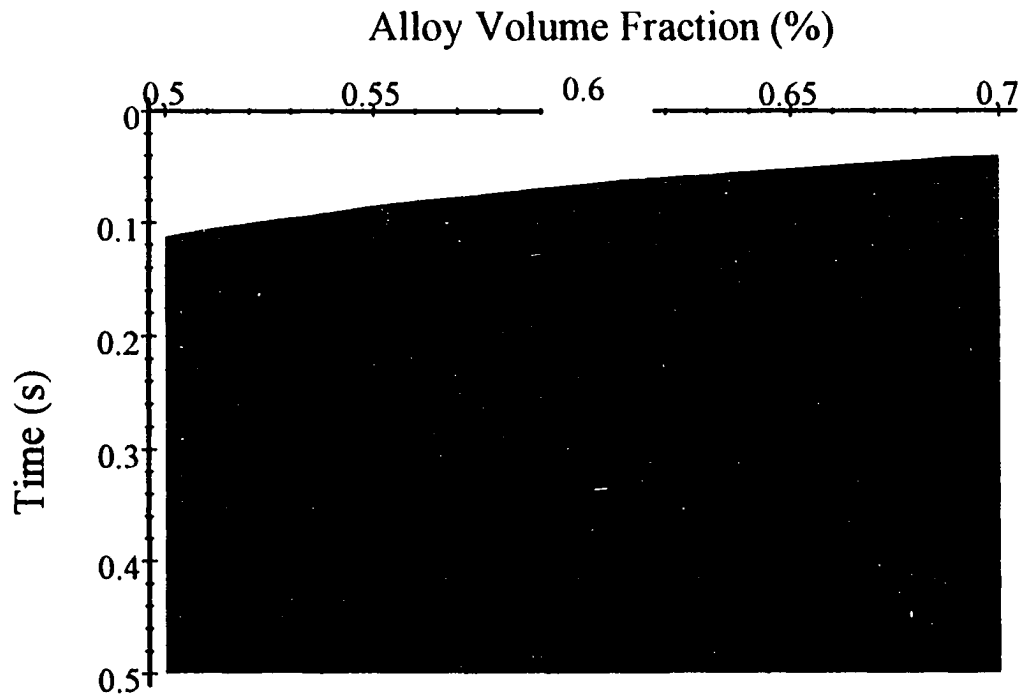


Figure 4-33: Variation of thermal response for various volume fractions of alloy. The nominal thickness has been assumed for this case. Red indicates higher temperature and blue indicates lower temperature. The black lines indicate isotherms.

thermal response. It is particularly important to have this capability when assessing the need to modify the inspection protocol. For instance, changes in the specifications for the material composition, thickness, or production rate can impact the resulting temperature transients. These changes may require modifications in the inspection protocol such as sampling rate, sampling duration, and span of calibration. Having a valid model minimizes the time required to optimize the inspection method.

## Chapter 5

# Results of Process Study

### 5.1 Introduction

Preliminary results from the thermal behavior of production samples, reference samples, and green sheet microstructure allowed for a direct association between the local volume fraction of FeAl and the thermal response obtained during flash inspection. This data demonstrated the viability of the technique and provided a justification for the dedication of production resources to conduct a process study. The objective of this study was to identify green sheet precursors to flaws in the final FeAl sheet as indicated by the heterogeneity of the heat transfer in production green sheet.

Figure 5-1 provides a convention for the sheet coordinate system. Final sheet material can be rejected for several reasons: cracks, thickness, porosity, flatness, wedge, and camber. Wedge is an unacceptable increase or decrease in thickness transverse to the length of the sheet. Camber results from rolling material which has a wedge. Figure 5-2 illustrates a sheet with excessive camber. Porous regions in the densified sheet arise from

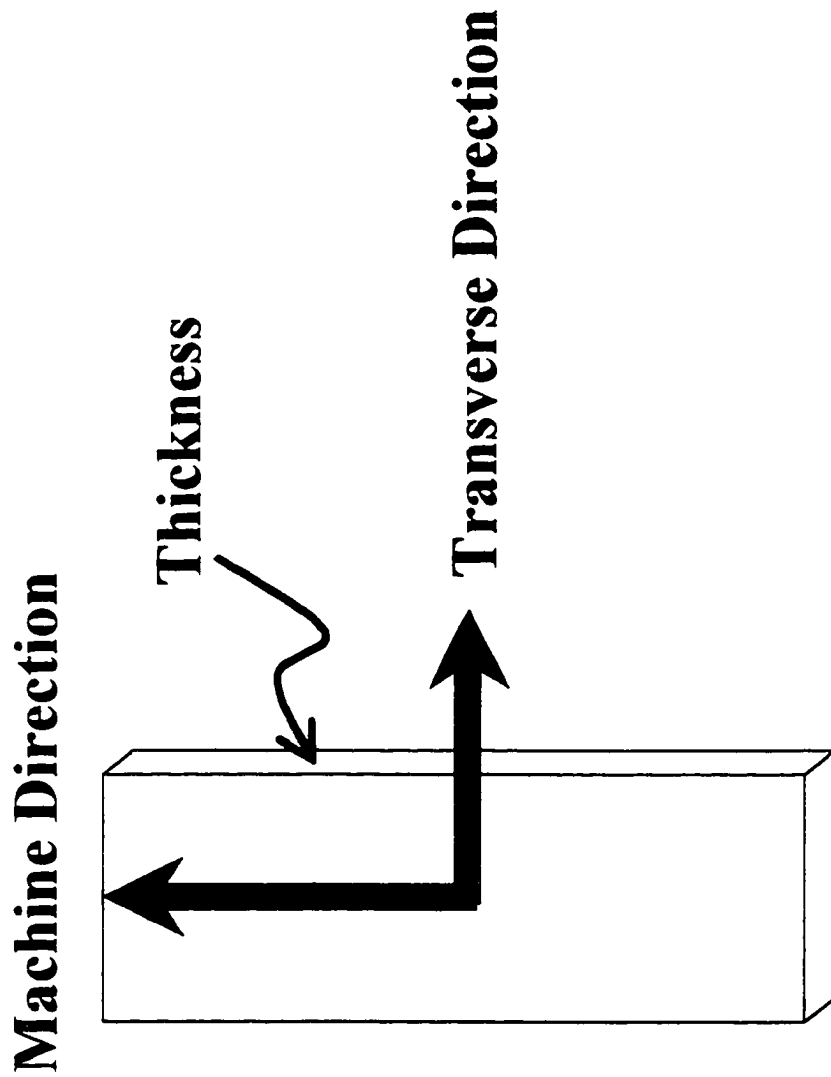


Figure S-1: Reference coordinates for FeAl sheet.

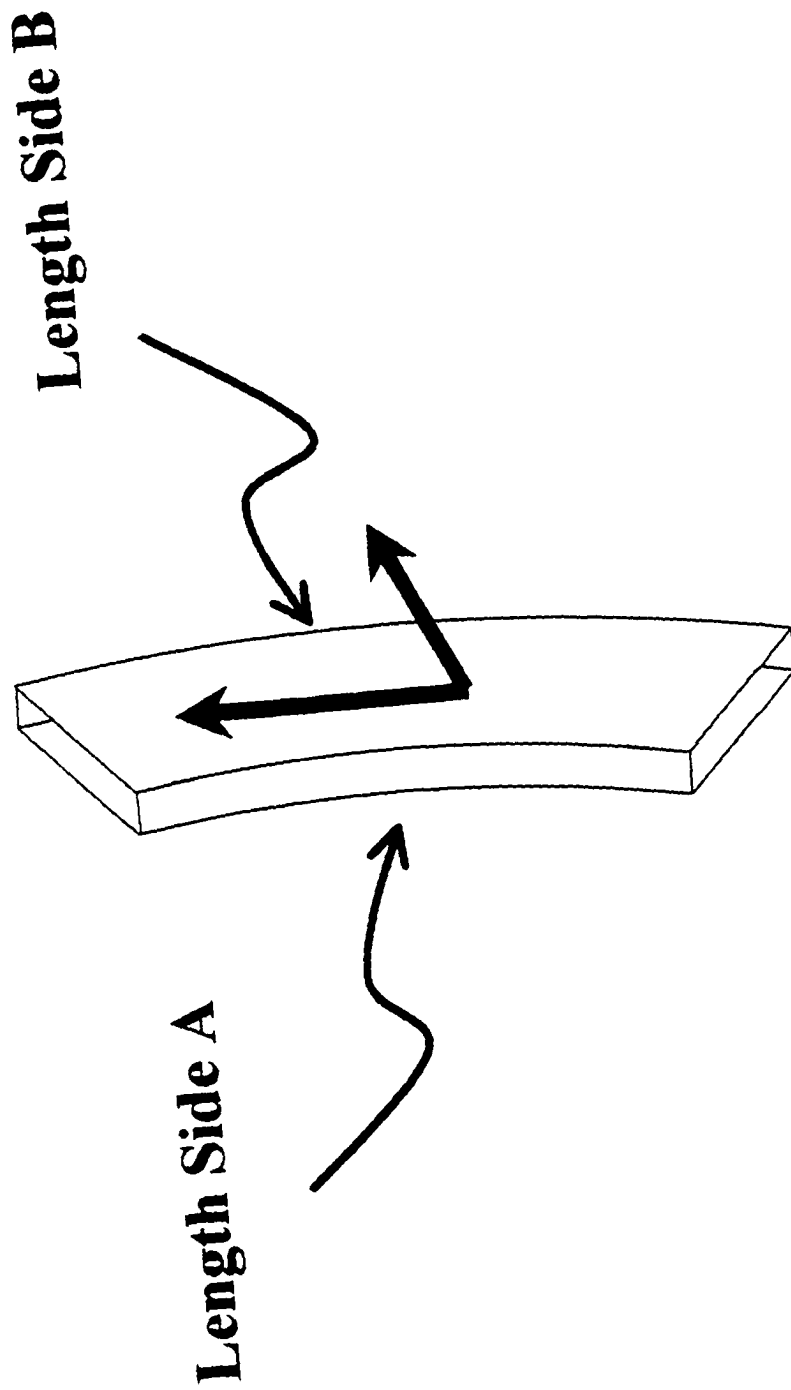


Figure 5-2: Camber results from excessive loading of FeAl on one side of the sheet. Edge A is shorter than edge B.

green sheet regions with low FeAl volume fraction. If large enough, on the order of millimeters, porous areas can be seen with the unaided eye. Regions smaller than this can cause problems, and are typically detected by sampling the production material and inspecting cross sections of the microstructure. Crack detection was based on visual inspection. Typical thresholds for crack detection, via operator inspection, is about one millimeter in length. Prior to final forming, the material variation from flat can be significant. "Waviness" results from the same mechanism that causes camber. If the asymmetry in alloy volume fraction varies over short distances, the camber reverses from one side to the other over the length of the sheet. This results in stresses that induce strains out of the sheet plane. A roller is used to flatten the sheet but this is done at the cost of inducing undesirable levels of residual stress within the sheet.

## 5.2 Methodology

A typical manufacturing run will involve the processing of 150 green sheet sections with an average length of approximately 86 cm (34 in.) and a width of 10 cm (4 in.). The manufacturer provided 10 sheets from a single production run. The normal yield for the process is about 50%. This 15% sampling was adequate to assure that a significant number of flaws would be obtained. The sheets were numbered according to the order of compaction. Each sheet was marked with the sample code and machine direction. This indicator also provided a reference for the top and bottom of the sample. The steps in the process study are as follows:

1. **Compaction**

2. **Collection of thermal data**
3. **De-binder green sheet**
4. **Collect thermal data**
5. **Roll down to 0.25 mm (0.010 in) and inspect for defects**
6. **Inspect suspect defective 0.25 mm (0.010 in) sheet using digital x-ray imaging**
7. **Roll down to 0.20 mm (0.008 in)**

Considerable effort was made to minimize deviations from the normal practices and procedures associated with processing. Production personnel were requested to follow all normal inspection and quality control procedures. However, the timing of some steps were obviously impacted. For instance the normal time from compaction to de-binder is about one day. The time lag for this thermally inspected green sheet was about two weeks because of the geographic separation of the manufacturing and laboratory facilities. Such details did not appear to have an impact on the quality of the material. Attempting to densify the sheet by cold rolling in only a few passes results in severe work hardening and cracking of the material. To minimize this problem densification is achieved by passing the de-bindered sheet through successively narrower roller clearances. It takes approximately 40 roll passes to achieve the 0.25 mm (0.010") thickness. The dimensional change transverse to the machine dimension is minimal (<10%). However, the elongation in the machine direction is typically 50%. Production workers visually inspect the material after each pass. If the flaw can be removed, leaving acceptable material, it is trimmed off using a standard



sheet-metal shear. Trimming on all four edges was common. If the flaw was too large or if trimming resulted in a piece too small for further processing, the part was discarded.

Tracking the morphology of the green sheet material through the process presented an interesting problem. While the material dimensional changes were minor in going from the green sheet (0.69 mm or 0.027" thick) to the de-bindered sheet (0.66 mm or 0.026"), the changes from the de-bindered sheet to the partially densified 0.25 mm (0.010") sheet were significant. In order to track the green sheet flaw evolution throughout the process it was necessary to devise a means of determining a coordinate transformation from the original green sheet to an arbitrary intermediate product. This was accomplished in the following manner. A coordinate system was established on the green sheet. The origin was located at the head of the arrow marking the machine direction on the part. Each location on the green sheet was defined by its longitudinal and transverse coordinates. Figure 5-3 illustrates this reference system. Before trimming a part several data were recorded. The description and dimensions of the flaw(s) to be removed were noted. In addition, the location and dimensions of the trimmed sections were recorded along with the number of the rolling pass at which the part was trimmed. This data was used to determine the original location of the flaw in the green sheet reference frame.

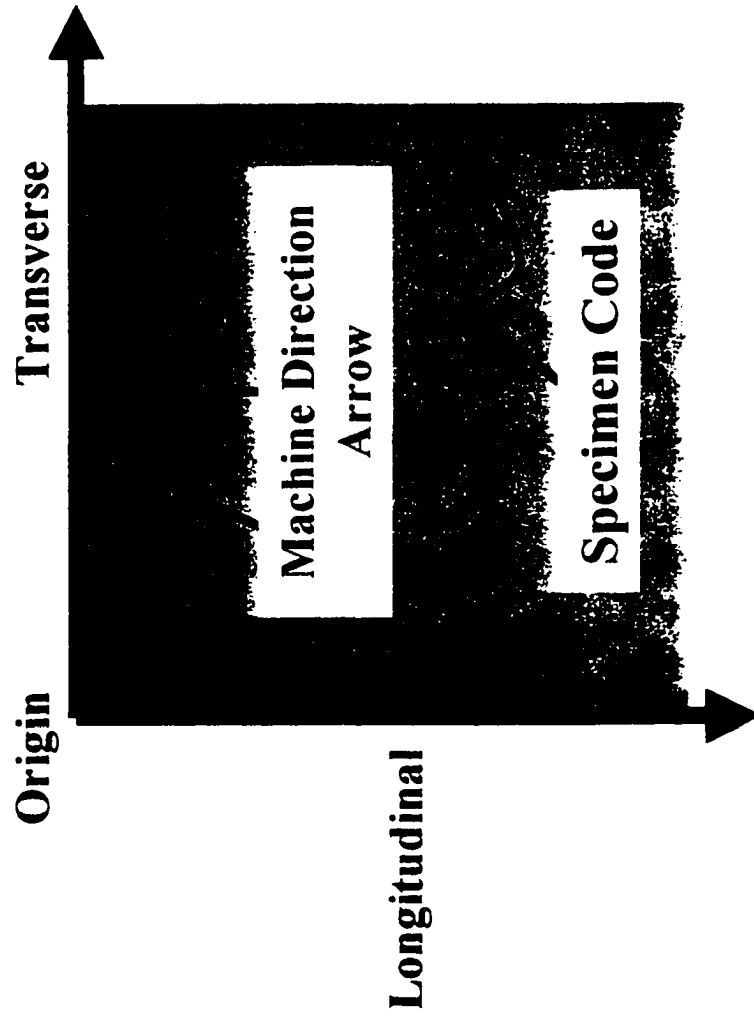


Figure 5-3: Reference frame for the location of green sheet flaw precursors.

## 5.3 Results

### 5.3.1 Yield

Table 5-1 is a summary chart from the process study. Before discussing the results a few comments are in order. Note that an alpha-numeric code is used. There are 2 processed sheets (A and B) associated with each numbered green sheet. This results from a step in which each sheet, after sintering, was bisected transverse to the machine direction resulting in two lengths. The result was 20 sintered sheets (e.g. 12A, 12B...54A, 54B) which were reduced to 0.25 mm (0.010") by rolling. Also note that sample 23B is not listed. It was pulled from the process, after the sintering operation, to provide a comparison among the thermal, production x-ray, and digital x-ray inspection techniques. This data will be discussed later.

Operators used no optical aids during part inspection. A total of 42 cracks were documented; 27 of these occurred in one sample (21B). The vast majority of visible cracks occurred in the process of rolling the sheets down to 0.25 mm (0.010"). Identified cracks ranged from a few millimeters to 20 mm with a mean crack length of 12 mm. All extended through the thickness of the material and most cracks occurred on the long edge of part. Cracking was predominantly transverse with one end open at the edge of the sheet. Only a few appeared in the interior of the sheet. The impact of a crack on the disposition of the work piece depended on several factors. The minimum length for the final stamping operation is 60 cm. Parts shorter than this were discarded. If a crack occurred at the edge of a part it could be easily trimmed without much loss in length. The initial sheet width was large enough that two or three trim cuts could be made, parallel to the length, before

Sample Code	Total Number Transverse Cracks	Absolute Process Yield Length @0.008" (mm)	Process Yield Length @0.008" (%)	Disposition Stamped Yes/No	Absolute Process Yield Stamped @0.008" (mm)	Stamped Yield%
12A	Damaged from roller nip	492	69	No	0	0
12B	0	609	86	Yes	609	86
14A	3	0	0	No	0	0
14B	1	470	66	No	0	0
21A	2	0	0	No	0	0
21B	27	0	0	No	0	0
23A	4	0	0	No	0	0
32A	0	635	89	Yes	635	89
32B	0	711	100	Yes	711	100
34A	1	688	97	Yes	688	97
34B	0	692	97	Yes	692	97
41A	2	0	0	No	0	0
41B	1	0	0	No	0	0
42A	1	427	60	No	0	0
42B	0	417	59	No	0	0
52A	0	659	93	Yes	659	93
52B	0	656	92	Yes	656	92
54A	0	673	95	Yes	673	95
54B	0	666	94	Yes	666	94
<b>Totals</b>	<b>42</b>	<b>7795</b>	<b>55</b>		<b>5989</b>	<b>42</b>

Table 5-1: Summary of process yield for flaw precursor study. The mass yield was typical for the production capability, 55%. Final sheets less than 60 cm fell below the minimum stamping criteria and did not contribute to the useable yield which was 42%.

the piece became too narrow for stamping. However, if a crack occurred in the center of the piece, requiring the part to be cut into two smaller lengths or if repeated end cuts were made, then the piece may not have been stamped. As can be seen from the chart, poor quality green sheets with process yields less than about 85% resulted in 0.20 mm (0.008") thick sheets below the minimum stamp length (60 cm). While the yield of 0.20 mm (0.008") material based on mass yield was 55%, the yield based on material suitable for stamping was only 12%.

### 5.3.2 Heterogeneity

Green sheet heterogeneity manifested itself in several forms throughout processing. Operators often anticipated cracks based on subtle surface, and, or sheet shape changes during rolling. Even after the first or second rolling pass, towards 0.25 mm (0.010"), the sintered material takes on a smooth specular appearance. Prior to actual crack formation the surface may exhibit a dulled finish in regions where cracks form. A high degree of camber and, or, waviness in the sheet may also precede cracking. These observations supported the contention that regions with low volume fractions of FeAl powder resulted in porosity, malformed sheet, and in the extreme case, cracks.

Based on the above observations and the experimental results on the effect of alloy volume fraction on material thermal response, a simple statistical approach to predicting the risk of crack formation was developed. A statistical description of image contrast is the standard deviation of the pixel grey levels. The effective physical pixel size was about 0.5 mm. This is an order of magnitude larger than the nominal FeAl particle size (0.06 mm) and several times larger than the largest observed FeAl depleted regions. Thus this statistic

was a good indication of the level of mixing in the green sheet. A green sheet with a fully dispersed binder would exhibit a single grey level intensity,  $S$  (i.e. an standard deviation of 0). Thermal images were normalized to the image mean in order to compensate for variations in camera drift and timing of the flash (i.e.  $t = 0$  reference). The coefficient of variance, which is the standard deviation normalizes by the mean, was used to describe the heterogeneity since it eliminates variations in the excitation flux and sampling time. The coefficient of variance is defined as

$$COV = \frac{\sqrt{\frac{\sum (S-s)^2}{n-1}}}{S} \quad (5.1)$$

Where  $S$  represents the pixel gray level from the raw thermal image just after the pulse. Since each specimen in the series was imaged at several 4" fields of view, the total number of data points for each sample was approximately 125,000.

Figure 5-4 illustrates that this COV is indeed a very strong predictor of which samples would develop cracks. The solid circles represent the specimens which exhibited cracks detected by the operator. The curve, which is a best fit to the data for cracks identified via visual inspection, is relatively flat and then turns sharply upward in the vicinity of a COV of 1.15 to 1.35. At first the significance of the data represented by the open triangles was not clear. These samples were not reported to have had a high number of cracks and thus fell far below the curve. Upon investigation it was found that the operators had discarded these samples during the 0.25 mm (0.010") rolling process. While not having a high number of cracks they did exhibit signs of porosity. Inspection of these samples revealed the presence of micro-cracks which could only be seen under magnification. Figure 5-5 illustrates such a microstructure. Further rolling of the specimens would have resulted

## Green Sheet Heterogeneity As a Predictor of FeAl Crack Formation

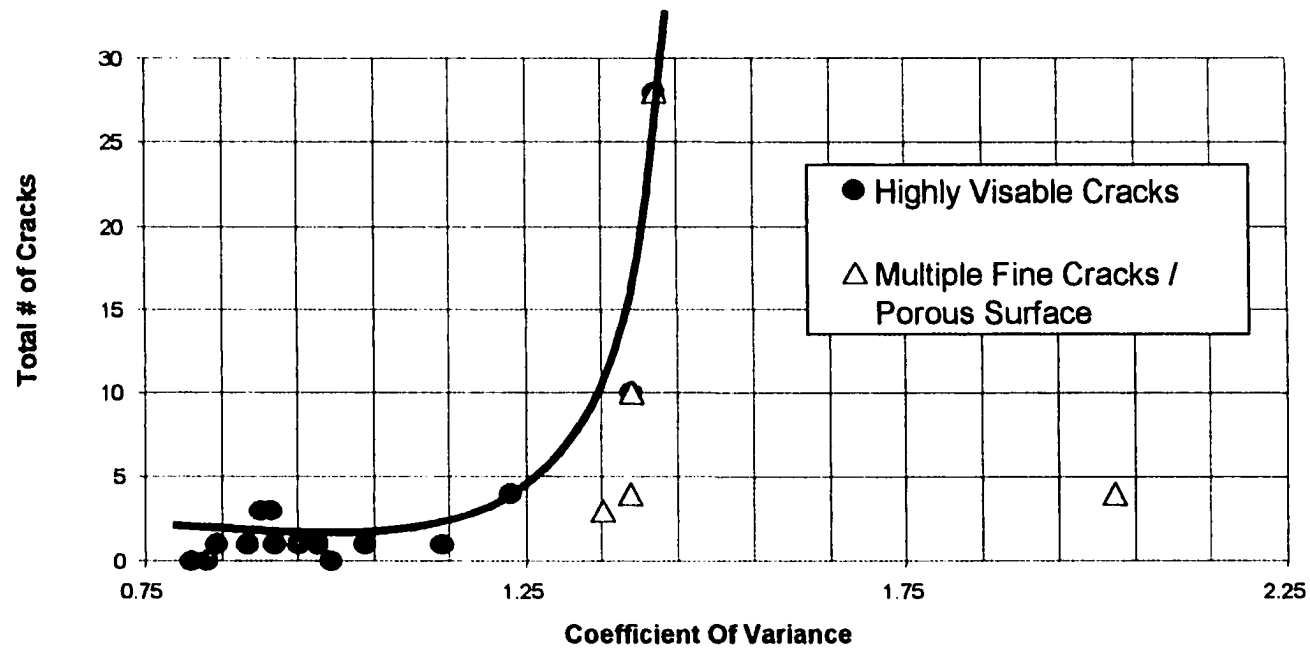
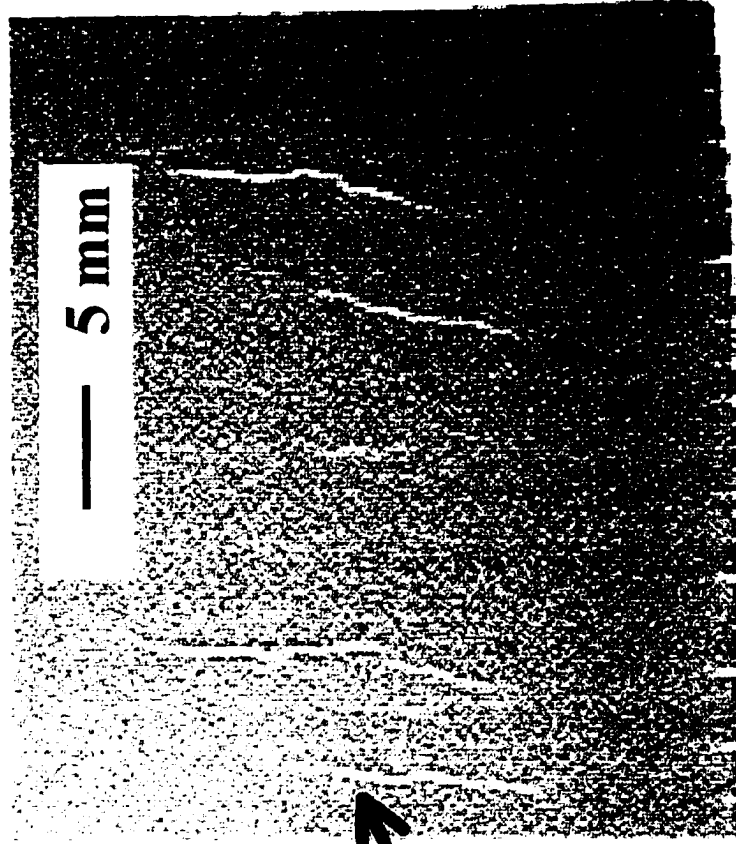


Figure 5-4: Green sheet heterogeneity as a predictor of crack formation during densification. The curve represents a best fit the cracks detected during processing.



**Multiple Fine  
Cracks**



Figure 5-5: Multiple fine cracks in FeAl sheet result from heterogeneity in green sheet.



in extensive cracking. Thus the fact that the triangular points lie below the curve in figure 5-4, is indicative of the ability of the thermal inspection technique to predict flaws below the threshold of the visual crack detection practice.

### **5.3.3 Characterization of production green sheet morphology**

While the approach of using the coefficient of variance statistic is useful, it provides no information on the location, size, nor formation mechanisms associated with green sheet defects. Review of the thermal data revealed several morphological features which provided further insight into the process. These features varied in their frequency and pronouncement.

The compaction mill is not particularly sophisticated and it is instructive to review the process in more detail before describing the morphological features encountered throughout the process. The operator loads the hopper by hand and provides a fresh charge prior to the depletion of the previous charge. The mill has two rollers, one with a fixed axis and one with an adjustable axis. The gap and alignment of the two compaction rollers is varied by manually adjusting the position of two large nuts along threaded rods. This changes the clearance between, and/or relative angle of, the adjustable roller with respect to the fixed roller. The operation is analogous to adjusting the alignment and chain tension for the rear wheel of a bicycle. The level of material in the hopper, roller alignment, and clearance significantly impact the quality of the green sheet. It is the operator's "sense" of these parameters that is the essence of the green sheet compaction art. Quantitative data for the state of these process variables are not recorded. Thus, a direct correlation between the process "state" and the green sheet morphology could not be obtained.

The qualitative nature of the morphology will be described first. At early times, after the end of the excitation pulse, the effusivity can be described by the decay in temperature by equation 5.2.

$$\epsilon = \sqrt{\rho C_p \kappa} = \frac{Q}{\Delta T \sqrt{\pi t}} \quad (5.2)$$

Where  $\rho$  is the bulk density,  $C_p$  is the specific heat,  $\kappa$  is the thermal conductivity,  $Q$  is the energy absorbed by the surface,  $t$  is the time referenced from the end of the pulse, and  $\Delta T$  is the change in the temperature as measured from the peak. The thermal impedance,  $Z = 1/\epsilon$ , is given by

$$Z = \frac{\Delta T \sqrt{\pi t}}{Q} \quad (5.3)$$

Thus for early times the thermal impedance, indicative of a region of green sheet below a point on the surface, is proportional to the decay in temperature at the surface. The convention for image presentation will be to assign high thermal impedance (lower effusivity) to brighter grey levels and a darker grey levels to low thermal impedance (higher effusivity). Thus regions of relatively high FeAl volume fraction show up as darker areas and regions of low FeAl volume fraction (high binder and/or, void volume fraction) are imaged as lighter areas.

Figure 5-6 illustrates a result from the preliminary thermography study. Both sides of the green sheet were imaged using same side excitation. The opposite sides exhibit the dominant features as "reflections" about the line separating the two images. These morphological features persist through the thickness of the sheet. The two dimensional

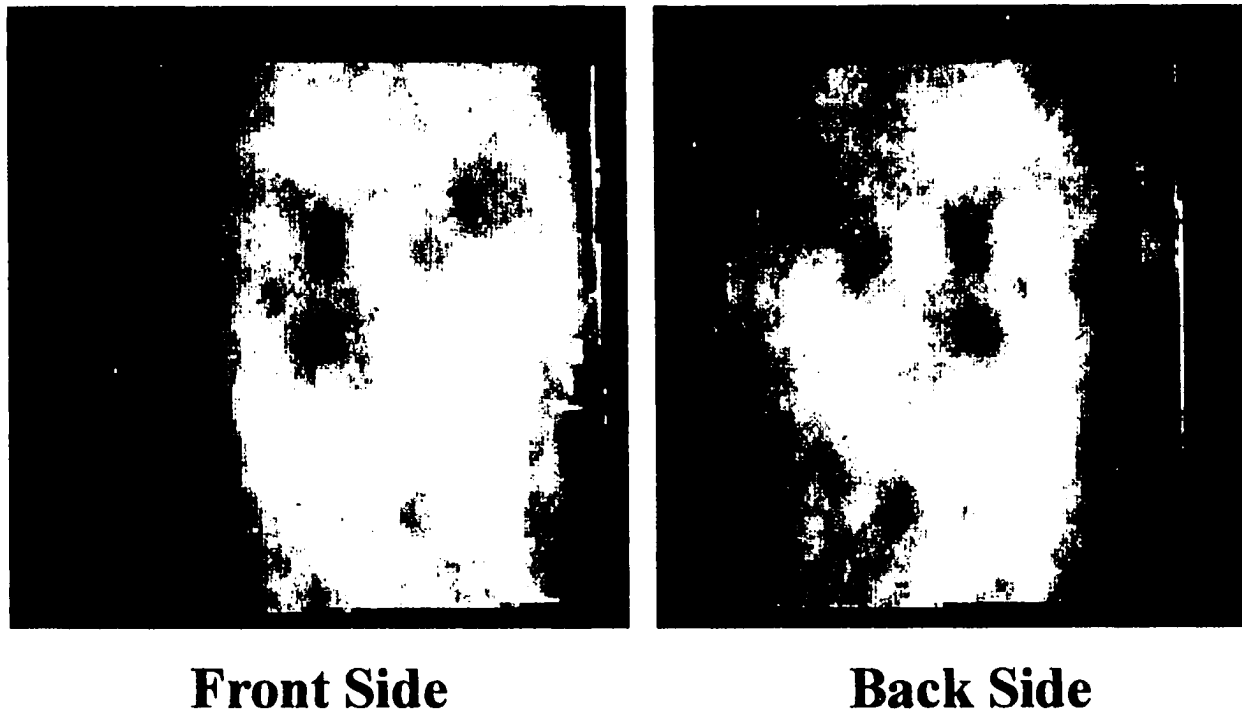
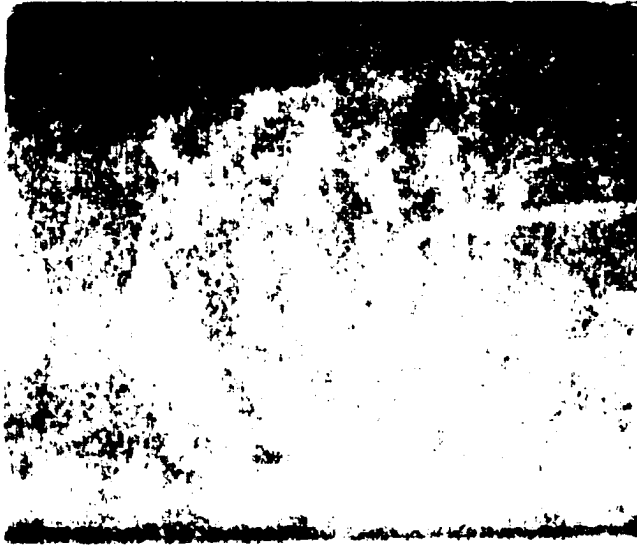


Figure 5-6: Thermal images illustrating the extension of morphological features through the thickness of the green sheet. These features are reflected about the center line between the two images.

nature of the sheet was found to hold for other samples. Figure 5-7 illustrates an example. The image has been reflected about the horizontal so that features which exist throughout the volume occupy the same locations in the front side and back side images. Note that the arrow head drawn on the front side to indicate the machine direction is visible in the image. Two common morphological features involved spatial variations of FeAl volume fraction transverse to the sheet. The first was a high alloy volume fraction edge associated with compact densification. Materials compacted with optimum roller alignment exhibit edges which were slightly denser than the center regions of the sheet. This is believed to be associated with the flexing or bowing of the rollers. Figure 5-8 illustrates such a sample. If the compaction roller axes were not in good alignment then one edge of the compact was "pinched" by the rollers. This feature can be seen in figure 5-9. The bottom edge was severely densified in comparison with the opposite edge. Based on the pressure effects obtained with the compaction reference samples and the observation that binder alloy segregation does not occur along the edge of the roll compacted material, it appears that the increase in pressure at the bottom edge is two to three times that experienced by the bulk of the sheet. During densification of the sintered sheet down to 0.25 mm (0.010") the dense edge experienced greater elongation. The result was a significant sheet camber. A higher frequency variation, similar to that observed for roller misalignment, was also observed. Figure 5-10 shows a high contrast thermal image illustrating this transverse variation. The period of the secondary feature is seen to be about one-fourth the width of the roller. This modulated concentration of alloy volume fraction is believed to be associated with non-uniform powder flow from the hopper.



**Front Side**



**Back Side**

Figure 5-7: Thermal images illustrating the extension of morphological features through the thickness of the green sheet. The specimen is sheet 14 at position 0.

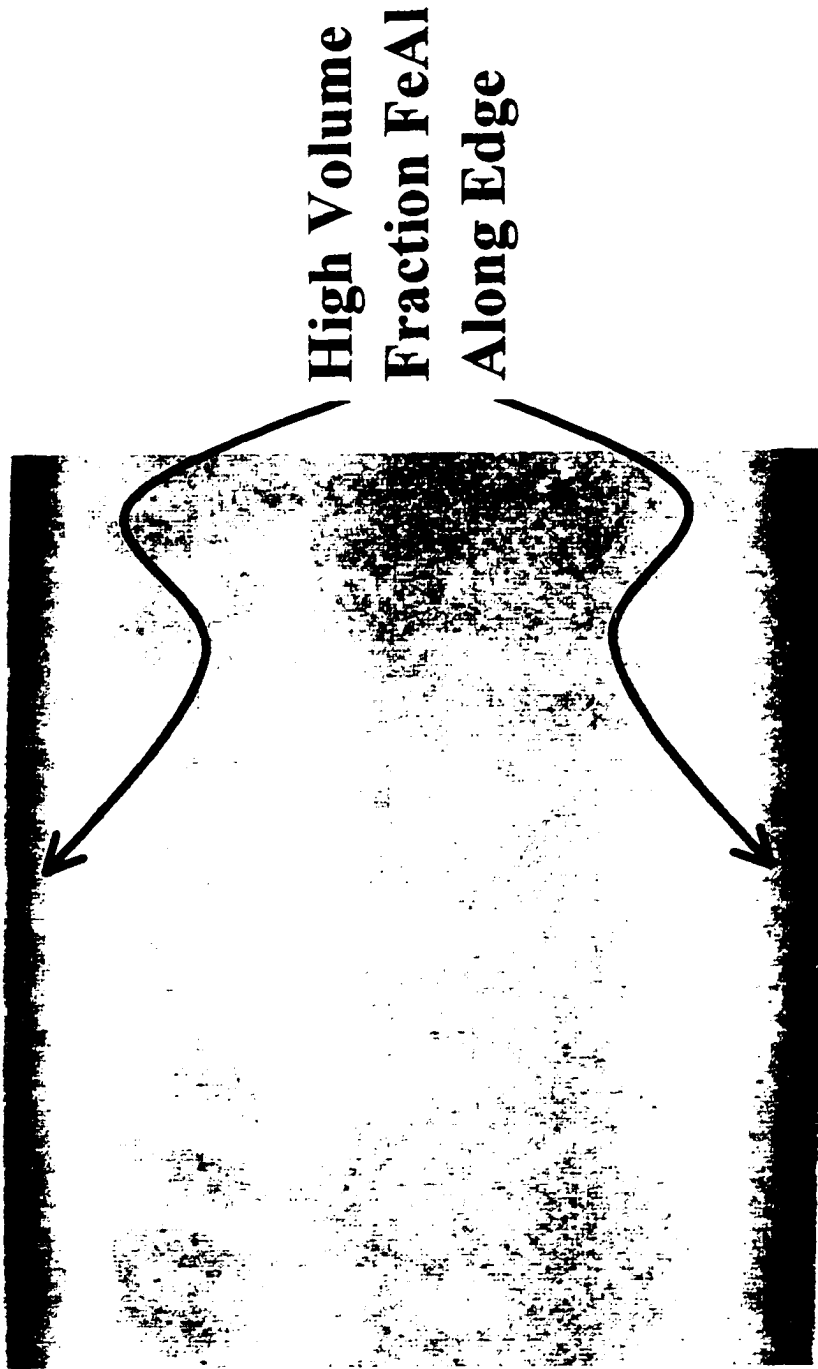


Figure 5-8: Normal edge symmetry. The specimen is sheet 41 at position 30.

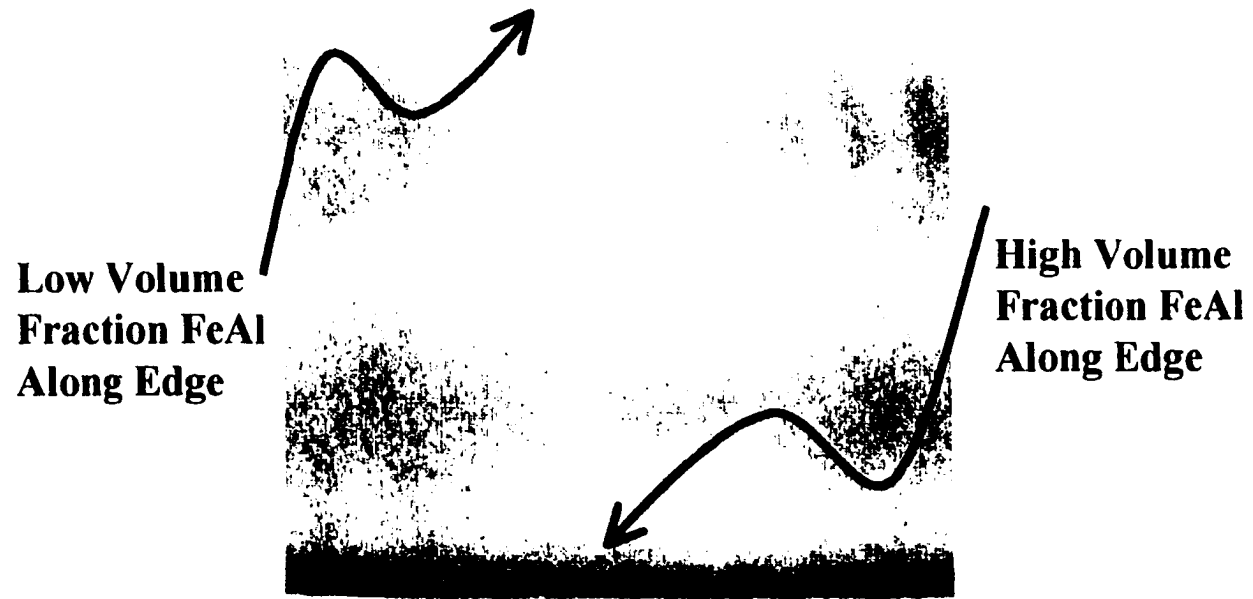


Figure 5-9: Asymmetry of green sheet edge due to roller misalignment. The specimen is sheet 23 at position 30.

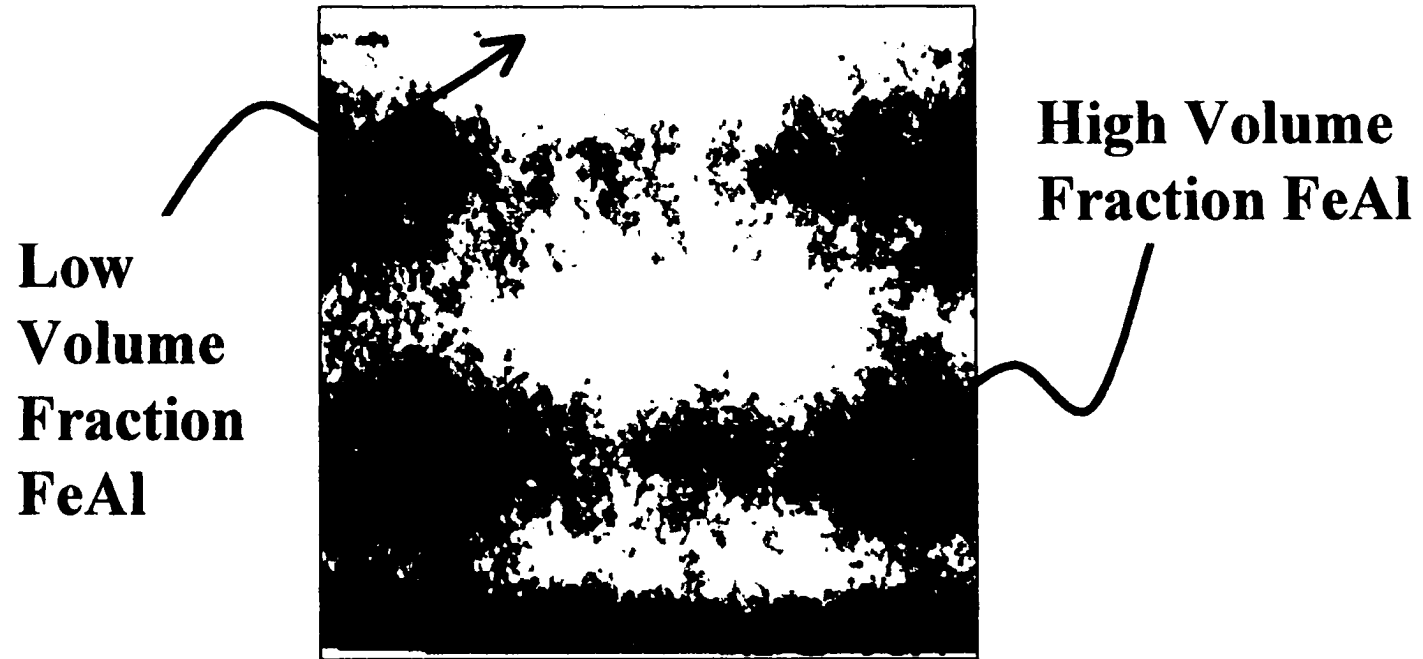


Figure 5-10: Transverse variation in FeAl volume fraction. The specimen is sheet 23 at position 30.



Another feature often observed was caused by the unstable flow and powder segregation associated with the end of one blend charge and the start of the next. Vibration during dispensing of the blend results in segregation with the heavier alloy preceding the lighter binder. On average this separation is minor, however the integrated effect at the end of the charge is noticeable. The last fraction of hopper material, 10% or so, is poorly mixed. Figure 5-11 illustrates how the contrast in binder and alloy rich regions highlight the differential flow of the blend from the hopper into the roller nip. A significant change in the morphology was often associated with the addition of the next charge. The left end of the image in figure 5-11 represents the normal compaction situation with the blend flow at some steady state. The right side of the image illustrates the unstable flow associated with blend separation and the addition of the next hopper charge. Figure 5-12 provides a magnified view of the unstable region at two different contrast levels.

The processing and handling of material with high gradients in alloy volume fraction created particular problems. The section of green sheet, described above, suffered damage during shipment from the laboratory back to the manufacturer. Figure 5-13 shows the original green part (A) adjacent to the same section of de-bindered material (B). The most striking features are a large transverse crack and material along the opposite edge which has dropped out or chipped away. Both of these features are associated with regions of high gradients of alloy volume fraction. Recall that the measured strength of a compact passed through a minimum and then began to increase with a decrease in alloy volume fraction. Gradients such as those seen here contain boundaries of "minimum strength" composition. It is these contours, particularly along edges, which are subject to damage.

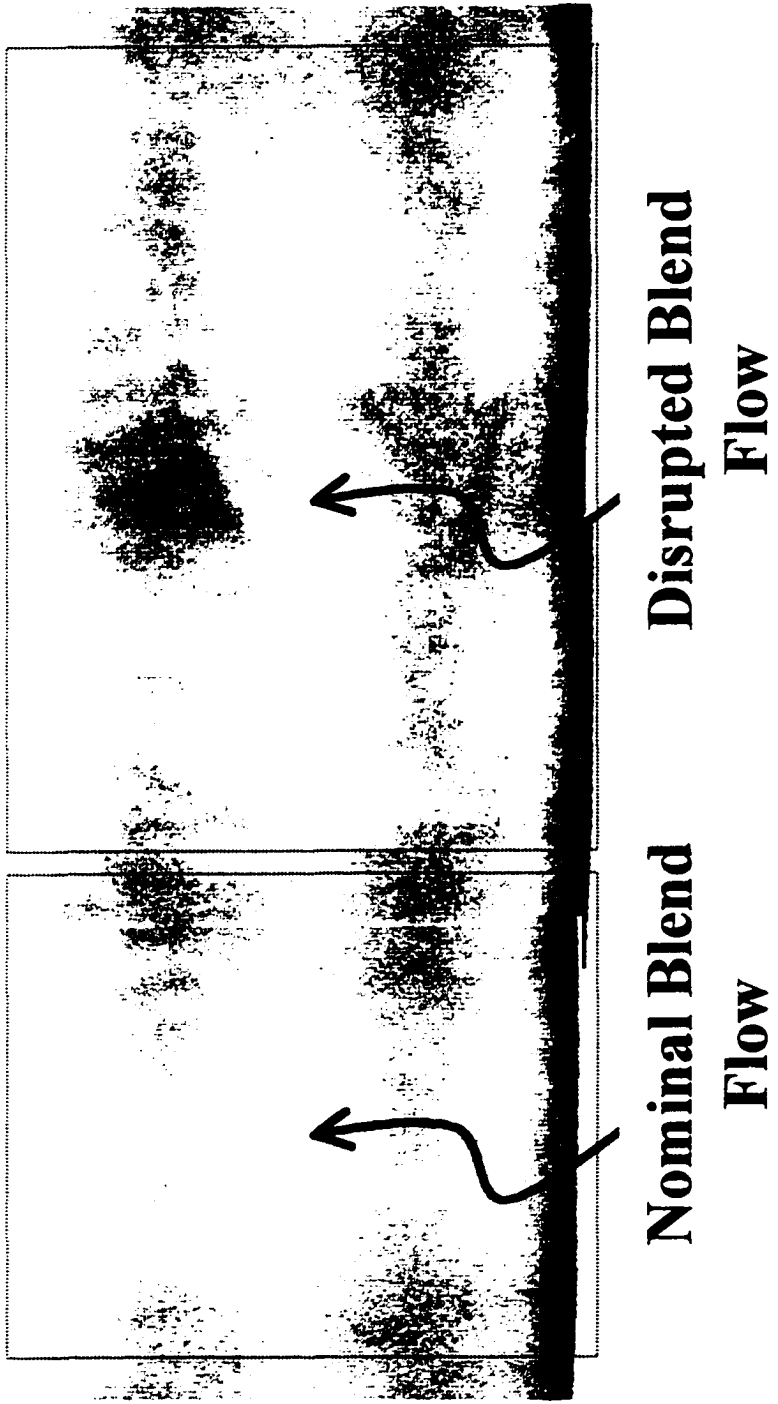
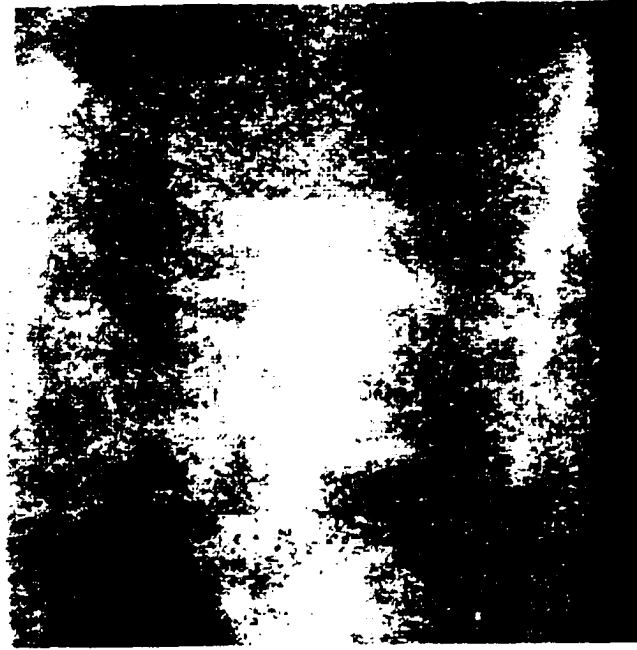


Figure 5-11: Disruption of blend flow from feed hopper. The specimen is sheet 23.

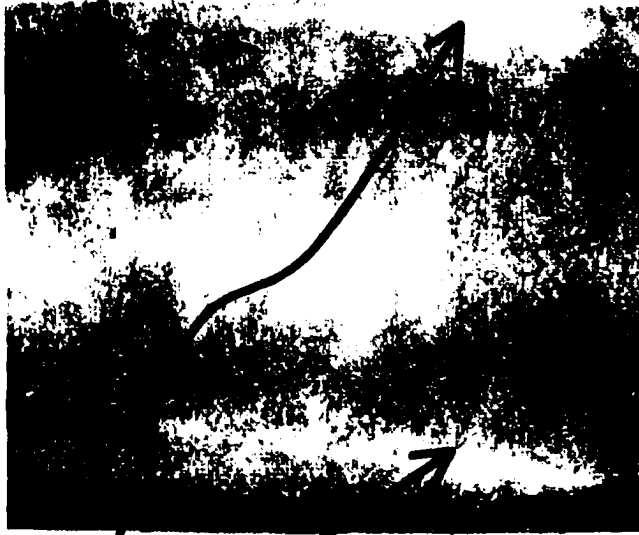


**Low Contrast**



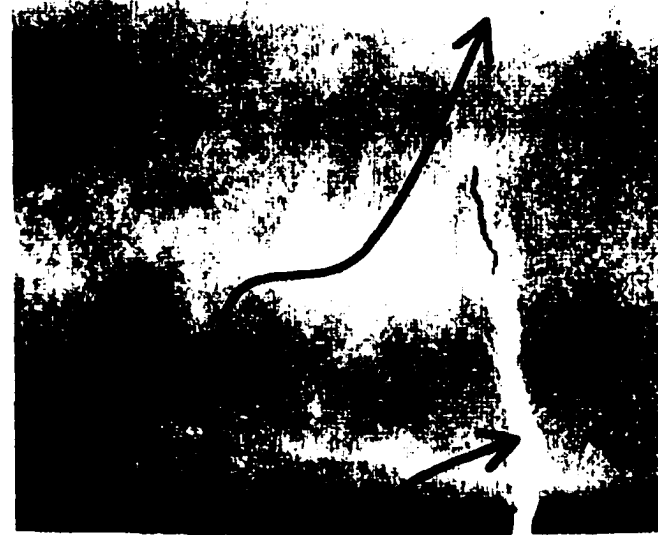
**High Contrast**

Figure 5-12: Morphology resulting from unstable blend flow. The specimen is sheet 23 at position 50.



**Low Volume Fraction FeAl**

## **A - Green Sheet**



**Crack and Edge Chip**

## **B - Sintered Sheet**

**Figure 5-13: Crack in sintered green sheet resulting from low volume fraction of FeAl during compaction of the green sheet. The specimen is sheet 23 at position 50.**

Another important outcome of comparing the green and de-bindered material is that the overall morphology is the same. This proved the capability to predict features one step into the process. It should be pointed out that the thermal impedance of the de-bindered material is several times lower than that of the green sheet. This is consistent with the green sheet microstructure previously described.

A third spatial frequency was believed to be associated with the drive train of the roller mill. Unlike the first two transverse variations previously described this mode was indicated by an alloy volume fraction modulated in the longitudinal direction. This variation is visible in figure 5-14. The spatial frequency was found to be about 3.3 cm (1.3") and the temporal frequency was about 0.13 Hz. Figure 5-15 shows a plot of the intensity profile along the at the transverse position indicated in figure 5-14. It was recommended that the manufacturer investigate the vibrational modes and mechanical specifications to identify likely causes.

It has been noted that a majority of the crack failures occurred during the densification to 0.25 mm (0.010") material. Failed samples were inspected with a digital x-ray imaging system provided by NASA. This instrumentation provided a full field map of x-ray extinction through the 0.25 mm (0.010") thick FeAl sheet. This data confirmed two facts. First, the morphology of densified alloy sheet is a directly related to the morphology of the green sheet. That is, regions of low FeAl volume fraction in the green sheet can be spatially correlated with regions of high porosity in the densified sheet. Secondly, these porous flaws give rise to transverse cracking. Figure 5-16 is an x-ray image depicting transverse line scans which were obtained for both the x-ray extinction and thermal effusivity. Figure 5-17

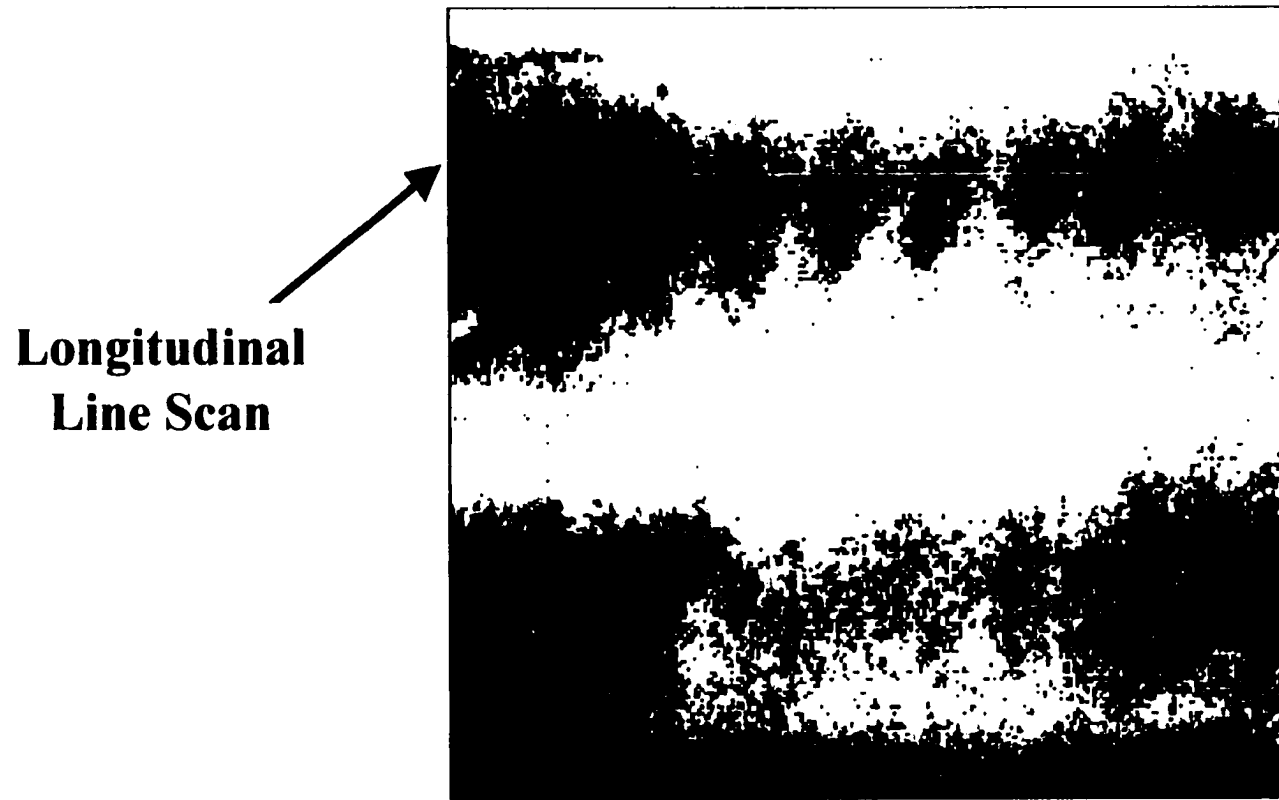


Figure 5-14: Characteristic longitudinal variation of FeAl volume fraction. The modulation is believed to be caused by characteristic mechanical modes associated with the mill. The specimen is sheet 21 at position 10.

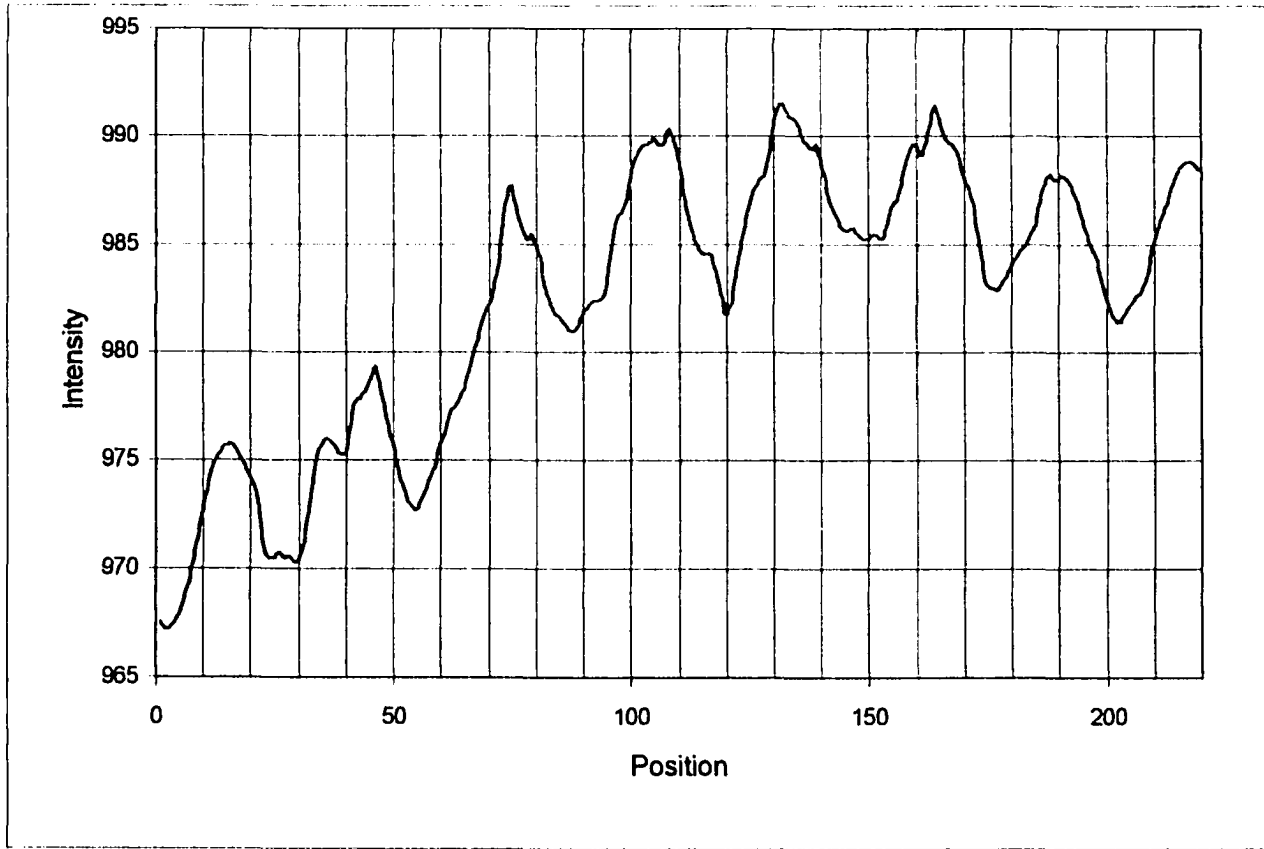


Figure 5-15: Longitudinal line scan illustrating the longitudinal modulation of FeAl volume fraction. The scan represents the intensity values along the line shown in figure 5-14.

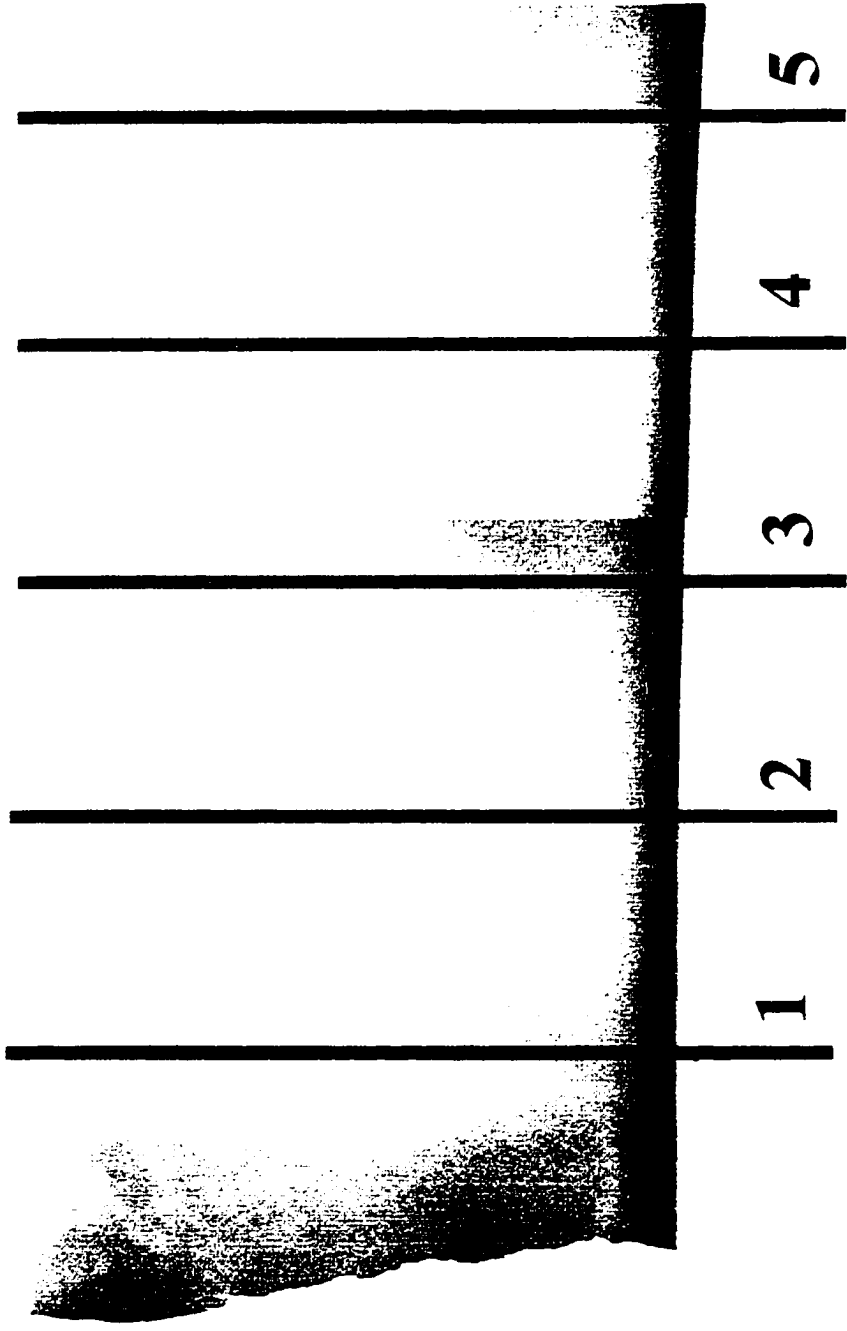


Figure 5-16: Digital x-ray image of sample 23B.



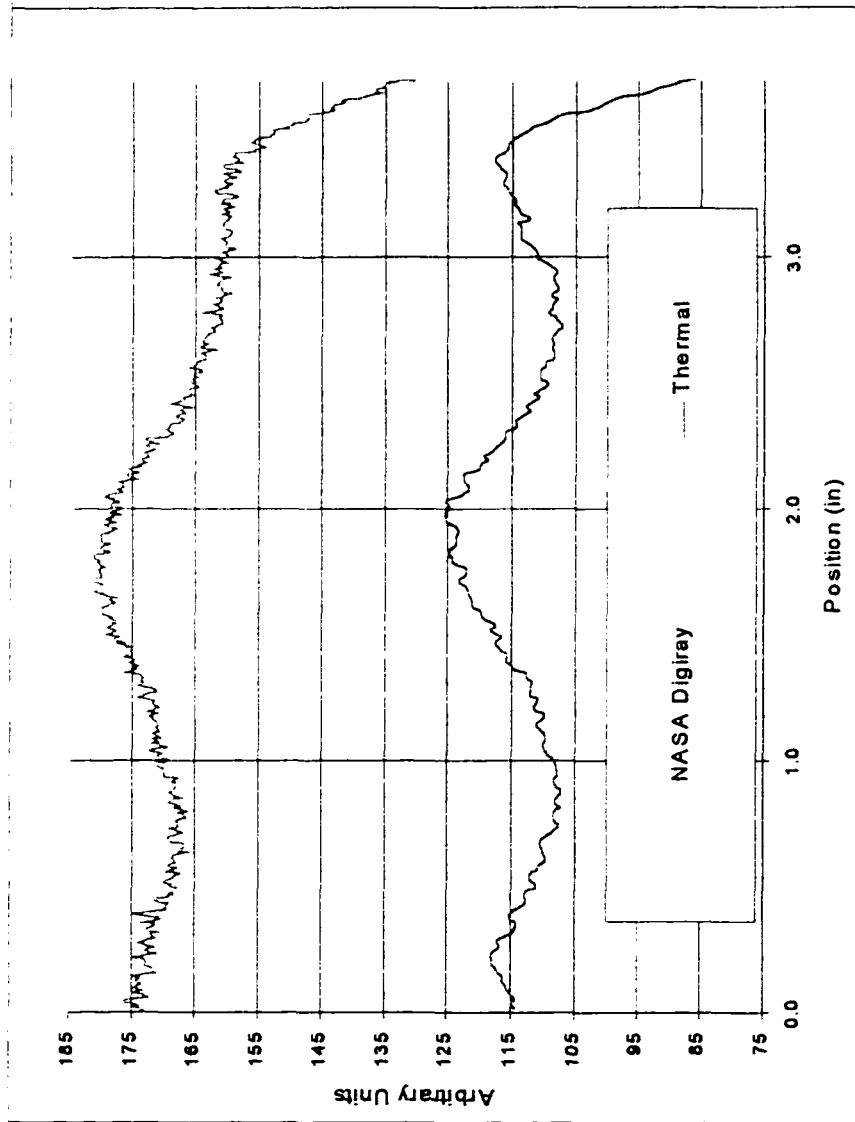


Figure 5-17: Transverse digital x-ray and thermal signals both indicate the relative alloy volume fraction.

compares the two signals (averaged over five transverse positions).

As an example figure 5-18 compares data for specimen 41. The regions of high green sheet thermal impedance are correlated with areas of low x-ray extinction. Both images indicate alloy poor regions as light grey levels. The machine direction is to the left. In the reference frame of the page the roller direction is to the right. The location of the crack precursor and the crack formation mechanism is clear. The region of green sheet resulting in high porosity sintered sheet is rolled from left to right. As the distributed void volume is displaced to the right it is concentrated to the point where a crack occurs. This crack easily identified by the production inspector and the surrounding porosity is clearly shown in the x-ray image. Another example of this phenomenon was a band of low density green material which extended most of the bottom length of a sheet. Figure 5-19 shows two sections. The band began about 12 cm from the machine end and extended over 65 cm along the bottom quarter of the sheet. The sample survived roll densification down to 0.25 mm (0.010") yet numerous visible cracks appeared in the last few of the 40 roll passes. Digital x-ray imaging (figure 5-20) reveals the extensive cracking associated with this morphology. This precursor was particularly prone to crack development because of the high transverse gradients existing between the band and the lower dense edge. During rolling this band acted as a stress relief zone. The band actually buckled out of the plan of the sheet. The significant shear stress, created by the differential strain of the high and low density regions, became concentrated in the crack tips. In this case the dense regions above and below the band act to arrest crack propagation.

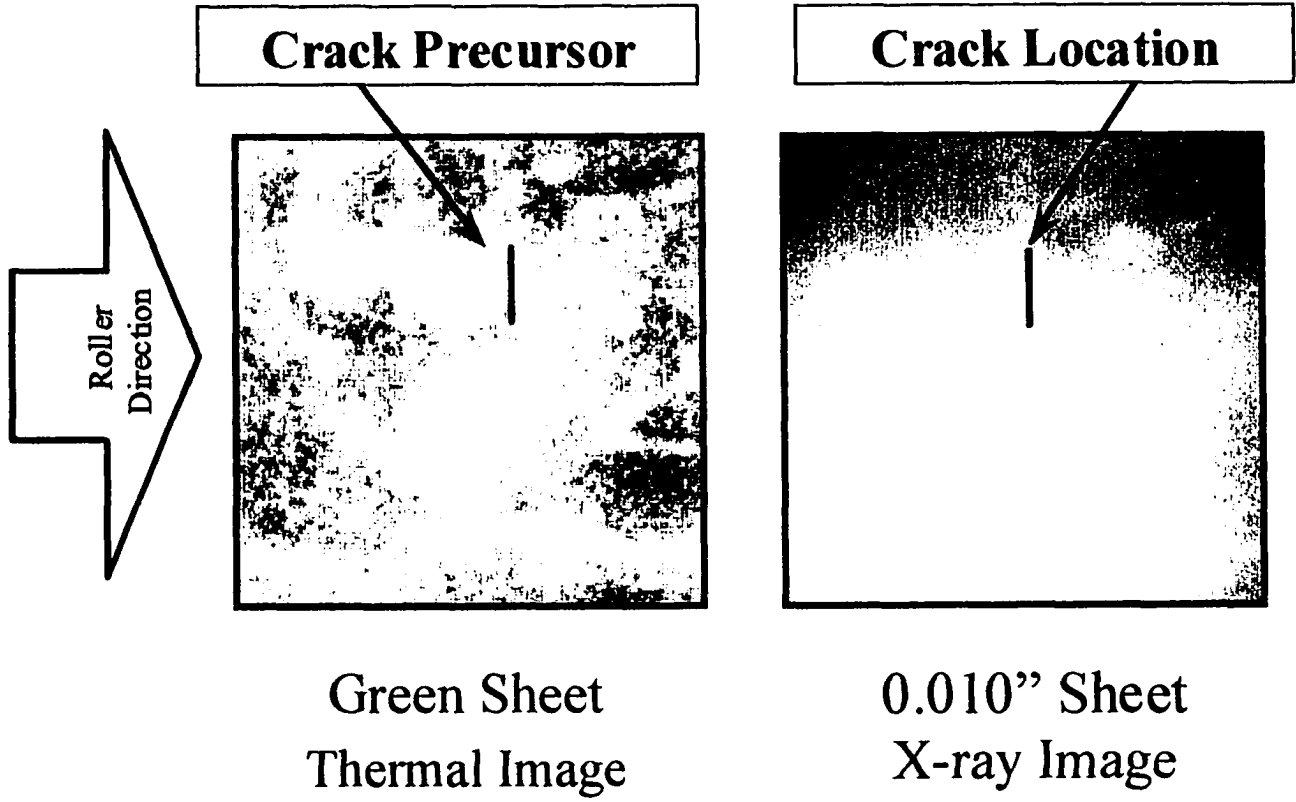


Figure 5-18: Location of low FeAl volume fraction in the green sheet predicts the location of cracks resulting from rolling down to 0.25 mm (0.010"). The specimen is sheet 41 at position 0.

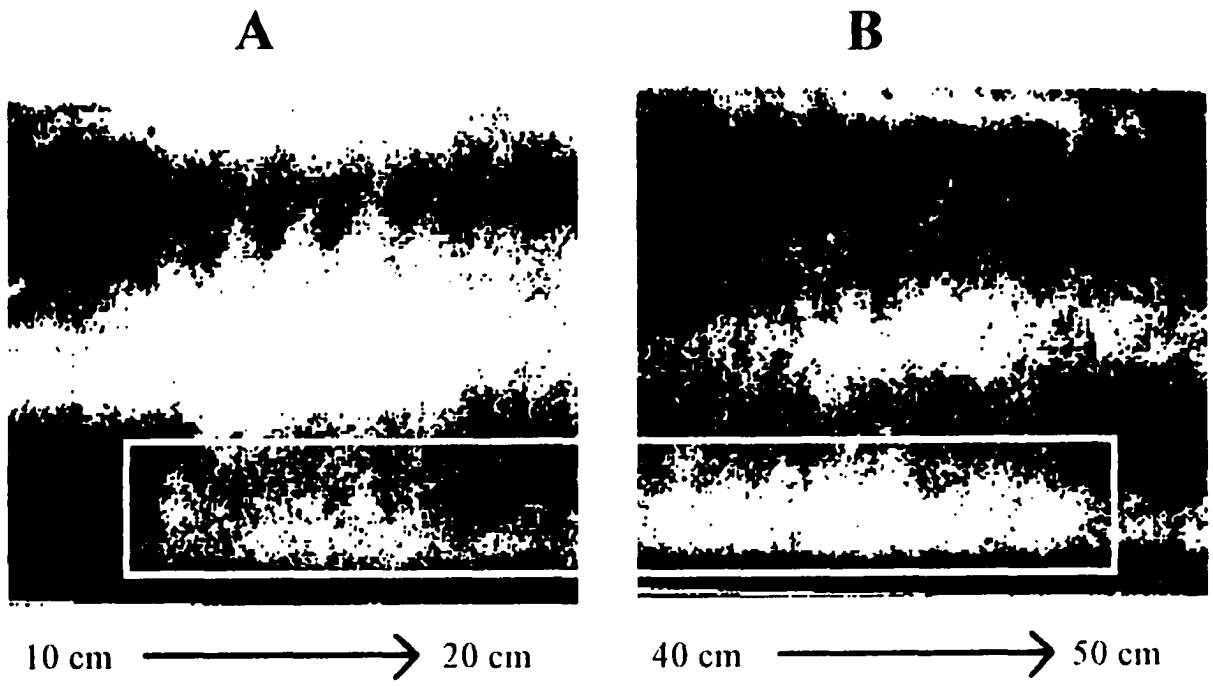


Figure 5-19: Longitudinal band of low alloy volume fraction in this green sheet resulted in severe cracking during rolling down to 0.25 mm (0.010").

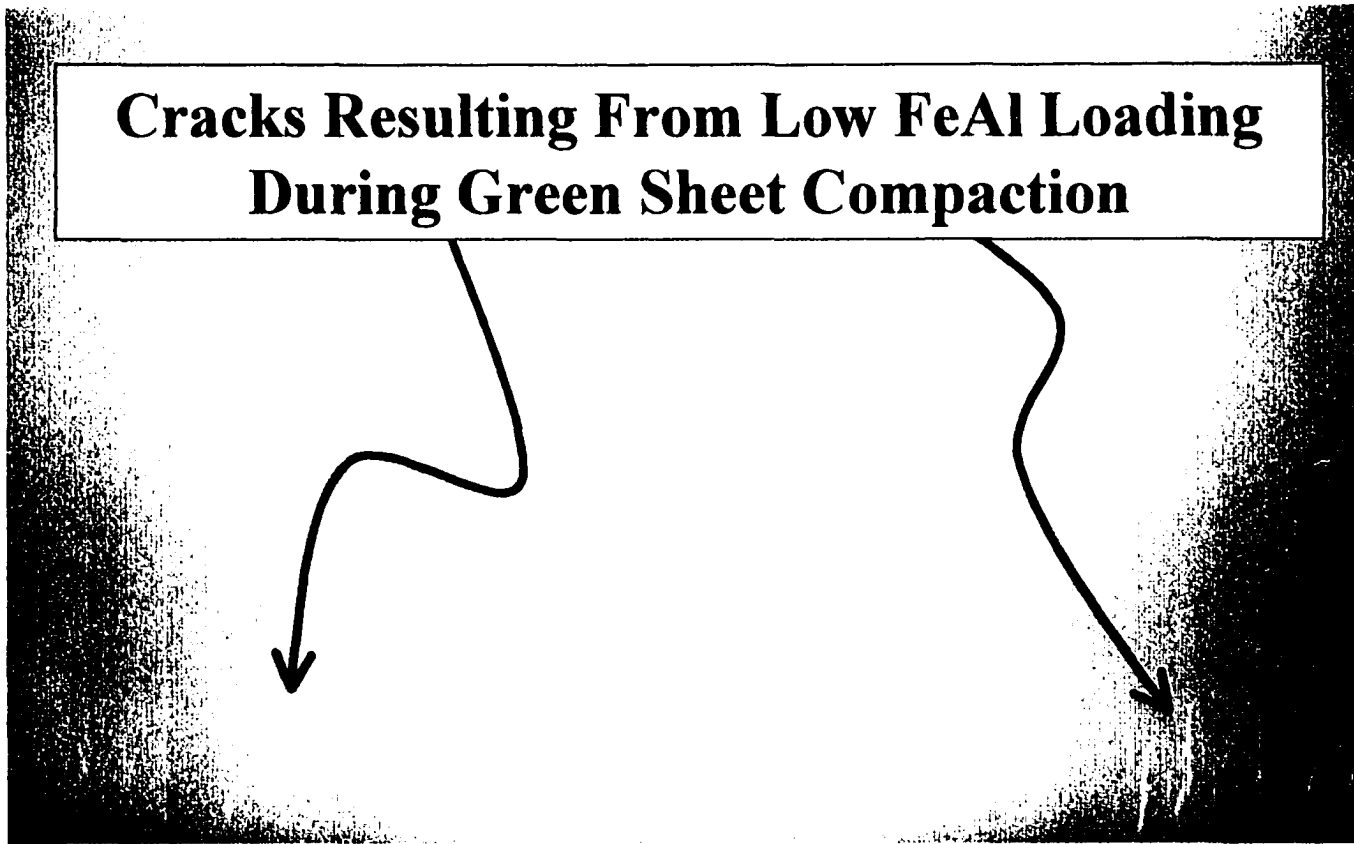


Figure 5-20: Severe cracking in the 0.010" sheet associated with low alloy volume in the green state.

#### 5.3.4 Development of green sheet conformance criteria

The section above describes qualitative characterizations of green sheet heterogeneity. The results confirm that the heterogeneity, as measured by the relative effusivity of the sheet, is indicative of FeAl sheet morphology throughout the process. The most significant flaw precursors, those responsible for crack formation, can be predicted based on green sheet morphology. The identification of prominent spatial patterns provides insight into flaw formation while the statistics of the thermal impedance map are useful in assessing the risk of crack formation. In this section a quantitative conformance criteria is presented which takes into account the natural variations in the manufacturing process, the severity, and the location, of the FeAl volume fraction deficiencies. The approach uses the population of reliable green sheet, that is the green sheet which survived processing into the 0.20 mm (0.008") thick alloy product, as the reference or "golden standard". This population will be referred to as conforming green sheet. Material which fell outside a confidence interval, was identified as non-conforming and unfit for further processing. This conformance criteria was tested by using it to assess green sheets with known defects.

It has been shown that regions of green sheet with low alloy volume fraction are associated with cracking, sheet deformation, and are indicated by relatively low effusivity. The conformance criteria was developed to reflect this. The earlier convention of assigning a bright grey scale image value to a low effusivity is maintained. All effusivity values are normalized to the mean effusivity of the conforming population which consists of approximately  $2 \times 10^6$  points. The relative effusivity data is presented in a format similar to that for the existing green sheet x-ray inspection unit. This format is intuitively familiar to production

personnel. For clarity the criteria is presented in the context of a single specimen followed by a description of the statistical conformance criteria. Figure 5-21 is a relative effusivity map of a non-conforming green sheet specimen. The vertical lines represent different pixel columns within the image. These columns are the basis for the quality assessment. The population of conforming material provided 7.800 profiles while 1.500 profiles were available from the population of non-conforming material. Figure 5-22 depicts two curves derived from the image in figure 5-21. The thin line represents the average effusivity profile, along all columns, while the heavy line represents the profile along the dotted line of figure 5-21. The details of the profile features will be discussed later.

Figures 5-23 and 5-24 provide a comparison between the statistics of the conforming and failed green sheet. These curves represent the mean with a three standard deviation confidence interval ( $\pm 3$  SD). The confidence interval is a parameter that can be varied based on the capability of the process. It was noted that the majority of the material was fabricated with measurable wedge due to roller miss-alignment. This is not surprising since this control setting is not typically changed during the course of a particular production run. The asymmetry of a given profile can be used as a good indicator of roller alignment. It was reasoned that wedge in the opposite direction would not change the quality of the material. In other words, symmetry in the wedge feature should be allowed in the conformance criteria. Thus the worst case end was reflected about the center of the "average conforming part" to provide the symmetry in figure 5-23. A comparison of the mean curves shows that the center region of the conforming sheet is much more uniform than that for the failed sheet. In addition, the standard deviation of the data is greater

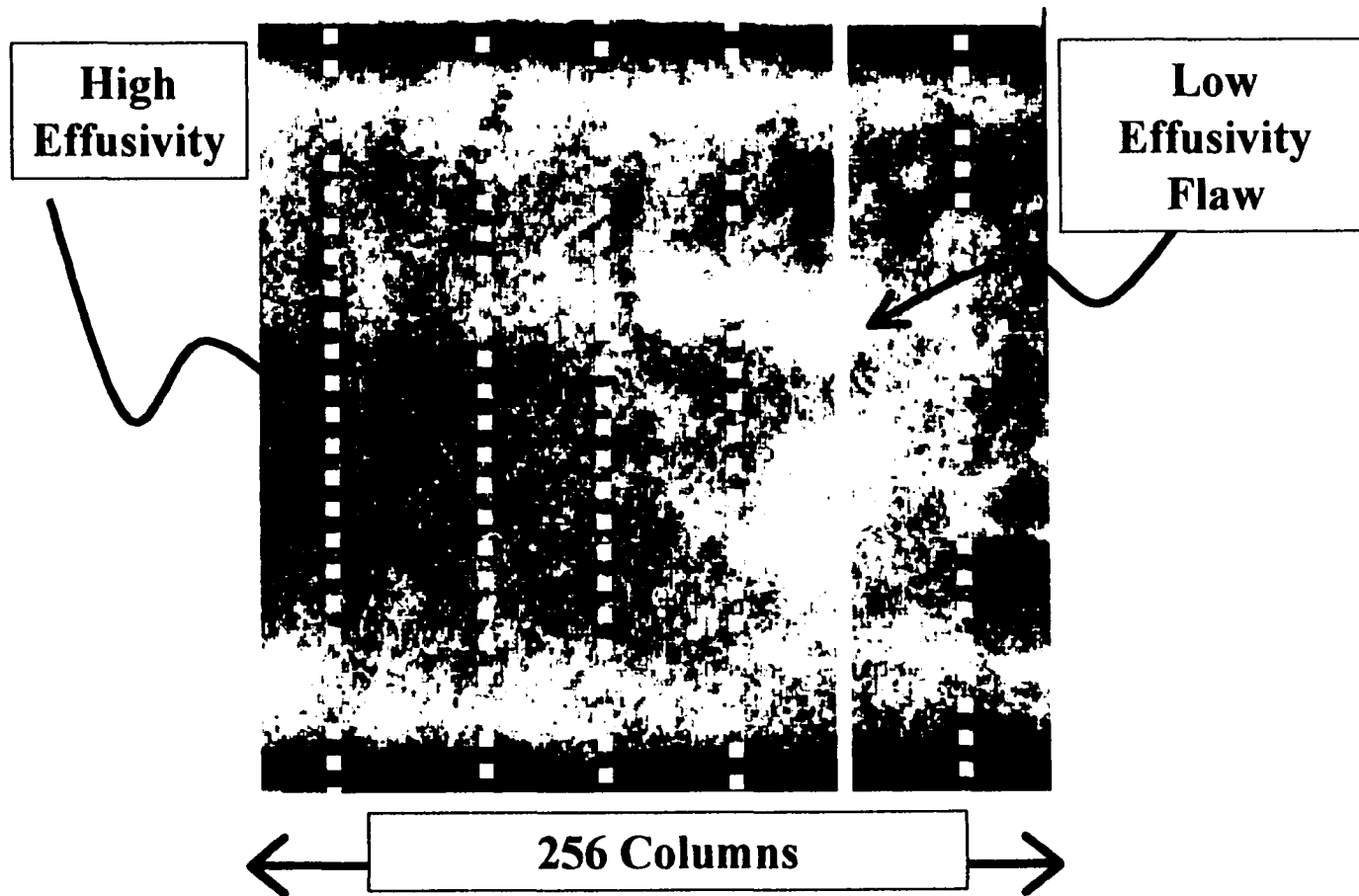


Figure 5-21: At early times variations in the thermal map is indicative of the relative effusivity across the green sheet.



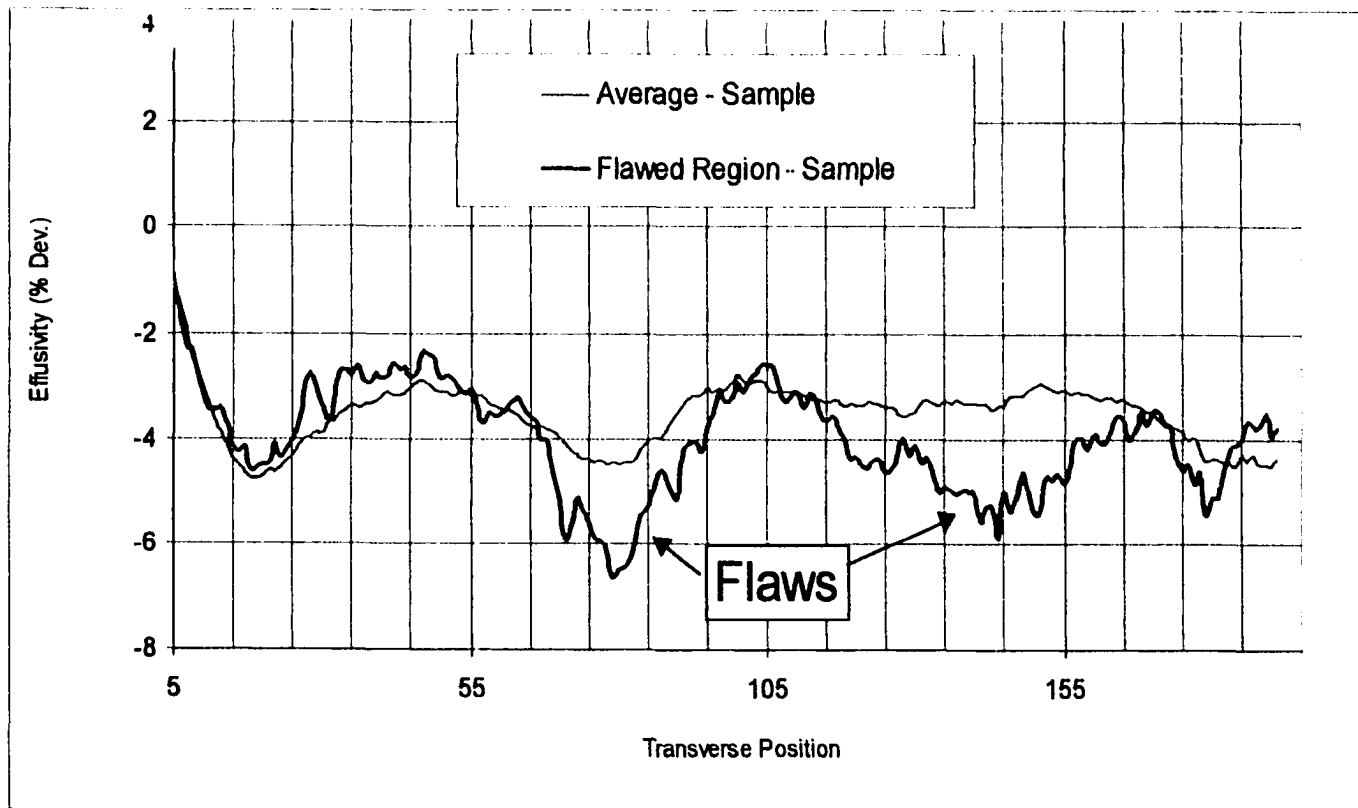


Figure 5-22: Transverse relative effusivity profiles associated with Sheet 41. The upper line is the average for the sheet. The lower line represents a line scan across regions which cracked during densification.

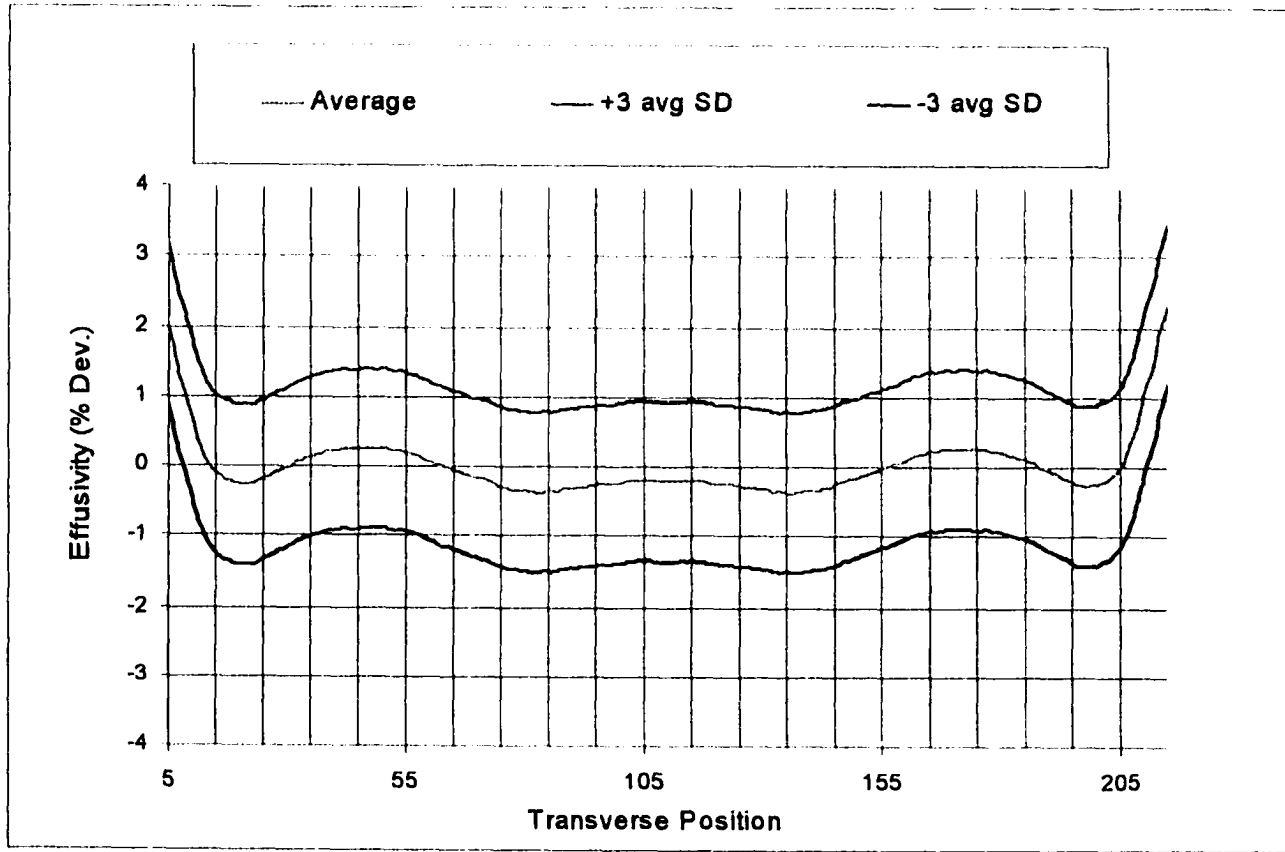


Figure 5-23: Transverse relative effusivity representing the population of green sheet which survived densification to provide acceptable alloy sheet. This profile is the basis for the conformance criteria.

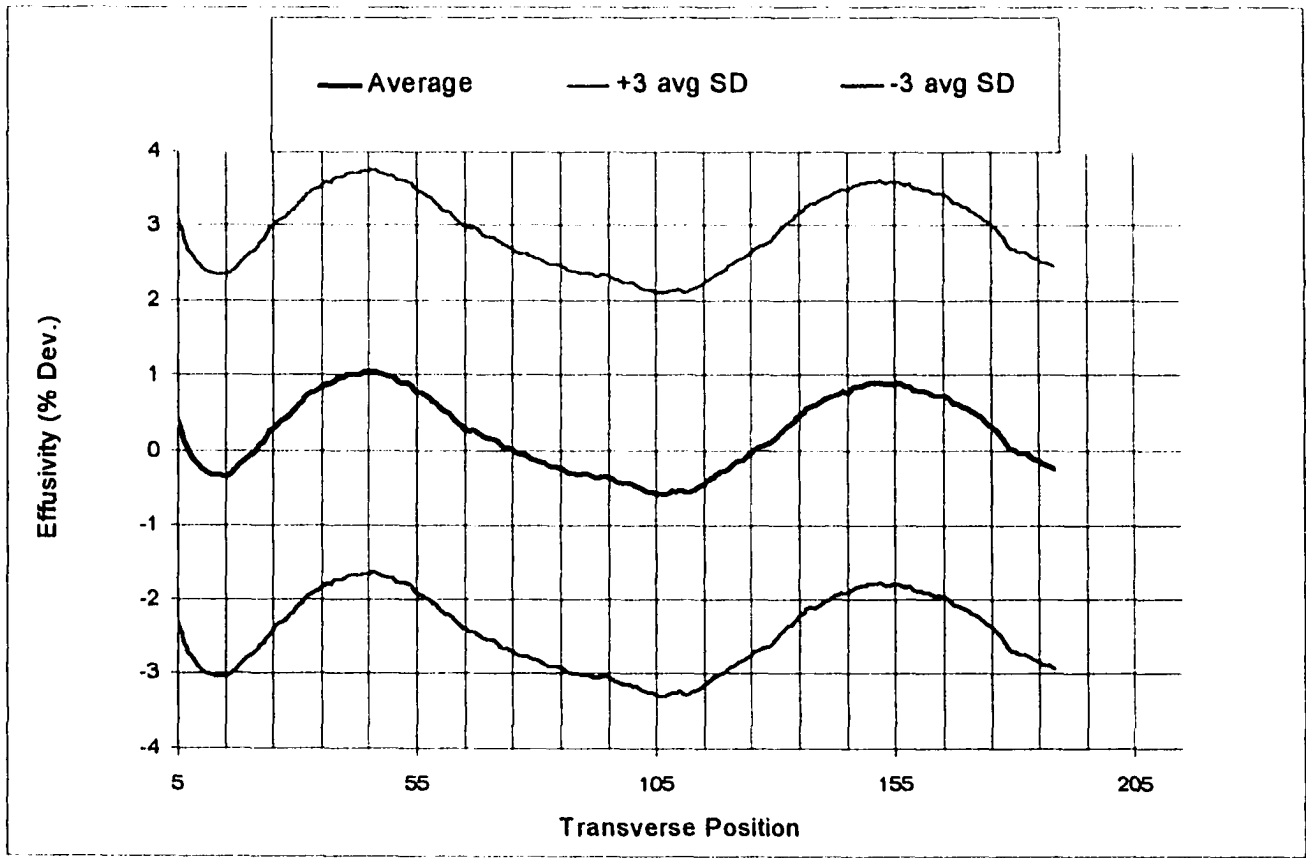


Figure 5-24: Transverse relative effusivity representing the population of green sheet which failed during the attempt process the green sheet. Note the increased variation from the profile in figure 5-23.

for the lower quality material. These results are consistent with the image coefficient of variance statistic which predicted an increased probability of cracking with poor mixing. Both of these statistical results are important because they demonstrate that the random variations associated with the inspection (e.g. timing of the excitation and camera drift) are small compared to the important variations in the material.

Figure 5-25 illustrates the data for the flawed region, offset below zero for clarity, displayed with the conformance band. Two features are significant. First, both the mean data and the data for the flawed region are well outside the conformance tolerance. Second, the two regions with low FeAl loading show up as distinct deviations from the sample mean curve. These regions are labeled as flaws. The top flaw resulted in a crack upon rolling down to 0.25 mm (0.010") and the sheet was removed from the process. It is very likely that further processing would have resulted in a defect adjacent to the crack. The location of the flaw precursor is determined from the zero crossing of the effusivity derivative (see figure 5-26). A measure of the width of the flaw can be determined from the distance between the maximum and minimum of the derivative curve.

The conformance criteria described by figure 5-23 was applied to all of the samples used in the process study. Figure 5-27 is an example of green sheet which contained defect precursors. The red line indicates the acceptance band. The blue line represent the relative effusivity along the region of the sheet where the material failed. Figure 5-28 is an example of green sheet which yielded acceptable material. The blue line represent the average over the sample. This method correctly categorized all of the 20 sheets as to their final disposition (i.e. pass or fail) during processing. Samples 14A, 21-A&B, 23A.

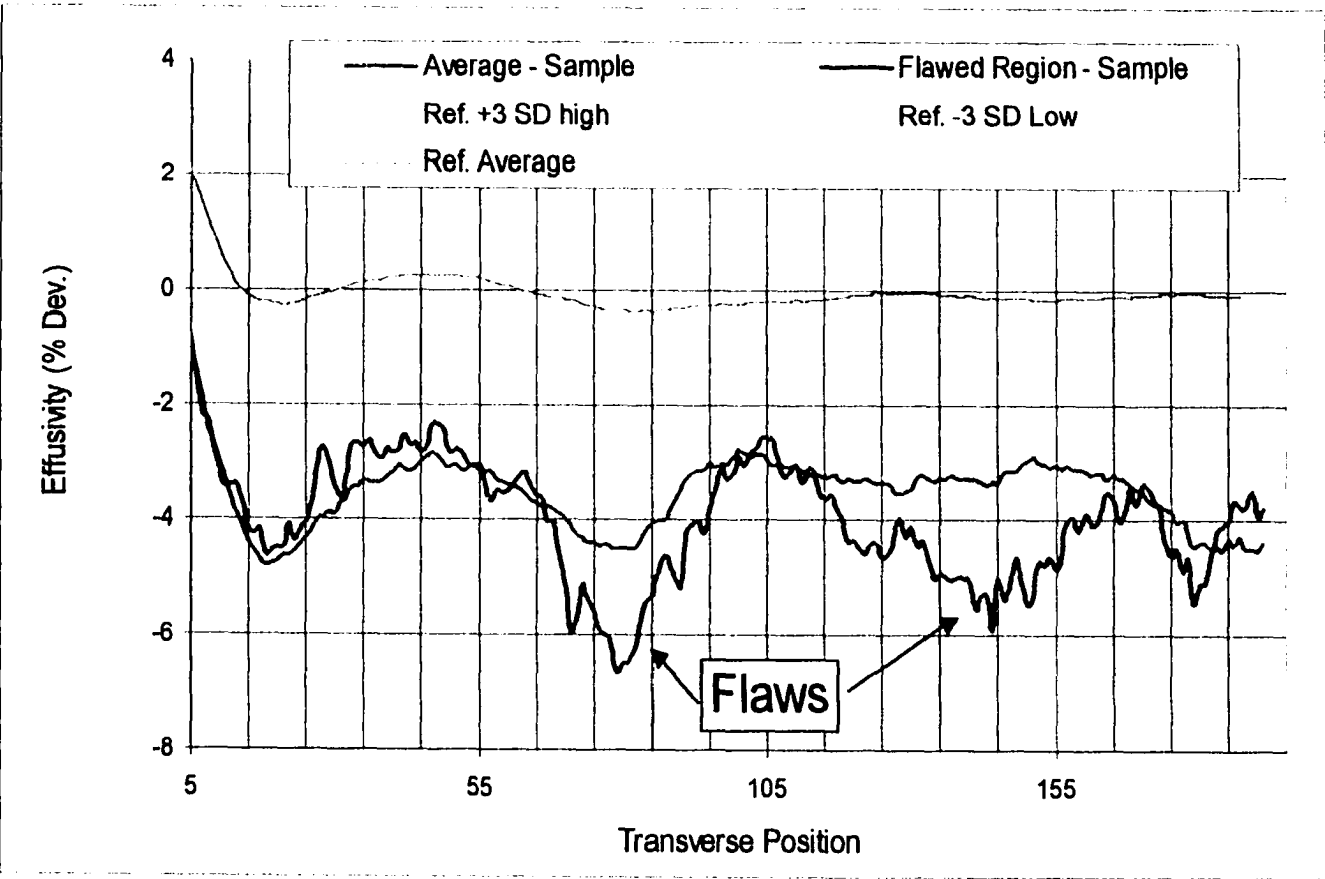


Figure 5-25: A comparison of the relative effusivity profiles for sheet 41 and the conformance standard predicted that the material would fail during post compaction processing.

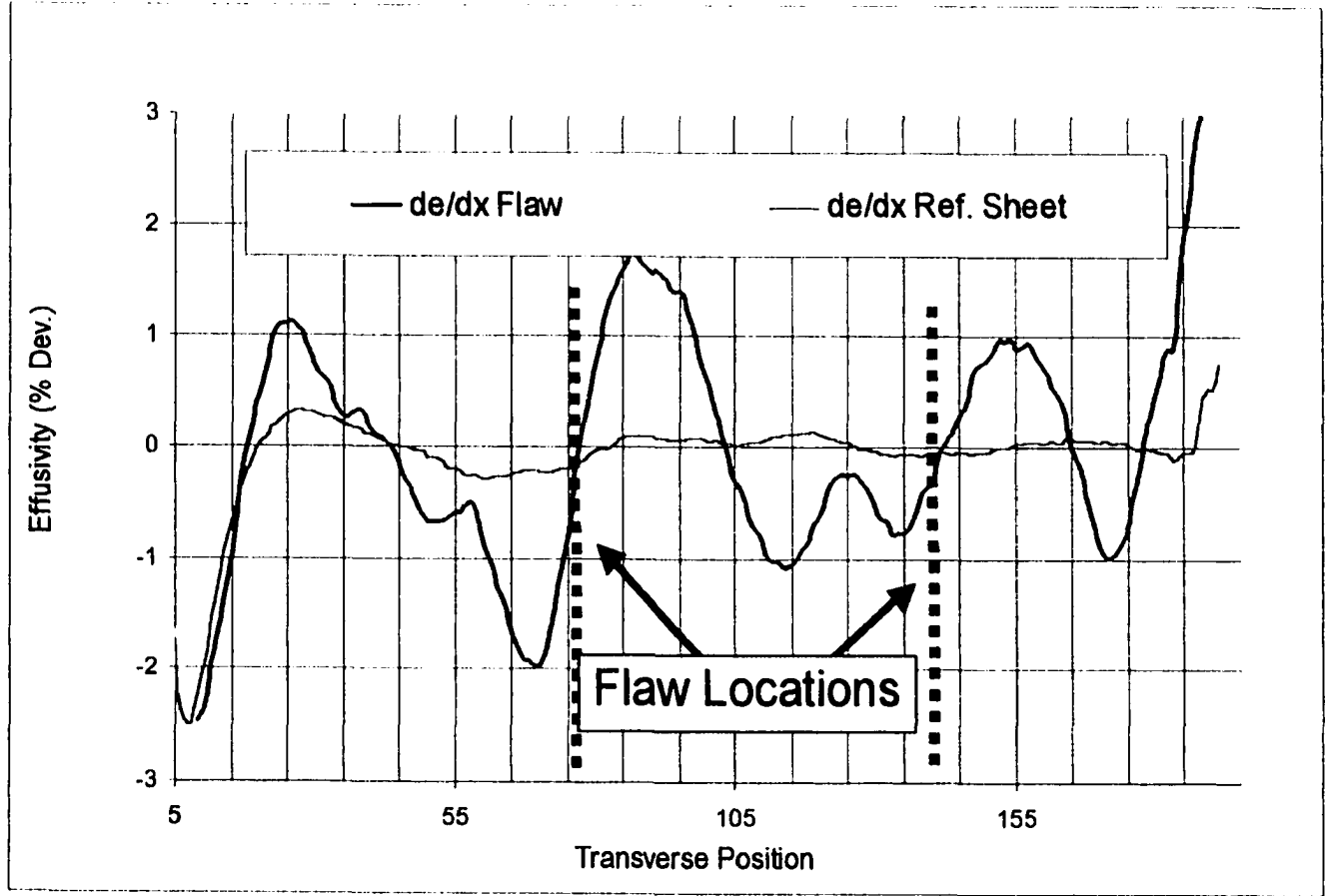


Figure 5-26: The zero crossing of the spatial derivative of the relative effusivity profile locates the green sheet flaw.

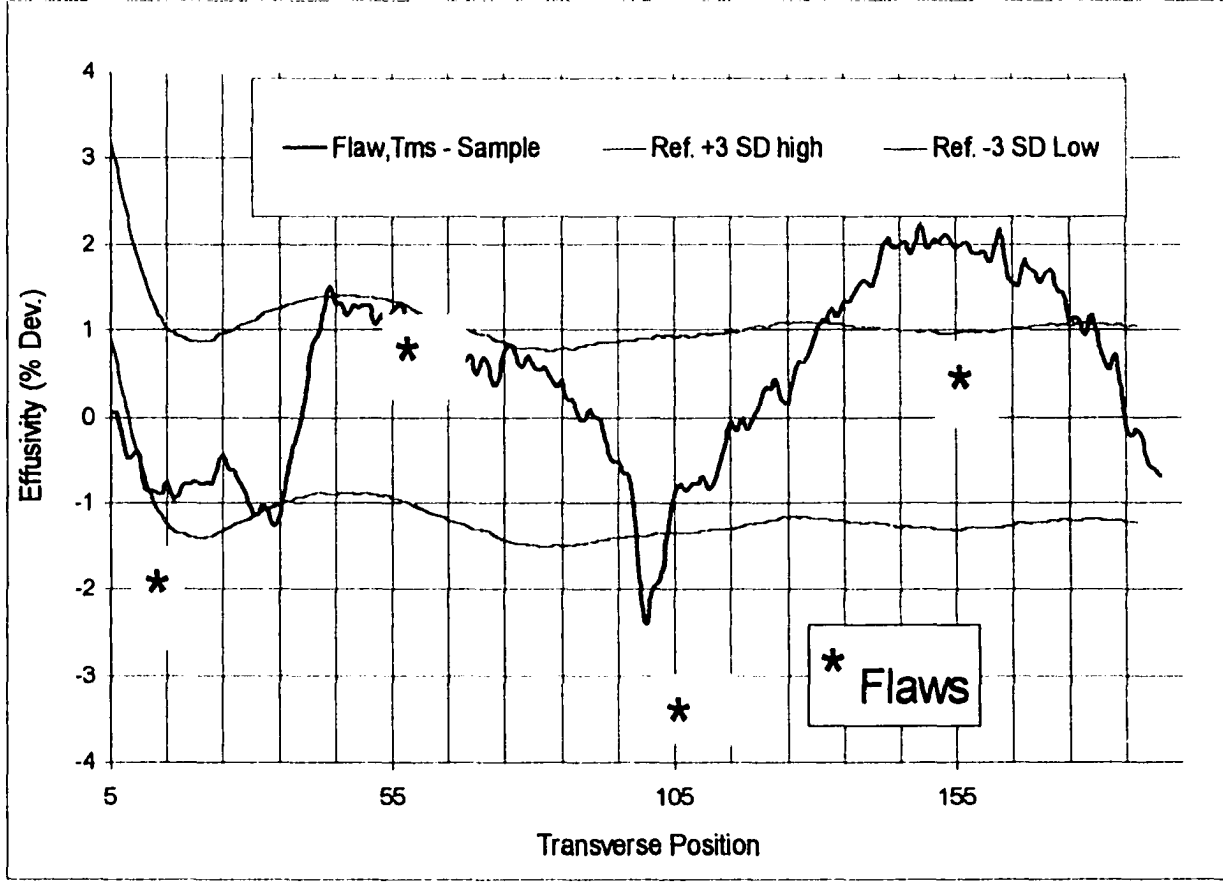


Figure 5-27: Relative effusivity profile showing that green sheet defect precursors fall outside the conformance band.

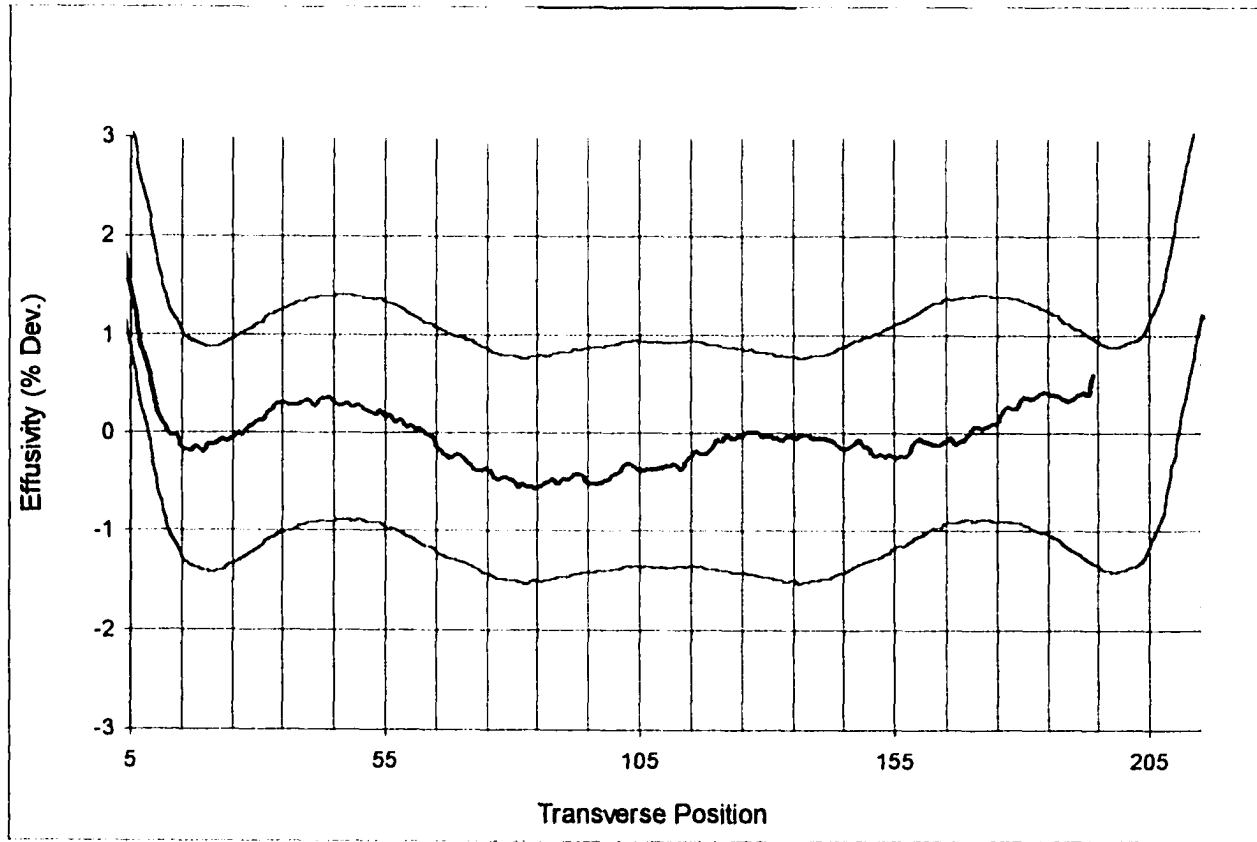


Figure 5-28: Relative effusivity profile for "good" green sheet. This sample provided acceptable fully dense alloy sheet upon processing.



and 41-A&B failed during processing while samples 12-A&B, 32-A&B, 34-A&B, 42-A&B, 52-A&B, 54-A&B survived to provide acceptable FeAl sheet. Determination of the methods statistical capability will require improvement in the reference samples and primary methods for flaw identification within manufacturing. The conclusion is that the developed criteria is as effective as the current manufacturing methods used to detect flaws in partially processed FeAl material. However, the advantage is that the thermal method predicts these defects by identifying their precursors in the green state. It is anticipated that as process development continues two factors will require the confidence interval to be tightened. First, as the manufacturing capability is improved the catastrophic flaws will be less frequent. In addition, less obvious and severe defects which have some yet undetermined distribution in the currently acceptable product would become of interest to detect. It is anticipated that the detection of such defects would improve machinability and component reliability. At some point in the process refinement a significant fraction of the production material will fall within the  $\pm 3SD$  band. Further utility of the method would require the confidence interval to be reduced appropriately.

## Chapter 6

# Conclusions

This research provides for a quantitative, non-contact, real-time method of inspecting 100% of the powder metal composite green sheet produced by an existing industrial process. The powder metallurgy process of interest involved the production of thin, approximately 200  $\mu\text{m}$  thick, metal iron aluminide alloy sheet. The starting green sheet composite, approximately 700  $\mu\text{m}$  thick, is formed by roll compacting a mixture of powder alloy, binding agent and solvent. The production rate is about 300  $\text{cm}^2/\text{min}$ . The green sheet then undergoes a series of process steps (binder elimination, densification, sintering, annealing) to form the final Fe-Al sheet product. The intermediate products have a thickness from 300  $\mu\text{m}$  to 200  $\mu\text{m}$  thick and densities as low as 60% of the theoretical density (about 6.1  $\text{g}/\text{cc}$  for the fully dense material).

The guiding principle has been to minimize the impact of defects by identifying the most significant flaws as early in the process as possible. Process factors associated with the severity and morphology of the composite heterogeneity were identified. The rela-

tive mass distribution of iron aluminide particles was influenced by both local compaction pressure and mixing of the alloy/binder material. The high viscosity of the compact and the characteristically low malleability of the iron aluminide particles inhibit modification of the mass distribution once the green sheet is formed. Process variables such as mixture feed rate, roller speed, pressure and alignment are candidates for statistical process control (SPC) using feedback from the inspection system. Early detection provides the opportunity to correct for defects downstream in the process. Alternatively, if the flaw cannot be repaired, the defective part can be systematically removed from the process before disrupting product flow or investing process resources in a bad part. This provides the opportunity for recycling the green sheet.

Several challenges were presented by this project. The current inspection is a combination of visual inspection by an operator and a scanning x-ray unit. This instrument samples the transmission of the material at some predetermined number of areas. The aperture has a sampling area of about 160 mm<sup>2</sup>. The maximum on-line sampling rate was approximately 50% of the manufactured material. While this approach is capable of detecting gross defects it does not have the capability to detect green sheet precursors resulting in down stream defects. The physical characteristics of the green sheet required special consideration in development of an improved NDE technique. A non-contact technique was demanded since the material has minimal mechanical integrity. The green sheet has a very high electrical impedance and is non-magnetic, thus conventional electromagnetic techniques (eddy current, magnetic flux leakage etc.) were not viable. Thermal techniques have traditionally been used for material thicknesses several times greater than those of

interest here. At the start of this work, very little information was available on the thermal properties, defects properties, nor defect geometries associated with the composite. The composite material had not been characterized in terms of particle/binder distributions and the constituent thermal properties. Visual/optical inspection provided no indication of defect precursors.

A two phase research strategy was adopted to develop the inspection protocol. The first phase consisted of an exploratory effort to characterize the thermal properties and defects exhibited by the production green sheet. Artificial defects and part geometries were used to explore the sensitivity of several techniques. The ratio of effusivities (binder to alloy) was an order of magnitude greater than the ratio of the diffusivities. This clearly showed that the sensitivity to differences in volume fraction alloy would be better for front heating versus through heating. It was determined that the required data acquisition, for flash thermography, would be small compared to the translation speed of the material on the production line. Thus for flash heating the material was effectively static. In the second phase a prototype inspection system was assembled to provide for the required inspection rate and to simulate the geometry of the part presentation in the manufacturing environment. Thermal flash data were collected using a state-of-the-art high speed InSb focal plane array camera.

The heat transfer behavior of the compacted blends is consistent with the physical changes resulting from variations in compaction pressure and composition. The relationship between binder concentration and filler particle separation is dominated by two effects. At low binder concentrations the addition of binder lubricates the composite by reducing the

friction between the filler particles. Thus, for a given compaction pressure, the alloy particle separation decreases with binder addition and the volume fraction of alloy increases. As the binder level increases the effect of dilution dominates and the alloy volume fraction decreases. This effect is manifested in the bulk density, strength, and thermal transport properties of the compact.

Reference samples were fabricated to systematically study heat transfer properties as a function of composition and compaction pressure. A mathematical model, based on these data, has been developed which predicts heat transfer within the green compact. The model combines a generalized effective media model with the appropriate analytical solution to account for green sheet constituent properties, their distribution in the compact, and a nominal alloy particle shape factor. This provides a platform for exploring the sensitivity of the inspection technique to materials outside the current production process. Furthermore, it provides a basis for inspecting a variety of composite materials which may be very different from the Fe-Al green sheet. This capability is particularly important in an environment where the inspection technology is being developed concurrently with the manufacturing process. For example, if the production specification for the ratio of binder to alloy were to change during process development it would be necessary to validate the effectiveness of the current inspection method for the new composite. The amount of experimental work can be significantly reduced using results provided by the model. In the extreme case a completely different process may be used. Tape casting is being explored as a replacement for compaction. In the tape casting process the alloy powder is mixed with binding agents and significant quantities of solvent. The result is a slurry which is cast directly onto a

conveyor belt. The slurry is dried to a green sheet yielding alloy volume fractions in the same range as those of the compaction process. At the time of this study the tape cast process was not stable enough to produce significant quantities of material. However, the model should be useful in exploring the response of this material.

The green sheet is best described as a composite material with three constituents: alloy particles, binder, and voids. Based on the constituent densities, weight fractions, and bulk green sheet density the compact mass is estimated at about 97% alloy occupying only 10 to 60 percent of the bulk volume. The green sheet is a loose assembly of thermally conductive particles which are partly coated by a much less conductive binder. The binder agglomerates to form regions of low diffusivity and effusivity. In addition, significant voids are present throughout the structure. Experimental results show that the production material can be treated as one dimensional i.e. the lateral heat flow is not significant. This results from the fact that areas with significantly different thermal responses are on a dimensional scale many time larger than the thickness of the sheet.

A process tracking study was undertaken to identify key morphological features which related to product defects. Sheet material was rejected for several reasons: cracks, thickness, porosity, flatness, wedge, and camber. The 42% yield and flaw distribution of the sampled material was representative of the remaining material. The spatial correlation of defect locations with green sheet morphology provided for the identification of green sheet flaw precursors. Identification of these precursors allowed for the prediction of defects which occurred several process steps later. Precursor morphologies were a direct measure of local variation in green sheet volume fraction. The thermal inspection technique was found to

have a spatial resolution 1000 times greater than the current x-ray unit with a 500 fold increase in spatial resolution.

Two types of conformance criteria were developed based on statistics of the conforming (green sheet which yielded viable product) and non-conforming (green sheet which failed during processing) green sheet. A statistical parameter, the coefficient of variance (COV) of effusivity, proved to be an effective indicator of the relative risk of subsequent crack formation. The advantage of using this parameter is that it indicates changes in the level of process control and is computationally simple and rapid. However, this statistic provides no spatial information. The ability to identify the location, distribution, and severity of a particular flaw precursor is necessary to determine specific causes and provide process feedback. This was achieved by identifying an acceptable transverse, normalized, effusivity profile and an acceptance band. This profile takes into account normal process variations (e.g. roller flexure). This criteria correctly categorized all of the 20 sheets regarding their final disposition (i.e. pass or fail) during processing. Determination of the methods statistical capability will require improvement in the reference samples and primary methods for flaw identification within manufacturing. Compaction standards, similar to the reference samples developed in the current work, will allow the thermal data to be calibrated with alloy volume fraction. Figure 6-1 depicts an arrangement for integrating a front-flash thermal inspection technique into the current production environment. The conclusion is that the developed method is an effective means to detect flaws in partially processed FeAl material. It is anticipated that as process development continues the flaws will become more subtle.

# Inspection Process

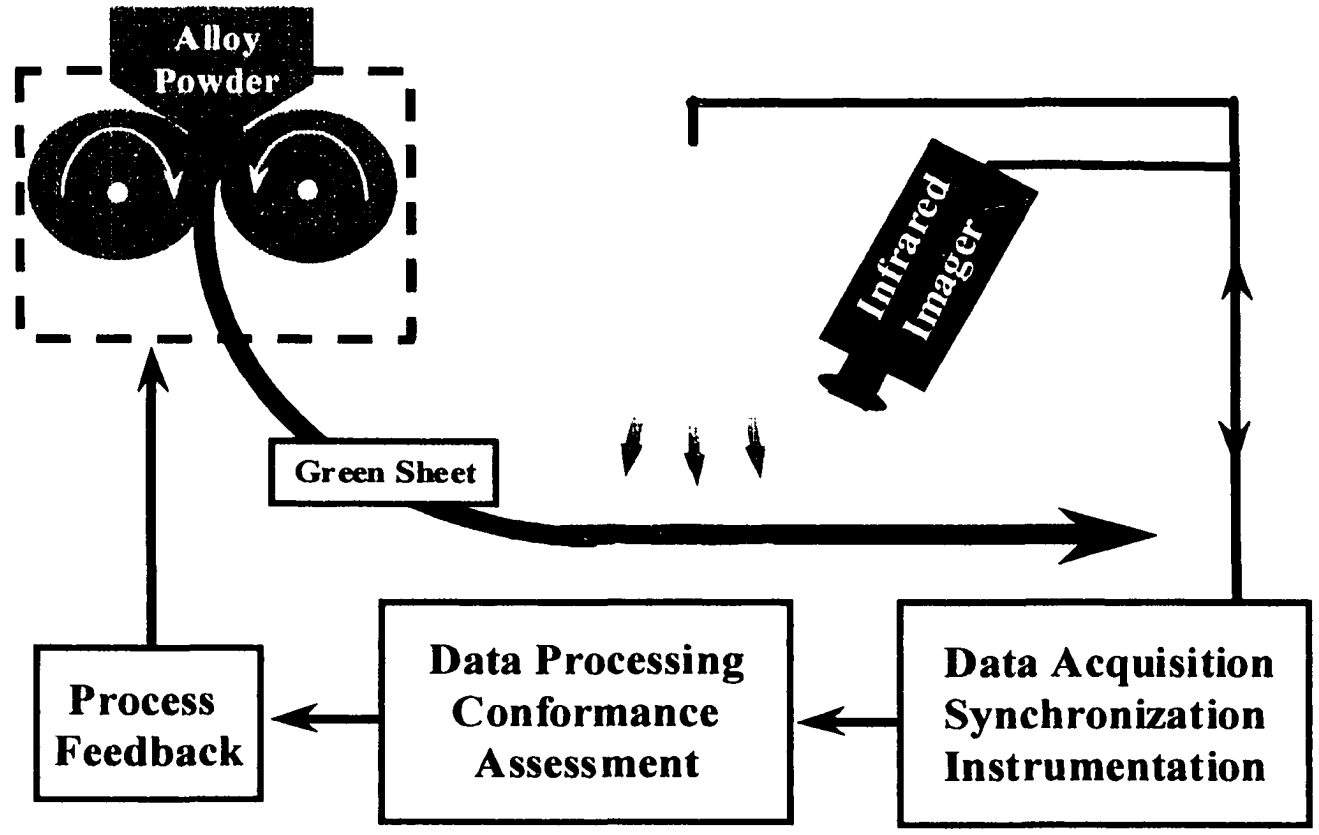


Figure 6-1: Arrangement depicting the integration of a front-flash thermal inspection technique into a roll compaction process.



As a result it may be necessary to reduce the confidence interval and modify the profile of the conformance criteria.

Research into the application of modern quantitative NDE techniques to enhance the quality of powder metal parts is relatively recent. Prior to the current effort thermography had not been considered a viable tool for the detection of green powder metallurgy defects nor as a vehicle for understanding and improving the processing of green parts. The current work clearly demonstrates the value of quantitative thermography within the powder metallurgy industry.

# Bibliography

- [1] R.M. German. *Powder Metallurgy*. Metal Powder Industries Federation, 1994.
- [2] *MPIF Website (HTTP:www.mpif.org)*, March 1999.
- [3] J. Porter. Equipment, productivity and quality in powder metallurgy. *The International Journal of Powder Metallurgy*, 29(1):13-14, 1993.
- [4] Metal Powder Industries Federation. *1998 Applications of Non-Destructive Evaluation in Powder Metallurgy Seminar*. 1998. Seminar Notes.
- [5] D.C. Zenger et al. Detecting cracks in green P/M components. In J. Porter and M. Phillips, editors, *Test Methods: Advances in Powder Metallurgy and Particulate Materials*. volume 9, pages 3-16. Metal Powder Industries Federation, 1995.
- [6] Standard test methods for metal powders and powder metallurgy products. Technical report, 1998.
- [7] D.P. DeWitt, G.D. Nutter. *Theory and Practice of Radiation Thermometry*. John Wiley & Sons, Inc., 1988.
- [8] A. Rogalski. Infrared heterodyne detection. In *Proceedings of the IEEE*. volume 56, pages xiii-xxiv, 1968.
- [9] H.S. Carslaw, J.C. Jaeger. *Conduction of Heat in Solids*. Clarendon Press, 1995.
- [10] W.M. Rohsenow et al. *Heat Transfer Fundamentals*. McGraw-Hill Book Company, 1985.
- [11] R. Berman. *Thermal Conduction in Solids*. Oxford University Press, 1978.
- [12] J.M. Hill, J.N. Dewynne. *Heat Conduction*. Blackwell Scientific Publications, 1987.

- [13] X. Maldague, editor. *Infrared Methodology and Technology*. Gordon and Breach Science Publishers S.A., 1994.
- [14] W.J. Parker et al. Flash method of determining thermal diffusivity, heat capacity, and thermal conductivity. *J. Appl. Phys.*, 32(9):1679-1684, 1961.
- [15] P.V. Vladimir. The Basics of Transient IR Thermographic NDT. SPIE's International Symposium on AeroSense, Short Course Notes, 1999.
- [16] C. Hobbs, A. Temple. The inspection of aerospace structure using transient thermography. *British Journal of NDT*; 35(4):183-189, 1993.
- [17] M.P. Connolly, D. Copley. *Materials Evaluation*, 48(12):1461-1463, 1990.
- [18] K.E. Cramer et al. Thermal diffusivity imaging of ceramic composites. In *International Gas Turbine and Aeroengine Congress and Expositions Proceedings*, pages 1-8. The American Society of Mechanical Engineers, 1993.
- [19] W.P. Winfree, D.M. Heath. Thermal diffusivity imaging of aerospace materials and structures. In J.R. Snell, Jr. and R.N. Wurzbach, editors, *Thermosense XX*, volume 3361, pages 282-290. SPIE Proceedings Series, 1998.
- [20] P.R. Emeric, W.P. Winfree. Characterization of composite materials from temporal thermal response. *Reviews of Progress in Quantitative NDE*. 15, 1996.
- [21] L.D. Favro et al. Fast infrared measurements of the thermal diffusivities of anisotropic materials. In J.R. Snell, Jr. and R.N. Wurzbach, editors, *Thermosense XX*, volume 3361, pages 248-253. SPIE Proceedings Series, 1998.
- [22] C.S. Welch et al. Remote determination of the two-dimensional diffusivity tensor in thin plates. In *1985 Ultrasonics Symposium*, pages 1139-1142.
- [23] C.S. Welch et al. Quantitative thermal characterization of thin plates. In D.E. Chimenti D.O. Thompson, editor, *Review of Progress in Quantitative Nondestructive Evaluation*, volume 5B, pages 1133-1139. Plenum Publishing Corp., 1986.
- [24] W. Winfree et al. Material property measurements with post-processed thermal image data. In *SPIE Thermosense XII*, volume 1313, pages 124-133, 1990.

- [25] C.S. Welch et al. Remote measurement of in-plane diffusivity components in plates. *J. Appl. Phys.*, 61(3):895-898, 1987.
- [26] D.M. Heath et al. Quantitative thermal diffusivity measurements of composites. In D.E. Chimenti and D.O. Thompson, editors, *Review of Progress in Quantitative Non-destructive Evaluation*, volume 5B, pages 1125-1132. Plenum Publishing Corp., 1986.
- [27] J. Hartikainen et al. Fast infrared line-scanning method and its application. In D.E. Chimenti and D.O. Thompson, editors, *Review of Progress in Quantitative Nondestructive Evaluation*, volume 13, pages 401-408. Plenum Press, 1994.
- [28] K.E. Cramer, W.P. Winfree. Thermographic imaging of cracks in thin metal sheets. *SPIE Thermosense XIV*; 1682:162-170, 1992.
- [29] K.E. Cramer et al. Thermographic detection of cracks in thin metal sheets. In D.E. Chimenti and D.O. Thompson, editors, *Review in Progress in Quantitative NDE*, volume 10A, pages 1087-1094. Plenum Press, 1991.
- [30] K.E. Cramer, W.P. Winfree. Thermographic detection and quantitative characterization of corrosion by application of thermal line source. In J.R. Snell, Jr. and R.N. Wurzbach, editors, *Thermosense XX*, volume 3361, pages 291-300. SPIE Proceeding Series, 1998.
- [31] M. Shiratori et al. Application of infrared thermography to detection of cracks. *JSME International Journal*. 37(3):296-302, 1994.
- [32] G. White, G. Torrington. Crack detection and measurement using laser pulse heating and thermal microscopy. *Materials Evaluation*, pages 1332-1334, December 1995.
- [33] G. White et al. A thermal imaging system for crack growth quantification in thermo-mechanical fatigue specimens. In D.E. Chimenti and D.O. Thompson, editors, *Review of Progress in Quantitative Nondestructive Evaluation*, volume 15, pages 1961-1967. Plenum Press, 1996.
- [34] M.L. Watkins. The characterization of rolled sheet alloy using infrared microscopy.

- In R.E. Green Jr., editor, *Nondestructive Characterization of Material VIII*; pages 263-268. Plenum Press, 1998.
- [35] R.L. Thomas et al. Subsurface flaw detection in metals by photoacoustic microscopy. *J. Appl. Phys.*, 51(2):1152-1156, 1980.
- [36] M.L. Watkins, M. Hinders. The characterization of iron aluminide green sheet thermal properties. *Materials Science and Engineering*, A258:266-269, 1998.
- [37] L.D. Favro et al. Thermal wave imaging for aging aircraft inspection. *Materials Evaluation*. pages 1386-1389, December 1993.
- [38] L.D. Favro et al. Thermal wave imaging of disbonding and corrosion on aircraft. In D.E. Chimenti and D.O. Thompson, editors, *Review of Progress in Quantitative Nondestructive Evaluation*, volume 15, pages 1747-1753. Plenum Press, 1996.
- [39] N. K. Del Grande, P. F. Durbin. Precise thermal nondestructive evaluation for quantifying structural damage. In D.O. Thompson and D.E. Chimenti, editors, *Review of Progress in Quantitative Nondestructive Evaluation*, volume 15, pages 525-531. Plenum Press, 1996.
- [40] P.H. James et al. A numerical grid generation scheme for thermal simulations in laminated structures. In D.O. Thompson and D.E. Chimenti, editors, *Review of Progress in Quantitative Nondestructive Evaluation*, volume 8A, pages 801-809. Plenum Press, 1989.
- [41] A. Daniels. Nondestructive pulsed infrared quantitative evaluation of metals. In *Thermosense XVIII: An International Conference on The Thermal Sensing and Imaging Diagnostic Applications*, pages 185-201. SPIE Proceedings Series, 1996.
- [42] J.J. Stiglich et al. The thermal inertia analysis technique in gas turbine component reliability assessment. In *ASM Materials Solutions, 12-15 October, 1998*.
- [43] L.C. Aamodt et al. Analysis of characteristic thermal transit times for time-resolved infrared radiometry studies of multilayered coatings. *J. Appl. Phys.*, 68(12):6087-6098, 1990.
- [44] D.L. Balageas et al. Pulsed photothermal modeling of layered materials. *J. Appl.*

*Phys.*, 59(2):348-357, 1986.

- [45] M. Oksanen et al. Photothermal and photoacoustic investigation of zirconia coating delaminations. In D.E. Chimenti and D.O. Thompson, editors, *Review of Progress in Quantitative Nondestructive Evaluation*, volume 15, pages 1559-1563. Plenum Press, 1996.
- [46] M.E. McKnight, J.W. Martin. Detection and quantitative characterization of blistering and corrosion of coatings on steel using infrared thermography. *Journal of Coatings Technology*, 61(775):57-62, 1989.
- [47] R. Vassen et al. Influence of binder content and particle size on green strength of wet powder pouring parts. *Powder Metallurgy*, 38(1):55-58, 1995.
- [48] R. Osiander et al. Analysis methods for full-field time-resolved infrared radiometry. In J.W. Spicer and D.D. Burleigh, editors, *Thermosense XVIII: An International Conference on Thermal Sensing and Imaging Diagnostic Applications*, volume 2766, pages 218-227. SPIE Proceedings Series, 1996.
- [49] Metal Powder Industries Federation. *Powder Metallurgy Design Seminar*, 1989. Design Pack Lecture Notes.
- [50] R. Pitchumani et al. A simplified model for estimating the anisotropic conductivities of Al/SiCp composites for process monitoring. *Transport Phenomena in Materials Processing and Manufacturing*, pages 201-207, 1992.
- [51] R. Pitchumani et al. Theoretical models for the anisotropic conductivities of two-phase and three-phase metal-matrix composites. *Acta metall. mater.*; 43(8):3045-3059, 1995.
- [52] S.F. Wang, A.A. Ogale. Continuum space simulation and experimental characterization of electrical percolation behavior of particulate composites. *Composites Science and Technology*, 46:93-103, 1993.
- [53] M. Weber, M.R. Kamal. Estimation of the volume resistivity of electrically conductive composites. *Polymer Composites*, 18(6):711-725, 1997.
- [54] P. Louis, A.M. Gokhale. Computer simulation of spatial arrangement and

- connectivity of particles in three-dimensional microstructure: Application to model electrical conductivity of polymer matrix composite. *Acta mater.* 44(4):1519-1528, 1996.
- [55] A. Jagota, C.Y. Hui. The effective thermal conductivity of a packing of spheres. *Journal of Applied Mechanics*, 57:789-791, 1990.
- [56] S.N. Maiti, K. Ghosh. Thermal characteristics of silver powder-filled polypropylene composites. *Journal of Applied Polymer Science*, 52:1091-1103, 1994.
- [57] R.L. McCullough. Generalized combining rules for predicting transport properties of composite materials. *Composites Science and Technology*, 22:3-21, 1985.

# Vita

## **Michael Lee Watkins**

Mike was born in Denver, Colorado on October 5, 1959. Shortly thereafter, his family moved to Virginia. He attended Matoaca High School and graduated in 1978. He received a Bachelor of Science degree in Physics from James Madison University (Harrisonburg, Virginia) in 1982 and a Masters of Science degree in Physics from Auburn University (Auburn, Alabama) in 1987. Later that year, he accepted an Associate Scientist position with Philip Morris, USA in Richmond, VA. From that position, Mike was promoted to Assistant Scientist, Scientist and then to Research Scientist. In 1997, he took a sabbatical from work to pursue his doctoral degree in Applied Science at The College of William and Mary (Williamsburg, Virginia). He received a Ph.D. in Applied Physics in May 1999. During his career, Mike has given presentations at numerous national and international conferences, published several articles, and has been granted 18 United States patents. Mike continues to work at Philip Morris. He resides in Chester, Virginia with his wife, two daughters, and their pet golden retriever, "Aubie".